

PROTON-CAPTURE CROSS-SECTION MEASUREMENTS FOR THE ASTROPHYSICAL
GAMMA PROCESS: FROM STABLE TO RADIOACTIVE ION BEAMS

By

Artemis Tsantiri

A DISSERTATION

Submitted to
Michigan State University
in partial fulfillment of the requirements
for the degree of

Physics—Doctor of Philosophy

2025

ABSTRACT

One of the key questions in nuclear astrophysics is understanding how elements heavier than iron are forged in the stars. Heavy element nucleosynthesis is primarily governed by the slow and rapid neutron capture processes. However, a relatively small group of naturally occurring, neutron-deficient isotopes, known as p nuclei, cannot be formed by either of those processes. These ~ 30 nuclei are believed to be synthesized in the γ process, where preexisting r - and s -process seeds are “burned” through a sequence of photodisintegration reactions. The astrophysical sites where such conditions occur has been a subject of controversy for more than 60 years, and is currently believed that the γ process can take place in the O/Ne layers of core collapse supernovae, and in thermonuclear supernovae.

Reproducing solar p -nuclei abundances through nuclear reaction networks requires input on a large number of mostly radioactive isotopes. However, as experimental cross sections of γ -process reactions are very limited, and almost entirely unknown for radioactive nuclei, the related reaction rates are based on Hauser-Feshbach (HF) theoretical calculations and therefore carry large uncertainties. Therefore, it is crucial to develop techniques to accurately measure these reactions within the astrophysically relevant Gamow window with radioactive beams. The SuN group at the Facility for Rare Isotope Beams (FRIB) has been developing such a program for the past decade.

This thesis focuses on implementing a technique to measure reaction cross sections in inverse kinematics with a radioactive beam. Specifically, this work presents data analysis from the proof-of-principle stable beam experiment for the $^{82}\text{Kr}(p,\gamma)^{83}\text{Rb}$ reaction, along with the measurement of the $^{73}\text{As}(p,\gamma)^{74}\text{Se}$ reaction in our first radioactive beam experiment. The latter reaction is particularly significant for the final abundance of the lightest p nucleus, ^{74}Se , since the inverse reaction $^{74}\text{Se}(\gamma,p)^{73}\text{As}$ is one of the primary destruction mechanisms of ^{74}Se .

The experiments were conducted at FRIB at Michigan State University using the ReA facility. The ^{82}Kr and ^{73}As beams were directed onto a hydrogen gas cell located in the center of the Summing NaI(Tl) (SuN) detector and the obtained spectra were analyzed using the γ -summing technique. In addition to the total cross section measurements, this thesis also presents the development of an

analysis technique to extract statistical properties of the compound nucleus (nuclear level density and γ -ray strength function) through a series of simulations. This approach enables the extraction of an experimentally constrained cross section across the entire Gamow window of the γ process. Finally, the experimentally constrained reaction rate for the $^{73}\text{As}(p, \gamma)^{74}\text{Se}$ reaction is used in Monte Carlo one-zone network simulations of the γ process to explore its impact on the production of the ^{74}Se .

Copyright by
ARTEMIS TSANTIRI
2025

Στη μάνα μου, που μου έδωσε φτερά να πετάζω.

ACKNOWLEDGEMENTS

First and foremost, I would like to express my deepest gratitude to my thesis supervisor, Artemis Spyrou, for accepting me as a graduate student and for being an incredible mentor over the past five years. Artemis generously provided the means for an excellent education with great emphasis on professional development, encouraging me to attend multiple summer schools, conferences and workshops. Through her guidance, I learned how to work within a research group and a larger collaboration, and I am especially grateful for her support in helping me build my own professional network by introducing me to her collaborators and providing opportunities to establish connections that will be invaluable throughout my career. Most importantly, I deeply appreciate the trust she placed in me by allowing me to choose my thesis topic, and her hands-off approach to supervision that gave me the freedom to explore beyond my thesis, develop my own ideas, and grow both scientifically and personally. Looking back, I am certain that my decision to move halfway across the world to work with her has been the best academic decision I have ever made.

I would like to thank Hendrik Schatz and Sean Liddick, for all their help and guidance during my graduate studies and my thesis project. I also want to express my gratitude to the rest of my supervisory committee, Scott Bogner, Kendall Mahn and Brian O'Shea for their advice, questions, and offering their valuable time to serve on my guidance committee.

I would like to thank all past and present members of the SuN group for their support and camaraderie. I am especially grateful to the former and current postdocs — Andrea, Erin, Mallory, and Sivi — for their guidance and friendship, with special thanks to Erin for her support and help during the execution of my experiment, and for teaching me to keep moving forward with a smile, calmness, and lightheartedness when things don't go as planned. I also want to acknowledge former graduate students Alicia, Steven, and Alex, whose work laid the foundation for this research. To my fellow current graduate students — Hannah, Jordan, Caley, Kostas, Amal, and Sydney — thank you for making this journey both productive and enjoyable, especially to Hannah who has been my academic sister, and best office and travel mate. I wish all of them the best in their next stages of their career. I also extend my gratitude to the members of the β group and everyone I have

interacted with through the SuN detector. This group has truly felt like a family, and I thank them for all the great memories and adventures.

I would also like to thank all the staff physicists and faculty at FRIB who contributed to the execution of my thesis experiment. I am especially grateful to Jorge Pereira and Remco Zegers for their support with the hydrogen gas handling system, Aaron Chester for teaching me the ins and outs of the FRIB DAQ and helping me set up the experiment's software, and Ana Henriques, Sam Nash, and Chandana Sumithrarachchi for assisting with the setup in ReA3 and providing such a beautiful—yet tricky—arsenic beam.

Additionally, I want to thank the members of the NuGrid Collaboration for welcoming me into their community and enabling the astrophysical calculation portion of my dissertation. In particular, I am grateful to Pavel Denissenkov and Falk Herwig for hosting me during my internship at the University of Victoria, introducing me to the NuGrid codes, and engaging in many interesting discussions during my visit. I also appreciate the support of Thanassis Psaltis and Lorenzo Roberti for their help in setting up this impact study, sharing their codes, and contributing valuable ideas and discussions. Finally I am thankful for Umberto Battino and Claudia Travaglio for providing the trajectories for the Type Ia impact study.

I am also grateful for the support of IReNA throughout my graduate studies, including the generous funding that allowed me to attend numerous conferences and summer schools, as well as the Visiting Fellowship that made my research stay at UVic possible.

I am deeply grateful for all my close friends, both near and far. To Pely, Nikos, Yannis, and Emily — thank you for the memories, adventures, and for making Lansing feel like home. To my friends from afar—Christos, Christina, Anna, Orestis, and Eva—your unwavering support has meant the world to me, no matter the distance. You have always been with me wherever I go. A very special thank you to my partner, best friend, roommate, and colleague, Jordan. Meeting you has been the best part of this journey, and I can't wait to see where our next adventures take us.

Finally, I would like to express my deepest gratitude to my family—my parents, Despoina and Nikos, and my sister, Christina. I cannot overstate my appreciation for their love, support, and

the countless sacrifices they have made. They have always encouraged me to pursue my goals, no matter how far they took me. Especially to my mother, to whom I dedicate this thesis—I doubt many people can say their mother followed them to a scientific conference because Austria was the closest they had been to home in a while.

And, of course, to my cat, who has been a constant source of comfort, chaos, and companionship through it all.

TABLE OF CONTENTS

CHAPTER 1	INTRODUCTION	1
CHAPTER 2	NUCLEAR PHYSICS FOR ASTROPHYSICS	2
	2.1 Nuclear Masses and Binding Energies	3
	2.2 Energetics of Nuclear Reactions	5
	2.3 Reaction Cross Section	6
	2.4 Nuclear Reactions	7
	2.4.1 Direct Reactions	9
	2.4.2 Compound Nucleus Reactions	9
	2.5 Nuclear Reactions in Stars	18
	2.5.1 Reactions at elevated temperatures	20
	2.5.2 Inverse Reactions	21
	2.5.3 Neutron-Induced Reactions	22
	2.5.4 Charged-Particle-Induced Reactions	22
CHAPTER 3	ASTROPHYSICS	26
	3.1 Abundances	26
	3.2 Stellar Evolution	27
	3.2.1 Supernovae	28
	3.3 Stellar Nucleosynthesis	30
	3.3.1 Hydrostatic Burning	31
	3.3.2 Nucleosynthesis During Core-Collapse SN	33
	3.3.3 Nucleosynthesis Beyond Iron	33
	3.4 Production of the p Nuclei	39
	3.4.1 The γ Process	41
	3.4.2 Other Scenarios for the p Process	44
	3.5 Nuclear Networks and Uncertainties	46
	3.6 The Lightest p Nucleus, ^{74}Se	48
CHAPTER 4	EXPERIMENTAL SETUP & TECHNIQUES	52
	4.1 Beam Delivery in ReA	53
	4.2 Hydrogen Gas Target	55
	4.3 The SuN Detector	57
	4.3.1 Summing Technique	58
	4.4 The SuNSCREEN Detector	60
CHAPTER 5	ANALYSIS	63
	5.1 Effective Energy	63
	5.2 Beam Particle Number	64
	5.3 Experimental Yield	66
	5.3.1 SuN Gainmatching & Energy Calibration	66
	5.3.2 The Sum Peak	69
	5.3.3 Doppler-Shift Corrections	69

5.3.4	Background Subtraction	70
5.4	Target Particle Density	75
5.5	Detection Efficiency	76
5.5.1	RAINIER Simulations	76
5.5.2	GEANT4 Simulations	77
5.5.3	Chi-Square Minimization	78
5.6	Theoretical Investigation with RAINIER and TALYS	80
5.6.1	Constraining the Statistical Properties of ^{83}Rb	82
5.6.2	Constraining the Statistical Properties of ^{74}Se	83
5.7	Uncertainty Quantification	85
CHAPTER 6	RESULTS & DISCUSSION	90
6.1	The $^{82}\text{Kr}(p, \gamma)^{83}\text{Rb}$ cross section	90
6.2	The $^{73}\text{As}(p, \gamma)^{74}\text{Se}$ cross section	95
CHAPTER 7	ASTROPHYSICAL IMPACT	100
7.1	Core-Collapse Supernova - SNIID	100
7.2	Type Ia Supernova - SNIa	105
CHAPTER 8	SUMMARY & CONCLUSIONS	108
BIBLIOGRAPHY	109
APPENDIX	TALYS SCORES FOR THE $^{73}\text{AS}(p, \gamma)^{74}\text{SE}$ REACTION	127

CHAPTER 1

INTRODUCTION

Carl Sagan said, “we are made of star stuff”. But how is this “star stuff” made? The carbon in our cells, the calcium in our bones, and the oxygen in our blood are all forged during the life of a star. But the silver and gold in our jewelry, the platinum in our cars, and the tungsten in our LED lights were all made during a star’s death.

The origins of nuclear astrophysics trace back over a century to Eddington’s 1920 manuscript, which, based on Aston’s demonstration that the mass of helium is less than four times that of the proton [1], proposed that an unknown process in the Sun’s core converts hydrogen into helium, releasing energy [2]. Nearly 40 years later, the groundbreaking review by Burbidge, Burbidge, Fowler, and Hoyle (B²FH) presented a detailed framework of stellar nucleosynthesis, describing how the elements are synthesized in stars [3]. These discoveries highlighted the need for a field that combines astronomy, astrophysics, and nuclear physics to explore how the elements in the universe came to be, the interdisciplinary field of nuclear astrophysics.

The following thesis aims to offer but a small contribution to this ongoing effort, by focusing on the nucleosynthesis of a particular isotope, namely ⁷⁴Se. Given the interdisciplinary nature of nuclear astrophysics, the necessary theoretical foundations are introduced in separate chapters covering nuclear physics and astrophysics. Then, the experimental study of the destruction mechanism of ⁷⁴Se is presented, followed by analysis of the experimental data. Finally, the impact of the measurement is investigated through astrophysical network calculations, aiming to constrain the final production of ⁷⁴Se in stars.

CHAPTER 2

NUCLEAR PHYSICS FOR ASTROPHYSICS

As per Rutherford's description, the majority of the atom's volume is comprised of empty space and electrons that surround a tiny, dense, positively charged central core called the *nucleus*. Composed of protons and neutrons, the nucleus is characterized by the *mass number*, A , which represents their total number. The number of protons is called the *atomic number* Z , and the *neutron number* N is defined as $N = A - Z$. Different *elements* are distinguished by the different atomic number Z , whereas nuclei of the same element with different neutron number N are called *isotopes*. The notation for different isotopes is A_ZX_N , or simply AX , where X represents the chemical symbol of the element.

Similarly to chemical elements in the periodic table, isotopes are represented in the *chart of the nuclides*. This two-dimensional chart, shown in Fig. 2.1 displays the number of protons, Z , on the

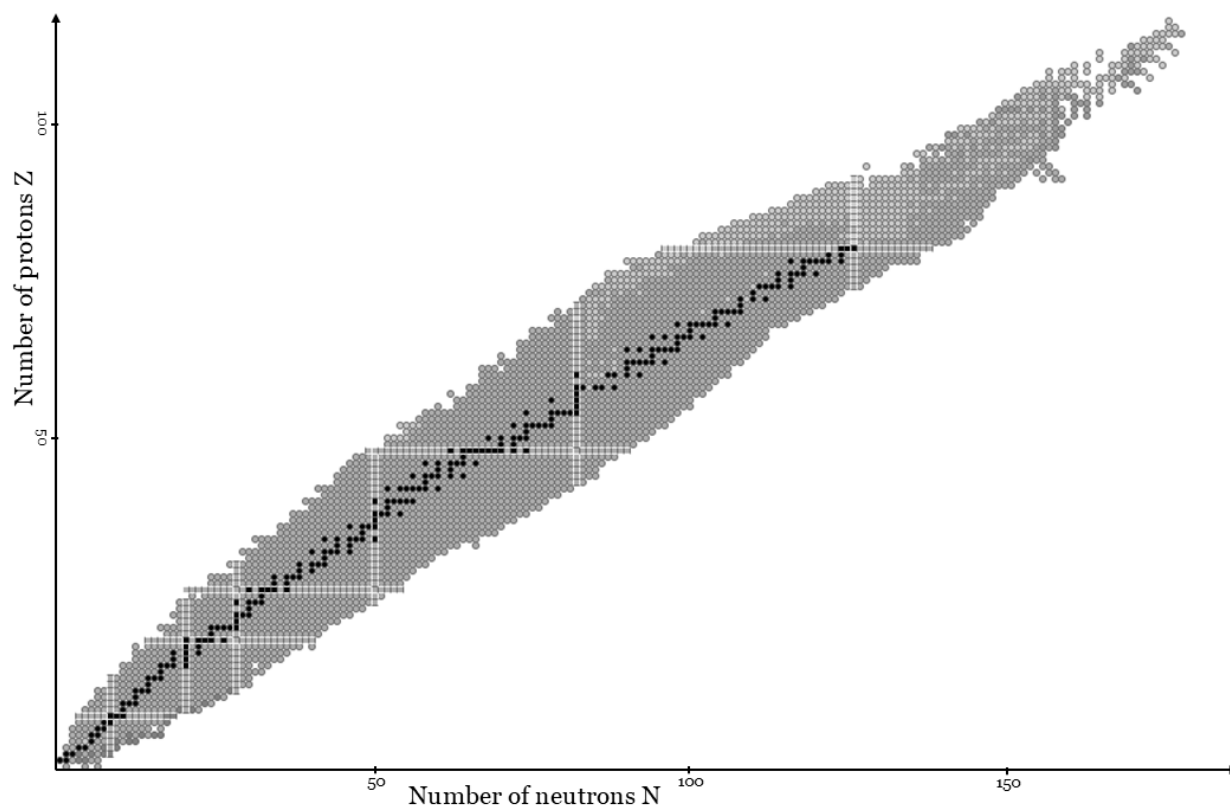


Figure 2.1 The chart of nuclides. The black squares correspond to stable nuclei, while the gray to radioactive. The white lines indicate proton and neutron magic numbers. Data from IAEA [4].

y-axis, and the number of neutrons N on the x-axis. Each square represents a different isotope with different properties. The black squares correspond to *stable* isotopes that can be found in nature, while the gray are *radioactive*, meaning that after some time they will lose energy by emitting radiation. The white lines correspond to proton and neutron *magic numbers*, which according to the *nuclear shell model* developed Mayer in 1948 [5], refer to specific numbers of protons or neutrons within a nucleus that result in significantly increased stability. The magic numbers for nuclei are 2, 8, 20, 28, 50, 82, and 126.

2.1 Nuclear Masses and Binding Energies

One might initially assume that the nuclear mass, m_{nuc} , equals $Z m_p + N m_n$, where m_p and m_n are the masses of protons and neutrons that comprise the nucleus, respectively. However, Aston's experiments in the 1910s revealed that the mass of helium (${}^4\text{He}$) is less than 4 times the mass of hydrogen (${}^1\text{H}$) [1]. This mass difference is called the *mass excess* or *mass defect*, Δm , and is a direct result of the *binding energy* that holds the nucleus together. The binding energy, $B(Z, N)$, represents the energy required to break a nucleus into its constituent Z protons and N neutrons, and can be expressed as

$$B(Z, N) = \Delta m \cdot c^2 = (Z m_p + N m_n - m_{\text{nuc}}) c^2 \quad (2.1)$$

[6], where c^2 often includes a unit conversion factor so that $c^2 = 931.50 \text{ MeV/u}$, and thus the binding energy is expressed in atomic mass units.

A useful nuclear property derived from the binding energy is the *particle separation energy*, which corresponds to the energy required to remove a proton or a neutron from a nucleus. Hence the *proton separation energy* is equal to the difference between the binding energy of ${}^A_Z X_N$ and ${}^{A-1}_{Z-1} X_N$:

$$\begin{aligned} S_p &= B(Z, N) - B(Z - 1, N) \\ &= [m({}^A_Z X_N) - m({}^{A-1}_{Z-1} X_N) + m({}^1\text{H})] c^2 \end{aligned} \quad (2.2)$$

and similarly the *neutron separation energy* is:

$$\begin{aligned}
 S_n &= B(Z, N) - B(Z, N - 1) \\
 &= [m({}_Z^A X_N) - m({}_Z^{A-1} X_{N-1}) + m_n] c^2
 \end{aligned}
 \tag{2.3}$$

The separation and binding energies carry important information about the stability and structure of the nuclides.

To allow for a systematic study of the nuclear binding energy, it is common to display the average binding energy per nucleon, B/A . Figure 2.2 shows B/A as a function of mass number A [7]. A few notable features shown in Fig. 2.2 include that, aside from the light nuclei, the average

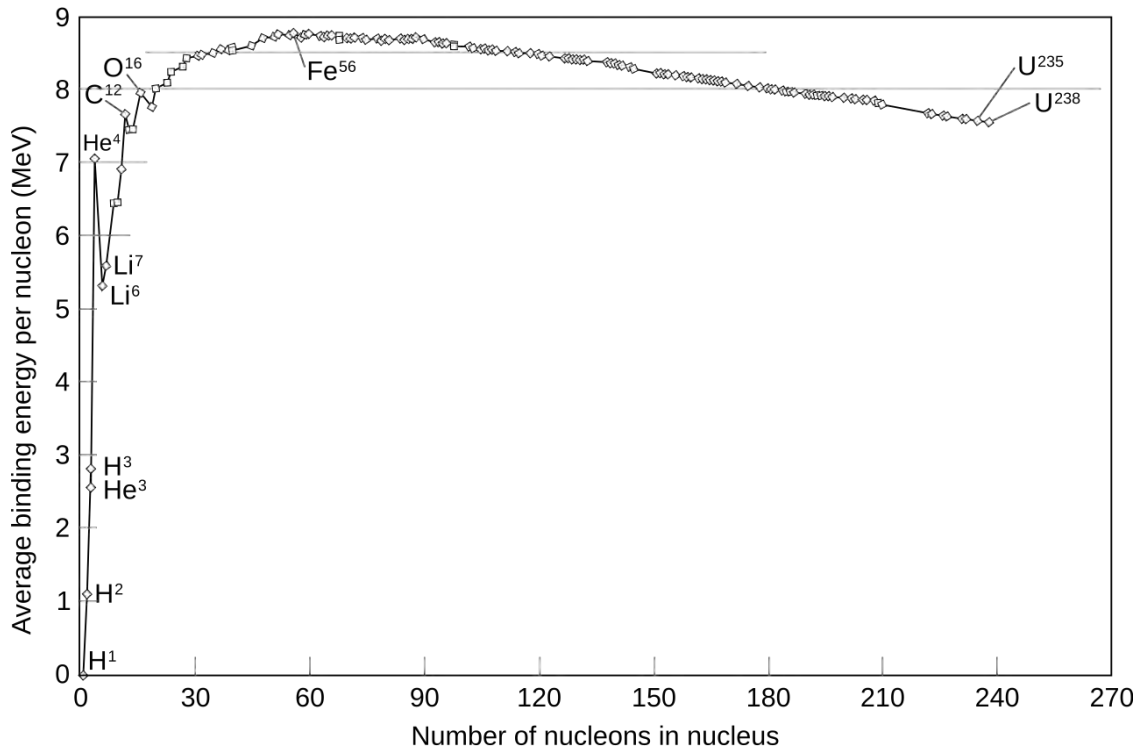


Figure 2.2 The binding energy per nucleon, $B(Z, N)/A$, as a function of the mass number, A . Figure from [8].

binding energy is around 8 MeV/u. The most bound nuclei, those with the maximum B/A , are found in the mass range of $A = 50 - 65$. This is the so-called *iron peak*, with the most tightly bound nuclides being ${}^{62}\text{Ni}$, ${}^{58}\text{Fe}$, and ${}^{56}\text{Fe}$ [9]. It follows that there are two ways to release energy through nuclear processes: for nuclei lighter than the iron peak energy is released by *fusion*, the assembly of light nuclei into heavier species, while for nuclei heavier than iron, energy is released by *fission*,

the breaking of heavy nuclei into lighter ones [7]. As will be described later in Ch. 3, these are the two main mechanisms for energy generation in a stellar environment.

2.2 Energetics of Nuclear Reactions

A binary nuclear interaction is written as

$$a + X \rightarrow Y + b \quad \text{or} \quad X(a, b)Y \quad (2.4)$$

where a and X are the two colliding nuclei (*entrance channel*), and b and Y are the reaction products (*exit channel*). Typically, a is an accelerated projectile of lighter mass and X is a stationary heavy target, while b is the light ejectile that can be directly measured and Y is the heavy recoil nucleus that stays in the target and is not observed. The various classifications of nuclear reactions are discussed in Sec. 2.4.

As with every other interaction in nature, nuclear reactions are governed by fundamental *conservation laws*, which provide a basis for deriving various characteristic quantities to describe the system. For example the *conservation of total energy and linear momentum* allows us to deduce the energy of the undetected recoil nucleus from the known energies of the reactants and the measured energy of the ejectile. Other conserved quantities include the *angular momentum*, proton and neutron number (or *baryon number*), and *parity* [7].

The conservation of total relativistic energy for a reaction of the form shown in Eq. 2.4 yields

$$m_X c^2 + E_X + m_a c^2 + E_a = m_Y c^2 + E_Y + m_b c^2 + E_b \quad (2.5)$$

where E_i are the kinetic energies in the center-of-mass system and m_i the rest masses. The energy available in the system for this reaction is defined as the *Q value*, and represents the difference in mass energy of the system before and after the reaction.

$$\begin{aligned} Q &= (m_{\text{initial}} - m_{\text{final}}) c^2 \\ &= (m_X + m_a - m_Y - m_b) c^2 \end{aligned} \quad (2.6)$$

or in terms of the excess of kinetic energy

$$\begin{aligned}
 Q &= E_{\text{final}} - E_{\text{initial}} \\
 &= E_Y + E_b - E_X - E_a
 \end{aligned}
 \tag{2.7}$$

If the Q is positive, then the reaction releases energy, and is called *exoergic* or *exothermic*. If Q is negative, then energy is consumed for the reaction to occur, and it is called *endoergic* or *endothermic* [7].

The particle separation energy introduced in Sec. 2.1 corresponds to the Q value for particle emission. The proton separation energy, S_p , corresponds to the Q value for proton emission, while the neutron separation energy, S_n , corresponds to that for neutron emission. This will become important later in Ch. 3, as these quantities define the limits of the nuclear landscape.

2.3 Reaction Cross Section

One of the most important quantities characterizing a nuclear reaction is the *cross section*, σ , which can be broadly understood as the probability for an interaction to occur. Consider the geometry illustrated in Fig. 2.3. An incident beam of I_a particles per unit time impinges on a target

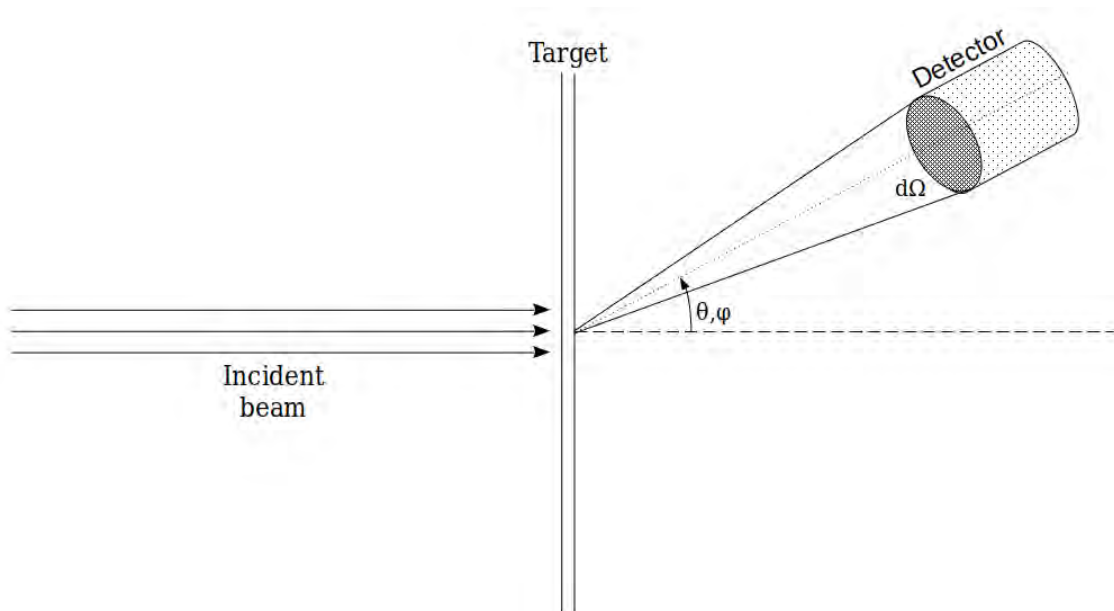


Figure 2.3 Illustration of a typical nuclear physics cross section measurement, showing an incident beam, target and detector. Figure recreated based on [6, 7].

of N_t particles per unit area. A detector is positioned at an angle (θ, ϕ) with respect to the beam

axis, and its surface covers a solid angle $d\Omega$. If the rate of outgoing ejectile particles is R_b , then the reaction cross section is defined by

$$\begin{aligned}\sigma &= \frac{\text{(interactions per unit time)}}{\text{(incident particles per unit time)(target nuclei per unit area)}} \\ &= \frac{R_b}{I_a N_t}\end{aligned}\quad (2.8)$$

By this definition, the cross section has dimensions of area, but is proportional to the reaction probability and is typically measured in *barns*, where $1 \text{ b} = 10^{-24} \text{ cm}^2$.

The detector of Fig. 2.3 covers but a small solid angle $d\Omega$, and therefore could not have possibly detected all outgoing particles. The ejectiles are emitted in a non uniform manner, and if we assume an angular distribution $r(\theta, \phi)$ for the emitted ejectiles, then the fraction of ejectiles detected would be $dR_b = r(\theta, \phi) d\Omega/4\pi$. The illustrated geometry would allow for the measurement of the *differential cross section*, $d\sigma/d\Omega = r(\theta, \phi)/(4\pi I_a N_t)$. The total reaction cross section can be calculated by integrating $d\sigma/d\Omega$ over all angles, where $d\Omega = \sin \theta d\theta d\phi$.

$$\sigma = \int \frac{d\sigma}{d\Omega} d\Omega = \int_0^\pi \sin \theta d\theta \int_0^{2\pi} d\phi \frac{d\sigma}{d\Omega}\quad (2.9)$$

In this work, as described later on in Ch. 4, the detector geometry has a solid angle of 4π . Therefore this work regards to a total cross section measurement, and the analysis follows Eq. 2.8, with the addition of a detection efficiency term, ϵ . The efficiency accounts for the fraction of the outgoing ejectiles that enter the active volume of the detector, but are not recorded, so that $R_b = Y/\epsilon$, where Y is the experimental yield, meaning the total number of particles detected. The analysis presented in Ch. 5 follows:

$$\sigma = \frac{Y}{I_a N_t \epsilon}\quad (2.10)$$

2.4 Nuclear Reactions

Nuclear interactions of the form $X(a, b)Y$ are categorized based on the nature of the species involved, as well as the mechanisms governing the process. If the reactants a and X are identical to the reaction products, the interaction is referred to as *scattering*. Scattering is classified as *elastic* if the products remain in their ground state and as *inelastic* if they are in an excited state. Otherwise,

the reactants and products are distinct species and a *nuclear reaction* occurs. If particle b is a γ ray, the reaction is called *radiative capture*, whereas if particle a is a γ ray, it is a *photodisintegration*. In cases where particles a and b are identical but an additional ejectile is present (resulting in three final products), the reaction is referred to as a *knockout* reaction. If one or two nucleons are exchanged between the projectile and target, this is classified as a *transfer* reaction. Transfer reactions can be further categorized as *pick-up* reactions, where the projectile acquires nucleons from the target, or *stripping* reactions, where the target removes nucleons from the projectile [7, 10]. Lastly, if the projectile exchanges a proton for a neutron or vice-versa, the process is known as a *charge – exchange* reaction.

Another important way to classify nuclear reactions is based on the governing mechanism, which determines the timescale of the interaction and the extent to which the target nucleus is affected. Imagine you're running through a forest. If you run slowly, you have the time to observe each tree, interact with them, and maybe even touch their leaves. The entire forest feels your presence as you pass through it. But if you're running really fast, you barely notice the trees. All the forest notices is a blur, like a bullet, and you might only interact with a single tree if you hit it directly. Most of the forest remains unaffected by your passage. Nuclear reactions work in a similar way.¹ At low energies, the incoming particle has a large de Broglie wavelength, comparable to the size of the whole nucleus. This allows it to interact with the entire nucleus, forming a *compound nucleus*. For example, a 1 MeV proton has a de Broglie wavelength of about 4 fm, which is equal to the average radius of the Fe nucleus. At higher energies, the particle's de Broglie wavelength becomes much smaller, and it's more likely to interact with individual nucleons. A 50 MeV proton, for instance, with a de Broglie wavelength of about 0.6 fm, is more likely to perform a *direct reaction*. In between these two mechanisms are the *pre-equilibrium* reactions, in which the system of the reactants breaks up before it reaches statistical equilibrium.

¹This metaphor was first introduced to me by my undergraduate supervisor, Mike Kokkoris.

2.4.1 Direct Reactions

Direct reactions, also called *peripheral*, involve the interaction of one or very few particles from the target with the projectile. These reactions occur on a timescale of approximately 10^{-22} seconds and primarily affect the surface of the target, leaving the remaining nucleons largely unaffected as spectators. An example of such reactions are transfer reactions, which are commonly used to study the structure of nuclei. They may insert or remove a particle from a specific state within the nucleus, leaving the rest of the system unperturbed. Such experiments allow to probe particle states of specific angular momentum, spin and parity, by detecting ejectile particles at different angles, and most often regard to the measurement of differential cross sections [7, 11].

2.4.2 Compound Nucleus Reactions

The bound nuclear states studied in direct reactions are stable against particle emission. Therefore, their lifetimes, τ , are very long, and have a narrow *width*, Γ , corresponding to a small uncertainty in their energy, based on Heisenberg's uncertainty principle $\Gamma = \Delta E = \hbar/\tau$ [12]. On the opposite side is the *compound nucleus* mechanism, in which the incoming particle a and target X merge, populating an excited state of a *compound nucleus* C^* . The captured particle remains in the compound system for an extended period, typically on the order of 10^{-16} to 10^{-18} seconds. Unlike direct reactions, this timescale allows the incoming particle to interact randomly with a very large number of nucleons, sharing its energy across the entire system. The resulting compound nucleus has undergone so many small interactions that loses any memory of its formation mechanism. As a result, the entrance and exit channels of the system can be treated independently, an idea described by Bohr's *independence hypothesis* [13, 14].

Compound reactions can populate either the *resonance* region or the *statistical* region (also known as *continuum*), depending on the excitation energy of the compound nucleus and the number of available states. The resonance region corresponds to discrete nuclear states, while the statistical region consists of numerous, closely spaced states that overlap.

2.4.2.1 Resonance Reactions

In *resonance reactions*, the incoming particle becomes “quasibound” to a nuclear state with a very high probability of formation, resulting in a very large cross section. These states of the compound nucleus have small widths and low excitation energies, and will decay either by emitting γ rays or by re-emitting the incident particle, as in scattering.

The cross section $\sigma(E)$ for a resonance with energy E_R and width Γ is described through the *Breit-Wigner formula* as

$$\sigma(E) = \sigma_0 \frac{\Gamma^2/4}{(E - E_R)^2 + \frac{1}{4}\Gamma^2} \quad (2.11)$$

where σ_0 is the cross section value at the maximum of the resonance peak [10]. An illustration of a resonance reaction is shown in Fig. 2.4, where the incident particle a is captured by the target X and populating the E_R state of the Y compound nucleus. The right-hand-side of the illustration shows the cross section for this capture. The resonant state then decays by either emitting γ rays, or re-emitting particle a .

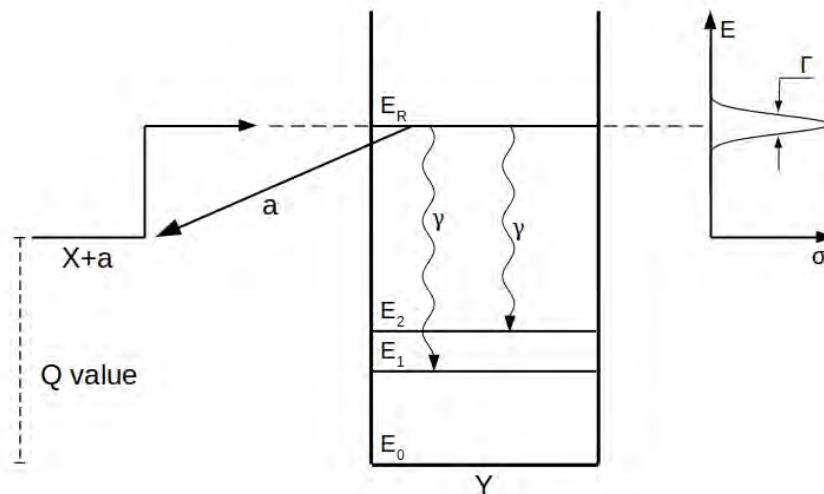


Figure 2.4 Illustration of a resonance reaction. Figure recreated based on [6, 15].

Resonant reactions are particularly important in nuclear astrophysics, as the existence of such resonances enables reactions that would otherwise hinder nucleosynthesis, due to very low cross sections, as described in Sec. 2.5.

2.4.2.2 Statistical Model of Compound Nucleus Reactions

As the excitation energy, E_X , of the compound nucleus populated by the reaction increases, the number of available nuclear states grows almost exponentially. At higher energies, the states become so numerous that their spacing is much smaller than their width, leading to significant overlap and resembling a structureless continuum. Under these conditions, the resonance reaction mechanism becomes inadequate, and the reaction is instead described by the *statistical model of compound reactions*, initially developed by N. Bohr in 1936 [13].

The most widely used implementation of Bohr's independence hypothesis in the statistical model is the *Hauser-Feshbach* (HF) theory [16], that results from averaging over a large number of Breit–Wigner resonances. The central quantities in the HF formalism are the averaged transmission coefficients T , that reflect the probability for a particle's wavefunction to cross an obstacle. In this context, the transmission coefficients, instead of a resonance behavior, they describe the formation of the system as an absorption of the incident particle's wavefunction in the nuclear potential.

The cross section σ of the reaction $a + X \rightarrow C^* \rightarrow Y + b$ (proceeding via compound nucleus C), is expressed as a summation over all possible spin and parity states of the compound system as

$$\sigma^{aX \rightarrow Yb}(E_{aX}) = \frac{\pi \hbar^2 / (2\mu_{aX} E_{aX})}{(2J_X + 1)(2J_a + 1)} \sum_{J, \pi} (2J + 1) \frac{T_a^X(E, J, \pi) T_b^Y(E, J, \pi)}{T_{\text{tot}}(E, J, \pi)} W^{aX \rightarrow Yb} \quad (2.12)$$

where E_{aX} the center mass energy, μ_{aX} the reduced mass, J and π the spin and parity, and T_a^X and T_b^Y the transmission coefficients for the entrance and exit channels respectively. The summation includes all individual transitions to all $J\pi$ states accessible by particle or photon emission from the same compound nucleus C , accounting for the quantum mechanical spin/parity selection rules. The final term $W^{aX \rightarrow Yb}$ is the *width fluctuation correction* (WFC) and describes non-statistical correlations between the widths of the entrance and exit channels and is close to unity [14, 17].

The transmission coefficient for the entrance channel T_a^X is typically calculated numerically by solving the Schrödinger equation with an optical nucleon-nucleus potential, which represents the average nuclear potential. The development of optical model potentials that accurately describe the complexity of the potential caused by the strong nuclear force has been an active field of study

for decades. As a detailed discussion of these potentials exceeds the scope of this thesis, further information can be found in Refs. [18, 19, 20].

The transmission coefficient for the exit channel can be described by assuming all possible bound and unbound states ν in all energetically accessible exit channels.

$$T_b^Y(E, J, \pi) = \sum_{\nu=0}^{\nu_m} T_b^\nu(E, J, \pi) + \int_{E^{\nu_m}}^{E_i} \sum_{J, \pi} T_b(E, J, \pi, E_i, J_i, \pi_i) \times \rho(E_i, J_i, \pi_i) dE_i \quad (2.13)$$

The first term on the right-hand side represents a summation over all experimentally known discrete states, ν_m . The second term is an integration that accounts for the transmission coefficient of all excited states above the highest experimentally known state, ν_m , weighted by the *nuclear level density* $\rho(E_i, J_i, \pi_i)$. This density corresponds to the number of available spin-parity states within an energy region dE_i . If the ejectile b is a particle, T_b is calculated in a similar manner as T_a^X , which requires knowledge of the optical potential that the ejectile must overcome in order to escape the compound system. In the case of radiative capture, however, particle b is a γ ray, and the exit channel will be described by the γ -ray transmission coefficient T_γ , which is directly proportional to the *γ -ray strength function*, and represents the escape probability of a γ ray that is stuck inside the volume of a nucleus. The nuclear level density and γ -ray strength function will be further discussed in the following paragraphs.

2.4.2.3 Nuclear Level Density

The *nuclear level density* (NLD) corresponds to the available quantum levels ΔN at a specific excitation energy E_x , spin J , and parity π , and is defined as:

$$\rho(E_x, J, \pi) = \frac{\Delta N(E_x, J, \pi)}{\Delta E_x} \quad (2.14)$$

where ΔE_x is the energy interval considered, typically 1 MeV. Summing over all possible spin and parity values gives the *total level density* $\rho(E_x)$ [21].

For the statistical-model formalism to apply, the total level density needs to be sufficiently high. While this criterion is somewhat relative, an accuracy of 20% in the description of the level densities with numerical calculations is achievable when $\rho \gtrsim 10 \text{ MeV}^{-1}$ (non-overlapping, narrow

resonances) [22]. For nuclei with mass $A > 60$, excitation energies above approximately 4 MeV have sufficiently high level density for the statistical model to be applicable.

The first theoretical description of level density was proposed by Bethe in 1936 [23], treating the nucleus as a gas of non-interacting fermions (protons and neutrons). While simplistic, this approach captured all the essential information, apart from the influence of the pairing between the nucleons, that was realized and described almost twenty years later by Bardeen, Cooper and Schrieffer [24]. This pairing was then introduced in the description of the level density as a simple constant energy shift, that was later on found to be too large of a correction. This led to the *back-shifted Fermi Gas* formula (BSFG) proposed by Gilbert and Cameron in 1965 [25]:

$$\rho(U) = \frac{1}{\sqrt{2\pi\sigma^2}} \frac{\sqrt{\pi} \exp(2\sqrt{aU})}{12 a^{1/4} U^{5/4}} \quad (2.15)$$

where $U = E_x - \Delta$ is the shifted excitation energy. The energy shift Δ is an empirical parameter closely associated with the pairing energy, accounting for odd-even effects in nuclei. The concept behind Δ is that nucleon pairs must first be separated before their individual components can be excited. In practice, Δ serves as an adjustable parameter to reproduce observables.

The a term in Eq. 2.15, referred to as the *level density parameter*, is, in its most simplistic form, given by $a = \frac{\pi}{6}(g_p + g_n)$, where g_p and g_n is the spacing of the proton or neutron single-particle states near the Fermi energy. Recognizing that a should include energy-dependent shell effects, more sophisticated expressions for a have been developed [26, 27, 28].

The *spin cut-off parameter*, σ^2 , of Eq. 2.15 represents the width of the angular momentum distribution of the level density. The description of σ^2 is based on the observation that the nucleus possesses collective rotational energy, and the spin cut-off parameter is related to the moment of inertia of the undeformed nucleus I_0 , and the thermodynamic temperature $t = \sqrt{U/a}$, so that $\sigma^2 = I_0 t$. Similarly to the parameter a , energy-dependent shell effects are often included in more advanced models for σ^2 [22, 29, 30].

An alternative analytical description of the level density is the *Constant Temperature* (CT) model, introduced by Ericson in 1959, who described it as incorporating “*a temperature τ which is somewhat different from the ordinary nuclear temperature T , defined by the level density*”, [31].

This temperature τ is related to the nuclear temperature T by:

$$\frac{d}{dE} \log \rho(E) = \frac{1}{T} = \frac{1}{\tau} \left(1 - \frac{d\tau}{dE} \right) \quad (2.16)$$

and the level density is then described as

$$\rho(E_X) = \frac{\exp[(E_X - E_0)]/\tau}{\tau} \quad (2.17)$$

where in practice, E_0 and τ are parameters used to adjust the formula to experimental discrete levels. Since the BSFG model diverges as $U \rightarrow 0$, a common practice is to use the CT model at low energies and the BSFG model at higher excitation energies, with parameters to ensure a smooth transition between the two models.

Additional approaches include the phenomenological *Generalized Superfluid Model* (GSM) [32, 33], which incorporates nucleon pairing correlations according to the Bardeen-Cooper-Schrieffer theory [24], along with various microscopic models grounded in first principles and fundamental interactions. These microscopic descriptions of the NLD can capture intricate details of nuclear structure that are beyond the capabilities of analytical expressions. One microscopic approach is the shell model Monte-Carlo by Alhassid [34], as well as the approach based on mean-field theory by Demetriou and Goriely [35]. Additional examples of microscopic models that will be included in the analysis in the next chapters include the calculated NLD by Goriely from Hartree-Fock calculations [36], parity-dependent NLD based on the microscopic combinatorial model by Hilaire [37], as well as temperature-dependent Hartree-Fock-Bogoliubov calculations using the Gogny force [38].

2.4.2.4 Radiative Decay, Transmission Coefficients and γ Strength Function

Gamma rays emitted from an excited nucleus must follow *selection rules* to conserve the angular momentum and parity. They are classified with an *electric* (E) or *magnetic* (M) character, along with a *multipolarity*, based on the angular momentum L they carry, and the parity change $\Delta\pi$

between the initial i and final state f :

$$|I_i - I_f| \leq L \leq I_i + I_f \quad (L \neq 0)$$

$$\Delta\pi = \text{no} : \quad \text{even electric, odd magnetic} \quad (2.18)$$

$$\Delta\pi = \text{yes} : \quad \text{odd electric, even magnetic}$$

For instance, a transition from an initial state of $J_i^\pi = 2^+$ to a final state of $J_f^\pi = 0^+$ involves angular momentum $L = 2$ without a change of parity, making it an $E2$ transition. When many multipoles are possible, the lower multipoles are significantly more likely to occur. For example the transition from $J_i^\pi = 3/2^+$ to $J_f^\pi = 5/2^+$ permits $M1$, $E2$, $M3$ and $E4$ transitions. Among these, $M1$ transition is typically a thousand times more probable than $E2$, $E2$ a thousand times more likely than $M3$, and so forth [7].

However, even if a photon can be emitted according to the selection rules, its probability of escaping the volume of the nucleus is much smaller than the probability of being reflected back. This escape probability is described by the γ -ray transmission coefficient T_γ , a quantity that characterizes the average electromagnetic properties of excited states, and can be described through the γ -ray strength function $f(E_\gamma)$ (also called *photon strength function* or *radiative strength function*) as:

$$T_{XL}(E_\gamma) = 2\pi E_\gamma^{(2L+1)} f_{XL}(E_\gamma) \quad (2.19)$$

where X denotes the character (E or M), L the multipolarity, and E_γ the energy of the γ ray.

Photon strength functions are important for the description of all transitions involving γ rays, but their significance is even more apparent in (n, γ) and (γ, n) reactions, as neutrons are not affected by the Coulomb force of the nucleus, and photon strength functions directly govern the reaction cross section. They are distinguished by the *upward* γ -strength function $\overrightarrow{f_{XL}}$, associated with the average photo-absorption, and the *downward* strength function $\overleftarrow{f_{XL}}$, related to the γ decay. The treatment of photon strength functions involves two key assumptions. First, the strength function is assumed to be independent of J and π [39], an approximation valid when the initial and final state have high excitation energies, and therefore overlap with many states of the same energy and different $J\pi$ values. Second, the upward and downward strength functions are assumed to be equal,

implying that the photo-absorption cross section on an excited state will have the same shape as the photo-absorption on the ground state. This assumption is known as the *Brink hypothesis* [40].

In calculations of the γ -ray transmission coefficient for astrophysics, at least the most dominant $E1$ and $M1$ transitions have to be considered. Similar to the level density, there is a plethora of models, both analytical and microscopic, to describe the dipole ($E1$ and $M1$) strength functions. The $E1$ transitions are calculated on the basis of the Lorentzian representation of the giant dipole resonance (GDR), that has been observed throughout the periodic table to strongly influence the strength function. Macroscopically, this strong resonance is described as a vibration of the charged (proton) matter in the nucleus against the neutral matter (neutrons).

The magnetic dipole ($M1$) strength function is also commonly described by Lorentzian resonance-like structures that are much smaller in magnitude compared to the GDR. Depending how deformed the many-body system is, collective excitations can appear as enhancements in the $M1$ strength function, such as the scissors mode around 3 MeV, or the spin-flip strength around 5-9 MeV [41, 42].

Examples of phenomenological models to describe the photon strength function that are widely used in astrophysics are the Standard Lorentzian function by Brink [40] and Axel [43], and the Generalized Lorentzian model of Kopecky and Chrien [44] and Kopecky and Uhl [45]. Microscopic models to describe $E1$ and $M1$ radiation include, but are not limited to, large-scale calculations based on the quasi-particle random-phase approximation (QRPA) model combined with the Hartree–Fock–Bogoliubov (HFB) method [46, 47, 48, 49], and the relativistic mean-field approach (RMF) [50, 51, 52, 53].

Additionally to the Lorentzian resonance-like structures that comprise the form of the strength function, an enhancement at low transition energies and excitation energies in the statistical region has been experimentally observed [54, 55]. This feature is called the *low energy enhancement* or *upbend*, and even though it is not clear whether it correspond to the electric or magnetic radiation [56, 57], it is believed to be of dipole character [58]. The upbend is parameterized in the form of

an exponential tail as

$$f_{\text{upbend}}(E_\gamma) = C \exp(-\eta E_\gamma) \quad (2.20)$$

where C and η are adjustable parameters [55]. The existence of the upbend has shown to have significant impact on capture reaction cross sections [59, 60], and its intensity appears to be dependent on the nuclear structure [61].

2.4.2.5 Statistical Model Calculations with TALYS

A software package for simulations and predictions of nuclear reactions that will be extensively used in the analysis of the following chapters is TALYS [62]. A variety of nuclear reactions can be simulated using TALYS including direct reactions, compound nucleus model, pre-equilibrium reactions and fission. In the context of this thesis, TALYS will be used for calculating (p, γ) reaction cross sections based on the statistical model for compound nucleus reactions. As discussed in the previous sections, main ingredients of the HF formalism include the optical model potential (OMP), the nuclear level density (NLD) and γ -ray strength function (γ SF). In this paragraph the models used for the description of these quantities will be listed along with their respective references.

Regarding the proton-OMP, the default option used in TALYS is the phenomenological parameterisation of Koning and Delaroche [63]. In addition to the default p -OMP option, a so-called “jlm-type” potential (based on the work of Jeukenne, Lejeunne, and Mahaux [64, 65, 66, 67] with later modifications by Bauge *et al.* [68, 69]) is utilized.

The various models of the NLD and γ SF used in TALYS were discussed in Sec. 2.4.2.3 and 2.4.2.4 and are listed in Tables 2.1 and 2.2.

Finally, the width fluctuation correction (WFC) from Eq. 2.12 takes into account that there are correlations between the incident and outgoing wave functions. By default, TALYS applies a WFC using the formalism of Moldauer (so-called “widthmode 1”) [76, 77]. A much stronger WFC is obtained for the approach of Hofmann, Richert, Tepel, and Weidenmüller (HRTW approach, “widthmode 2”) [78, 79, 80], leading to significantly lower calculated (p, γ) cross sections, especially at low energies.

Table 2.1 The available models for the nuclear level density in TALYS [62].

TALYS Keyword	Model	Ref.
ldmodel 1	Constant Temperature & Fermi Gas Model	[31]
ldmodel 2	Back-shifted Fermi Gas Model	[25]
ldmodel 3	Generalized Superfluid Model	[32, 33]
ldmodel 4	Skyrme-Hartree-Fock-Bogolyubov level densities from numerical tables	[36]
ldmodel 5	Skyrme-Hartree-Fock-Bogolyubov combinatorial level densities from numerical tables	[37]
ldmodel 6	Temperature-dependent Gogny-Hartree-Fock-Bogolyubov combinatorial level densities from numerical tables	[38]

Table 2.2 The available models for the γ -ray strength function in TALYS [62].

TALYS Keyword	Transition	Model	Ref.
strength 1	$E1$	Kopecky-Uhl Generalized Lorentzian	[45]
strength 2	$E1$	Brink-Axel Standard Lorentzian	[70, 71]
strength 3	$E1$	Skyrme-Hartree-Fock BCS model with QRPA	[46]
strength 4	$E1$	Skyrme-Hartree-Fock-Bogoliubov model with QRPA	[48]
strength 5	$E1$	Hybrid model (Lorentzian model with energy and temperature dependent width)	[72]
strength 6	$E1$	Temperature-dependent Skyrme-Hartree-Fock-Bogoliubov model with QRPA	[48]
strength 7	$E1$	Temperature-dependent Relativistic Mean Field Model	[53]
strength 8	$E1$	Gogny-Hartree-Fock-Bogoliubov model with QRPA by based on the DIM version of the Gogny force	[49]
strength 9	$E1$	Simplified Modified Lorentzian Model	[73]
strengthM1 1	$M1$	Standard Lorentzian Model as parameterized in RIPL3 Library	[74]
strengthM1 2	$M1$	$M1$ normalized on $E1$ as $f_{E1}/(0.0588A^{0.878})$	
strengthM1 3	$M1$	Addition of spin-flip and scissors mode	[41, 75, 42]
upbend y/n	$M1$	Flag to include upbend or not	[55, 54, 59, 61]

2.5 Nuclear Reactions in Stars

In the previous sections, we introduced the concept of nuclei and nuclear reactions, describing the probabilities and mechanisms through which these reactions occur. As nuclear reactions can transform nuclei while releasing energy, they play a crucial role in understanding both the production of energy and the nucleosynthesis of elements in stars. While the various stellar environments and

astrophysical processes will be explored in detail in Ch. 3, it is helpful to introduce the key concepts needed to bridge the theory of nuclear physics discussed earlier with stellar nucleosynthesis.

The energy dependence of the cross section $\sigma(E)$, can be interpreted as velocity dependence $\sigma(v)$, where v represents the relative velocity between the projectile and target nucleus. Instead of projectile beam and stationary target we can consider nuclear species being part of a stellar gas, where the kinetic energy available for the reaction comes from thermal movement. The reactions initiated by such motion are called *thermonuclear reactions* [6].

In a stellar gas that consists of N_a nuclei per cubic centimeter of species a , and N_X nuclei per cubic centimeter of species X the *reaction rate* r between species a and X is given by:

$$r = N_X N_a v \sigma(v) \quad (2.21)$$

where r is in reactions per cubic centimeter per second. The velocities of gas particles vary over a wide range of values, described by a probability distribution $\phi(v)$ that is normalized to unity, $\int_0^\infty \phi(v)dv = 1$. Averaging the product $v\sigma(v)$ over this distribution gives the *reaction rate per particle pair*:

$$\langle \sigma v \rangle = \int_0^\infty \phi(v) v \sigma(v) dv \quad (2.22)$$

The total reaction rate r then becomes:

$$r = N_X N_a \langle \sigma v \rangle \quad (2.23)$$

Stellar matter is normally non-degenerate, and nuclei move non-relativistically. Therefore, in most cases, the velocities of nuclei can be described by the Maxwell-Boltzmann velocity distribution:

$$\phi(v) = 4\pi v^2 \left(\frac{m}{2\pi kT} \right)^{3/2} \exp\left(-\frac{mv^2}{2kT} \right) \quad (2.24)$$

or in terms of energy

$$\phi(E) \propto E \exp(-E/kT) \quad (2.25)$$

where T refers to the temperature of the gas, m the mass of the nucleus of interest, and k the Boltzmann constant. As shown in Fig. 2.5 at low energies the function increases almost linearly

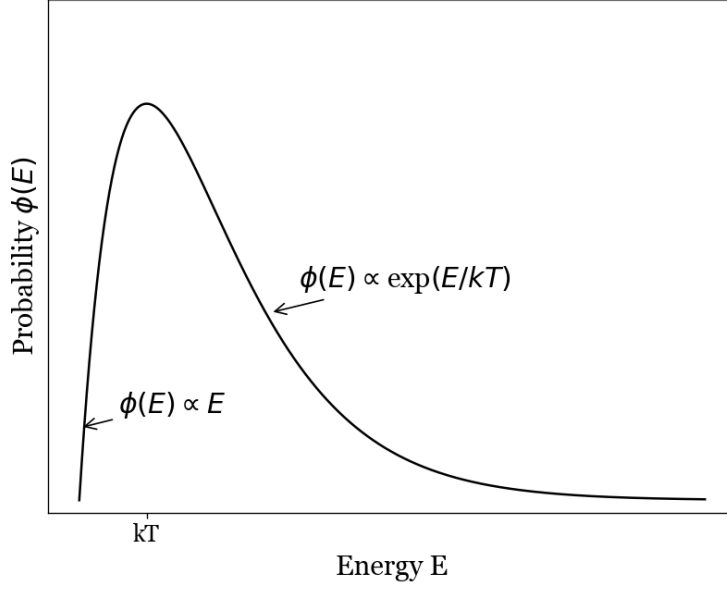


Figure 2.5 The Maxwell-Boltzmann energy distribution of a gas at temperature T .

with T until it reaches its maximum value at $E = kT$. At higher energies, the function decreases exponentially [15].

In a stellar gas, the velocities of both species a and X follow the Maxwell-Boltzmann distribution. By combining Eq. 2.22 and 2.24 we obtain:

$$\langle \sigma v \rangle = \left(\frac{8}{\pi \mu} \right)^{1/2} \frac{1}{(kT)^{3/2}} \int_0^{\infty} \sigma(E) E \exp\left(-\frac{E}{kT}\right) dE \quad (2.26)$$

where E is the center-of-mass energy and μ the reduced mass [15].

2.5.1 Reactions at elevated temperatures

In stellar plasma at elevated temperatures, nuclei are thermally excited, so a significant fraction of reacting nuclei will not be in their ground state. The fraction of nuclei in an excited state μ is given by the Boltzmann distribution:

$$\frac{N_{\mu}}{N} = \frac{(2J_{\mu} + 1)e^{-E_{\mu}/kT}}{\sum_{\mu} (2J_{\mu} + 1)e^{-E_{\mu}/kT}} = \frac{(2J_{\mu} + 1)e^{-E_{\mu}/kT}}{G} \quad (2.27)$$

where G is the *partition function* that reflects the Boltzmann factor, and J_{μ} and E_{μ} the spin and excitation energy of the μ state, respectively.

The ratio of the reaction rate involving thermally excited nuclei, $\langle \sigma v \rangle^*$, to the reaction rate

involving only the ground state $\langle\sigma\nu\rangle$, is known as the *stellar enhancement factor* (SEF):

$$\text{SEF} \equiv \frac{\langle\sigma\nu\rangle^*}{\langle\sigma\nu\rangle} = \frac{\sum_{\mu}(2J_{\mu}+1)e^{-E_{\mu}/kT}\sum_{\nu}\langle\sigma\nu\rangle^{\mu\rightarrow\nu}}{G\sum_{\nu}\langle\sigma\nu\rangle^{\text{g.s.}\rightarrow\nu}} \quad (2.28)$$

Here, the summations over μ and ν include all the possible excited states of the target nucleus and all available states of the final nucleus, respectively [15].

2.5.2 Inverse Reactions

At low stellar temperatures, a nuclear reaction requires a positive Q value to proceed. However, as the temperature increases, the number of particles with energy exceeding the Q value also increases, allowing the inverse process to become energetically possible. Thus, when calculating the total reaction rate r , contributions from both reactions $a + X \leftrightarrow b + Y$ should be considered:

$$r = r_{aX} - r_{bY} = \frac{N_X N_a}{1 + \delta_{aX}} \langle\sigma\nu\rangle_{aX} - \frac{N_Y N_b}{1 + \delta_{bY}} \langle\sigma\nu\rangle_{bY} \quad (2.29)$$

where δ_{ij} is the Kronecker delta, and the term $(1 + \delta_{ij})$ accounts for identical particles.

If the cross section $\langle\sigma\nu\rangle_{aX}$ is known, the cross section for the inverse reaction $\langle\sigma\nu\rangle_{bY}$ can be calculated using the *reciprocity theorem*, which relies on the invariance of the strong and electromagnetic interactions under time-reversal symmetry, meaning they are independent of the direction of time. As long as the cross sections depends on these two interactions, the ratio of the two cross sections can be written as:

$$\frac{\sigma_{aX}}{\sigma_{bY}} = \frac{m_b m_Y E_{bY} (2J_b + 1) (2J_Y + 1) (1 + \delta_{aX})}{m_a m_X E_{aX} (2J_a + 1) (2J_X + 1) (1 + \delta_{bY})} \quad (2.30)$$

Then, by using Eq. 2.26 and the relation $E_{bY} = E_{aX} + Q$ ($Q > 0$), we obtain:

$$\frac{\langle\sigma_{bY}\rangle}{\langle\sigma_{aX}\rangle} = \frac{(2J_a + 1)(2J_X + 1)(1 + \delta_{bY})}{(2J_b + 1)(2J_Y + 1)(1 + \delta_{aX})} \left(\frac{\mu_{aX}}{\mu_{bY}}\right)^{3/2} \exp\left(-\frac{Q}{kT}\right) \quad (2.31)$$

which, replacing back in Eq. 2.29 leads to:

$$r = \frac{\langle\sigma_{aX}\rangle}{1 + \delta_{aX}} \left[N_a N_X - N_b N_Y \frac{(2J_a + 1)(2J_X + 1)}{(2J_b + 1)(2J_Y + 1)} \left(\frac{\mu_{aX}}{\mu_{bY}}\right)^{3/2} \exp\left(-\frac{Q}{kT}\right) \right] \quad (2.32)$$

It is important to note that Eq. 2.32 refers to ground state contributions. For an accurate astrophysical calculation the stellar enhancement factor described in Sec. 2.5.1 needs to be accounted for [15].

2.5.3 Neutron-Induced Reactions

Neutrons play an important role in stellar nucleosynthesis, however due to their short lifetime of about 10 minutes, they only exist in stellar environments in which they can be produced. Some important neutron producing reactions in stars are the $^{13}\text{C}(\alpha,n)^{16}\text{O}$, $^{18}\text{O}(\alpha,n)^{21}\text{Ne}$, and $^{22}\text{Ne}(\alpha,n)^{25}\text{Mg}$. Neutrons produced in stars are very quickly thermalized due to elastic scattering, so their velocities are described by the Maxwell-Boltzmann distribution. Being electrically neutral, neutrons do not experience the Coulomb barrier of nuclei. Additionally, for angular momentum $l = 0$ (s-wave), they do not encounter a centrifugal barrier, meaning their penetrability depends solely on their velocity. As a result, neutron capture is mainly proceeding with s-wave neutrons,

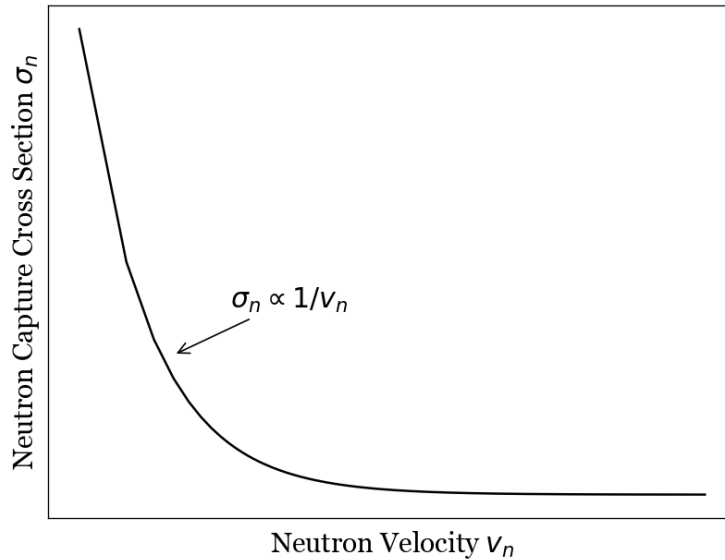


Figure 2.6 Cross section for thermal s-wave neutrons follows the $1/v$ law.

and the cross section is given by the $1/v$ law:

$$\sigma_n(E_n) \propto \frac{1}{v_n} \quad (2.33)$$

It follows that the reaction rate per particle pair $\langle\sigma v\rangle$ is approximately constant [15].

2.5.4 Charged-Particle-Induced Reactions

As will be discussed in more detail in Chapter 3, stars consist mainly of hydrogen and helium. Therefore proton and α (^4He) capture reactions are some of the most common and important

reactions that can happen in a star. Unlike the case of neutrons, charged particles need to overcome the repulsive Coulomb barrier of nuclei to be captured. The Coulomb barrier is of the form:

$$V_C = \frac{Z_1 Z_2 e^2}{r} \quad (2.34)$$

where Z_i the atomic number, e the electron charge and r the distance between nuclei. It is apparent that the closer to the nucleus, the larger the Coulomb barrier encountered. Combined with the attractive potential caused by the strong nuclear force leads to the effective potential shown in Fig. 2.7.

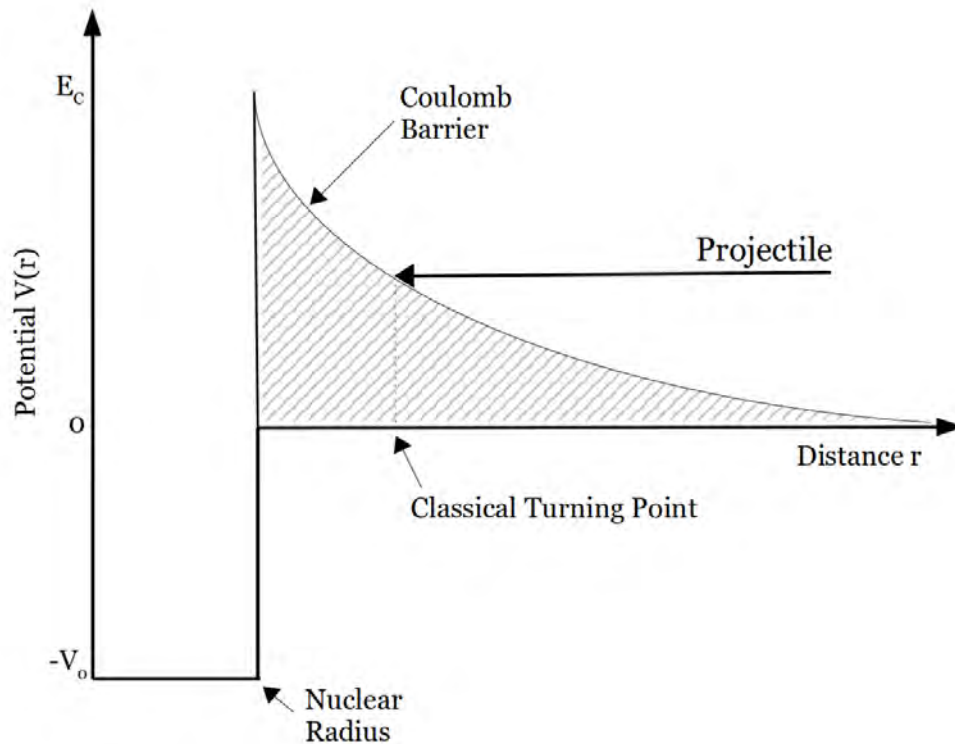


Figure 2.7 Schematic of the combined Coulomb and nuclear potential. The incident projectile needs to penetrate the Coulomb barrier to be captured in the nucleus. Classically, the nearest allowed distance it would reach is the turning point. Figure recreated based on [15].

Classically, a charged particle reaction can occur only when the projectile energy is sufficient to overcome the Coulomb barrier. However, as will be discussed in Ch. 3, the temperatures reached in stellar environments during the majority of a star's lifetime are not sufficient to thermally excite nuclei to such energies. Fortunately, quantum mechanics provides a solution: charged particles

can penetrate the Coulomb barrier through *quantum tunneling*, allowing stellar nucleosynthesis to begin at lower temperatures, an idea first proposed in 1929 [81].

The probability for tunneling through the Coulomb potential can be found by solving the Schrödinger equation as

$$P = e^{-2\pi\eta} \quad (2.35)$$

where $\eta = \frac{Z_1 Z_2 e^2}{\hbar v}$ is the *Sommerfeld* parameter. The exponent can be numerically calculated as $2\pi\eta = 31.29 Z_1 Z_2 \sqrt{\mu/E}$. The cross section, being proportional to $\exp(-2\pi\eta)$, decreases sharply below the Coulomb barrier. To make experiments feasible, cross section measurements are typically performed at higher energies and then extrapolated to the lower energies relevant to astrophysical temperatures. However, the rapid decline of the cross section below the Coulomb barrier significantly limits the accuracy of this extrapolation. To address this issue, it is more useful to express the cross section in terms of the *astrophysical S-factor*, $S(E)$, defined as:

$$\sigma(E) = \frac{1}{E} \exp(-2\pi\eta) S(E) \quad (2.36)$$

The S-factor has much smoother variations in the non-resonant region, and contains only the nuclear information, eliminating the rapidly decreasing energy-dependent factors.

Calculating the charged-particle reaction rate involves combining the probability of a particle being in a specific energy, meaning the Maxwell-Boltzmann rate from Eq. 2.26, with the probability of tunneling through the Coulomb barrier. These probabilities overlap within a narrow energy range, $E_0 \pm \Delta E_0/2$, where the S-factor, $S(E_0)$, can be considered approximately constant. Therefore, substituting Eq. 2.36 into Eq. 2.26 yields:

$$\langle \sigma v \rangle = \left(\frac{8}{\pi \mu} \right)^{1/2} \frac{1}{(kT)^{3/2}} S(E_0) \int_0^\infty \exp\left(-\frac{E}{kT} - \frac{b}{\sqrt{E}}\right) dE \quad (2.37)$$

where $b = (2\mu)^{1/2} \pi e^2 Z_1 Z_2 / \hbar = 0.989 Z_1 Z_2 \mu^{1/2} \text{ MeV}^{1/2}$. The quantity b^2 is called the *Gamow energy*. The peak shown in Fig. 2.8 is formed by the overlap of the two probability distributions at energy E_0 , and is called the *Gamow peak*. It represents the energy range in which the reaction can happen in a star [15]. The width of the Gamow peak can be approximated by

$$\Delta = \frac{4}{\sqrt{3}} \sqrt{E_0 kT} = 0.2368 \left(Z_0^2 Z_1^2 \mu T_9^5 \right)^{1/6} \quad (\text{MeV}) \quad (2.38)$$

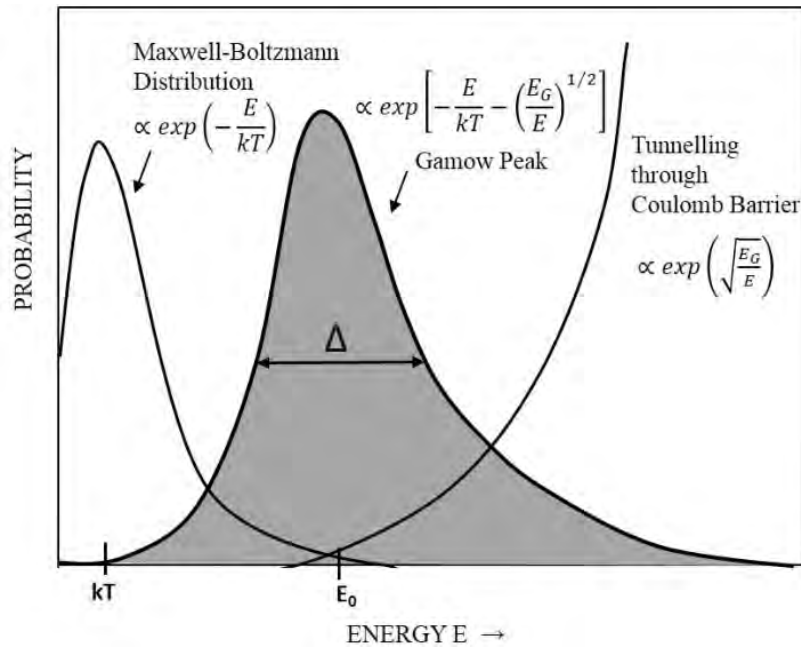


Figure 2.8 The convolution of the Maxwell-Boltzmann energy distribution and the quantum mechanical tunneling function through the Coulomb barrier produce the Gamow peak at energy $E_0 \pm \Delta E_0/2$. Figure from [82].

where μ is the reduced mass, Z_i the atomic number and T_9 the stellar temperature in GK [6].

It should be noted that the resonances introduced in Sec. 2.4.2.1 play a crucial role in charged-particle reactions within stellar environments. When a resonance lies within the Gamow peak, it can contribute significantly to the total reaction rate. As will be discussed in the next chapter, the existence of such narrow resonances within the Gamow window enables the nucleosynthesis of elements vital to life, such as carbon.

CHAPTER 3

ASTROPHYSICS

In the previous chapter, the fundamental concepts of nuclei, nuclear reactions, and the mechanisms by which these reactions occur in stellar environments were introduced. This chapter begins with a discussion of the observed element abundances, as any description of nucleosynthesis processes must ultimately account for these observations. The evolution of stars is then discussed to provide the context for the environments where nucleosynthesis takes place. The various nucleosynthesis processes are then presented, leading to the main topic of this thesis, the astrophysical γ process.

3.1 Abundances

Understanding the origin of the elements in the universe involves explaining and reproducing their abundances, meaning the relative amounts of nuclides. Astronomical observations provide spectra that identify elements found in the interstellar medium and on the surface of stars. Pre-solar grains that were ejected in stellar winds, can become embedded in meteorites in our solar system. Many of those grains are carbonaceous materials such as diamond, silicon carbide (SiC), and graphite, and can offer isotopic ratios of their original environment. By analyzing the patterns of the elemental abundances, nuclear astrophysics can infer the mechanisms responsible for producing each element.

Among the elemental abundances across all stars, the solar abundance pattern is the most extensively studied. The solar system formed from a uniform gaseous nebula that contained contributions from many generations of stars and explosive events. Today, 280 naturally occurring isotopes remain in 83 elements [14]. The solar system's elemental abundances are shown in Fig. 3.1 normalized to silicon atoms. The most abundant elements, hydrogen and helium, make up approximately 98% of the solar mass. About 1.5% of the mass is carbon and oxygen, while all other elements account for the remaining 0.5%. A significant drop is observed near the very weakly bound elements lithium, beryllium and boron ($A = 5 - 8$), known as the *mass gaps*, and a peak forms in the region around iron. As discussed in Sec 2.1, this corresponds to the most tightly

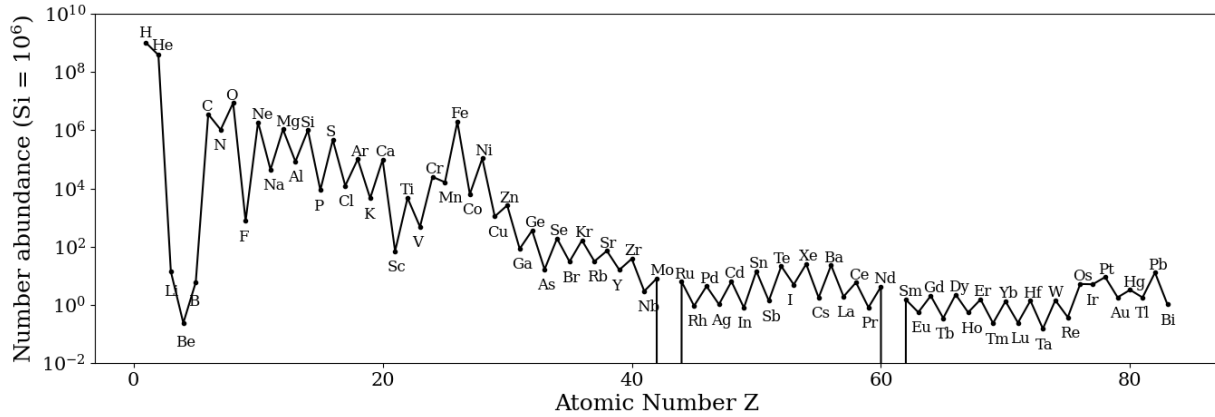


Figure 3.1 Solar system abundances based on data from Asplund [83]. The data is normalized to 10^6 Si atoms.

bound nuclides in the iron peak. The zig-zag structure reflects the differences in binding energies between nuclei with odd and even number of nucleons, due to pairing effects.

3.2 Stellar Evolution

The life of a star begins as a collapsing molecular cloud primarily composed of hydrogen (H) and helium (He). As the cloud contracts, its temperature rises due to an increase in gravitational potential energy. This rise in temperature causes the pressure at the cloud's center to increase, which counteracts further contraction. Smaller clouds may remain in this balanced state and never contract further, but larger ones continue collapsing until thermonuclear reactions ignite in the core, and hydrostatic equilibrium maintains stability.

The different *burning phases* will be discussed in Sec. 3.3, but they generally follow a pattern. A primary nuclear “fuel” undergoes fusion in the core, releasing energy that temporarily halts gravitational contraction. As the fuel depletes, the burning region shifts outward, and the star transitions from *core burning* to *shell burning*. With insufficient energy production in the core to counteract gravity, contraction resumes, increasing the temperature until the next fuel ignites. The cycle repeats as long as fusion is possible [14].

The lifetime of a star varies vastly, from several billion years for smaller stars to just a few million years or less for the most massive ones. Small stars with masses below $0.08 M_{\odot}$ (where $1 M_{\odot}$ is the mass of the Sun) cannot ignite hydrogen and remain as *brown dwarfs*, supported by

molecular gas pressure. Stars between $0.6\text{--}2.3 M_{\odot}$, like the Sun, spend billions of years burning hydrogen. Once the hydrogen in the core is depleted, these stars expand into *red giants*, burning hydrogen in a shell. Helium ignition leads to a *core He-flash* and He-shell burning during the *asymptotic giant branch* (AGB) phase. Unable to ignite carbon, they eventually shed their outer layers, leaving behind a *white dwarf*. Stars up to $8 M_{\odot}$ evolve further, igniting carbon in their C-O cores. These stars are very luminous and lose most of their mass during the AGB phase through stellar winds, ending their lives as white dwarfs. Such AGB stars, as will be discussed in the next section, are responsible for synthesizing almost half of the heavy elements [6, 14].

The evolution of stars with masses larger than $8 M_{\odot}$ is fundamentally different and much more spectacular than the previous cases. These massive stars have significantly shorter lifetimes, lasting only a few million years. However, within this relatively brief period, stars more massive than $12 M_{\odot}$ undergo all burning phases, successively fusing hydrogen, helium, carbon, neon, oxygen, and finally silicon. Each phase becomes progressively shorter, with silicon burning lasting only about a day. By the time silicon is exhausted in the core, the star has developed an “onion-like” structure, with layers of elements separated by thin nuclear burning shells, as illustrated in Fig. 3.2. Stars more massive than $25 M_{\odot}$, or those that rotate rapidly, lose a significant fraction of their mass through strong stellar winds and eruptions, resulting in the loss of most of their outer envelopes.

At this stage, the core primarily consists of iron-peak nuclei, which, as discussed in the previous chapter, have the highest binding energy and fusion is no longer energetically favorable. Without a nuclear source to counteract gravity, the core continues shrinking. Once the core’s mass exceeds the Chandrasekhar limit of $1.4 M_{\odot}$, it collapses [6, 14].

3.2.1 Supernovae

Supernovae are among the brightest, most complex and cataclysmic events in the universe. They are mainly classified based on the type of light emitted and their detailed mechanisms remain an active area of research.

The endpoint of the evolution of a red supergiant described above, is a *core-collapse supernova* (CCSN) known as *Type II* (SNII), and is characterized by strong presence of hydrogen in the

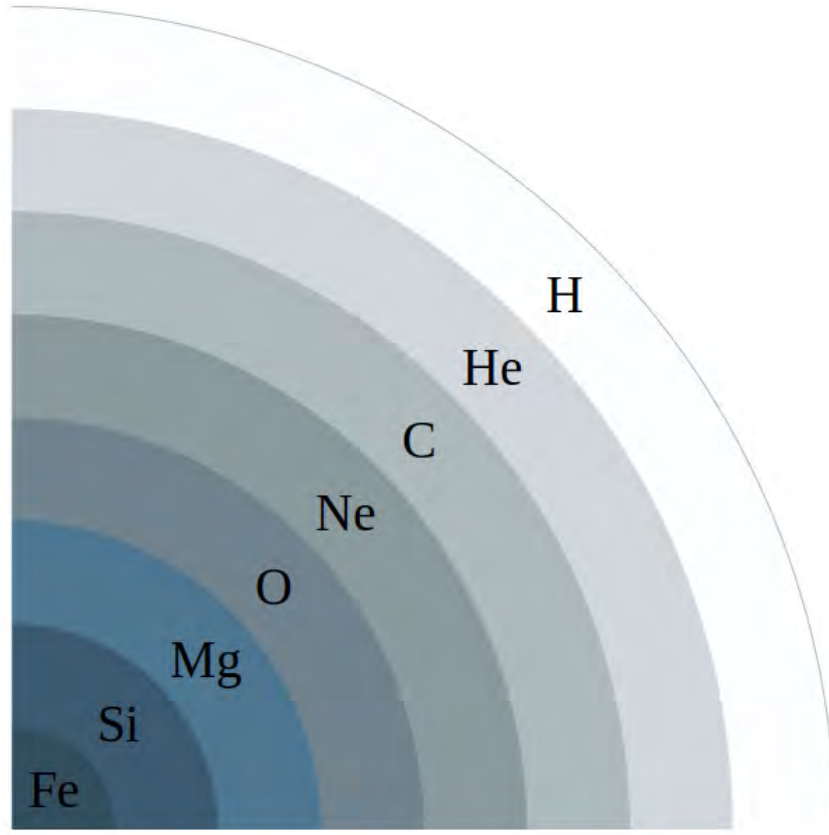


Figure 3.2 Schematic drawing of the onion shell structure of massive stars of $12 \lesssim M \lesssim 25M_{\odot}$ at the end of their evolution, with the dominant elements indicated. The outer envelopes of stars of $M > 25M_{\odot}$ are stripped before they explode as supernovae. Note that the figure is not to scale.

emitted light spectra (light curves). As the core reaches $T > 10^{10}$ K, photons break apart ^{56}Fe into α particles and neutrons, an endothermic reaction that accelerates the collapse. Within a fraction of a second, a core with size of several thousand kilometers collapses to tens of kilometers radius. Rising density enables electron capture, forming a degenerate neutron gas that can support very high pressure. If the collapsing core's mass is below $\sim 2 M_{\odot}$ (the Oppenheimer-Volkoff limit [84]), the pressure halts the collapse, forming a *neutron star*. If not, then it continues until a *black hole* forms [85].

During the collapse, several phenomena occur, leading to the ejection of the star's outer envelopes into the interstellar medium at extreme velocities. The infalling matter encounters the very compact proto-neutron star and experiences an intense shock, that pushes matter outwards as it bounces back. The outward moving shock wave compresses and heats the outer layers for short

periods of time, giving grounds for *explosive nucleosynthesis*. The temperature in the collapsing core is so high that photons can be captured by electrons, creating neutrinos. The neutrinos either escape or get trapped due to the high density and are captured by the infalling layers further increasing the temperature. The strong neutrino and antineutrino fluxes drive a continuous flow of protons and neutrons, known as *neutrino-driven wind*, that enables further nucleosynthesis to take place [6].

Another important category is *Type Ia* (SNIa), that has no hydrogen in the light spectra, but a lot of silicon. These are created in binary systems, where a white dwarf is accreting mass from a companion star. Once the white dwarf's mass approaches the Chandrasekhar limit, carbon ignites under degenerate conditions, increasing temperature while supporting very high pressure. Once the degeneracy is lifted, the energy generation rate is so large that an explosion occurs. In the *single-degenerate* (SD) *scenario* the companion star is a red giant, supplying hydrogen and helium-rich material onto the primary star, and after the explosion a remnant of the secondary star remains. In the *double-degenerate* (DD) *scenario*, both stars are white dwarfs that eventually merge, and the collapse leaves no remnant behind [6, 85].

Other types include SN Ib and Ic, that are most likely caused by supermassive stars that have lost almost all their envelope, called Wolf-Rayet stars, and are characterized by absence of hydrogen and silicon in their light spectra [85].

3.3 Stellar Nucleosynthesis

The previous section described the evolution of stars starting from clouds of dust. In the early stages of the universe, these molecular clouds consisted of light elements formed during the Big Bang. A few seconds after the Big Bang, the universe had cooled down sufficiently for free protons and neutrons to form. About 20 minutes later, primordial nucleosynthesis established the abundances of light elements, consisting of 75% ^1H , 25% ^4He , and traces of the stable deuterium (^2H), ^3He , and ^7Li , as well as unstable tritium (^3H) and ^7Be that decayed shortly after [86].

Any elements heavier than $A=7$ were not formed until hundreds of millions of years later, when the first nuclear reactions started taking place in stellar cores. As it was pointed out in the previous

section, nuclear reactions allow the star to maintain hydrostatic equilibrium, preventing it from gravitational collapse. Initially, the fuel consists of nuclei with the smallest nuclear charges, as their low Coulomb barrier allows fusion to occur at lower temperatures. Once this fuel is consumed, the core contracts, increasing the temperature and enabling fusion of nuclei with progressively higher Coulomb barriers.

3.3.1 Hydrostatic Burning

The first nuclear fuel is the lightest and most abundant hydrogen. H-burning occurs through the *net* reaction:



with a Q -value of 26.731 MeV. The two positrons are immediately annihilated with free electrons in the stellar plasma. However, the probability of four protons interacting simultaneously is too small for this reaction to occur directly. Instead, the net reaction is achieved with sequences of two-particle interactions. There are two main mechanisms for H-burning, the *proton-proton* (or *pp*) *chains* and the *CNO-cycles*. Which mechanism dominates depends on the core temperature and the availability of CNO-cycle nuclei, which act as catalysts, converting ${}^1\text{H}$ into ${}^4\text{He}$. The *pp* chains are dominant in first-generation stars, which formed from primordial material, or in less massive stars with lower central core temperatures. In contrast, the CNO cycle becomes significant in more massive, and later-generation stars enriched with heavier elements synthesized in massive first-generation stars that have already exploded [6, 14, 15].

After the hydrogen fuel has been consumed, the stellar core consists mainly of ${}^4\text{He}$, as the creation of heavier elements is blocked by instabilities at the mass gaps $A = 5$ and 8. However, ${}^{12}\text{C}$, the third most abundant element in the universe, is not a product of primordial nucleosynthesis and must therefore be synthesized in stars. This problem was solved by Öpik and Salpeter [87, 88, 89] who proposed that ${}^{12}\text{C}$ is produced through a two-step process known as the *triple-alpha process*. In this process, two alpha particles fuse to form an unstable ${}^8\text{Be}$ nucleus, which can occasionally capture another alpha particle before decaying, resulting in ${}^{12}\text{C}$. As the non-resonant tunneling probability for this reaction is too low to explain the observed abundance of ${}^{12}\text{C}$ in the universe,

Fred Hoyle [90] proposed that the reaction proceeds via a resonance in ^{12}C just above the $^8\text{Be}+\alpha$ threshold, at $E_X \simeq 7.68$ MeV. This resonance, now known as the *Hoyle state*, has been subject of extensive research since its discovery and continues to be studied today [91, 92, 93, 94, 95, 96].

After the formation of ^{12}C , further reactions like $^{12}\text{C}(\alpha, \gamma)^{16}\text{O}$ occur, but the subsequent $^{16}\text{O}(\alpha, \gamma)^{20}\text{Ne}$ proceeds at an extremely low rate, blocking significant nucleosynthesis via He-burning beyond ^{16}O . As carbon-based life forms that depend on the existence of oxygen in the atmosphere, we should appreciate that it is only through some fortunate nuclear properties of carbon and oxygen that they are produced so plentifully and survive the red giant phase of stars.

With the exhaustion of helium in the core, the star transitions to helium-shell burning. As the density increases, thermal pulses, known as *helium-shell flashes*, can occur. Similar to the He-core flash, these thermal pulses cause mixing of the material between the He-burning and H-burning shells. These thermal pulses combined with a complicated convective mixing process in the inter-shell regions combines the p-rich material of the H-burning shell with ^{12}C from the He-burning shell, forming ^{13}C through the $^{12}\text{C}(p, \gamma)^{13}\text{N}(\beta^-)^{13}\text{C}$ reaction sequence [97]. The reaction $^{13}\text{C}(\alpha, n)^{16}\text{O}$ is an important neutron source for heavy element nucleosynthesis, as will be discussed in Sec. 3.3.3. Another significant source of neutrons for heavy element nucleosynthesis is the $^{22}\text{Ne}(\alpha, n)^{25}\text{Mg}$ reaction, making the availability of ^{22}Ne very important during He-burning.

The exhaustion of He in the center of the star, leaves a core rich in C and O contracting under gravity. As discussed in Sec. 3.2, stars with mass above $8 M_\odot$ will proceed to more advanced burning stages, while only stars above $12 M_\odot$ undergo all burning stages. Carbon burning ignites first in the CO-rich core, followed by neon burning and then oxygen burning. While carbon and oxygen burning proceed mostly through fusion, Ne-burning mostly proceeds through photodisintegration reactions on ^{20}Ne , making this phase particularly brief due to its lower energy output. Similarly, the final burning phase, Si-burning, is based on photodisintegrations of silicon isotopes rather than fusion, leading to a complex network of reactions. In this network, many forward and reverse reaction rates become comparable to the burning timescales, leading to the formation of certain “clusters” in the nuclear chart where particle captures and photodisintegrations are in equilibrium,

a state known as a quasi-statistical nuclear equilibrium (QSE). The nuclear flow is therefore largely confined within these clusters. The final abundances produced during Si-burning depend on where those clusters form, which depends on the available neutrons in the system (also known as *neutron excess* η , *neutron to proton ratio*, or *electron fraction* Y_e). This dependency on Y_e determines the composition of the core and sets the stage for the subsequent core-collapse [6, 14, 15].

3.3.2 Nucleosynthesis During Core-Collapse SN

The collapse of a stellar core discussed in Sec. 3.2, enables two main mechanisms for nucleosynthesis. The first is driven by the outward-moving shock wave during the explosion, and the second by the large amount of energy released from the core in the form of neutrinos.

As the shock wave moves outward, it heats and compresses the star's layers almost instantaneously. First, it passes through the silicon-burning shell, followed by the oxygen-rich layer, and finally the region primarily composed of neon, carbon, and oxygen. Each layer undergoes a specific explosive burning process at varying peak temperatures, producing a range of nuclei. The resulting abundances depend strongly on the expansion timescale during cooling and the availability of free particles (α, p, n) [6].

The launch of the shock generates a strong flux of electron neutrinos and antineutrinos, which drive protons and neutrons from the region near the proto-neutron star in what is known as the *neutrino-driven wind* [98]. Neutrinos interact with nuclei from infalling layers, populating excited nuclear levels that decay via particle emission (p, n, α). This neutrino-driven nucleosynthesis, known as the ν process, depends on the wind's properties, such as electron fraction Y_e and entropy (or photon-to-baryon ratio), determining whether the wind is proton-rich or neutron-rich. Final abundances also depend on the expansion and cooling timescales, as in hotter environments the wind will consist mainly of neutrons and protons, but in cooler environments protons and neutrons will combine to α particles.

3.3.3 Nucleosynthesis Beyond Iron

As discussed in previous sections, hydrostatic burning stages synthesize elements through fusion up to the iron region. At very high temperatures, where charged-particle capture reactions

are enabled, nucleosynthesis occurs in clusters where nuclear statistical equilibrium is established, favoring either iron peak nuclei or lighter elements. However, during hydrostatic burning, neutrons are produced through the $^{13}\text{C}(\alpha, n)^{16}\text{O}$ and $^{22}\text{Ne}(\alpha, n)^{25}\text{Mg}$ reactions. As neutrons are not affected by the increasingly large Coulomb barrier of heavy nuclei, neutron capture reactions are able to synthesize elements heavier than iron.

In their pioneering work in 1957, Burbidge, Burbidge, Fowler, and Hoyle (henceforth B²FH) described two main neutron-capture processes for heavy-element nucleosynthesis [3]. The distinction between the two lies on the vastly different timescales on which they operate. These processes are known as the *slow* and *rapid neutron-capture process*, or *s-* and *r-process* for short. These two processes are responsible for synthesizing the majority of heavy elements. However, it is now known that additional neutron-capture processes such as the *intermediate (i-)* [99, 100] and *n-process* [101], are also required to accurately reproduce the observed abundances of stars. Additional processes are also required for the production of the proton-rich elements, and those will be discussed in Sec. 3.4.

One of the most compelling pieces of evidence for the two neutron-capture mechanisms is their ability to naturally explain the existence of peaks in the solar system abundance pattern of heavy elements. As shown in Fig. 3.3, double peaks appear in the regions of $A \simeq 84, 138$ and 208 . These patterns arise from the neutron magic numbers $N = 50, 82$ and 126 . The sharp peaks correspond to abundances formed by the *s-process*, whereas the broader peaks about 10 mass units below reflect *r-process* enhanced abundances. The *s-* and *r-processes* are discussed in more detail in the following sections, along with the *i-* and *n-process*.

3.3.3.1 The *s* Process

First evidence of the slow neutron-capture process (*s-process*) nucleosynthesis was found in spectra of AGB stars, where radioactive Tc was observed [102]. The *s-process* involves a series of neutron-capture reactions followed by β^- decays and is responsible for the production of almost half of the isotopes of heavy elements. The name “slow” reflects the time intervals between successive captures that are inversely proportional to the neutron capture reaction rates and the

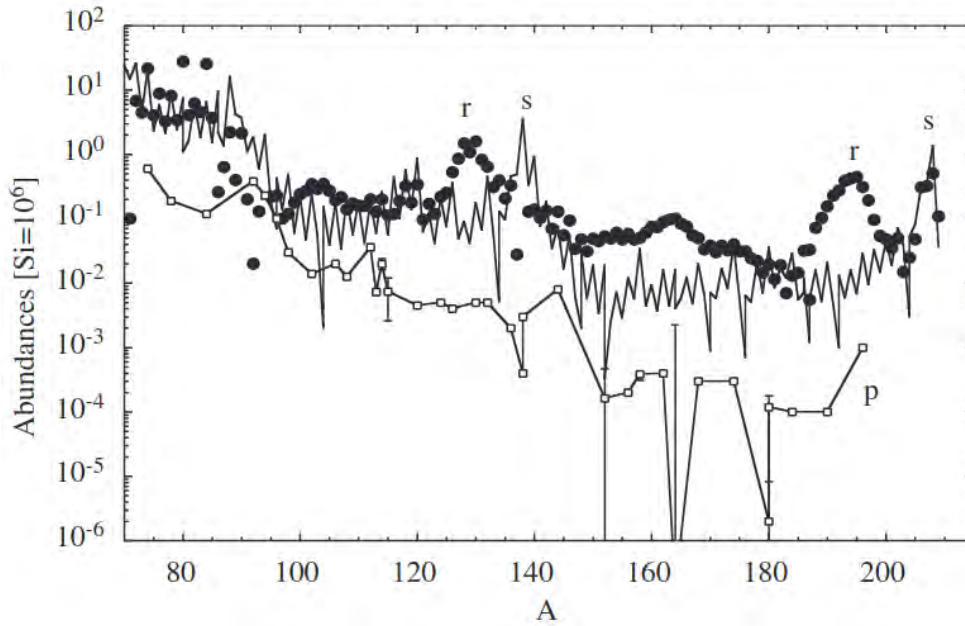


Figure 3.3 Decomposition of solar s– (solid line), r– (black circles) and p–abundances (white squares) relative to silicon. Figure from M. Arnould *et al.*, Physics Reports 450 (2007), with permission from Elsevier.

neutron flux. In environments of typical neutron density $\approx 10^{7-11}$ neutrons/cm³, the rate for n-captures is comparable to that of the β^- decay, and therefore the synthesis path follows closely the valley of stability in the nuclear chart. The process terminates in Bi, as any heavier elements are unstable and decay by α emission back to stability.

An example of the *s*-process path is shown in Fig. 3.4, starting from ⁷⁷Se. The path can be calculated by comparing the decay rate $\lambda = \ln 2/t_{1/2}$, with the neutron-capture reaction rate. If the two are comparable, such as in ⁸⁵Kr, a *branching point* occurs, where the path can follow both directions, leading to different abundance patterns. There are about 15-20 significant branching points along the *s*-process path. Branching points can provide information on the detailed conditions of the stellar environment, such as neutron density and temperature. However, achieving this requires accurate knowledge of neutron-capture reaction cross sections, decay half-lives and any temperature dependence of the rates [6, 14].

The example path of Fig. 3.4 passes through the neutron magic number $N = 50$. This configuration is energetically more favorable than $N = 51$, and therefore the neutron-capture cross section

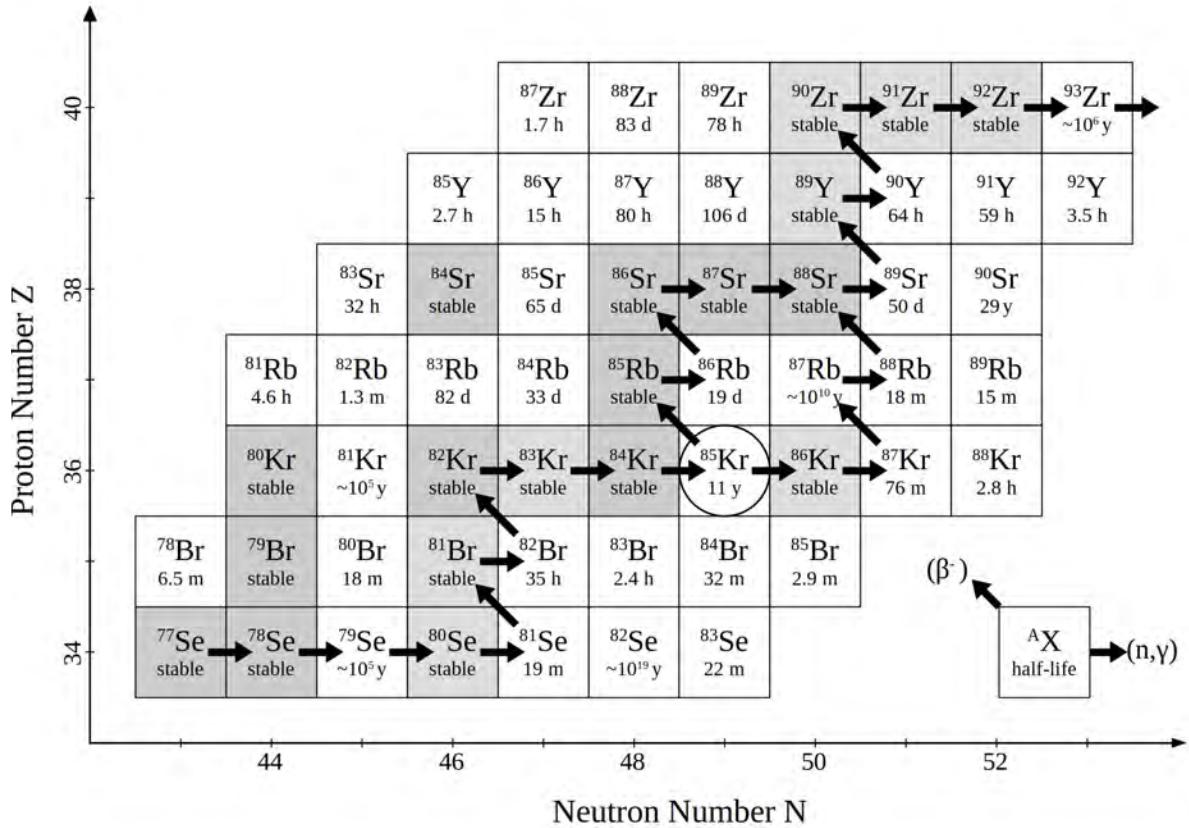


Figure 3.4 An example of the s -process path in the region around $A = 85$. The half-lives are obtained from [4]. The gray and white squares correspond to stable and radioactive isotopes, respectively, and the circle indicates a branching point.

on nuclei with $N = 50$ will drop significantly, blocking the s -process path from more n -rich nuclei, and pushing the reaction flow to higher elemental chains. This results in the first peak in the solar abundance pattern from Fig. 3.3.

The s process is a *secondary* process, as it requires the existence of iron-peak nuclei to act as *seeds*, unlike the hydrostatic burning phases that are *primary* processes, and do not depend on preexisting nuclei. As a secondary process, the produced abundances can vary significantly based on the stellar conditions. As discussed in Sec. 3.3.1, during He-burning in AGB stars, neutrons are produced by the reactions $^{13}\text{C}(\alpha, n)^{16}\text{O}$ and $^{22}\text{Ne}(\alpha, n)^{25}\text{Mg}$. A significant amount of ^{13}C can be produced in thermally pulsing, low mass ($1.5\text{-}3 M_{\odot}$) AGB stars. A complex mixing of the intershell, which is the region between the He- and H-burning shells, mixes protons with material rich in ^{12}C

and ${}^4\text{He}$. This enables the sequence ${}^{12}\text{C}(p, \gamma){}^{13}\text{N}(\beta^+ \nu){}^{13}\text{C}$, forming a region known as the ${}^{13}\text{C}$ *pocket* [97]. At temperatures near $T \approx 0.09$ GK, a neutron density in the order of $\approx 10^7$ n/cm³ produced by the ${}^{13}\text{C}(\alpha, n){}^{16}\text{O}$ reaction, provides fuel for *s*-process nucleosynthesis for a period of $\approx 20\,000$ years. This is known as the *main s-process component* and provides about 95% of the total neutron exposure, synthesizing elements up to Pb. The remaining neutron exposure is achieved with the ${}^{22}\text{Ne}(\alpha, n){}^{25}\text{Mg}$ source. This so-called *weak s-process component*, is achieved during the recursive He-shell flashes at much higher neutron densities of up to $\approx 10^{11}$ n/cm³. Even though this components accounts for only the lighter *s*-process nuclei near the Kr–Rb–Sr abundance peak ($N = 50$), the higher temperatures significantly influence the *s*-process branchings points [103].

3.3.3.2 The *r* Process

The presence of abundance peaks that can't be explained by the *s* process, along with the existence of long-lived isotopes heavier than Bi, such as ${}^{232}\text{Th}$ and ${}^{238}\text{U}$, highlights the need for an additional neutron-capture process beyond the *s* process. The environment for such a process can be found in extreme stellar environments, where neutron fluxes are so high ($\approx 10^{20-22}$ n/cm³) that the β -decay rate of unstable nuclei is small compared the rate of neutron capture. In this case, the nucleosynthesis path may move close to the neutron dripline. Only when the neutron flux terminates, the neutron-rich nuclei decay back to stability through β^- decays. This nucleosynthesis mechanism is named the *rapid (r) neutron-capture process* and is responsible for the synthesis of approximately the other half of the isotopes of heavy elements [3].

Similarly to the *s* process, the magic neutron numbers impact the reaction flow, leading to the creation of two peaks at mass numbers $A = 130$ and 195 , which are about 10 mass units below the *s*-process peaks near $A = 138$ and 208 , as shown in Fig. 3.3. At neutron densities in the order of 10^{20-22} n/cm³ neutron captures can drive the *r*-process flux close to magic neutron numbers. However, the neutron separation energy S_n decreases for more neutron-rich nuclei. Therefore in each isotopic chain (n, γ) and (γ, n) reactions may eventually reach a quasi-statistical equilibrium (QSE), similar to the clusters formed during Si-burning. The flow toward higher elemental chains depends on the β -decay rates of the nuclei in QSE. As these rates are slow compared to the rates in

equilibrium, *waiting points* may be established, usually one or two per chain in QSE. These waiting points can determine the timescale of the reaction network and influence the final abundance, as β^- decays will follow the isobaric chain ($A = \text{const}$). As a consequence the r -process peaks are located in mass regions below the corresponding s -process peaks.

The r -process network can extend to the neutron dripline, where most nuclear properties remain experimentally unknown, especially for nuclei far from stability. Extensive efforts are underway to both theoretically and experimentally determine key nuclear properties such as masses, level schemes, half-lives, β -decay rates, fission rates, and neutron-capture cross sections [21, 104, 105, 106, 107]. Improving our understanding of these quantities is essential for enhancing the predictive power of r -process models, which are critical for explaining observed abundances in the Sun and other stars.

The site of the r process has been one of the most significant open questions in the field for decades, further complicated by the lack of nuclear data for exotic isotopes. Over the years, numerous potential sites have been proposed, including neutrino-driven core collapse supernovae [108, 109], electron-capture supernovae [110], magneto-rotational supernovae leading to magnetars (i.e. neutron stars with very high magnetic fields) [111, 112, 113], collapsars (massive stars that collapse into a black hole) that produce powerful relativistic jets [114, 115], as well as black hole - neutron star mergers [116]. Compact binary mergers (NS-NS mergers) have been suggested as r -process sites since the 1970s [116] with first nucleosynthesis predictions in 1999 [117]. In August 2017 LIGO and Virgo detected gravitational waves from the NS-NS merger GW170817 [118], providing the first direct evidence of an r -process event. Since then, research on r -process nucleosynthesis in NS-NS mergers has been exponentially growing [119, 120, 121].

3.3.3.3 Other Neutron-Capture Processes

The solar abundances shown in Fig. 3.3 can be sufficiently explained by a combination of the s and r processes, but this is not the case for many other stars. The abundance patterns of a group of very old, carbon-enriched stars known as *carbon-enhanced metal poor* (CEMP) stars can instead be explained by an alternative neutron-capture mechanism, operating at intermediate neutron

densities between those of the *s* and *r* process. This *intermediate (i-) neutron capture process* was first proposed by Cowan in 1977 [99], and was found to match the observed abundances of CEMP stars in 2016 [100]. Since then, many studies have been dedicated to the *i* process and its potential sites, with candidates including rapidly rotating white dwarfs accreting material from a companion red giant [122], and thermal-pulsing AGB stars [123]. The mechanism is similar to that of the *s* and *r* process, but intermediate neutron fluxes of $\approx 10^{12-15}$ n/cm³ drive neutron-capture reactions a few steps away from stability before β decays return the nuclear flow to stable species. This proximity to stability makes the *i* process particularly promising for experimental studies, as many of the relevant neutron-capture reactions are accessible with current facilities [124, 125].

Another neutron-capture process, the *n process*, has been proposed to occur in the He shell after its composition is modified by the SN shock passage. A neutron flux of $\approx 10^{18}$ n/cm³ or higher can then be produced by the $^{22}\text{Ne}(\alpha, n)^{25}\text{Mg}$ reaction. The *n* process is able to reproduce anomalous Mo isotopic abundances measured in SiC meteorites, motivating further study of this mechanism [101].

3.4 Production of the *p* Nuclei

As discussed in the previous section, neutron-capture processes dominate heavy element nucleosynthesis. However, these processes cannot produce all isotopes of heavy elements. In their pioneering work, B²FH identified 35 proton-rich nuclides that are shielded by the valley of stability and cannot receive contributions from the *s* or *r* process. These isotopes were named *p nuclei*, and the mechanism responsible for their synthesis, the *p process*.

The 35 classical *p* nuclei as identified by B²FH are listed in Table. 3.1, along with their isotopic fractions within their respective elements and their solar abundances [126]. Subsequent research has shown that many of these *p* isotopes also receive contributions from neutron-capture [127, 129] or neutrino-driven processes [128, 130], meaning they cannot be strictly classified as *p*-only isotopes. Additionally, certain unstable nuclides, such as ^{92}Nb , $^{97,98}\text{Tc}$ and ^{146}Sm , though not part of the original list of classical *p* nuclei, play a significant role in studies of the *p* process. These isotopes, with half-lives comparable to astronomical timescales, are believed to form in the same events as

Table 3.1 The classical p nuclei, their fraction (in %) of the isotopic composition of the elements and solar abundances (relative to Si= 10^6). Data from Lodders [126].

Isotope	Element (%)	Solar Abundance	Comment
^{74}Se	0.889	$5.80 \cdot 10^{-1}$	
^{78}Kr	0.362	$2.00 \cdot 10^{-1}$	
^{84}Sr	0.555	$1.31 \cdot 10^{-1}$	
^{92}Mo	14.8	$3.86 \cdot 10^{-1}$	
^{94}Mo	9.25	$2.41 \cdot 10^{-1}$	
^{96}Ru	5.54	$1.05 \cdot 10^{-1}$	
^{98}Ru	1.87	$3.55 \cdot 10^{-2}$	
^{102}Pd	1.02	$1.46 \cdot 10^{-2}$	
^{106}Cd	1.25	$1.98 \cdot 10^{-2}$	
^{108}Cd	0.89	$1.41 \cdot 10^{-2}$	
^{113}In	4.29	$7.80 \cdot 10^{-3}$	r -process contribution [127]
^{112}Sn	0.971	$3.62 \cdot 10^{-2}$	
^{114}Sn	0.659	$2.46 \cdot 10^{-2}$	
^{115}Sn	0.339	$1.26 \cdot 10^{-2}$	r -process contribution [127]
^{120}Te	0.096	$4.60 \cdot 10^{-3}$	
^{124}Xe	0.129	$6.94 \cdot 10^{-3}$	
^{126}Xe	0.112	$6.02 \cdot 10^{-3}$	
^{130}Ba	0.106	$4.60 \cdot 10^{-3}$	
^{132}Ba	0.101	$4.40 \cdot 10^{-3}$	
^{136}Ce	0.186	$2.17 \cdot 10^{-3}$	
^{138}Ce	0.251	$2.93 \cdot 10^{-3}$	
^{138}La	0.0902	$3.97 \cdot 10^{-4}$	ν -process contribution [128]
^{144}Sm	3.07	$7.81 \cdot 10^{-3}$	
^{152}Gd	0.203	$6.70 \cdot 10^{-4}$	s -process contribution [129]
^{156}Dy	0.056	$2.16 \cdot 10^{-4}$	
^{158}Dy	0.096	$3.71 \cdot 10^{-4}$	
^{162}Er	0.137	$3.50 \cdot 10^{-4}$	
^{164}Er	1.61	$4.11 \cdot 10^{-3}$	s -process contribution [129]
^{168}Yb	0.13	$3.23 \cdot 10^{-4}$	
^{174}Hf	0.162	$2.75 \cdot 10^{-4}$	
^{180}Ta	0.0123	$2.58 \cdot 10^{-6}$	s -process [129] and ν -process contributions [130]
^{180}W	0.12	$1.53 \cdot 10^{-4}$	
^{184}Os	0.0198	$1.33 \cdot 10^{-4}$	
^{190}Pt	0.0136	$1.85 \cdot 10^{-4}$	
^{196}Hg	0.153	$6.30 \cdot 10^{-4}$	

stable p nuclei and can be used as *cosmochronometers*, providing important information on the composition of the early Solar system [131, 132].

The p process was initially described in B²FH as occurring in the hydrogen-rich layers of core

collapse supernovae, through a series of (p, γ) and (γ, n) reactions on existing s - and r -process seeds during the passage of the shock wave [3]. In 1978, Woosley and Howard [133] suggested that the required conditions for the process, including high densities, elevated temperatures, and extended time scales, are unlikely to exist in the hydrogen-rich regions of most stars. Alternatively, they proposed an explosive nucleosynthesis mechanism based on a series of photodisintegration reactions on s - or r -process seed nuclei, which was named the γ process.

The production of p nuclei remains an active area of research. Various mechanisms have been proposed in different astrophysical environments, involving both explosive and neutrino-driven nucleosynthesis. The term p process has been retained within the astrophysics community for historical reasons and now serves as an “umbrella” term that includes these diverse processes. The following provides an overview of the primary scenarios currently under investigation.

3.4.1 The γ Process

The γ process is widely regarded as the main mechanism for the synthesis of the p nuclei. It occurs in stellar environments of sufficiently high plasma temperatures through particle emission from thermally excited nuclei. Rather than the hydrogen-rich layer proposed by B²FH, it is thought to occur in a zone where hydrogen is exhausted and heavy elements are subjected to a “hot photon bath” [133]. Under these conditions, the most likely reactions are *photodisintegrations*, meaning (γ, n) , (γ, p) and (γ, α) , as shown schematically in Fig. 3.5.

The first reactions to take place are (γ, n) , as these dominate the photodisintegration processes for most stable nuclei [134]. As the nuclear flow progresses to more neutron-deficient nuclei, the (γ, n) reaction rate decreases. At the same time, the proton-richer the isotope, the less energy is needed to remove a proton or an α particle. Consequently, (γ, p) and (γ, α) reactions take over, moving the nuclear flow to lower elemental chains and eventually the p nucleus of interest.

The process is highly sensitive to temperature, as higher temperatures or prolonged exposure would completely photodissociate the seeds into iron peak nuclei. On the other hand, cooler environments would not allow thermally excited nuclei to decay by particle emission. The temperature range for γ -process nucleosynthesis to occur is between 1.8 and 3.2 GK. As these photodisintegra-

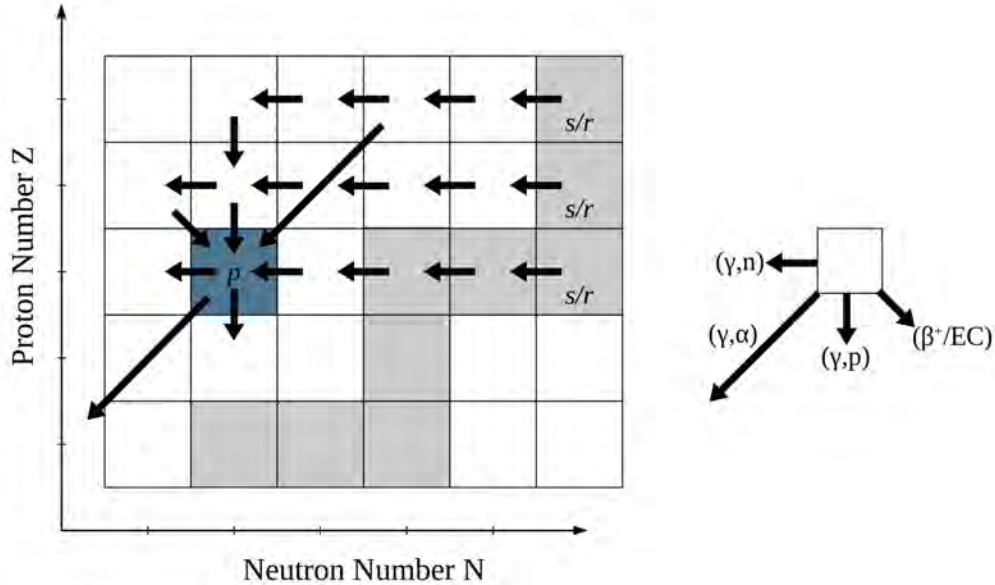


Figure 3.5 An schematic illustration of the γ -process path. The gray and white squares correspond to stable and radioactive isotopes, respectively, and the blue square indicates the produced p nucleus.

tion reactions are strongly influenced by the particle separation energies of the seed nuclei, lighter p nuclei require higher plasma temperatures ($T \approx 3\text{--}3.2$ GK) because their seeds, being closer to the iron peak, are more tightly bound. The heavier p nuclei are synthesized in lower temperatures ($T \approx 1.8\text{--}2$ GK) as their seeds are less bound.

Any site capable of sustaining γ -process nucleosynthesis must maintain these temperatures for a short period of time, while providing an adequate supply of seed nuclei. The most viable candidates are stellar explosions that involve a rapid expansion and subsequent cooling of the material. As a result, the γ -process nucleosynthesis is highly sensitive to factors such as the temperature and density profile, expansion timescales, the initial abundances of seed nuclei, and the hydrodynamic properties of the explosion. The two main explosive environments where the γ process is thought to occur are the oxygen and neon enriched layers of a core-collapse supernovae (O/Ne SNII) [133, 135, 136], and thermonuclear Type Ia supernovae [137, 138, 139].

The mechanism of SNII, as discussed in Sec. 3.2, involves the propagation of an outward moving shock wave. There are two main components of the SNII that contribute to the γ process: the explosive component during shock wave propagation [133, 135, 136, 140], and the pre-explosive component [141, 136, 142, 143]. During the explosion, the shock encounters the O/Ne burning

shell, which has been enriched in s -process material. The inner layers reach higher temperatures, enabling the synthesis of the lightest p nuclei, while the heavier ones are formed in the cooler outer layers [135, 136, 134].

In the final stages of stellar evolution, just before the explosion, C-rich material may be ingested in the convective O-burning shell, forming a merged convective zone. This zone, known as the *C-O shell merger* [136, 142], provides a sustainable environment for synthesizing p nuclei heavier than Pd [143]. The produced material is mixed throughout the extended C-O shell and as it is not fully reprocessed by the shock wave, it maintains its pre-supernova abundances in the ejecta.

It is important to note that the γ -process abundances depend strongly on the s -process seed distributions. Early studies assumed solar s -process distributions [133, 136], however more recent studies have shown that these seeds may be enhanced. This can occur either through the presence of additional ^{13}C from the convective C core, which leads to enhanced s -process seed distributions [144], or through stellar rotation, which enhances the weak s -process abundances driven by the $^{22}\text{Ne}(\alpha, n)^{25}\text{Mg}$ neutron source [145].

The other main environment for γ -process nucleosynthesis is thermonuclear Type Ia supernovae, which was briefly discussed in Sec. 3.2. In the single-degenerate (SD) scenario, a CO white dwarf (WD) accretes material from a main-sequence or red giant companion. The WD explodes once its growing mass approaches the Chandrasekhar limit. During the explosion, a broad range of peak temperatures are reached across different mass coordinates of the WD, including temperatures sufficient to sustain γ -process nucleosynthesis in the outer layers [138]. However, it is again essential to determine the available seed distributions in the exploding WD. These seeds can be provided by the s process during the AGB or TP-AGB phase [138], by the n process from recurring H-shell flashes [146], or by the i process from recurring He-shell flashes in the WD [147]. Although there have been efforts to explore the γ process in a sub-Chandrasekhar helium detonation model, there were significant uncertainties in the seed distributions, and sufficient p -nuclei abundances could only be achieved with highly enhanced seed abundances [148]. Additionally, ongoing research is exploring the potential role of the double-degenerate scenario in Type Ia SNe.

The γ process is the most established scenario for the production of the p nuclei, as it has so far been the most successful at reproducing the majority of the observed solar abundances within a factor of three. However, several discrepancies arise, especially in the region near $A = 95$, as the $^{92,94}\text{Mo}$ and $^{96,98}\text{Ru}$ are systematically underproduced by one order of magnitude compared to other γ -process nuclei [131, 134, 149]. An example overproduction factor divided by the average overproduction factor of all 35 p nuclei is shown in Fig. 3.6 by Roberti *et al.* [143], using a $20 M_{\odot}$ SNII model by Ritter *et al.* [142].

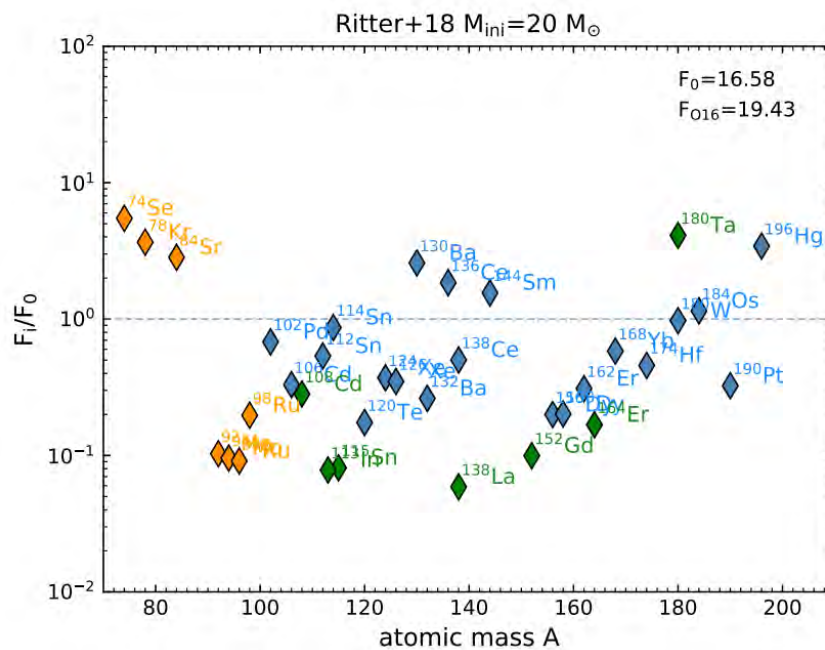


Figure 3.6 p -nuclide overproduction factors divided by their average, from a $20 M_{\odot}$ SNII model by Ritter *et al.* [142]. The different color symbols represent nuclei explicitly produced by the γ process (blue), and nuclei that may have an additional explosive contribution (orange) or an s , r process, or neutrino-capture contribution. (Figure from Roberti *et al.* *Astronomy & Astrophysics* 677, A22 (2023), under CC BY 4.0 (<https://creativecommons.org/licenses/by/4.0>))

3.4.2 Other Scenarios for the p Process

Such discrepancies in the produced p -nuclei abundances lead to investigate possible contributions from multiple processes other than the γ process. Alternative scenarios include the rp , νp , and νr processes, which will be briefly discussed here.

An alternative mechanism for the production of the p nuclei was proposed to take place on the

surface of a neutron star that accretes H- and He-rich material from a companion star. This accretion leads to a large gravitational energy release called an *X-ray burst*. Within this environment, some of the lighter p nuclides can be synthesized through the *rp-process* (short for *rapid proton capture process*) [150]. The *rp-process* path proceeds through a series of proton captures on CNO nuclei toward progressively heavier nuclei, until the proton dripline is approached and β^+ decay takes place. While this process can produce the lightest p nuclei, it remains uncertain whether the synthesized material can escape the strong gravitational pull of the neutron star [151]. Recent studies suggest that if the neutron star is accreting in binary common envelopes, where the expanding star envelops its companion, then the material produced by the *rp-process* may escape the strong gravitational field and be ejected into the interstellar medium [152].

An additional mechanism involves the neutrino-driven winds produced in CCSN. For values of the electron fraction $Y_e > 0.5$, a *proton-rich* neutrino-driven wind can be obtained, and the so-called *νp process* can occur [153, 154]. The proton-rich environment is constantly supplied by a small number of free neutrons created by antineutrino captures on free protons. The resulting nucleosynthesis flow near the heavy elements is similar to the *r-process*, as it is characterized by rapid proton captures in a (p, γ) - (γ, p) equilibrium, with (n, p) reactions connecting the isotonic ($N = \text{const}$) chains. This process has been shown to produce the lightest p nuclei [155], however such calculations depend on large uncertainties in neutrino interaction cross sections, the average energies associated with different neutrino flavors, the overall neutrino luminosity, and the specific details of the stellar evolution and explosion models used in the simulations.

A recent research worth highlighting proposed a new nucleosynthesis mechanism that could contribute to p -nuclei production, called the *νr process* [156]. This process is suggested to take place on neutron-rich ejecta, where *r* process occurs. In this scenario, *r*-process seeds experience strong neutrino irradiation, and thus the (n, γ) (γ, n) equilibrium is broken by the neutrino interactions instead of β decays. This pushes the nuclear flow toward and beyond the valley of stability, producing p nuclei. This process is highly dependent on uncertainties on neutrino interactions, and the specific astrophysical conditions required for such strong neutrino fluxes are still uncertain.

3.5 Nuclear Networks and Uncertainties

As discussed in the previous sections, stellar nucleosynthesis involves various complex processes that occur simultaneously in a stellar environment. Simulating these processes requires stellar evolution codes that integrate nuclear physics with the physical mechanisms governing stars, such as gas properties, hydrodynamics for hydrostatic equilibrium, and energy transport via radiation or convection. An example of such a code is Modules for Experiments in Stellar Astrophysics (MESA) [157], a 1D stellar evolution code that employs modern numerical and software techniques to solve stellar structure and composition equations while incorporating nuclear physics.

However, simulating an entire star is computationally intensive, particularly for environments such as the p or r process, which involve hundreds of thousands of reactions across thousands of isotopes. To simplify the problem and reduce computational costs, one approach is *post-processing*. Post-processing nuclear network calculations requires a prior stellar evolution simulation, such as one produced by MESA, using a reduced network of isotopes and reactions. These networks are limited to reactions critical for energy generation and those that significantly alter the star's composition. For example, simulating hydrostatic hydrogen burning only necessitates reactions from the pp-chains and CNO cycles (see Sec. 3.3.1), as these are key to energy production. Reactions on other light nuclei, while important for accurately reproducing final abundances, can be omitted during the evolution phase without affecting the star's structure, density, or temperature.

Once the stellar evolution simulation is complete, the temperature and density profiles as functions of time (trajectories) are extracted. Post-processing then uses these trajectories along with the initial abundances of all isotopes and nuclear physics inputs, such as masses, half-lives, and reaction rates to calculate nucleosynthesis. At this stage, the problem is reduced to solving a system of ordinary differential equations that describe the production and destruction of each nuclear species. This decoupling of nucleosynthesis calculations from stellar structure and evolution allows the inclusion of extensive networks of isotopes and reactions without making the computation prohibitively expensive.

An example of such a post-processing framework is provided by the nucleosynthesis grid (Nu-

Grid) collaboration to perform both single-zone (PPN) and multizone parallel (MPPNP) simulations for given thermodynamic conditions [158, 159]. The difference between a single-zone and a multi-zone model lies in the mass coordinates that the model can simulate. A single-zone model would follow the evolution of a single mass coordinate of the star for one trajectory, while a multi-zone model can follow multiple zones with different initial abundances and trajectories.

In such complex calculations, uncertainties in input quantities naturally have a significant impact on the calculated abundances. For the γ -process network, in addition to the astrophysical uncertainties described in Sec. 3.4.1 regarding the astrophysical site and the distribution of seed nuclei, numerous nuclear uncertainties affect the network calculations, as there are nearly 20 000 nuclear reactions on almost 2000 nuclei that must be considered [131]. As the nuclides involved in the γ process are predominantly stable or moderately unstable proton-rich nuclei, their masses and corresponding reaction Q -values are generally well-known. Similarly, half-lives are in principle known, aside from the dependence of electron captures and β^+ -decay rates on ionization and thermal excitation in the stellar plasma that require theoretical corrections [134].

The main uncertainty on the nuclear physics lies in the photodisintegration reaction rates, which must be determined with high accuracy for many possible reactions. As experimental data are scarce, uncertainties in the predicted reaction rates increase substantially for nuclei farther from stability [160]. Given that the γ -process network involves thousands of possible reactions, it is crucial to focus on those with the most significant impact to address the problem effectively. To this end, several sensitivity studies have been conducted over the years [160, 161, 162] to identify reactions whose uncertainties notably influence the production of specific p nuclei, helping in the planning of nuclear physics experiments.

During the recent decades, significant experimental efforts have been made to measure cross sections relevant to the γ process on stable nuclei [163, 164, 165, 166, 167, 168, 169, 170, 171, 172]. However, only one experiment involving a radioactive beam has been conducted to date [173]. For the thousands of reactions yet to be measured experimentally, reaction rates rely primarily on Hauser-Feshbach (HF) theoretical calculations. The HF model calculations most commonly

adapted for γ -process networks are obtained from the NON-SMOKER code [174].

As discussed in Sec. 2.4.2.2, HF cross-section calculations depend on the nuclear optical model potential (OMP), nuclear level density (NLD), and γ -ray strength functions (γ SF). For heavier p nuclei, where lower temperatures are required and the relevant energies lie near the lower end of the Gamow window, uncertainties in the OMP dominate. In contrast, for lighter p nuclei, which require higher temperatures and relevant energies correspond to the higher end of the Gamow window, uncertainties in the NLD and γ SF have a greater impact on the calculated reaction rates.

Developing experimental techniques to directly measure γ -process reactions involving unstable isotopes is therefore critically important. This thesis focuses on the application of such an experimental technique, to study the destruction of the lightest p nucleus, ^{74}Se .

3.6 The Lightest p Nucleus, ^{74}Se

^{74}Se is the lightest of the p nuclei, as its production is shielded from the s -process path and r -process decay chains as shown in Fig. 3.7. In sensitivity studies of the γ process during SNII scenario the $^{74}\text{Se}(\gamma, p)^{73}\text{As}$ reaction has been identified as key reaction rate to impact the final abundances of ^{74}Se [160, 161]. While stellar models for SNII [136, 176, 142, 177] show some variation, ^{74}Se is often found to be overproduced compared to solar abundances, as shown in Fig. 3.6. The possible production and destruction mechanisms of ^{74}Se in a SNII, shown in Fig. 3.8, have been a topic of experimental studies for many decades. Of those reactions the $^{74}\text{Se}(p, \gamma)^{75}\text{Br}$ [178, 179, 180, 181], $^{70}\text{Ge}(\alpha, \gamma)^{74}\text{Se}$ [182], and $^{74}\text{Se}(n, \gamma)^{75}\text{Se}$ [183] have been measured directly, and the $^{75}\text{Se}(\gamma, n)^{74}\text{Se}$ can be inferred from the latter through the reciprocity theorem (see Sec. 2.5.2). The only reaction channels that immediately affect the final ^{74}Se abundance, for which no experimental data exist are the $^{74}\text{Se}(\gamma, p)^{73}\text{As}$ and the $^{74}\text{Se}(\gamma, n)^{73}\text{Se}$. This work focuses on the measurement of the inverse $^{73}\text{As}(p, \gamma)^{74}\text{Se}$ reaction, that can be used to calculate the ground-state contribution of the $^{74}\text{Se}(\gamma, p)^{73}\text{As}$ reaction through the reciprocity theorem.

In simulations of SNII [142], the maximum production of ^{74}Se is found in layers with peak temperature $T \approx 3$ GK. For such temperature, the Gamow window for the $^{73}\text{As}(p, \gamma)^{74}\text{Se}$ reaction is located at center-mass-energy ranging from 1.7 to 3.6 MeV. The predicted cross section of the

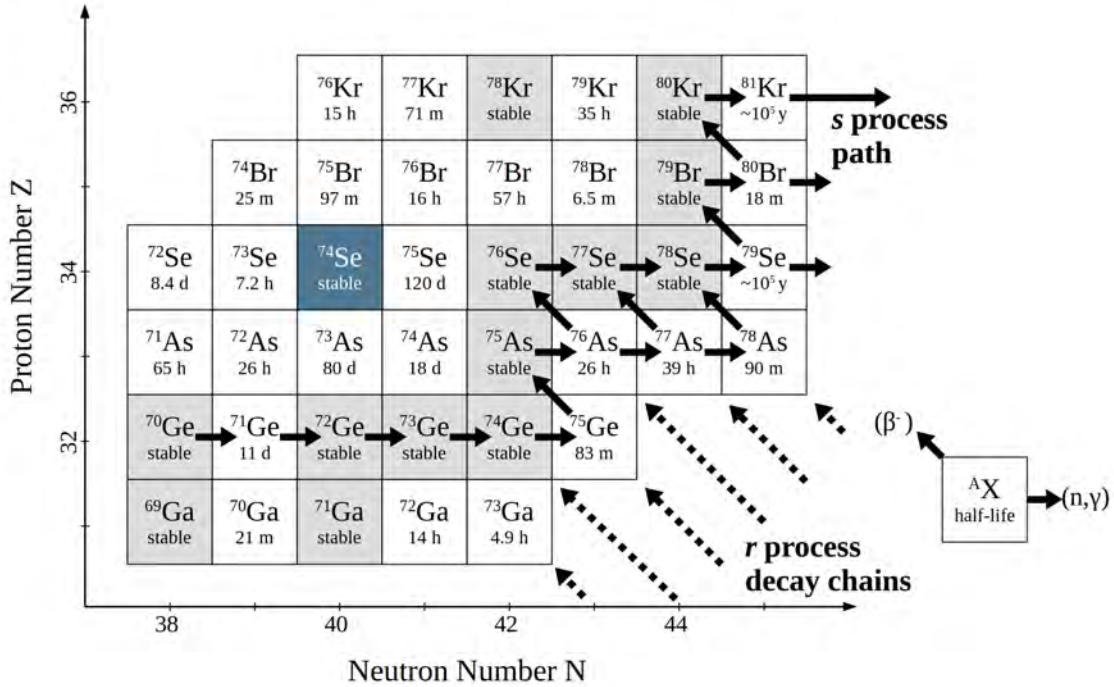


Figure 3.7 The lightest p nucleus, ^{74}Se , is shielded by the valley of stability from the s -process path and the r -process decay chain. The gray and white squares correspond to stable and radioactive isotopes, respectively, and the blue square indicates the ^{74}Se nucleus of interest. The half-lives are obtained from [4].

$^{73}\text{As}(p, \gamma)^{74}\text{Se}$ reaction in this energy range is shown in Fig. 3.9. The solid black line corresponds to standard statistical model calculations using the NON-SMOKER code [174], and the blue band is calculated through TALYS [62], using the various possible models for the OMP, NLD, and γSF discussed in Sec. 2.4.2.5. It can be seen that the statistical properties of the ^{74}Se nucleus result in a cross section uncertainty of a factor of 6 at center-mass-energy near 3 MeV. This thesis aims to investigate whether this uncertainty in the reaction rate is responsible for the overproduction of ^{74}Se in SNII models and whether an experimental measurement can help resolve this discrepancy. Regarding the SNIa scenario, while sensitivity studies suggest that nuclear uncertainties in ^{74}Se reactions do not significantly affect ^{74}Se production [162], this work aims to provide a quantitative assessment of their potential role.

The following chapter discusses the experimental setup for the measurement of the $^{73}\text{As}(p, \gamma)^{74}\text{Se}$ cross section using a radioactive ^{73}As beam. Chapter 5 presents the analysis from the proof-of-principle stable beam experiment on the $^{82}\text{Kr}(p, \gamma)^{83}\text{Rb}$ reaction, the measured $^{73}\text{As}(p, \gamma)^{74}\text{Se}$

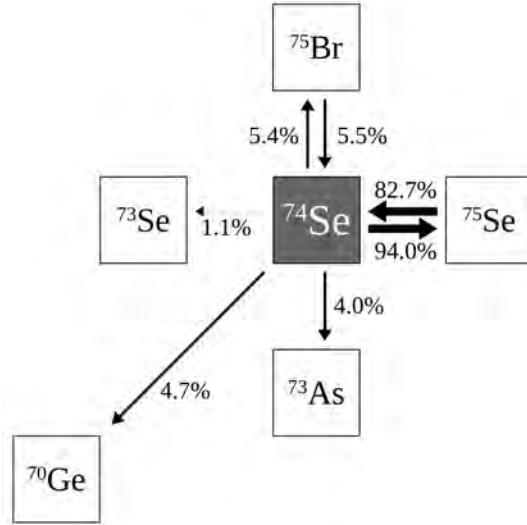


Figure 3.8 The γ -process fluxes producing and destroying ^{74}Se during a SNII. The sum of all production and destruction fluxes is normalized 100%. Fluxes smaller than 1% are not shown. Fluxes obtained from [175], using trajectories from [160].

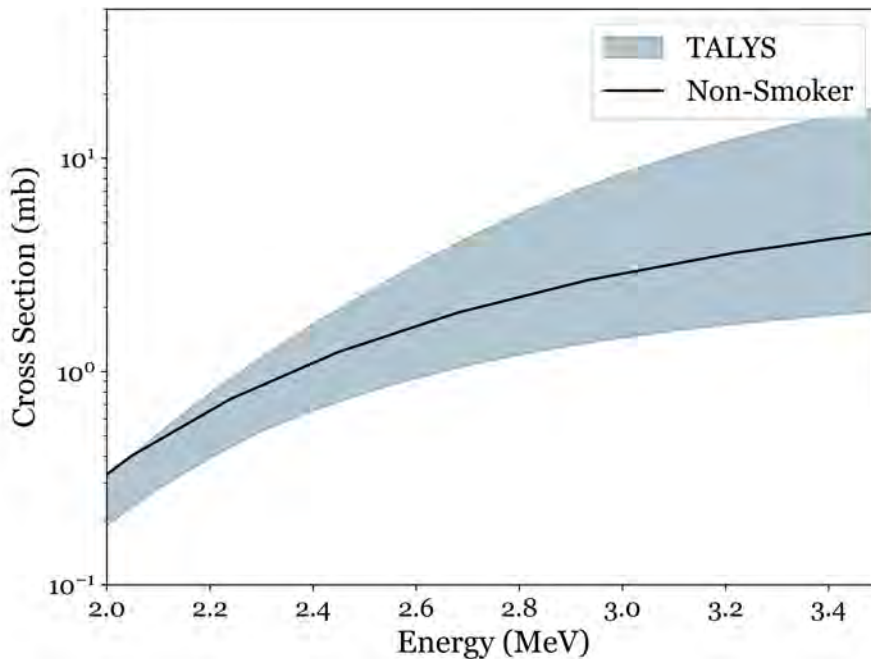


Figure 3.9 The cross section of the $^{73}\text{As}(p, \gamma)^{74}\text{Se}$ reaction using standard statistical model calculations from the NON-SMOKER code [174] (black line) and TALYS [62] (blue band). The TALYS calculations include all possible NLD and γ SF options listed in Tables 2.1 and 2.2, as well as the default and JLM OMP discussed in Sec. 2.4.2.5. The energy range covers the Gamow window for the γ process at $T = 3$ GK.

reaction, as well as the development of an analysis method to constrain the NLD and γ SF used in the statistical model calculations. Chapter 6 presents the results of the two cross section mea-

surements, and in chapter 7 the impact of the measured $^{73}\text{As}(p, \gamma)^{74}\text{Se}$ reaction cross section is investigated in a SNII and SNIa scenario.

CHAPTER 4

EXPERIMENTAL SETUP & TECHNIQUES

This work regards to two experiments in inverse kinematics using the same experimental setup. The first experiment, conducted in 2017, served as the proof-of-principle stable beam experiment for the measurement of the $^{82}\text{Kr}(p, \gamma)^{83}\text{Rb}$ and $^{84}\text{Kr}(p, \gamma)^{85}\text{Rb}$ reaction cross sections. The $^{84}\text{Kr}(p, \gamma)^{85}\text{Rb}$ reaction has been analyzed and published by a former student of the group [184], therefore this work focuses only on the $^{82}\text{Kr}(p, \gamma)^{83}\text{Rb}$ measurement [185]. The second experiment is the radioactive beam experiment for the measurement $^{73}\text{As}(p, \gamma)^{74}\text{Se}$ reaction cross section that took place in 2023. The experiments took place in the ReA post-accelerator of the Facility for Rare Isotope Beams (FRIB) (formerly known as National Superconducting Cyclotron Laboratory) at Michigan State University. More details on the facility and the delivered beams are discussed in Sec. 4.1.

An illustration of the experimental setup is shown in Fig. 4.1. The ^{82}Kr and ^{73}As beams

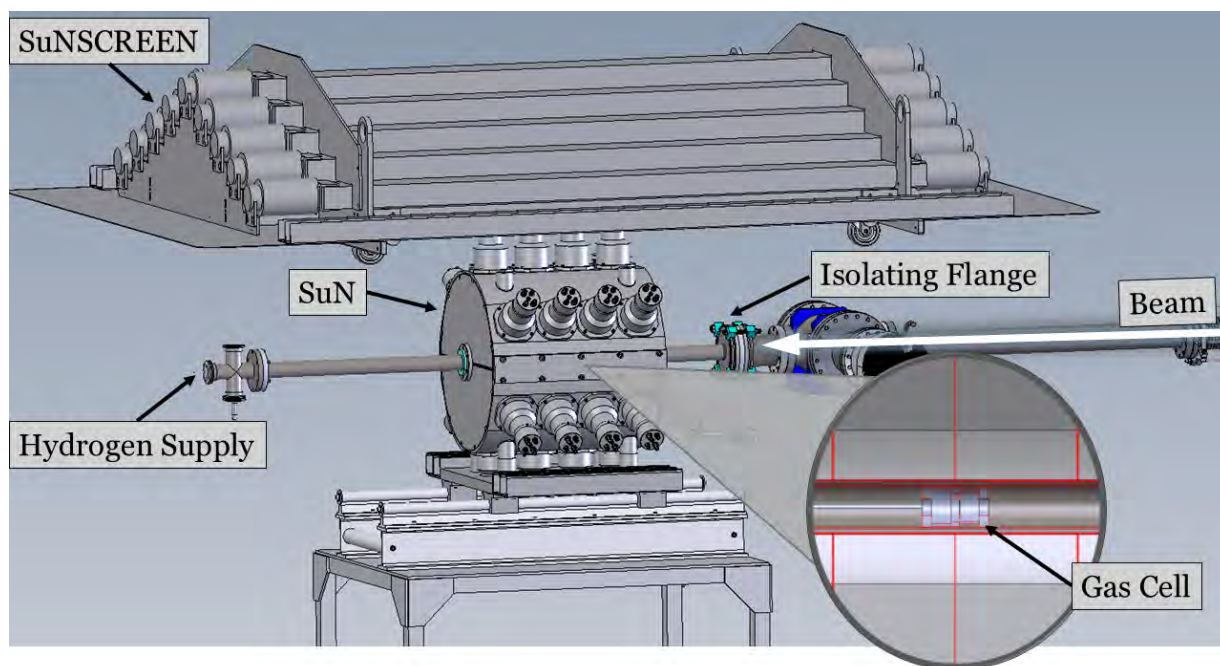


Figure 4.1 The experimental setup with the SuN and SuNSCREEN detectors in ReA3. The beam enters from the right, as shown by the white arrow. The inset shows a side-section view of the SuN detector, indicating the location of the hydrogen gas cell.

impinged onto a hydrogen gas-cell target described in Sec. 4.2. The γ rays produced by the

(p, γ) reaction were detected using the Summing NaI (SuN) detector and analyzed using the γ -summing technique, as discussed in Sec. 4.3. To minimize cosmic-ray background contributions, the Scintillating Cosmic Ray Eliminating ENsemble (SuNSCREEN) was used, as explained in Sec. 4.4.

4.1 Beam Delivery in ReA

The Facility for Rare Isotope Beams (FRIB) is a national scientific user facility that can provide access to thousands of nuclei far from stability [186]. It succeeded the Coupled Cyclotron Facility at the National Superconducting Cyclotron Laboratory (NSCL) that pursued a very successful science program with rare isotopes produced by projectile fragmentation until early 2021 [187]. Along with fast and stopped beams, the facility can provide reaccelerated beams in energies ranging from 300 keV/nucleon to 6 MeV/nucleon, providing unique opportunities for nuclear astrophysics experiments. Ion beams can alternatively be generated in the so-called “offline mode”, using radioactive or stable source samples [188]. Such was the case for the stable ^{82}Kr , and the radioactive ^{73}As beam.

Firstly the source samples were evaporated in an ion source and directed toward the ReAccelerator charge breeder. For the ^{73}As source, the Batch-Mode Ion Source (BMIS) was used (Fig. 4.2), which is an oven ion source combination commissioned in 2021 [188]. The ^{73}As sample was inserted inside a cylindrical tantalum oven, and heated up to about 1000 $^{\circ}\text{C}$. With the oven-ion source biased to a few tens of kV, the evaporated material exited through a transfer tube and was directed to the ReAccelerator charge breeder. Details on the preparation of the radioactive ^{73}As source sample can be found in Ref. [189].

The ReA charge breeder is the Electron Beam Ion Trap (EBIT) [190]. EBIT is a superconducting magnet in which the evaporated ions were injected and charge bred to high charge states ($^{73}\text{As}^{+23}$ and $^{82}\text{Kr}^{27+}$). After the EBIT, the beam was mass selected in a charge-over-mass (Q/A) separator and accelerated through the Radio Frequency Quadrupole (RFQ) [191] and superconducting LINAC (short for linear accelerator) [192]. The ReA LINAC has three accelerating cryomodules that include superconducting quarter wave resonators (QWR) and superconducting solenoids (SS) that



Figure 4.2 The batch mode ion source: (left) internal components of the oven-ion source and (right) the fully assembled front end.

accelerated the ^{82}Kr and ^{73}As beams.

The beams were delivered to the experimental end station in the ReA3 area, shown in Fig. 4.1, with energies 3.1, 3.4 and 3.7 MeV/nucleon for the ^{82}Kr beam, and 3.1 and 3.7 MeV/nucleon for the ^{73}As beam. The measurement of the beam current for the ^{82}Kr experiment was achieved by electrically isolating the beam pipe with an isolating flange upstream of SuN and using the entire beamline as a Faraday cup. This way, any electrons produced by ionization in the cell or beam pipe were still recorded and the total current did not get affected. Due to issues with grounding the beamline was not properly isolated during the ^{73}As experiment and the beam current was measured in regular intervals through a Faraday cup upstream.

More details on the current measurements are provided in Sec. 5.2. However, it is worth noting that while the proof-of-principle experiment was performed with a stable ^{82}Kr beam of intensity on the order of 10^7 particles/sec, the radioactive ^{73}As beam was around 10^5 particles/sec, almost two orders of magnitude lower. This highlights the inherent challenges of working with radioactive beams, particularly with a highly toxic element like arsenic. Nevertheless, as will be shown in the following chapters, the measurement was successfully achieved.

4.2 Hydrogen Gas Target

The beam impinged on a hydrogen gas target positioned at the center of the SuN detector. The target system involved two main components: the gas cell, which held the hydrogen gas, and the gas handling system.

The gas cell, designed at Hope College, consisted of two plastic halves. A schematic side section of the cell is shown in Fig.4.3, with construction images in Fig.4.4. A 2- μm thick molybdenum

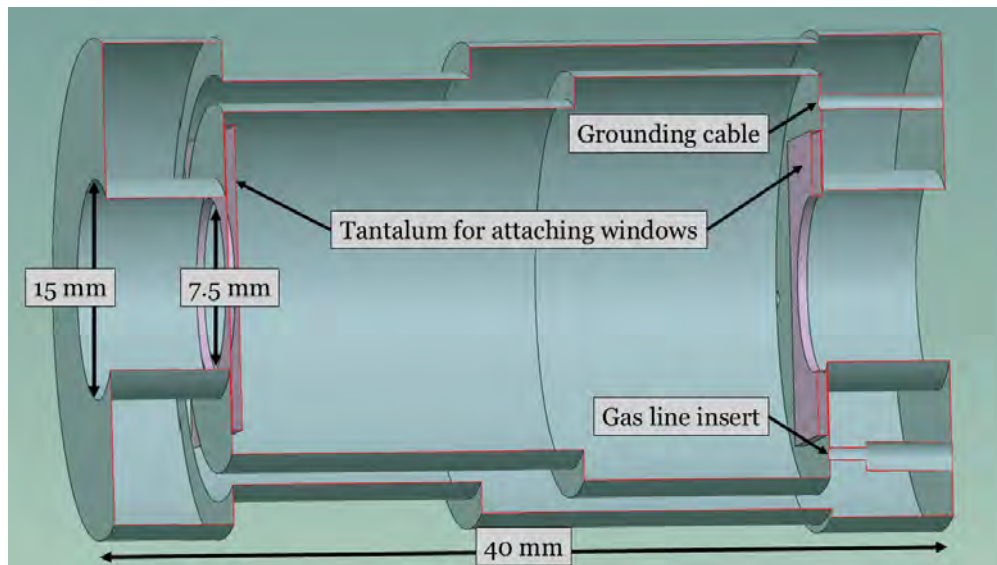


Figure 4.3 Side-section illustration of the gas cell showing the tantalum rings supporting the entrance and exit molybdenum windows, along with openings for the gas supply and grounding cable.

entrance and 5- μm thick exit window were glued onto the tantalum rings, as shown in the figures. The choice of molybdenum for the target window was based on several criteria. High atomic number (Z) materials are required to ensure that the Coulomb barrier is high enough, keeping the threshold for fusion-evaporation reactions well above the maximum beam energy. Additionally, the target window needs to be as thin as possible to minimize beam straggling and energy loss. At the same time, the material must have high strain tolerance, allowing the very thin foil to withstand the atmospheric pressure of the hydrogen gas against the vacuum in the beamline without rupturing. Lastly, it must be available from the manufacturer as leak-tight, so the hydrogen gas remains secured in the cell.

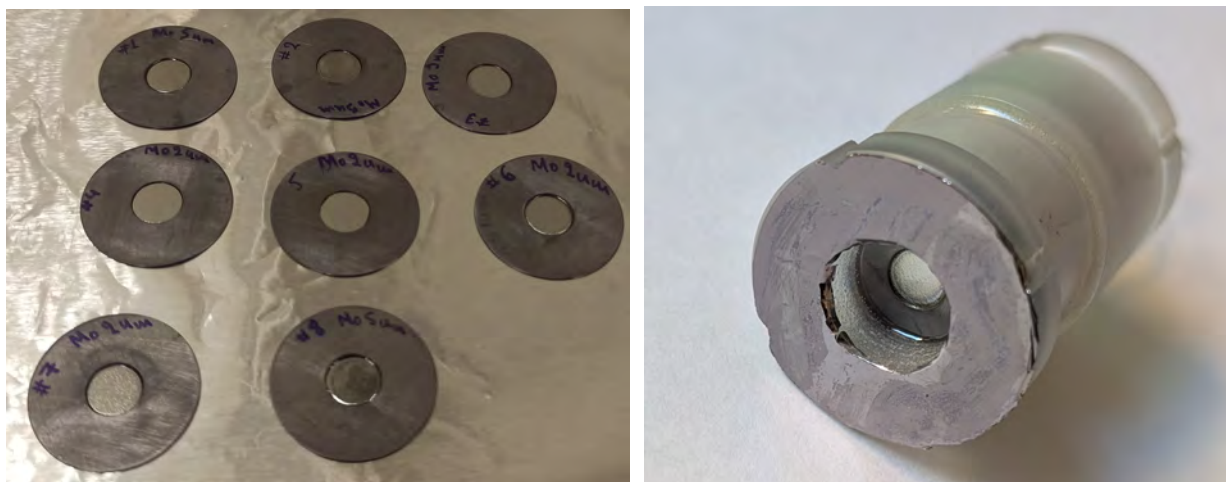


Figure 4.4 (left) tantalum rings with molybdenum entrance and exit windows during construction (right) assembled gas cell

Ensuring that the components of the gas-cell interacting with the beam do not create significant beam-induced background is critical. This background can become significant, especially if the beam interacts with anything plastic, as synthetic polymers consist mostly of carbon and hydrogen atoms, which can become target for the (p, γ) reaction of interest, or get scattered, affecting the quality of the data. For these reasons, the inner volume and front face of the cell were lined with tantalum foil to shield the plastic components from the beam. The tantalum also allowed charge collection from the entire inner volume of the cell. The back half of the cell contained two small openings: one for the grounding cable that was connected to the inner lining, which prevents charging and discharging inside the cell, and another for attaching the gas supply pipe. Both openings were sealed with epoxy glue after assembly to ensure leak-tight operation.

The gas handling system ensured safe handling and proper disposal of the flammable hydrogen gas. The system, shown in Fig. 4.5, consisted of a 10 L hydrogen reservoir, flowmeters, and regulators to control the slow filling and emptying of the cell, preventing rupture of the thin window foils. It also included a dry nitrogen supply line to purge the hydrogen before venting, preventing hazardous mixtures with atmospheric oxygen. A series of valves regulated the flow, while two manometers monitored the pressure of the reservoir and gas cell. The reservoir remained overpressurized at ≈ 850 -900 Torr, to mitigate the risk of atmospheric oxygen entering the small volume of the container. The cell was filled with 600 Torr of hydrogen during operation, with its

pressure continuously monitored and recorded throughout the experiment. The system featured detailed procedures for pumping down, filling the reservoir and gas cell with hydrogen, purging hydrogen, and venting. Multiple interlocks were incorporated to ensure that, in the event of target failure—such as a rupture of the target window—any potential hazards were effectively mitigated.

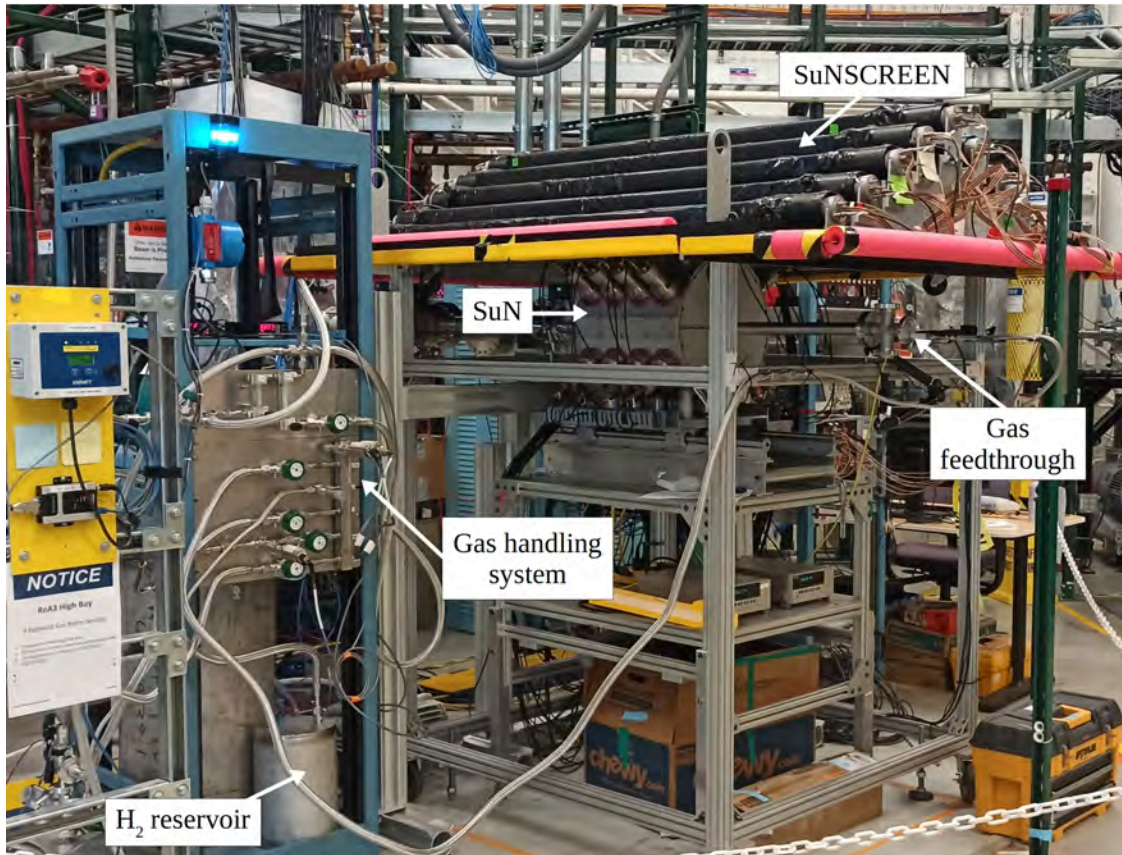


Figure 4.5 The setup of the $^{73}\text{As}(p, \gamma)^{74}\text{Se}$ experiment in the ReA3 experimental area. The picture shows the SuN and SuNSCREEN detectors and the hydrogen gas supply system.

4.3 The SuN Detector

Surrounding the hydrogen gas target was the Summing NaI (SuN) γ -ray detector, shown in Fig. 4.1 and 4.5. SuN is a calorimeter with the shape of a 16×16 inch barrel with a 1.8 inch diameter borehole along its axis. The barrel is segmented into 8 NaI(Tl) crystals, each connected to three photomultiplier tubes (PMTs) [193, 194]. The large volume of the detector allows for high γ -ray detection efficiency and nearly 4π solid angle coverage for a source placed in its center.

Sodium iodide (NaI) crystals doped with traces thallium (Tl) are the most common inorganic

scintillation material, widely used for the detection and spectroscopy of γ -ray radiation. Introduced in 1948 [195], NaI(Tl) crystals are valued for their availability in large volumes at relatively low costs, which often outweighs the advantages of newer inorganic scintillators offering higher light output, better energy resolution or faster timing capabilities [196]. However, NaI(Tl) is highly hygroscopic and deteriorates upon contact with atmospheric water. To prevent this, the top and bottom SuN crystals are encapsulated in aluminum casing. Additionally, the crystals are surrounded by a reflective polytetrafluoroethylene layer, therefore they are optically isolated from each other and can function as individual detectors.

When ionizing radiation enters the active volume of the detector, it excites the crystal atoms, leading to emission of visible light with wavelength of approximately 415 nm during de-excitation. This light is collected by the PMTs, where it is converted to photoelectrons. These photoelectrons are accelerated and multiplied through a series of dynodes, creating an electrical signal whose magnitude is proportional to the incident radiation energy [196]. The signals from the PMTs are amplified by a pre-amplifier and processed by XIA Pixie-16 digitizers. In the Pixie-16 modules the analog electronic signal from the PMTs is converted to a digital representation through an analog to digital converter (ADC). The digitizers are configured, read out and analyzed using the Digital Data Acquisition System (DDAS) [197], a lab-supported framework built around the Pixie-16 digitizers. The FRIBDAQ software suite manages the data flow and sets up the analysis pipeline, transforming the raw data from its hexadecimal format into physically meaningful parameters, such as energy and time spectra [194].

4.3.1 Summing Technique

The large angular coverage and high detection efficiency of the detector allows for the application of the γ -summing technique [198, 193]. In this technique, the spectra obtained by the individual crystals (segments) provide sensitivity to the individual γ -ray transitions, whereas the full energy deposited in SuN provides sensitivity to the populated excitation energies. More specifically, there are three main types of spectra used in this analysis: the *Sum of Segments* (SoS), the *Total Absorption Spectrum* (TAS), and *multiplicity* spectrum. The SoS corresponds to the sum of the energy spectra

recorded by each one of the optically isolated segments. This contains all the individual γ -ray transitions that occurred within the compound nucleus and got detected by SuN. TAS includes the energy deposited in all segments added up on an event-by-event basis. This represents to the full energy deposited inside the detector and reflects the populated excitation energy in the compound nucleus. Finally, the multiplicity spectrum indicates how many segments of SuN recorded energy in each event, which is indicative of the γ -ray multiplicity in a γ cascade.

An example of the summing technique using the spectra of a ^{60}Co calibration source is shown in Fig. 4.6. The ^{60}Co nucleus populates excited states in the ^{60}Ni compound nucleus by β^- decay. In most cases (99.88%), the β^- decay populates a state of $E_X = 2.505$ MeV, that will subsequently decay by the emission of two γ rays, of energies 1.173 MeV and 1.332 MeV. A small fraction (0.12%) of the decays populate the 1.332 MeV state and therefore only one γ ray is emitted. The SoS spectra (Fig. 4.6b) contain both the 1.173 MeV and 1.332 MeV, with a slightly higher intensity on the 1.332 MeV γ ray, as well as a small peak at 2.505 MeV, in case both γ rays are recorded by the same segment. The dominant feature of the TAS spectrum (Fig. 4.6c) is a *sum peak* at 2.505 MeV corresponding to the excitation energy of the ^{60}Ni compound nucleus, and small peaks at 1.173 MeV and 1.332 MeV, corresponding to the 0.12% chance of populating the 1.332 MeV, as well as the few instances of incomplete summation. The multiplicity spectrum (Fig. 4.6d) shows the majority of events with multiplicity 2, and the average multiplicity is 2.06. Events with multiplicity higher than 2 correspond to scattered γ rays deposited their energy to more than one segment.

Building on the simplistic example of the ^{60}Co decay, Fig. 4.7 shows the application of the summing technique in a more complex scenario, such as a capture reaction experiment. The sum peak forms in the TAS spectrum at energy $E_X = E_{\text{CMS}} + Q$, where E_{CMS} is the center-of-mass energy and Q the reaction Q value. As will be discussed in Sec. 5.5, the efficiency of the sum peak depends on the multiplicity of the cascade [193], and therefore it is important to take all three types of spectra into consideration when applying the summing technique.

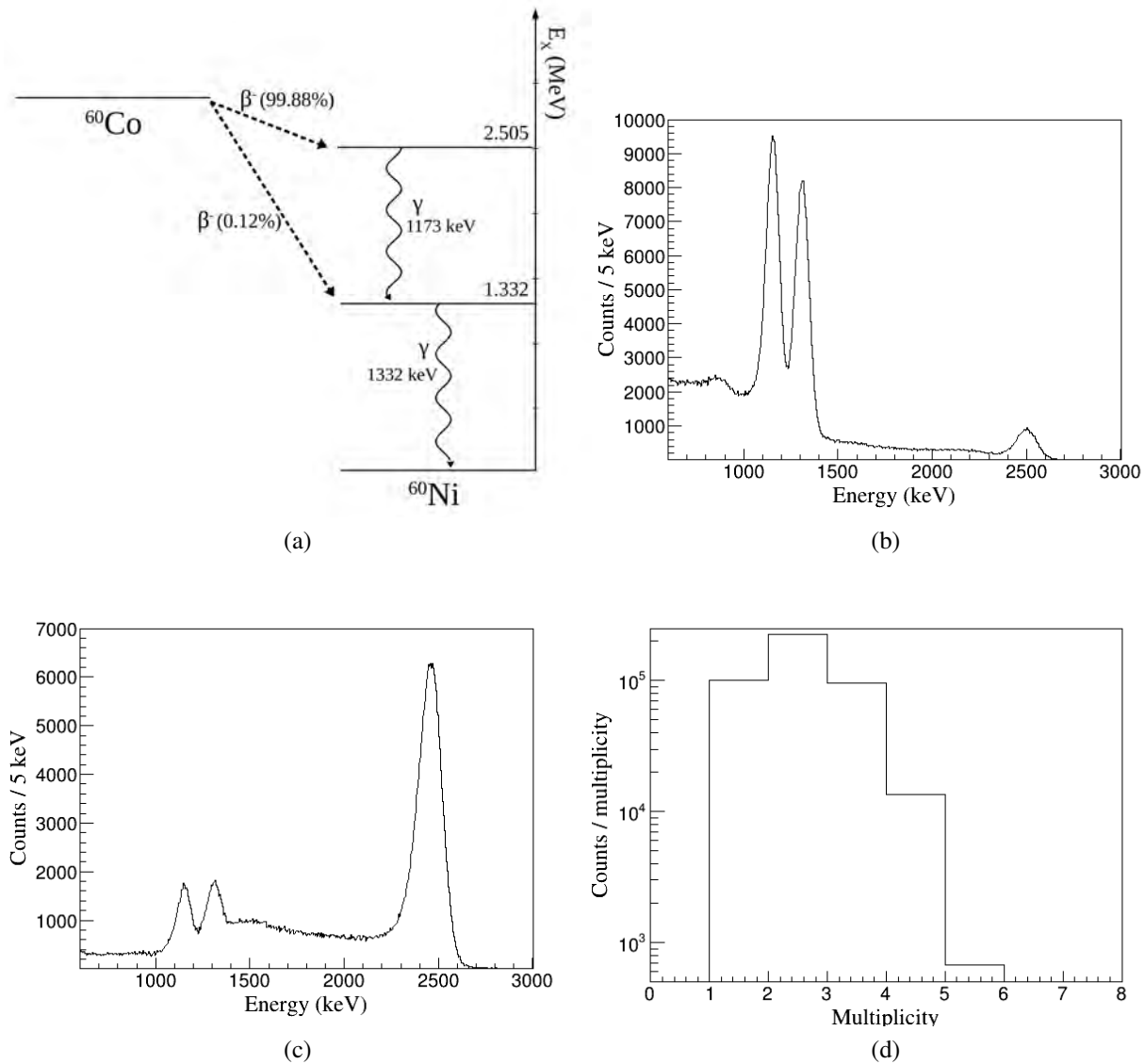


Figure 4.6 SuN spectra from a ^{60}Co nucleus: (a) decay scheme of ^{60}Co , (b) SoS spectra showing the two characteristic γ rays, (c) TAS with a sum peak at 2.5MeV and (d) multiplicity spectrum showing the majority of cascades to have multiplicity two.

4.4 The SuNSCREEN Detector

In the energy region of interest for these measurements, the main source of background comes from cosmic rays, which pose a significant challenge when trying to measure very small cross sections on the order of millibarns. To address this issue and increase the sensitivity of the SuN detector, the Scintillating Cosmic Ray Eliminating ENsemble (SuNSCREEN) [199] was positioned above SuN, as shown in Fig. 4.1 and 4.5. SuNSCREEN is a plastic scintillator detector

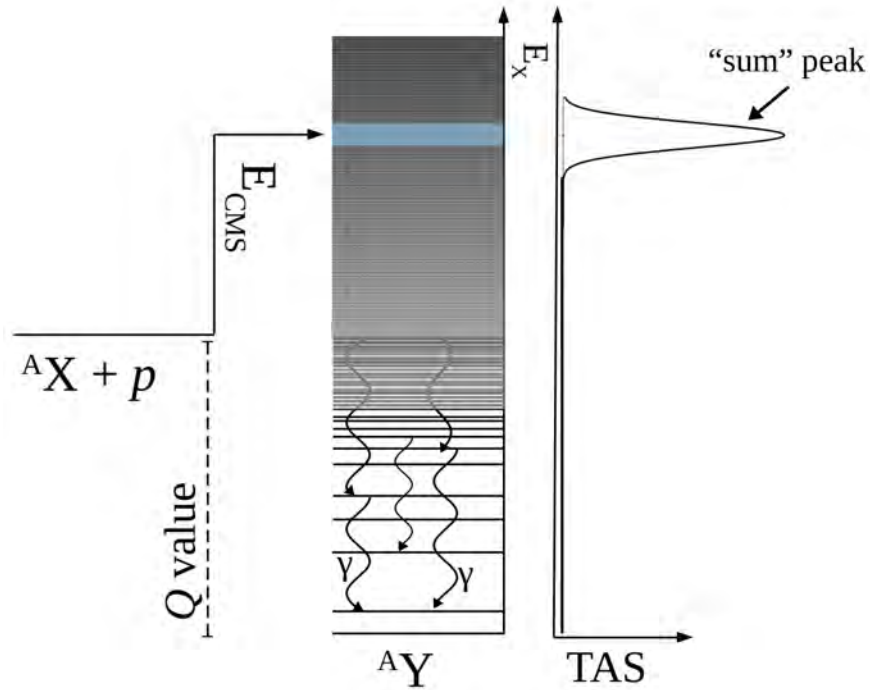


Figure 4.7 Illustration of the energetics of a ${}^A X(p, \gamma){}^A Y$ reaction with the summing technique. The compound nucleus ${}^A Y$ is populated at an excitation energy $E_X = E_{CMS} + Q$ and a sum peak forms at the TAS spectrum at energy E_X .

array comprised of nine bars, each with two PMTs, forming a roof-like arrangement above the SuN detector. To reduce the cosmic-ray induced background, SuNSCREEN was used as a veto detector. For this reason, all events that recorded signals in both PMTs of a SuNSCREEN bar, and at least one segment of SuN were rejected from the SuN spectra.

During the SuNSCREEN's commissioning this method was shown to reduce the cosmic-ray background contributions by up to a factor of four in the SoS spectra and a factor of two in TAS [199]. Spectra of the background radiation with and without the SuNSCREEN veto gate applied are shown in Fig. 4.8, where in the region around 10 MeV, which is the relevant region for the present work, a background reduction of a factor of three is observed in both SoS spectra and TAS. The spectra also show characteristic background peaks at 1461 keV and 2614 keV from natural radiation, as well as a small peak at 6.8 MeV in the TAS from neutron capture on the NaI crystal via the ${}^{127}\text{I}(n, \gamma){}^{128}\text{I}$ reaction with Q -value of 6.8 MeV. Additional background reduction is achieved by taking advantage of the time structure of the beam as discussed in Sec. 5.3.4.

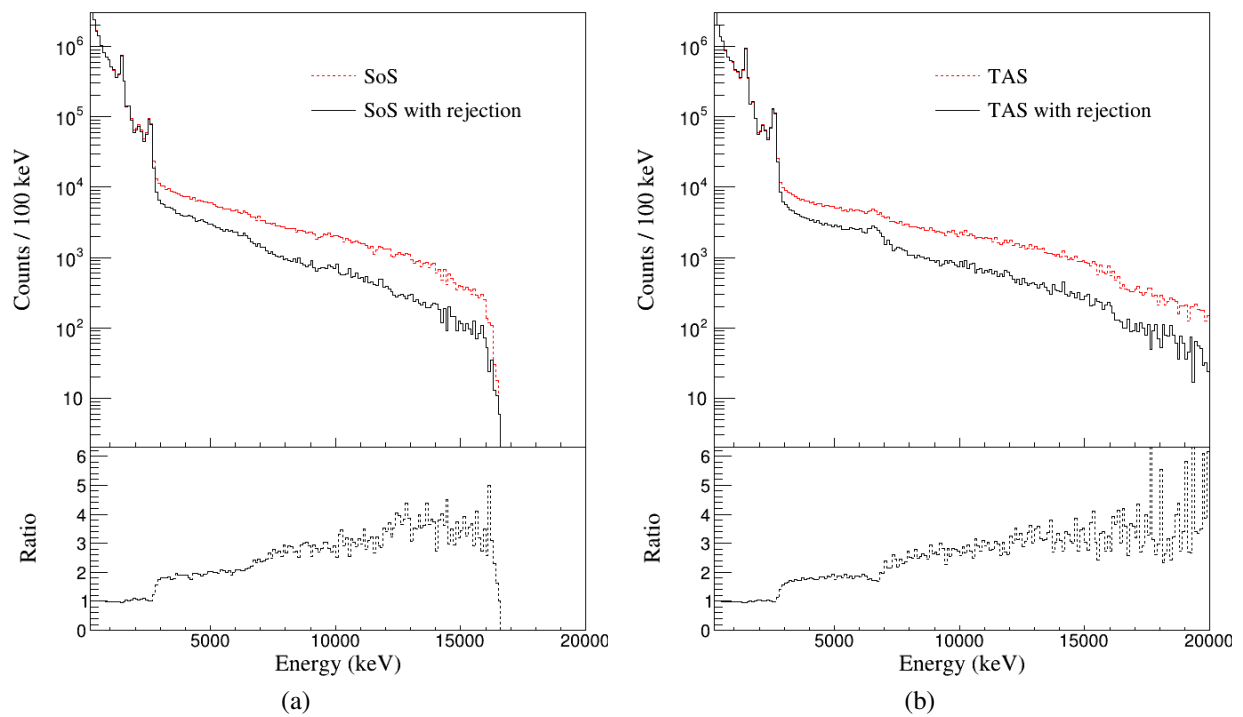


Figure 4.8 Typical room background (a) sum of segments and (b) total absorption spectra shown in red dashed line. The same spectra are shown with black solid line after SuNSCREEN veto rejection. The lower panels show the ratio before and after rejection.

CHAPTER 5

ANALYSIS

As discussed in Ch. 2, the cross section formula used in this analysis is given by Eq. 2.10

$$\sigma = \frac{Y}{I_a N_t \epsilon} \quad (5.1)$$

where Y the experimental yield, meaning the number of reactions recorded by the detector, I_a the total number of beam particles, N_t the number of target nuclei and ϵ the detection efficiency.

This chapter focuses on calculating the cross sections for the $^{82}\text{Kr}(p, \gamma)^{83}\text{Rb}$ and $^{73}\text{As}(p, \gamma)^{74}\text{Se}$ reactions. Details on the calculation of each parameter, along with the associated uncertainties are discussed, and the resulting cross section values are presented in Ch. 6.

5.1 Effective Energy

Before calculating the individual parameters of Eq. 5.1, it is useful to determine the center-of-mass energy at which the cross section is measured. In thin target experiments, where energy loss through the target is minimal, it is common to assume that the reaction energy corresponds to the one in the middle of the target. However, for the 4-cm-long gas cell used in this experiment, the effective center-of-mass energy E_{eff} needed to be calculated [15]. The effective energy E_{eff} , represents the beam energy within the target at which half of the total yield is produced.

For non-resonant reactions the astrophysical S factor (Sec. 2.5.4) can be considered nearly constant over a relatively small energy interval of the target thickness Δ . This can be utilized to calculate the E_{eff} from the integral of the cross section from Eq. 2.36 over the target thickness Δ as

$$\int_{E_0 - \Delta E}^{E_0} \frac{1}{E} \exp(-2\pi\eta) dE = 2 \int_{E_{\text{eff}}}^{E_0} \frac{1}{E} \exp(-2\pi\eta) dE \quad (5.2)$$

where E_0 is the incident projectile energy and ΔE is the energy loss within the target. Assuming the cross section decreases linearly between σ_1 at E_0 and σ_2 at $E_0 - \Delta E$, the effective energy E_{eff} can be calculated from Eq. 5.2 as

$$E_{\text{eff}} = E_0 - \Delta E + \Delta E \left\{ -\frac{\sigma_2}{\sigma_1 - \sigma_2} + \left[\frac{\sigma_1^2 + \sigma_2^2}{2(\sigma_1 - \sigma_2)^2} \right]^{1/2} \right\} \quad (5.3)$$

which is a good approximation for $\sigma_1/\sigma_2 < 10$ [15]. The values of σ_1 and σ_2 are obtained from NON-SMOKER [174], and their ratios are 1.6, 1.7, and 2.0 for initial ^{82}Kr beam energy of 3.7, 3.4, and 3.1 MeV/u, and 1.4 and 2.0 for the ^{73}As beam at 3.7 and 3.1 MeV/u.

5.2 Beam Particle Number

The design of the experimental setup includes an isolating flange upstream of SuN, and a plastic feedthrough in the end of the beamline for the gas supply. This way the beamline is electrically isolated from the rest of the setup and is used as a Faraday cup. The beam current in the ^{82}Kr experiment was calculated from the ammeter measurement of the beamline. Unfortunately, during the ^{73}As experiment the isolation was not successful and as shown in Fig. 5.1 a clear charge and discharge of the beamline can be seen in the measured current in the order of tens of fA. As the deposited beam current was in the order of a couple fA, the measured current from the

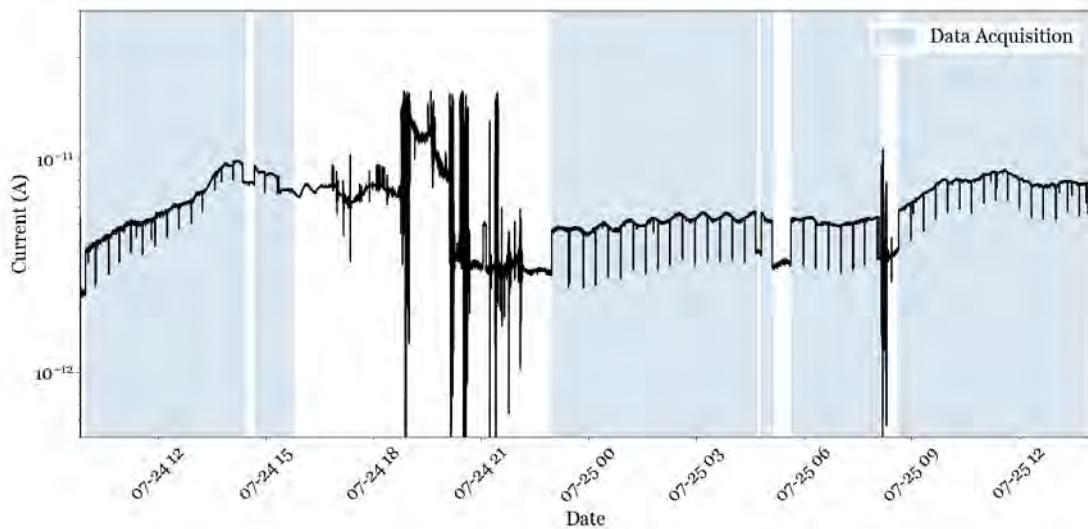


Figure 5.1 The ^{73}As beam current measured from the ammeter connected to the improperly isolated beamline as a function of time. The blue highlighted areas correspond to data acquisition times. The small frequent drops correspond to upstream Faraday cup measurement where no beam is present. As the baseline varies by tens of fA, whereas the beam current was only a few fA, this measurement cannot be used for analysis.

dowstream ammeter cannot be used for this analysis. Instead, throughout the experiment, Faraday cup measurements were taken every 20 minutes that interrupted the beam momentarily, as can be seen from the frequent dips in Fig. 5.1 that reflect the position of the baseline during that time.

The beam current calculations are shown in Fig.5.2. Every 20 minutes a Faraday cup interrupted the beam upstream of the SuN detector, and the current was measured off of that cup. The top

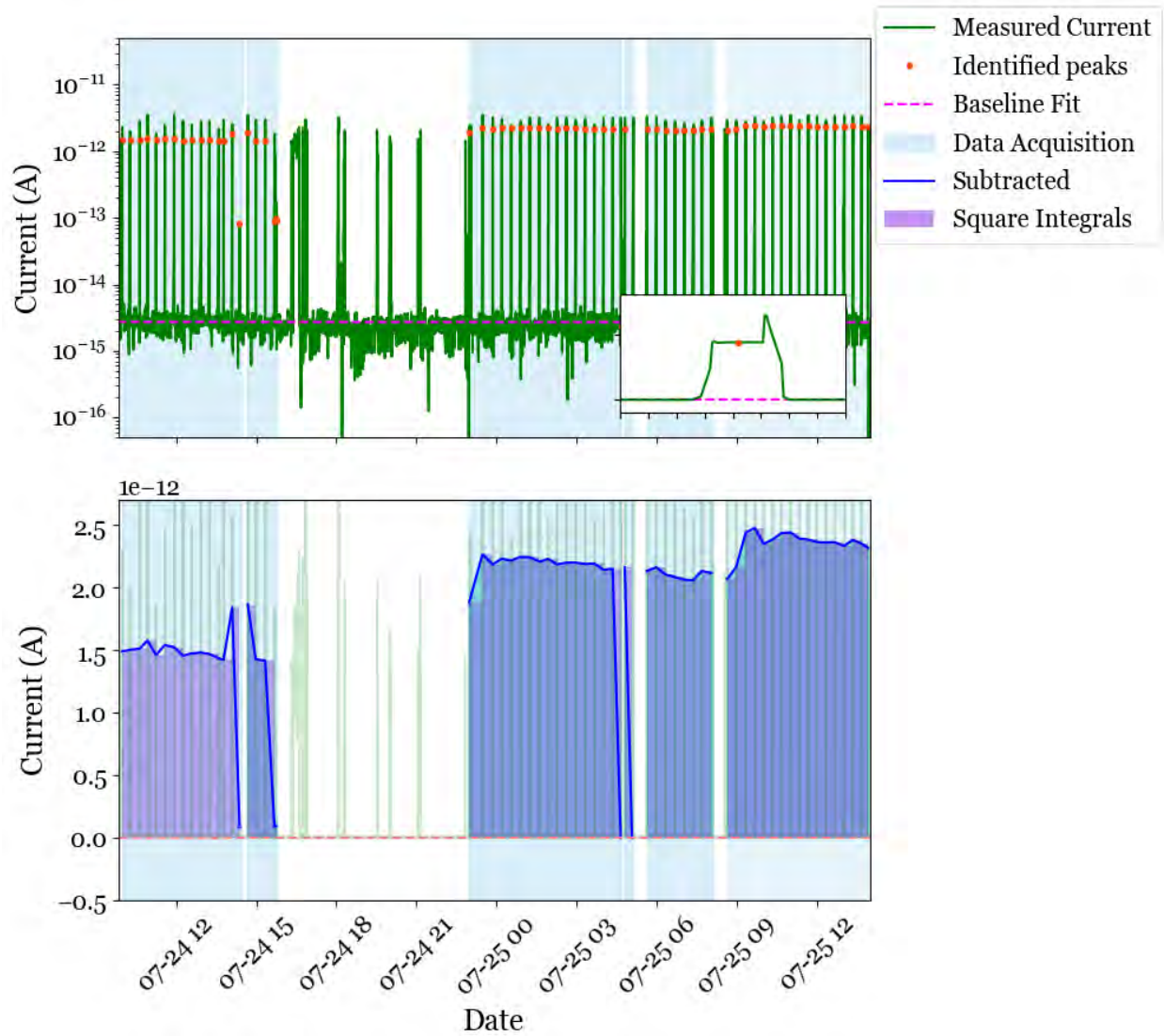


Figure 5.2 Beam current calculation for the ^{73}As experiment. The top panel displays the upstream Faraday cup measurements taken every 20 minutes, with the inset zooming in on one minute of data and identifying the plateau region used for the calculation. The bottom panel highlights the integrated regions, with shaded areas indicating data acquisition periods.

panel shows the current recorded by that collimator, where each peak corresponds to a current measurement. The beam intensity was considered at the plateau of the peak, shown in the inset. The baseline was fitted with a linear fit, reflected by the dashed line. The blue solid line in the bottom panel corresponds to the subtracted baseline from the peaks. The total deposited beam

charge, C_{tot} , was calculated using square integrals between consecutive peaks, shown by the shaded region in the bottom panel.

The total number of beam particles, I_α , was calculated as

$$I_\alpha = \frac{C_{\text{tot}}}{Q_{\text{beam}} \cdot q_e} \quad (5.4)$$

where C_{tot} is the integral of the beam current, Q_{beam} is the charge state of the beam (23 for ^{73}As and 27 for ^{82}Kr), and q_e the electron charge.

5.3 Experimental Yield

5.3.1 SuN Gainmatching & Energy Calibration

The energy spectra from the SuN detector, acquired using the 12-bit digitizers discussed in Sec. 4.3, are expressed in $2^{12} = 4096$ ADC channels. Each channel corresponds to a specific voltage height of a PMT output signal. The first step in analyzing these spectra is to ensure that all 24 PMTs respond consistently to γ rays of the same energy. This procedure is known as gainmatching.

To eliminate position dependence of the PMTs within each crystal, gainmatching is typically performed with γ rays from natural background radiation, such as ^{40}K . Approximately 10% of the β^- decays of ^{40}K populate an excited state of ^{40}Ar , resulting in the emission of a characteristic 1461 keV γ ray.

Gainmatching for the SuN PMTs is conducted in two stages. The first stage, hardware gainmatching, involves adjusting the voltages applied to each PMT before the experiment so that the 1461 keV γ ray from ^{40}K appears in approximately the same ADC channel in the recorded spectrum. The second stage, software gainmatching, fine tunes the PMT gains by normalizing the obtained spectra so the ^{40}K peak appears in the exact same channel for each PMT. Fig. 5.3 shows the spectra from all PMTs in the 1461 keV region before software gainmatching during the ^{73}As experiment. Gaussian fits on a linear background were applied to locate the peak centroids, and the resulting gainmatching factors, listed in Table 5.1, were calculated to align the peaks to the same ADC channel, as shown in Fig. 5.4.

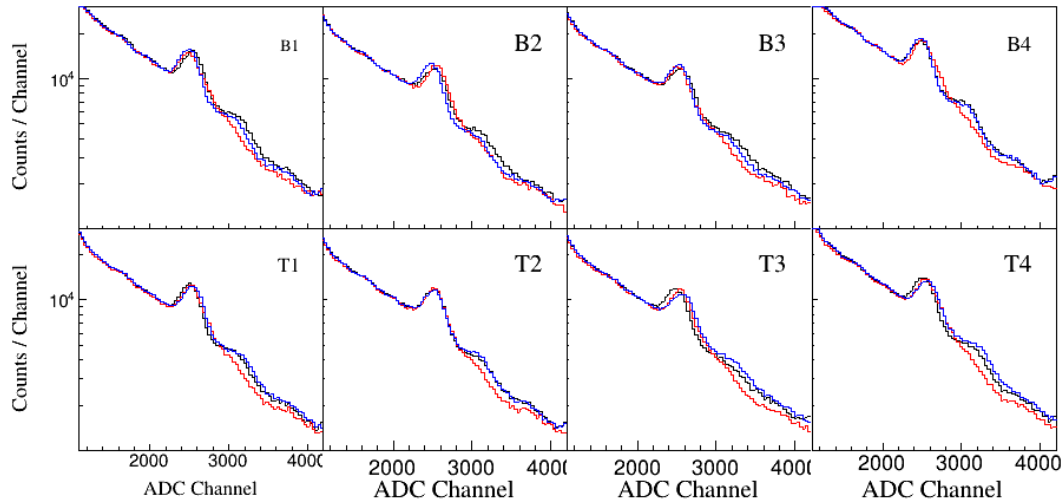


Figure 5.3 Background spectra of all 24 SuN PMTs before gainmatching in the region near the 1461 keV ^{40}K peak during the ^{73}As experiment. Each panel represents one detector segment, showing spectra from its three associated PMTs, with black, red, and blue lines corresponding to PMTs 1, 2, and 3, respectively.

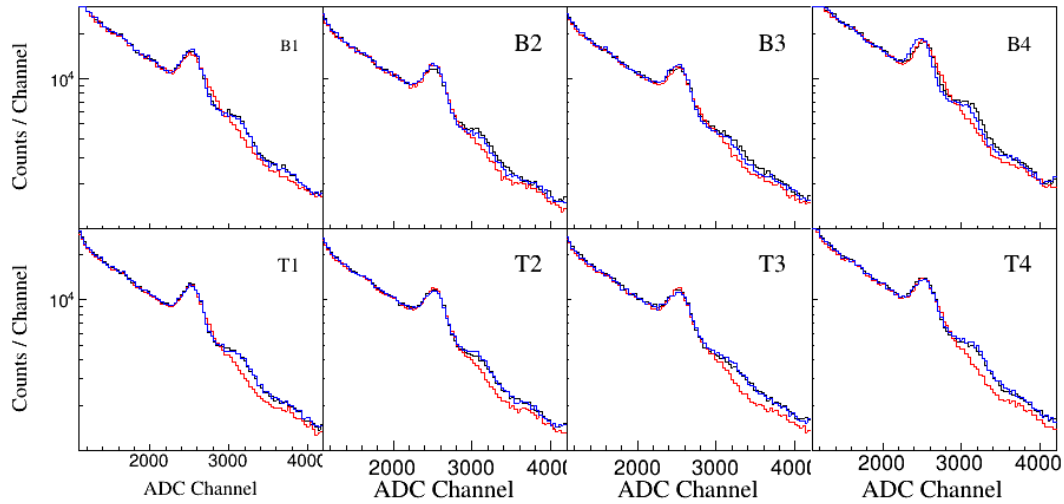


Figure 5.4 Same as Fig. 5.3 after applying the gainmatching factors from Table 5.1.

After gainmatching, all PMTs produce consistent spectra, however, the spectra remain in arbitrary ADC units. To find the correlation between ADC units and energy, an energy calibration is performed using sources that emit characteristic γ rays of known energy. The γ rays used were the 59.5 keV ^{241}Am peak, the 661.7 keV ^{137}Cs peak, and the 1173.2 keV and 1332.5 keV peaks from ^{60}Co . Additionally, γ rays from a ^{228}Th source were used, specifically the 238.6 keV peak from the ^{212}Pb daughter nucleus and the 583.2 keV and 2614.5 keV peaks from ^{208}Tl . The resulting

calibrations are shown in Fig. 5.5 and the fit parameters are listed in Table 5.1.

Table 5.1 The gainmatching and calibration factors for SuN for the ^{73}As experiment.

Gainmatching Factors

PMT	Factor	PMT	Factor
B11	1.0075	T11	0.9927
B12	0.9997	T12	1.0141
B13	0.9929	T13	1.0135
B21	1.0005	T21	0.9948
B22	1.0000	T22	0.9873
B23	1.0022	T23	1.0141
B31	1.0116	T31	0.9863
B32	0.9903	T32	1.0003
B33	0.9812	T33	0.9962
B41	1.0018	T41	1.0166
B42	0.9892	T42	1.0059
B43	0.9825	T43	1.0136

Calibration Factors

Segment	Scale	Intercept
B1	0.1815	-28.0864
B2	0.1839	-29.7079
B3	0.1801	-27.8599
B4	0.1817	-29.5897
T1	0.1812	-27.6117
T2	0.1837	-26.6570
T3	0.1801	-26.8405
T4	0.1824	-27.9716

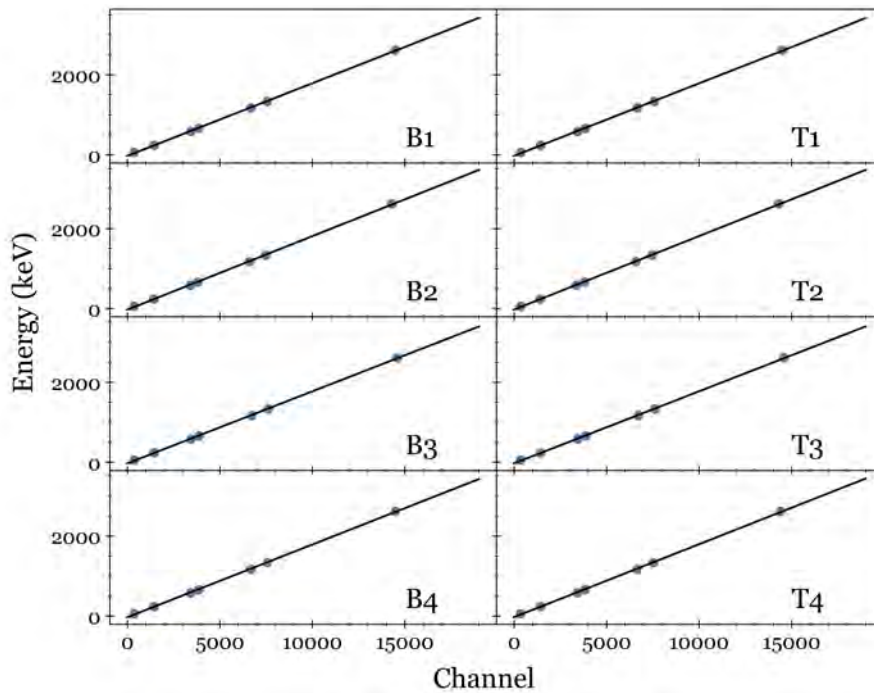


Figure 5.5 SuN calibration fits. Each panel corresponds to one segment of SuN.

5.3.2 The Sum Peak

As discussed in Sec. 4.3, in the summing technique the experimental yield Y is calculated from the integral of the sum peak, that forms in the TAS spectrum at energy $E_X = E_{\text{CMS}} + Q$, where E_{CMS} is the center-of-mass energy and Q the reaction Q value.

The summing technique has been successfully applied to a plethora of (p, γ) and (α, γ) reaction measurements on stable nuclei [198, 200, 201, 202, 203]. These experiments are typically conducted in regular kinematics, where a p or α beam impinges on a heavy, solid, stable target. For radioactive isotopes, however, it becomes necessary to transition to inverse kinematics, as constructing targets from exotic isotopes with short half-lives is highly challenging.

Inverse kinematics is a widely used approach at many facilities for γ -process measurements using mass separators [204] and storage rings [166], but there has so far been only one experiment with a radioactive beam [173]. The summing technique has been successfully applied in inverse kinematics using a solid target [205]. However, as the beam intensity in radioactive beams decreases by orders of magnitude compared to stable beams, the introduction of a gas target was necessary to increase the purity of the target, and allow for more efficient measurements.

Transitioning to inverse kinematics and the introduction of a gas target increases the complexity of this method. Firstly, due to the experiment being conducted in inverse kinematics, the recoil nucleus has significant momentum and continues its path along with the unreacted beam, rather than remaining stationary in the target. Therefore the γ rays are emitted from a moving source, and Doppler corrections need to be applied for the detected γ -ray energy [206]. Additionally, the beam's passage through the target entrance window introduces energy straggling, resulting in a range of incident beam energies. This, in turn, populates the compound nucleus at a range of excitation energies, causing a significant widening of the resulting sum peak.

5.3.3 Doppler-Shift Corrections

The Doppler effect is the change in frequency of a wave emitted by a moving source relative to a stationary observer, compared to the frequency that would be measured if the source were at rest. For a relativistic moving particle, such as light, the observed energy will be shifted according to

the velocity of the moving source. Therefore the energy of the γ rays emitted by the moving recoil nucleus are shifted by

$$E_0 = \frac{1 - \beta \cos \theta}{\sqrt{1 - \beta^2}} E \quad (5.5)$$

where E_0 the γ -ray energy emitted by the source, E is the detected γ -ray energy by the stationary observer, $\beta = v/c$ the recoil relative velocity and θ the relative angle between the recoil and the detector. Assuming the decay of the moving recoil in the center of the detector, each SuN segment has a different angle corresponding to the center of the segment, as shown in Table 5.2. Table 5.3 shows the different beam energy for the ^{73}As and ^{82}Kr beam in the laboratory frame, the center-of-mass energy at the center of the target accounting for the energy loss through the entrance window and the recoil relative velocity β .

Table 5.2 SuN segment angles from Ref. [194].

Segment	Angle (deg)
1	2.550
2	2.024
3	1.118
4	0.592

Table 5.3 ^{82}Kr and ^{73}As beam energies and relativistic velocities.

Beam	Energy Lab (MeV/u)	CoM energy in middle of target (MeV/u)	$\beta = v/c$
^{82}Kr	3.7	2.98	0.079
	3.4	2.67	0.075
	3.1	2.37	0.071
^{73}As	3.7	2.95	0.079
	3.1	2.31	0.070

Once all acquired spectra were corrected on a segment-by-segment basis, they were summed to form a Doppler-shift corrected sum peak.

5.3.4 Background Subtraction

There were two main types of background contributions that could interfere with the sum peak in the energy region of interest: cosmic-ray background and beam-induced background. Minimizing those background contributions in the region where the sum peak was expected was important for the accurate determination of the experimental yield.

The cosmic-ray background, as discussed in Sec. 4.4, was significantly reduced using the SuNSCREEN veto detector. Any remainder cosmic-ray background contributions, were removed by utilizing the pulsed structure of the beam. The beam was delivered in $80 \mu\text{s}$ pulses every 200

ms. While data was recorded continuously, two distinct time gates were applied during processing. The first gate corresponded to the $80\ \mu\text{s}$ beam-on intervals, triggered by a signal from the EBIT charge breeder. The second gate, applied 100 ms later, captured $800\ \mu\text{s}$ of background data between pulses. An illustration of this structure is shown in Fig. 5.6. The background data were scaled

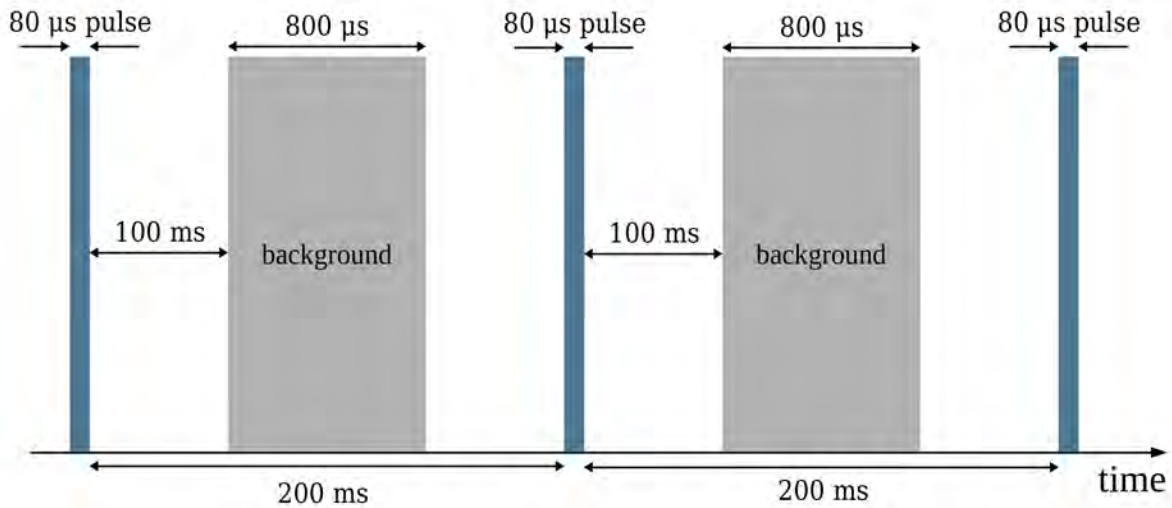


Figure 5.6 Illustration of the pulsed-beam structure. Blue boxes correspond to $80\ \mu\text{s}$ beam pulses occurring every 200 ms, while grey boxes reflect the 100 ms time-shifted gate used to record $800\ \mu\text{s}$ of background between beam pulses. The time axis is not to scale.

down by a factor of ten to account for the shorter recorded time and subtracted from the beam-on data to remove room-background contributions.

The last form of background originates from the beam and regards to any beam-induced reactions other than the reaction of interest. This includes beam scattering on any beamline components, or any interaction with the gas cell and its entrance and exit windows. As discussed in Sec. 4.2 high Z materials are used to cover all parts of the cell the beam may interact with. Unfortunately, during the ^{73}As experiment, of the two gas cell targets used, one had significant scattering background caused by epoxy glue residue that had seeped onto the entrance window. Therefore, the data acquired with that gas target could not be analyzed, as the sum peak was not visible above the background.

Removing beam-induced background contributions requires isolating them from the data corresponding to the reaction of interest. For this purpose data are acquired while the gas cell is full of hydrogen gas, as well as while the cell is empty. The empty cell data are scaled based on the

ratio of beam current during full cell and empty cell runs and subtracted from the full cell data. Fig.5.7 shows the Doppler corrected TAS spectrum for the 3.7 MeV/u ^{82}Kr background subtracted sum peak, after subtracting cosmic-ray and room background. The black line corresponds to the full cell data and the red line is the empty cell data scaled based on the total deposited beam current of the full and empty cell runs. Subtracting the two gives the sum peak shown in the blue line. The blue band corresponds to the statistical uncertainty from the background subtraction.

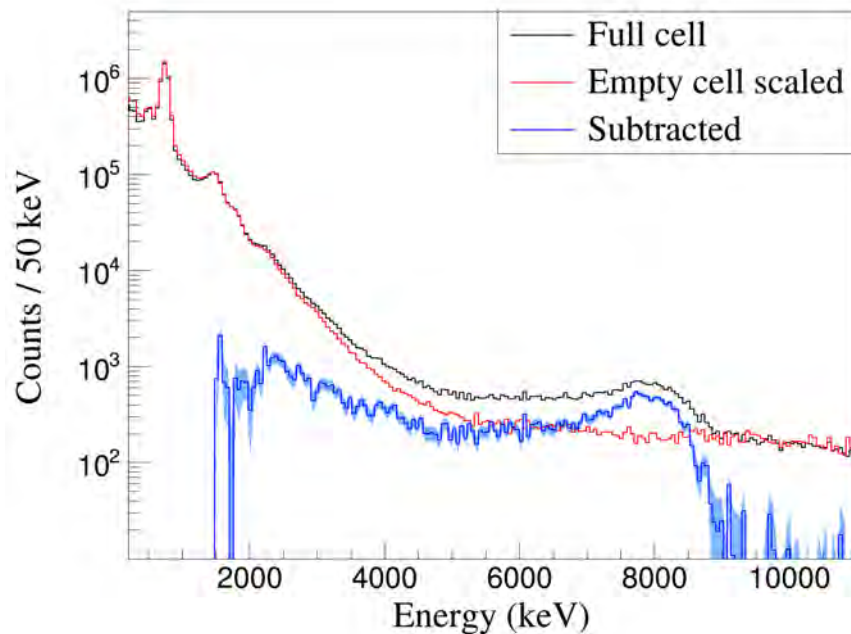


Figure 5.7 Doppler-corrected TAS spectra showing the background subtraction for the sum peak for the $^{82}\text{Kr}(p, \gamma)^{83}\text{Rb}$ reaction at the initial beam energy 3.7 MeV/nucleon. The black histogram corresponds to the gas cell filled with hydrogen gas, the red histogram corresponds to the empty gas cell scaled to the beam current, and the blue histogram is the fully subtracted sum peak that was used for the remaining analysis. The blue band corresponds to the statistical uncertainty of the background subtraction. (Figure adapted with permission from Tsantiri *et al.*, Phys. Rev. C 107, 035808 2023. Copyright 2023 by the American Physical Society)

The low energy region of the TAS spectrum shows a number of peaks from scattering of the beam on the molybdenum window. This serves as a useful tool to identify if the position of the incoming beam remains the same between full and empty cell runs, as the two spectra should overlap after scaling on the beam current. Similarly in the energy region higher than the sum peak the spectra should overlap as well. In the case of the ^{73}As experiment, scaling on the beam current did not result in overlapping scattering peaks or high energies, indicating that the position

of the beam had changed during data acquisition, as shown in Fig. 5.8. For this reason, instead of

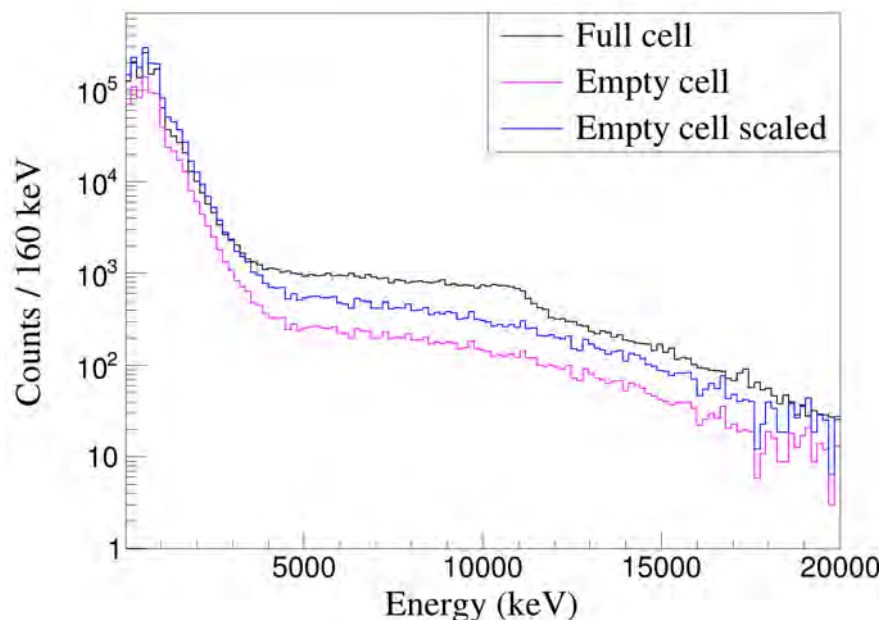


Figure 5.8 Doppler-corrected TAS spectra for the $^{73}\text{As}(p, \gamma)^{74}\text{Se}$ reaction at the initial beam energy 3.7 MeV/nucleon. The black histogram corresponds to the gas cell filled with hydrogen gas, the magenta histogram corresponds to the empty gas cell, and the blue to the empty gas cell scaled to the beam current. The disagreement of the full cell and scaled empty cell spectra indicates the beam position on the cell has shifted.

scaling on the beam current, the empty cell data were scaled based on the high energy region of the spectrum. Specifically, for energies between 13 and 18 MeV, where no contribution of the sum peak is expected, more than 1000 integrals over different energy ranges and regions were sampled. This created a distribution of scaling factors as shown in Fig. 5.9. The background subtraction was performed using the mean scaling factor, and the deviation of the distribution was introduced as an additional source of uncertainty for the remainder of this analysis.

Figure 5.10(a) shows the background subtraction for the 3.7 MeV/u ^{73}As beam. The challenge of running a radioactive beam experiment is apparent from the significantly lower statistics and large statistical uncertainties compared to the stable beam experiment. For the 3.1 MeV/u sum peak there was an additional challenge faced. Unfortunately, a few minutes after the beginning of full cell data acquisition in the 3.1 MeV/u beam energy the 2- μm thin molybdenum entrance window ruptured, allowing only for 30-minutes-worth of data acquisition. Regardless of this unfortunate

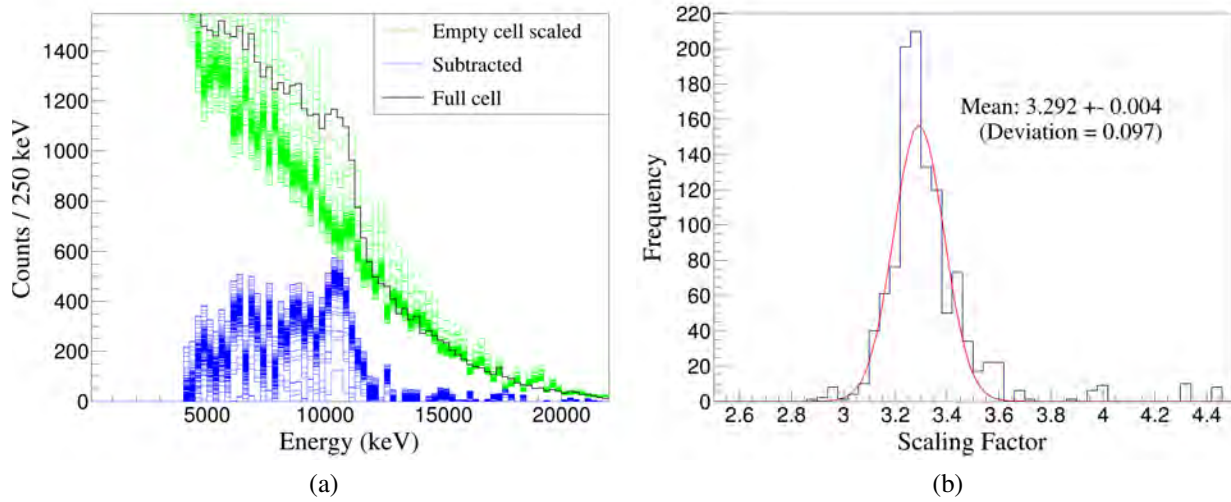


Figure 5.9 Sampling of various high energy regions for empty cell data scaling. Figure (a) shows the full cell data spectrum with black, the various empty cell scaled data with green and the resulting background subtracted sum peaks with blue, where each line corresponds to a different scaling factor. Figure (b) reflects the distribution of scaling factors. More details in text.

event, the data were deemed worth analyzing, as this reaction has never been measured before, and any new information that may be provided is important. The significantly low statistics accumulated result in very large statistical uncertainty, as shown by the blue error band in the resulting sum peak of Fig. 5.10(b). The uncertainty quantification is discussed in detail in Sec. 5.7.

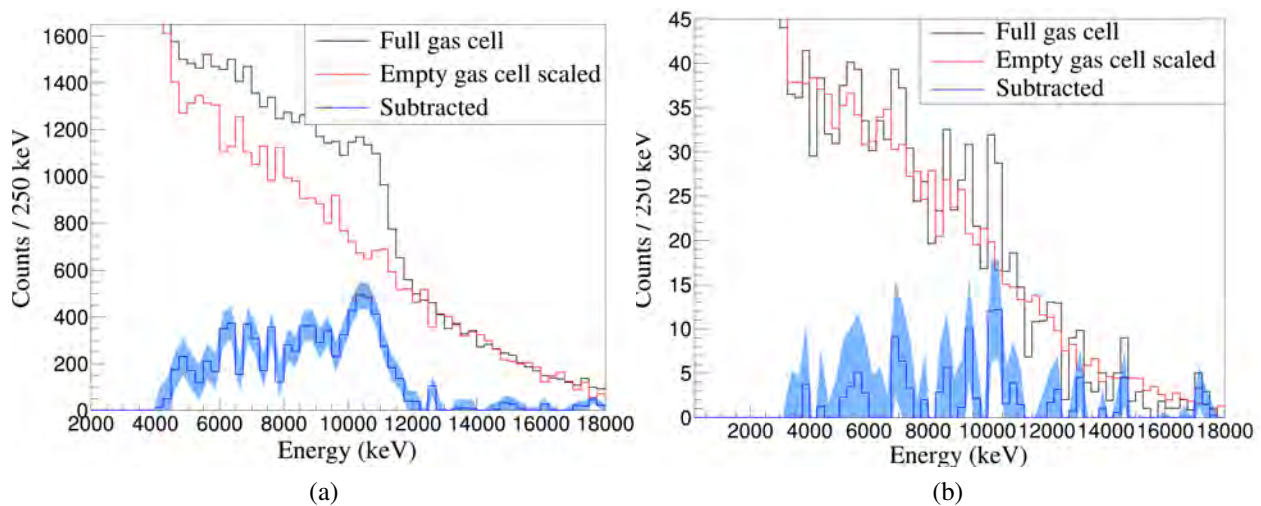


Figure 5.10 Same as Fig. 5.7 for the $^{73}\text{As}(p, \gamma)^{74}\text{Se}$ reaction at the initial beam energy of (a) 3.7 MeV/nucleon and (b) 3.1 MeV/nucleon. The blue bands correspond to statistical uncertainty. The uncertainty introduced by the empty cell scaling methodology is not included here.

5.4 Target Particle Density

The next parameter in Eq. 5.1, the target particle density N_t , is calculated based on the average target pressure. The pressure was recorded throughout the experiment and it can be seen for the ^{73}As experiment in Fig. 5.11.

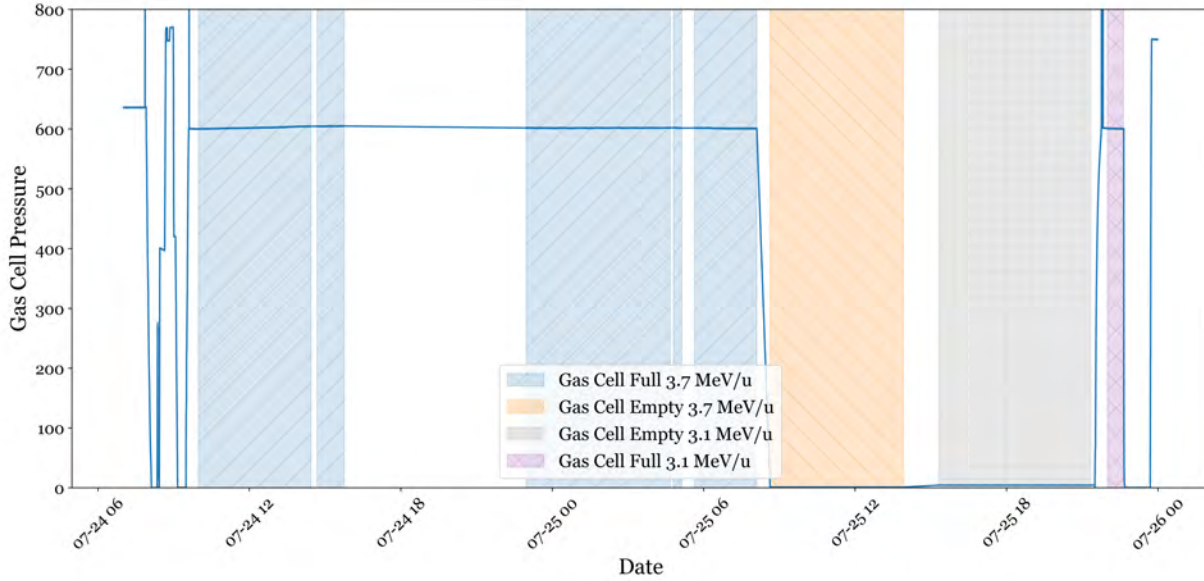


Figure 5.11 The gas cell pressure recorded during the ^{73}As experiment. The highlighted regions correspond to the full cell and empty cell runs of the 3.7 and 3.1 MeV/u beam energies.

From the target density, the effective target thickness can be calculated using LISE++ [207], an FRIB software used primarily for beam production and transmission calculations. It features many useful calculators, including a physics calculator used in this analysis that calculates effective target thickness of gas target based on the target material, pressure and width.

The target particle density N_t , can be calculated through:

$$N_t = \frac{N_A \cdot t}{m_H} \quad (5.6)$$

where t is the target thickness in grams/cm^3 from LISE++, N_A is the Avogadro's number, and m_H the hydrogen mass.

5.5 Detection Efficiency

The final term to be calculated in Eq.5.1 is the detector efficiency, ϵ , which represents the fraction of particles recorded relative to the total number emitted. For the SuN detector, a 4π calorimeter, the geometric efficiency is nearly 100% from its design. As a result, the detection efficiency is primarily governed by the intrinsic efficiency, defined as the ratio of detected particles to incident particles. Since uncharged radiations such as γ rays can travel large distances before interacting, or may interact with materials other than the scintillator, such as the casing, scintillating detectors are typically less than 100% efficient [196].

The intrinsic efficiency varies with energy, $\epsilon(E)$, and for a total absorption spectrometer like SuN, it also depends on the multiplicity of the cascade [193]. For example, the efficiency of detecting a single γ ray of $E_\gamma = 10$ MeV is higher than detecting two γ rays of 5 MeV each, emitted from a state of $E_x = 10$ MeV. Beyond this multiplicity dependence, regular kinematics experiments are characterized by narrow sum peaks, which allow the efficiency to be approximated for a single excitation energy. However, in this work, the sum peak is significantly broader, as discussed in Sec.5.3.2. The Doppler shift corrections were applied assuming the angle at the center of each segment, which is an approximation given the large angular coverage of each segment. Beyond any incomplete Doppler broadening corrections, substantial energy straggling also occurs as the beam passes through the target window foil. This results in sum peak widths around 2 MeV, as shown in Fig.5.7 and 5.10. Consequently, the efficiency must be calculated as a function of all energies contributing to the sum peak, while also accounting for the multiplicity of the cascades. For this reason, the detection efficiency is determined through a series of simulations, as outlined in the following paragraphs.

5.5.1 RAINIER Simulations

The first step in calculating the detection efficiency is to simulate the γ -ray deexcitation of the compound nucleus for all possible excitation energies populated during the reactions. The Q values for the reactions of interest are 8.55 MeV for $^{73}\text{As}(p, \gamma)^{74}\text{Se}$ and 5.77 MeV for $^{82}\text{Kr}(p, \gamma)^{83}\text{Rb}$. These values are sufficiently high for the excitation energy E_x of the compound nucleus to be in the

nuclear continuum region, where statistical model calculations are applicable (see Sec. 2.4.2.2). To simulate the γ -ray deexcitation of the compound nucleus, the RAINIER code [208] was used.

RAINIER is a Monte Carlo code that simulates the deexcitation of a compound nucleus using statistical nuclear properties. For these simulations, the nuclear level structure of the compound nucleus is provided as input. The low-energy level schemes for ^{74}Se and ^{83}Rb were taken from Ref. [74], up to approximately 3.3 MeV and 1.8 MeV, respectively, where the level schemes are considered complete. The upper portion of the level scheme can be constructed using the analytical nuclear level density (NLD) models described in Sec. 2.4.2.3, namely the constant temperature (CT) model [31] and the back-shifted Fermi gas (BSFG) model [25].

RAINIER also requires a description of the E_x and J_π of the entry state. The values of E_x were considered throughout the range that the experimental sum peak extends. For example in the 3.7 MeV/u beam energy, this corresponds to energies between 9.8 and 11.8 MeV for ^{74}Se , and between 7.0 and 8.8 MeV for ^{83}Rb . For the J_π of the state, s -wave proton capture ($1/2^+$) on the ground state of ^{82}Kr (0^+) was considered, while for the ^{74}Se compound nucleus, higher order corrections were needed. The J_π population was obtained from TALYS (Sec. 2.4.2.5) by enabling the outdecay and outpopulation options, that output detailed information of the population and statistical decay of the compound nucleus to all possible states. The J_π distribution used is shown in Fig. 5.12.

Once the level scheme is built and the entry state defined, the deexcitation of the nucleus is governed by the γ -ray strength function (γSF), where a generalized Lorentzian of the form of Kopecky and Uhl [45] (Sec. 2.4.2.4) was adopted. As RAINIER is a Monte Carlo code, for each excitation energy component, 10 or 20 realizations of 1000 cascades were calculated for the ^{74}Se and ^{83}Rb compound nucleus, respectively.

5.5.2 GEANT4 Simulations

The γ rays obtained by the deexcitation of each contributing E_x of the compound nucleus through RAINIER were then input in GEANT4 simulations [209] to account for the detector's response function. An example of TAS, SoS and multiplicity spectra obtained from GEANT4 for the decay a ^{83}Rb compound nucleus at an $E_x = 8$ MeV is shown in Fig. 5.13.

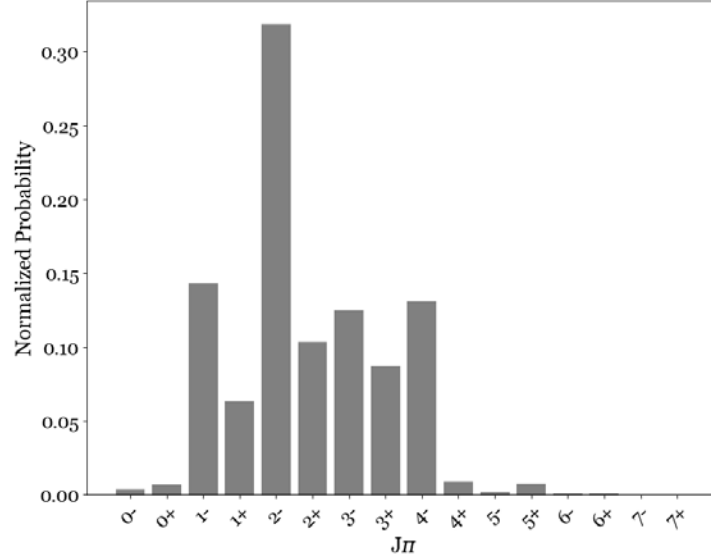


Figure 5.12 The J_{π} distribution of populated excitation energies in the ^{74}Se compound nucleus, calculated using TALYS .

5.5.3 Chi-Square Minimization

The last step is to determine the contribution of each possible excitation energy in the experimental spectra. For this purpose, a χ^2 minimization algorithm was implemented [210]. The χ^2 code uses the simulated TAS, SoS, and multiplicity spectra, along with the experimental spectra gated on the sum peak, to minimize the following global χ^2 value

$$\chi_{\text{global}}^2 = \sum_i \sum_j \left(\frac{C_{\text{exp}}^{ij} - \sum_k f_k C_{\text{sim}}^{ij}}{\sqrt{C_{\text{exp}}^{ij}}} \right)^2 \quad (5.7)$$

where the summations are over i types of histograms (TAS, SoS and multiplicity) and j number of bins in the i -th histogram. C_{exp}^{ij} and C_{sim}^{ij} are the counts of the j -th bin in the i -th experimental or simulated histogram respectively [210]. The simulated histograms are summed over the k different components contributing in the spectra, with f_k their respective scaling factor. The code utilizes the MINUIT algorithm [211] from the ROOT data analysis toolkit [212], to assign values to the f_k factors until the minimum global χ^2 is achieved.

Eq. 5.7 assumes that the error in C_{exp}^{ij} is equal to its square root, which is a valid assumption for spectra that do not carry uncertainty from subtractions. However, in the case of ^{73}As , the error was dominated by statistical uncertainty from the background subtractions (Sec. 5.3.4). Therefore, for

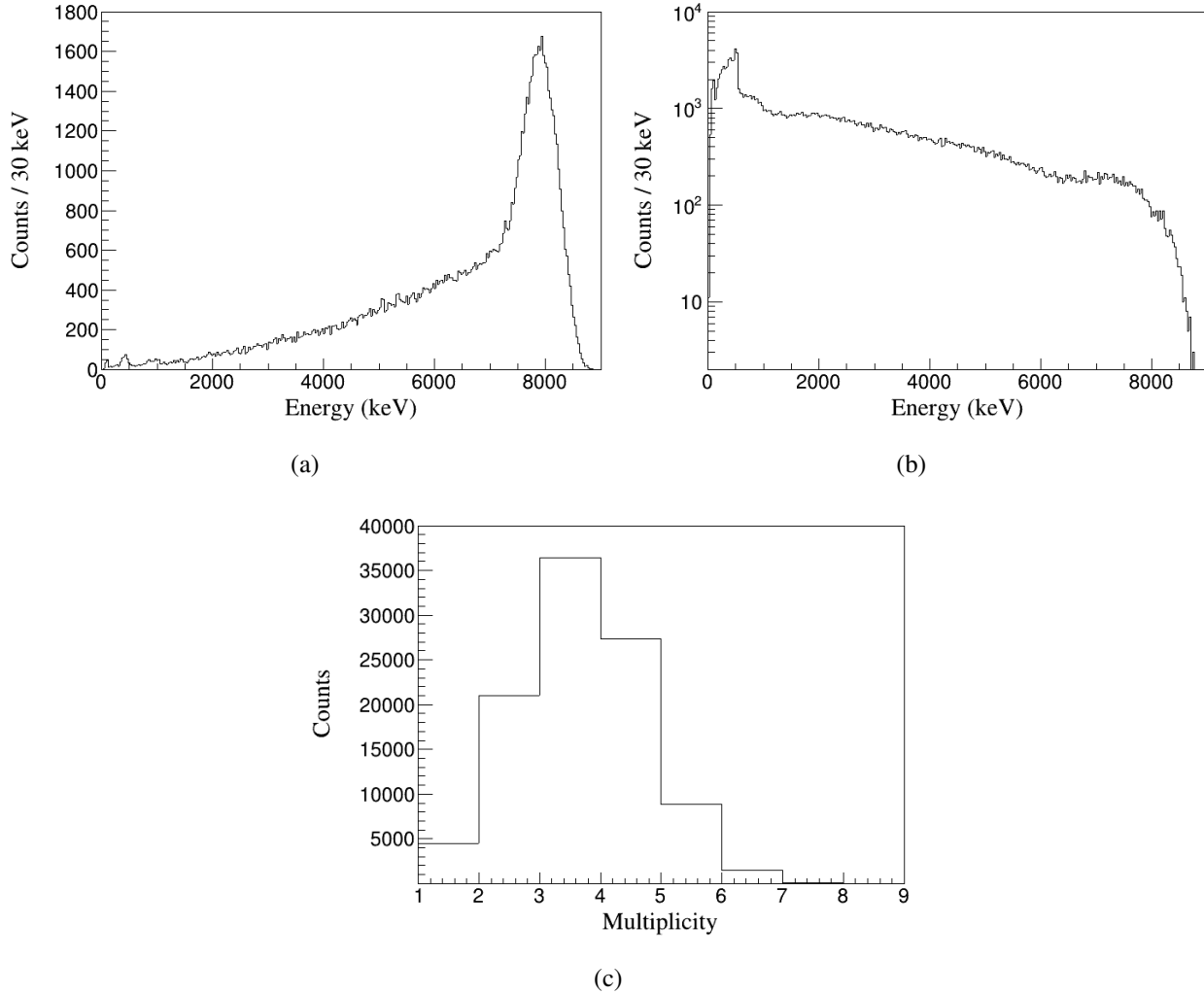


Figure 5.13 Simulated (a) TAS, (b) SoS and (c) multiplicity spectra of a $E_x = 8$ MeV ^{83}Rb state decay using GEANT4.

the ^{73}As analysis, the denominator in Eq. 5.7 was replaced with the statistical uncertainty shown in Fig. 5.10 for each bin.

The detection efficiency is inherently accounted for in the GEANT4 simulations, as the detector's material and geometry are included in the model. Therefore, from the χ^2 minimization output, the efficiency can be extracted in the form of a ratio Y/ϵ , where Y is the experimental yield. In more detail, based on Eq. 5.7, the χ^2 code calculates scaling factors to match the integral of the sum peak with a weighted linear combination of the simulated spectra. For example, consider a sum peak with 100 counts, where two energies contribute to the peak with weights of 60% and 40%. For 10 000 simulated events at each energy, the scaling factors would be 0.006 and 0.004

respectively, so that $0.006 \cdot 10\,000 + 0.004 \cdot 10\,000 = 100$ counts. However, if the detector had a 50% intrinsic efficiency, only 5 000 of the 10 000 simulated events would contribute to the sum peak. In that case, the factors would be 0.012 ($= 0.006/0.5$) and 0.008 ($= 0.004/0.5$), so that $(0.012 \cdot 10\,000 + 0.008 \cdot 10\,000) \times 0.5 = 100$ counts.

Based on the example, the efficiency-corrected yield Y/ϵ , can be expressed as the product of the sum of all scaling factors and the number of simulated events as

$$\frac{Y}{\epsilon} = \sum_k f_k \cdot N_{\text{sim}} \quad (5.8)$$

where f_k represents the scaling factor of the k -th energy contributing to the peak as calculated through Eq. 5.7, and N_{sim} the number of simulated events for each energy.

The number of E_x components simulated for each case reflects the resolution of the sum peak. For ^{83}Rb where the sum peak has significant statistics, ~ 20 energy components were simulated, one every 100 keV. For the case of ^{74}Se , where the statistics are small and large energy binning was required (Fig. 5.10), only 5 energy components were simulated, one for every 400 keV. Simulating more than 5 components, accounting for the statistical uncertainty of the spectra, resulted in the minimizer not properly converging.

The segmentation of SuN allows to extract valuable information on the statistical properties of the compound nucleus. Specifically, the choice of NLD and γ SF model parameters that are input in RAINIER, significantly affects the γ rays that can be emitted through the deexcitation of a nuclear level in the continuum. This dependence is mostly apparent in the shape of the SoS spectra, and as discussed in detail in the next section, it allowed for the development of an analysis method to constrain the products of NLD and γ SF used in statistical model calculations, and provide predictions for the cross section in a much larger energy range than the experimentally measured.

5.6 Theoretical Investigation with RAINIER and TALYS

The shape of the SoS spectrum depends on the product of the NLD and γ SF. The theoretical models for the NLD (Sec. 2.4.2.3) and γ SF (Se. 2.4.2.4) include multiple adjustable parameters. The default parameters for the constant temperature (CT) and back-shifted Fermi gas (BSFG) models

for the NLD, as well as the Generalized Lorentzian for the γ SF found in literature [74, 213, 62], do not appear to reproduce the shape of the SoS spectra, as shown in Fig.5.14. In particular, the

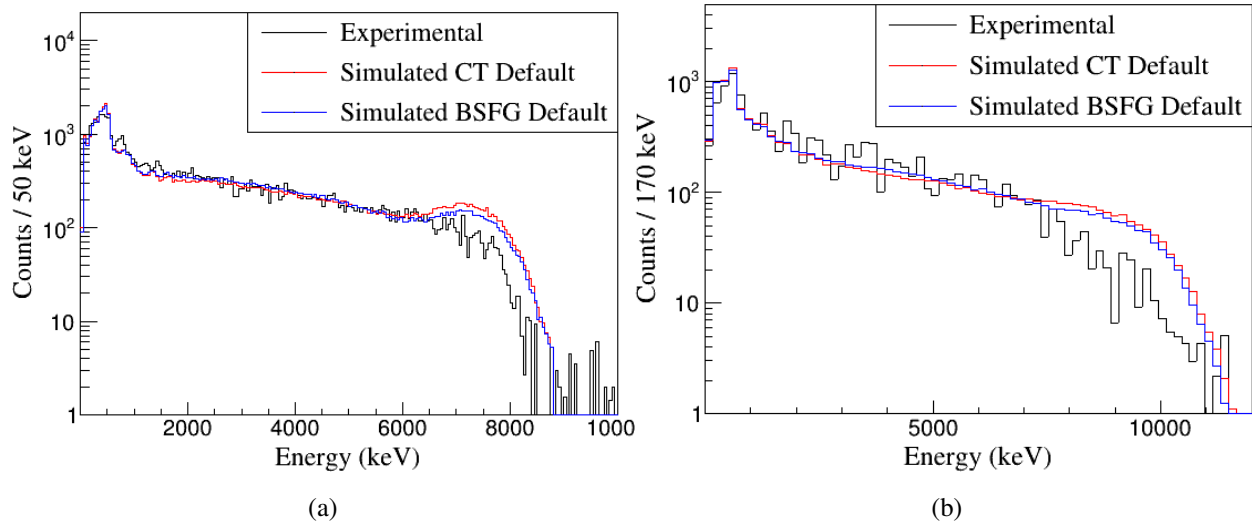


Figure 5.14 The χ^2 minimization SoS fits for the (a) $^{82}\text{Kr}(p, \gamma)^{83}\text{Rb}$ and (b) $^{73}\text{As}(p, \gamma)^{74}\text{Se}$ reactions at initial beam energy 3.7 MeV/u. The black lines are the experimental spectra and the red and blue lines correspond to the default initial parameters of the BSFG and CT model NLD from Ref. [213] and γ SF from Ref. [45, 62]. (Figure (a) adapted with permission from Tsantiri *et al.*, Phys. Rev. C 107, 035808 2023. Copyright 2023 by the American Physical Society)

simulations overestimate high-energy γ rays while, in the case of ^{83}Rb , underestimating low-energy ones. These discrepancies could stem from several factors. One possibility is that, for the same γ SF, a higher NLD is needed to reproduce the spectra. In that case, instead of emitting fewer high-energy γ rays, the compound nucleus would emit multiple lower-energy ones, de-exciting in smaller steps. Alternatively, for the same NLD, the γ SF may assign a lower probability to emitting low-energy γ rays. An enhancement in the lower-energy region of the γ SF could then resolve the discrepancy, especially in the case of ^{83}Rb .

Since this method is sensitive only to the product of the NLD and γ SF, rather than their individual values, this analysis focuses on identifying suitable combinations of these two quantities that reproduce the experimental spectra, and not absolute values for the two quantities independently.

5.6.1 Constraining the Statistical Properties of ^{83}Rb

For the ^{82}Kr analysis, five NLD and γSF combinations were identified as listed in Table 5.4. The first two rows show the literature values for default parameters shown in Fig. 5.14(a). In the first three combinations, the NLD is modified using different parameterizations of the CT and BSFG models (Eqs. 2.17 and 2.15), while the γSF follows the Generalized Lorentzian model of Kopecky and Uhl [45]. Specifically combination number 2 includes CT parameters obtained from Ref. [214]. In the last two combinations the NLD is considered to follow the default BSFG model parameters, while an upbend in the M1 strength function was implemented, following Eq. 2.20. In combination number 4 the upbend follows data from Ref. [215]. Simulations using those five different combinations create the bands shown in Fig. 5.15 for the TAS, SoS, and multiplicity spectra.

Table 5.4 Parameters for modeling the NLD and γSF of the ^{83}Rb nucleus. The default parameters in the first two rows are shown in Fig. 5.14(a) with a red and blue lines. The rest of the parameters were chosen for the calculation of the ratio Y/ϵ , and form the band shown in Fig. 5.15. See text for details on parameters. (Table with permission from Tsantiri *et al.*, Phys. Rev. C 107, 035808 2023. Copyright 2023 by the American Physical Society)

NLD Model	NLD Model Details	Upbend in γSF
CT default	$T = 0.824$ $E_0 = -1.16$ [213]	No
BSFG default	$\alpha = 10.17$ $\Delta = -0.54$ [213]	No
1. CT	$T = 0.824$ $E_0 = -2.2$	No
2. CT	$T = 0.861$ $E_0 = -3.34$ [214]	No
3. BSFG	$\alpha = 10.17$ $\Delta = -1.6$	No
4. BSFG	$\alpha = 10.17$ $\Delta = -0.54$	$a = 1.5$ $c = 8.7 \times 10^{-8}$ [215]
5. BSFG	$\alpha = 10.17$ $\Delta = -0.54$	$a = 1.0$ $c = 1.0 \times 10^{-7}$

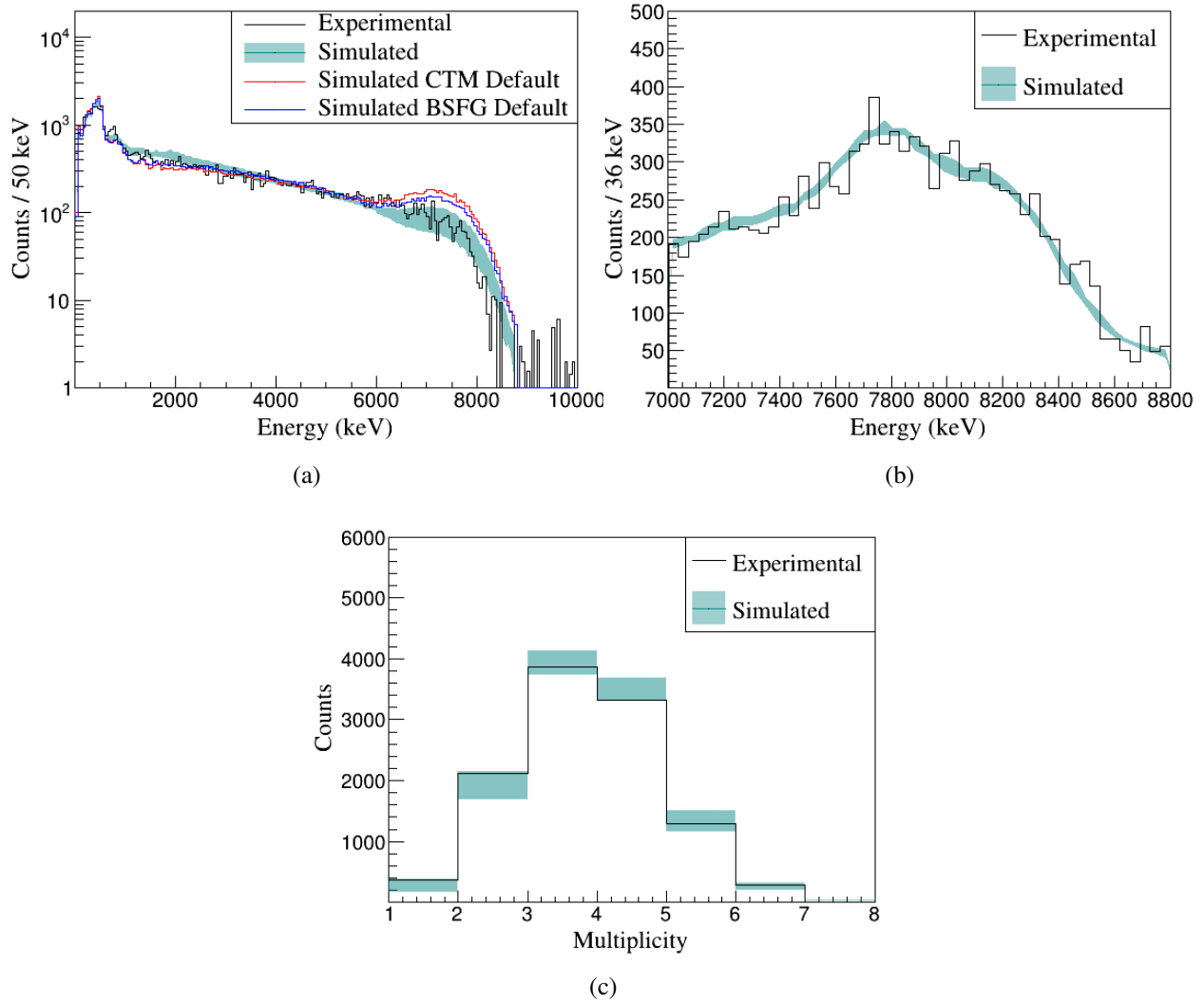


Figure 5.15 The χ^2 minimization fits for the SoS (a), TAS (b) and multiplicity (c) for the $^{82}\text{Kr}(p,\gamma)^{83}\text{Rb}$ reaction at an initial beam energy 3.7 MeV/nucleon. The black lines are the experimental spectra and the light blue bands indicate the simulated spectra for the combinations of the NLD and γ SF models listed in Table 5.4. In (a) the red and blue lines are the same as in Fig. 5.14(a). (Figure adapted with permission from Tsantiri *et al.*, Phys. Rev. C 107, 035808 2023. Copyright 2023 by the American Physical Society)

5.6.2 Constraining the Statistical Properties of ^{74}Se

There are infinite possible combinations of NLD and γ SF that produce the same transmission coefficient (Eq.2.13). In the previous section, only five suitable combinations were identified. Given the large number of free parameters in this problem, the ^{74}Se analysis aimed not just to find a set of possible solutions, but to systematically characterize the different model combinations available in TALYS. As seen in Fig. 3.9, the variations in NLD, γ SF and p OMP result in a cross-section

uncertainty of a factor of six at a center-of-mass energy of approximately 3 MeV, which is the energy region relevant for the production of ^{74}Se in the γ process. Thus, aside from extracting the detection efficiency, the goal of this analysis was to identify suitable NLD and γ SF combinations within the available TALYS models, in an attempt to constrain the cross section of the reaction even further.

As shown in Tables 2.1 and 2.2, there are six models available to describe the NLD, nine for the $E1$ SF, three for the $M1$, and an option to include an $M1$ upbend or not. This produces 324 possible combinations. Additionally, there two main models for the p OMP (Sec. 2.4.2.5), and while fitting the experimental spectra is only sensitive to the NLD and γ SF, these will be included in reproducing the experimental cross section in the next chapter, resulting in 648 total possible combinations. TALYS is able to output the NLD and γ SF used in each calculation, and therefore those tables were directly input in RAINIER.

The ability of each TALYS model to reproduce the experimental data can be expressed by adapting the concept of a *likelihood function* from Bayesian analysis [216] as

$$P(Y|m) \propto \exp \left[- \sum_j^N \frac{(y_j - f_m(x_j))^2}{2\sigma_j^2} \right] \quad (5.9)$$

where $P(Y|m)$ represents the likelihood of model m to reproduce the data Y , the summation goes over the N data-points y_j of the dataset Y , σ_j is the uncertainty of y_j , and $f_m(x_j)$ is the prediction of model m at value x_j . This is often expressed in terms of the log-likelihood $\log P(Y|m)$.

The log-likelihood was applied in this analysis as

$$\log P(Y|m) \propto - \sum_j^{Nbins} \frac{(C_{\text{exp}}^j - \sum_k f_k C_{\text{sim}}^j(m))^2}{2\sigma_j^2} = -\frac{\chi^2}{2} \quad (5.10)$$

where for each TALYS model m , the three histograms Y (TAS, SoS, and multiplicity) were compared with the simulated ones on a bin-by-bin basis. The values C_{exp}^j were the experimental counts per bin j and σ_j was the corresponding statistical uncertainty from the background subtraction. The simulated histograms, as described in Sec. 5.5.3, were a linear combination of all energy components weighted by f_k as calculated in Eq. 5.7. As each of the three types of histograms is treated individually the first summation of Eq. 5.7 is omitted.

A few things should be considered in this analysis. Firstly, treating the TAS, SoS and multiplicity spectra independently is an assumption. A more accurate approach would require including correlations between them, but this is beyond the scope of this thesis. Additionally, the log-likelihood obtained for each of the three types of spectra was normalized to the number of data points (bins) in the respective spectrum, N_{bins} . This normalization ensures that each type of spectrum contributes equally to the overall likelihood, independently of how many bins it contains [217]. The “score” derived by the modified log-likelihood for each type of spectrum is

$$\text{Score} = \exp\left(\frac{\log P}{N_{\text{bins}}}\right) = \exp\left(-\frac{\chi^2}{2N_{\text{bins}}}\right) \quad (5.11)$$

The simulated spectra obtained from the various TALYS model combinations for initial beam energy of 3.7 MeV/u, are shown in Fig. 5.16, color-coded based on their score, $\exp(\log P/N_{\text{bins}})$. For the 3.1 MeV/u datapoint, due to the low statistics, the Y/ϵ was extracted using the NLD and γ SF model combination that produces the lowest χ^2 for the 3.7 MeV/u data. No further investigation was performed for that energy.

5.7 Uncertainty Quantification

The following describes the uncertainties that contribute to the cross-section calculation for all the quantities discussed in the previous sections.

The uncertainty in the effective energy E_{eff} is mainly attributed to energy straggling as the beam passes through the Mo foil and hydrogen gas. The beam’s energy distribution was calculated using SRIM[218]. Fig 5.17 shows an example distribution for ^{73}As at an initial beam energy of 3.7 MeV/u. The blue distribution represents the energy straggling after the 2- μm -thick Mo entrance window, while the red corresponds to the energy at the end of the 4-cm-long gas cell filled with 600 torr of hydrogen. The mean of each distribution was used as E_0 and $E_0 - \Delta E$ in Eq. 5.3. The upper and lower uncertainties in E_{eff} were determined using the maximum and mean- 3σ of each distribution, respectively. Due to the asymmetrical energy straggling distribution, which has a long low-energy tail, the errors in the effective energy are similarly asymmetric. An additional 1% uncertainty was included to reflect the uncertainty in the delivered beam by the facility.

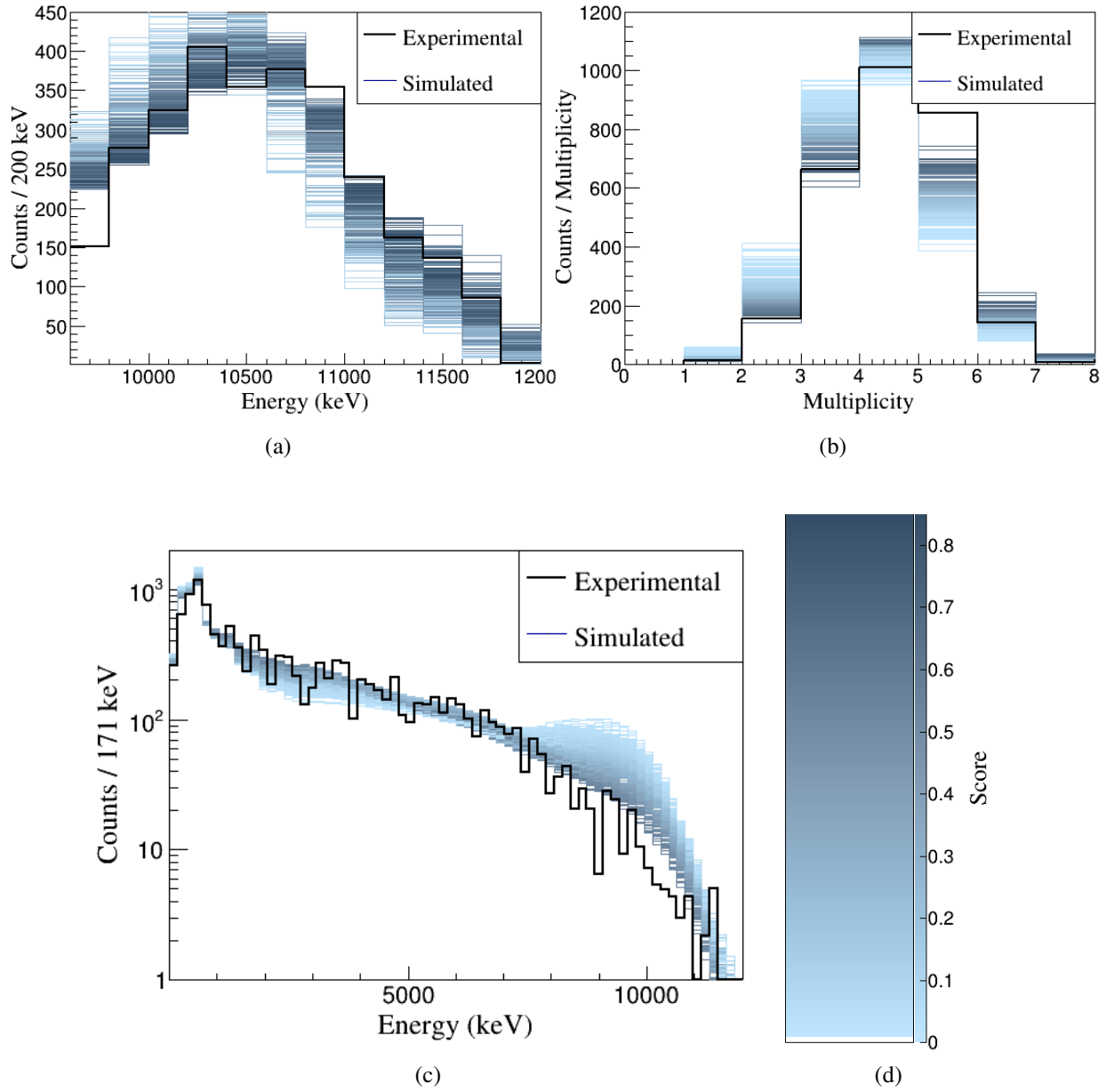


Figure 5.16 The χ^2 minimization fits for the TAS (a), multiplicity (b), and SoS (c) for the $^{73}\text{As}(p,\gamma)^{74}\text{Se}$ reaction at an initial beam energy 3.7 MeV/nucleon. The black lines represent the experimental spectra and the various blue lines correspond to the simulated spectra for the combinations of the NLD and γ SF models from TALYS. The varying shades of blue in each line reflect different scores from Eq. 5.11. Darker tones represent higher scores, as shown by the color bar (d).

The uncertainty in the total number of beam particles I_α (Sec. 5.2) in the ^{82}Kr measurement was considered to be 5% from the beam-charge accumulation. For the ^{73}As measurement in addition to the 5% uncertainty for the ammeter measurement, there were two methods used for the

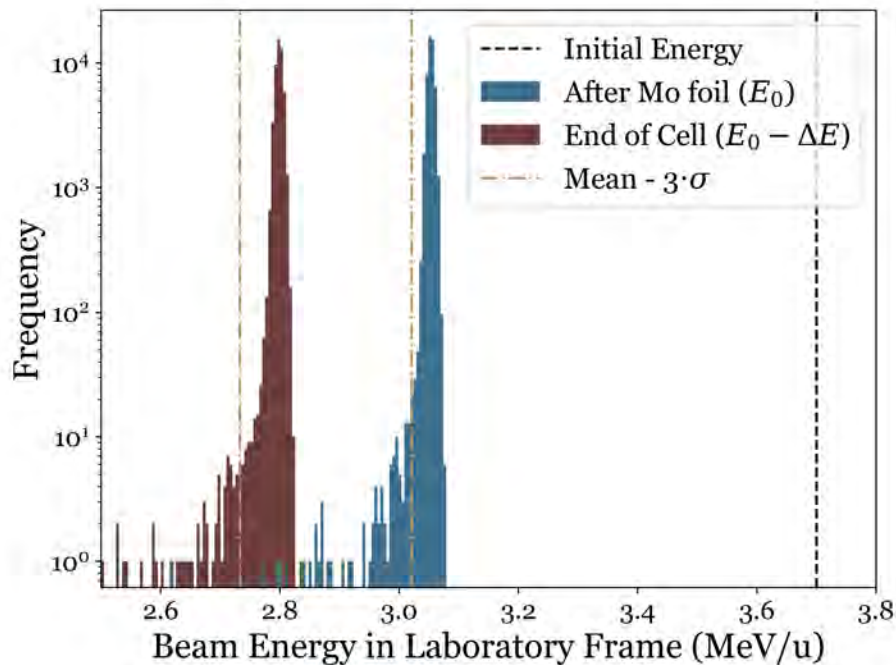


Figure 5.17 Beam energy distributions calculated using SRIM for ^{73}As at an initial beam energy of 3.7 MeV/u. The blue distribution represents the beam energy after the Mo entrance window, and the red to energy at the end of the cell. The mean of each distribution was used to calculate the effective energy, while the maximum and mean- 3σ values determined the upper and lower uncertainty, respectively.

integration of the current shown in Fig. 5.2, introducing an additional 2% uncertainty, as well as a 6% uncertainty from the baseline fits. Overall the uncertainty in the beam current for the ^{73}As measurement was 8.3%.

The target particle density N_t was considered to carry an uncertainty of 5%. This includes systematic uncertainty from the calibration of the manometer to the atmospheric pressure and the zero offset, as well as the random error from the instrument resolution.

The uncertainty in the Y/ϵ for the ^{82}Kr measurement includes statistical uncertainty varying between 1% and 4%, along with uncertainty from the various parameters chosen for the NLD and γSF models varying between 26% and 17%, with the latter value corresponding to the smaller energy. For the ^{73}As measurement the uncertainty is dominated by the statistical uncertainty from the background subtraction varying between 18% and 72%, for the larger and smaller beam energies, respectively. An additional 6% uncertainty was assumed for the 3σ deviation of the scaling factors

distribution for the empty cell measurement (Fig. 5.9(b)). Finally the various TALYS combinations produced a range of Y/ϵ values. In Fig. 5.18, for the 3.7 MeV/u measurement, the various Y/ϵ values produced by all the different fits are shown compared to their total fitting score, defined as the product of all three scores from Eq. 5.11. The higher scores that reproduce the best fits, converge near $Y/\epsilon \approx 6000$. By weighing each Y/ϵ with the score of the corresponding model, the distribution shown in Fig. 5.19 was obtained. An uncertainty of 13.5% was obtained from the 3σ deviation of that distribution. The overall uncertainty for Y/ϵ of the ^{73}As measurement was 24% and 74% for the 3.7 and 3.1 MeV/u beam energies.

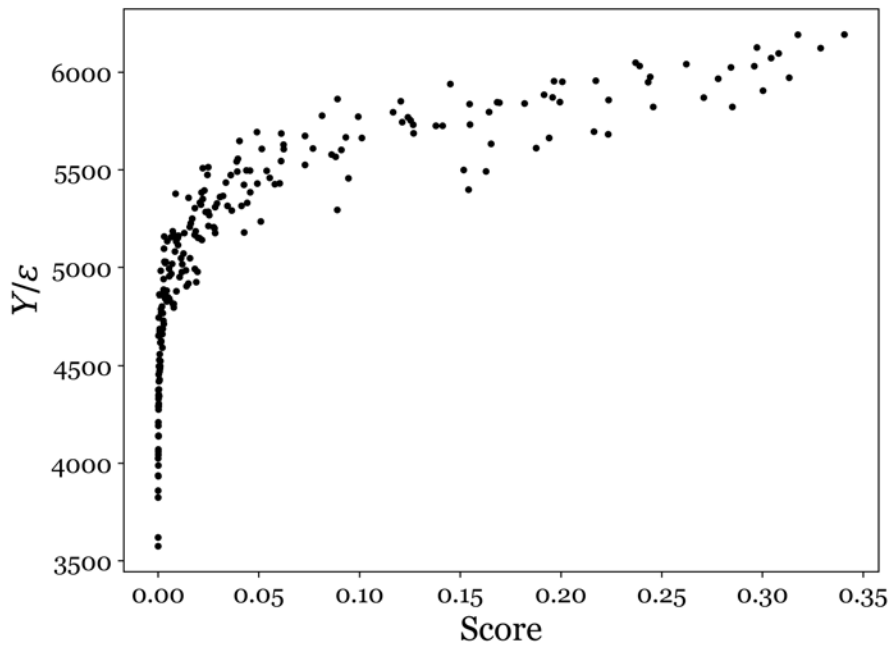


Figure 5.18 The Y/ϵ values produced using the various available TALYS combinations of NLD and γ SF compared to the fitting score, defined as the product of all three $\exp(\log P/N_{\text{bins}})$ for the three types of histograms (TAS, SoS and multiplicity). The fits with the highest score converge around $Y/\epsilon \approx 6000$.

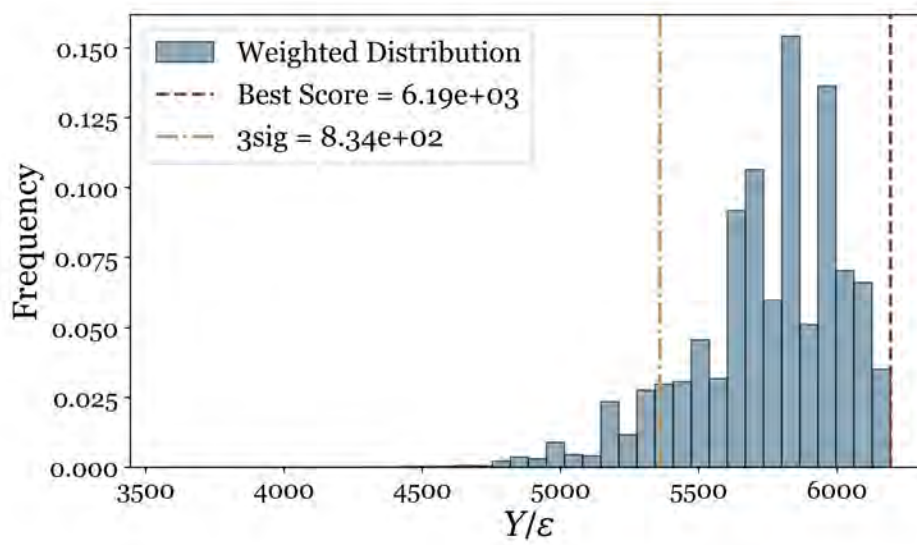


Figure 5.19 The distribution of Y/ϵ values shown in Fig. 5.18 weighted by their respective score. The value of Y/ϵ used in the analysis was obtained from the best fit (dashed line), and the 3σ uncertainty of the distribution was assumed as model uncertainty for this measurement (dot-dashed line).

CHAPTER 6

RESULTS & DISCUSSION

6.1 The $^{82}\text{Kr}(p, \gamma)^{83}\text{Rb}$ cross section

The cross section for the $^{82}\text{Kr}(p, \gamma)^{83}\text{Rb}$ reaction as calculated using Eq. 5.1 is presented in Table 6.1 along with all calculated quantities described in Ch. 5. In Fig. 6.1 the cross section is shown along with statistical model calculations using the NON-SMOKER code [174] and TALYS, for all available NLD and γ SF models.

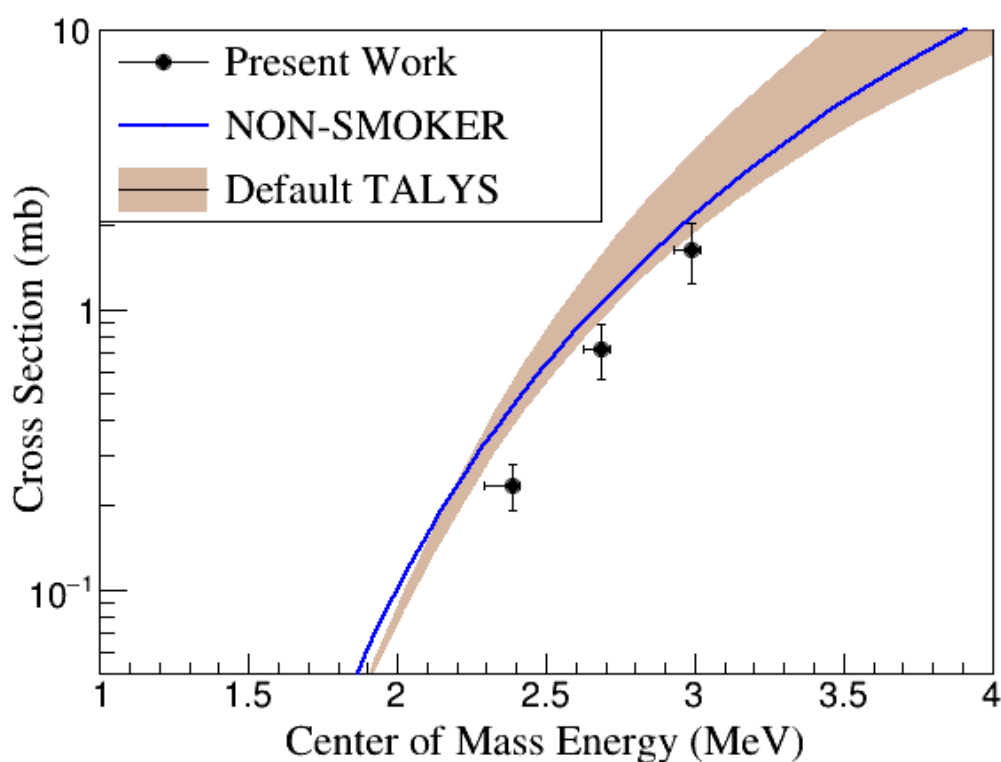


Figure 6.1 The measured cross section of the $^{82}\text{Kr}(p, \gamma)^{83}\text{Rb}$ reaction (black dots) compared with standard NON-SMOKER theoretical calculations [174] (blue solid line) and default TALYS 1.96 calculations [62] (orange band). (Figure with permission from Tsantiri et al, Phys. Rev. C 107, 035808 2023. Copyright 2023 by the American Physical Society)

Table 6.1 Measured cross section of the $^{82}\text{Kr}(p, \gamma)^{83}\text{Rb}$ reaction. The first column represents the initial beam energy in the lab system, the second column the center-of-mass effective energy of the reaction, and the third shows the total number of incident beam particles on target. The fourth and fifth columns represents the total number of incident and target particles, and the sixth the total number of reactions that occurred Y/ϵ . The last two columns represent the efficiency in detecting γ -rays from the de-excitation of the ^{83}Rb compound nucleus, and the measured cross section. (Table with permission from Tsantiri *et al.*, Phys. Rev. C 107, 035808 2023. Copyright 2023 by the American Physical Society)

Initial Beam Energy (MeV/u)	Effective Energy E_{eff} (MeV)	Total Incident Particles I_α	Total Target Particles N_t	Number of Reactions Y/ϵ	Efficiency ϵ (%)	Cross Section σ (mb)
3.7	$2.99^{+0.03}_{-0.06}$	$(2.15 \pm 0.11) \times 10^{11}$	$(7.44 \pm 0.39) \times 10^{19}$	26079 ± 6707	51.6 ± 5.6	1.63 ± 0.40
3.4	$2.68^{+0.03}_{-0.06}$	$(2.05 \pm 0.10) \times 10^{11}$	$(7.43 \pm 0.39) \times 10^{19}$	11011 ± 2460	51.3 ± 5.7	0.72 ± 0.16
3.1	$2.38^{+0.02}_{-0.09}$	$(2.07 \pm 0.10) \times 10^{11}$	$(7.39 \pm 0.39) \times 10^{19}$	3578 ± 595	52.6 ± 6.0	0.23 ± 0.04

The comparison in Fig. 6.1 shows that standard statistical model calculations with default model parameters generally overestimate the cross section for the $^{82}\text{Kr}(p, \gamma)^{83}\text{Rb}$ reaction relative to the experimental measurements. The discrepancies between the experimental data and predictions from the NON-SMOKER code range from 23% to 47%, with the largest deviation observed at the lowest beam energy. A similar trend has been reported by Lotay *et al.* [173] for the (p, γ) reaction on the neighboring ^{83}Rb nucleus, as well as by Gyürky *et al.* [219] on various proton-rich Sr isotopes. In both instances, the experimental cross sections were systematically lower than those predicted by the Hauser-Feshbach (HF) theory, indicating the existence of a trend in this mass region.

This substantial overestimation by theoretical models motivated further investigation on the model parameters used in TALYS. As discussed in Sec. 5.6.1, specific parameters were identified to model the NLD and γ SF of the ^{83}Rb nucleus (Table 5.4). These parameters were selected to reproduce the experimental spectra, and therefore, should provide a more accurate representation of the calculated cross section. Interestingly, the various combinations of NLD and γ SF primarily impact the upper range of the calculated $^{82}\text{Kr}(p, \gamma)^{83}\text{Rb}$ cross sections, while the lower energy range near the 3.1 MeV/u measurement appears to not be as sensitive. Consequently, a better description could be obtained by modifying other input quantities in TALYS.

As discussed in Sec. 2.4.2.2, the cross section in the statistical model includes the transmission coefficients T_a^X and T_b^Y between the $X + a$ entrance and $Y + b$ exit channel, and the width fluctuation correction $W^{aX \rightarrow Yb}$ (WFC). At the low energies examined in this experiment, the only available exit channels are the proton and γ emission. The neutron channel opens just above 5 MeV, and the α channel remains negligible throughout the energy range under study, due to the higher Coulomb barrier. Therefore in this case, Eq. 2.12 simplifies to

$$\sigma(p, \gamma) \sim \frac{T_p T_\gamma}{T_p + T_\gamma} W^{p\gamma} \quad (6.1)$$

where the T_p corresponds to the proton capture and T_γ to the γ decay. It is significant to examine the competition between the available open channels. Fig. 6.2 shows a decomposition of the total reaction cross section into the different exit channels, expressed in terms of astrophysical S factor

(Sec. 2.5), for better readability. The dashed lines in Fig. 6.2 correspond to a TALYS calculation

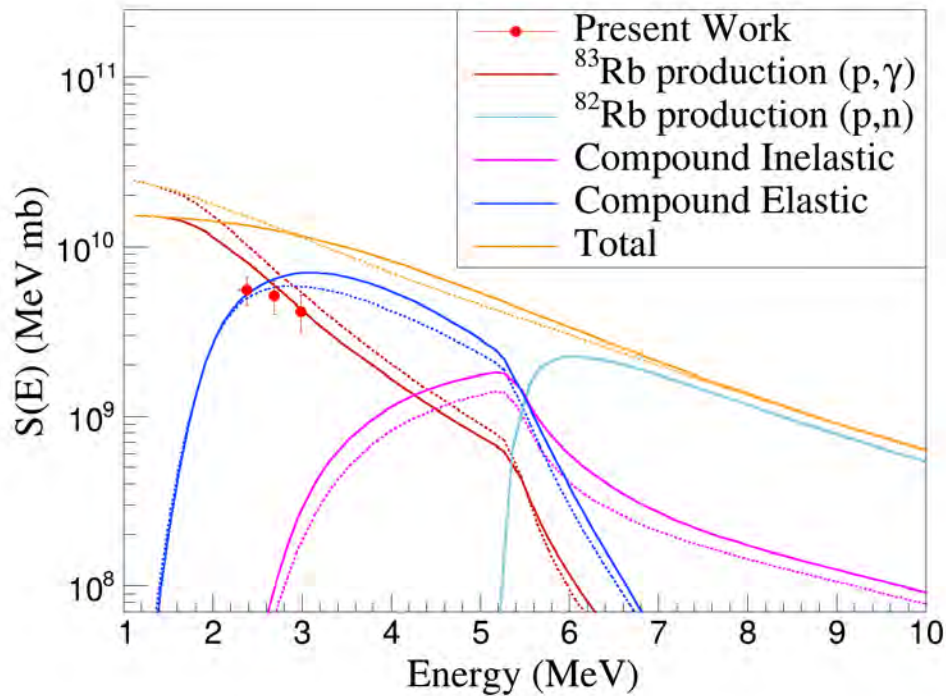


Figure 6.2 Decomposition of the astrophysical S factor for proton capture on ^{82}Kr . Dashed lines correspond to a standard TALYS calculation, while solid lines use an optimized set of parameters. See text for more details on the optimized parameters. The contribution of the $^{82}\text{Kr}(p,\alpha)^{79}\text{Br}$ reaction is below the scale of the figure. (Figure adapted with permission from Tsantiri *et al.*, Phys. Rev. C 107, 035808 2023. Copyright 2023 by the American Physical Society)

using the NLD and γ SF parameter set No.5 from Table 5.4. Since these models are fixed, the cross section remains dependent only to the T_p , meaning the proton optical model potential (p OMP), as well as the WFC. As discussed in Sec. 2.4.2.5, another option provided in TALYS for the description of the p OMP is the “jlm-type” potential, based on the work of Jeukenne, Lejeunne, and Mahaux [64, 65, 66, 67] with later modifications by Bauge *et al.* [68, 69]). This potential predicts a slightly lower cross section at lower energies, providing a better agreement with the experimental data.

The WFC accounts for correlations between the incident and outgoing wave functions, which typically enhance the compound-elastic channel. The WFC becomes most significant when only a few channels are open, which is the case for lower energies. At higher energies, where many channels are accessible, the relevance of the WFC becomes negligible. The default WFC used in TALYS is based on Moldauer’s formalism [76, 77] (`widthmode 1`). An alternative approach is

that of Hofmann, Richert, Tepel, and Weidenmüller (HRTW, widthmode 2) [78, 79, 80]. This approach provides a stronger correction, enhancing the compound-elastic channel and reducing the calculated (p, γ) cross section.

Combining a HWRT-based WFC with a “jlm-type” potential yields the solid lines in Fig. 6.2, showing an improved agreement with the experimental data, particularly at lower energies. This combination along with the different NLD and γ SF models of Table 5.4 produce the teal band in Fig. 6.3.

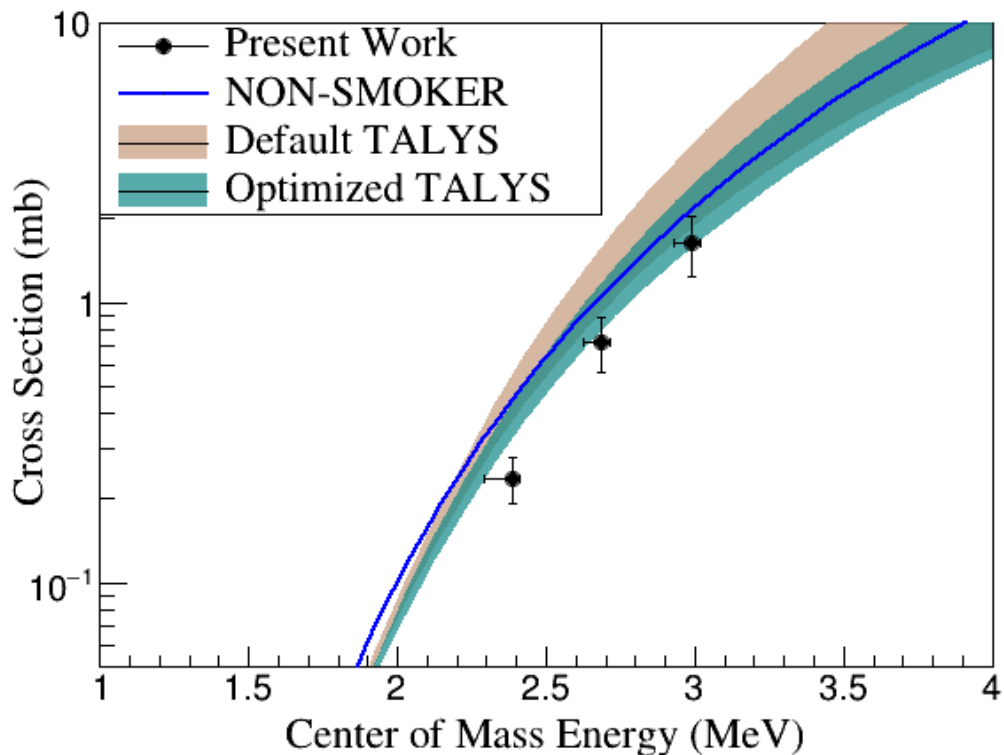


Figure 6.3 Same as Fig. 6.1, with the addition of the optimized TALYS band, resulting from the NLD and γ SF combinations of Table 6.1 along with a HWRT-based WFC and a “jlm-type” potential. (Figure with permission from Tsantiri *et al.*, Phys. Rev. C 107, 035808 2023. Copyright 2023 by the American Physical Society)

This result demonstrates the successful proof-of-principle implementation of the summing technique in inverse kinematics using this experimental setup and a gas cell target for the measurement of (p, γ) reactions. Additionally, this study shows that a consistent description of the cross section, SoS, TAS, and multiplicity spectra can be achieved through a careful choice of parameters in the

statistical model. The ability to simultaneously describe multiple observables provides stronger constraints on the model parameters than a comparison with cross-section data alone, enabling a more constrained cross section over a broader energy range than the one directly measured.

6.2 The $^{73}\text{As}(p, \gamma)^{74}\text{Se}$ cross section

Similarly to the previous section, the cross section for the $^{73}\text{As}(p, \gamma)^{74}\text{Se}$ reaction as calculated using Eq. 5.1 is presented in Table 6.2 along with all calculated quantities. Due to the low statistics of the low-energy data point, the measurement efficiency was assumed to be the value calculated for the 3.7 MeV/u data point for both energies. The asymmetry in the errors of Y/ϵ results from avoiding negative counts in specific bins. In Fig. 6.4 the cross section is shown along with statistical model calculations using the NON-SMOKER code [174] and TALYS, for all available NLD and γ SF models, and the two p OMP options (default and JLM).

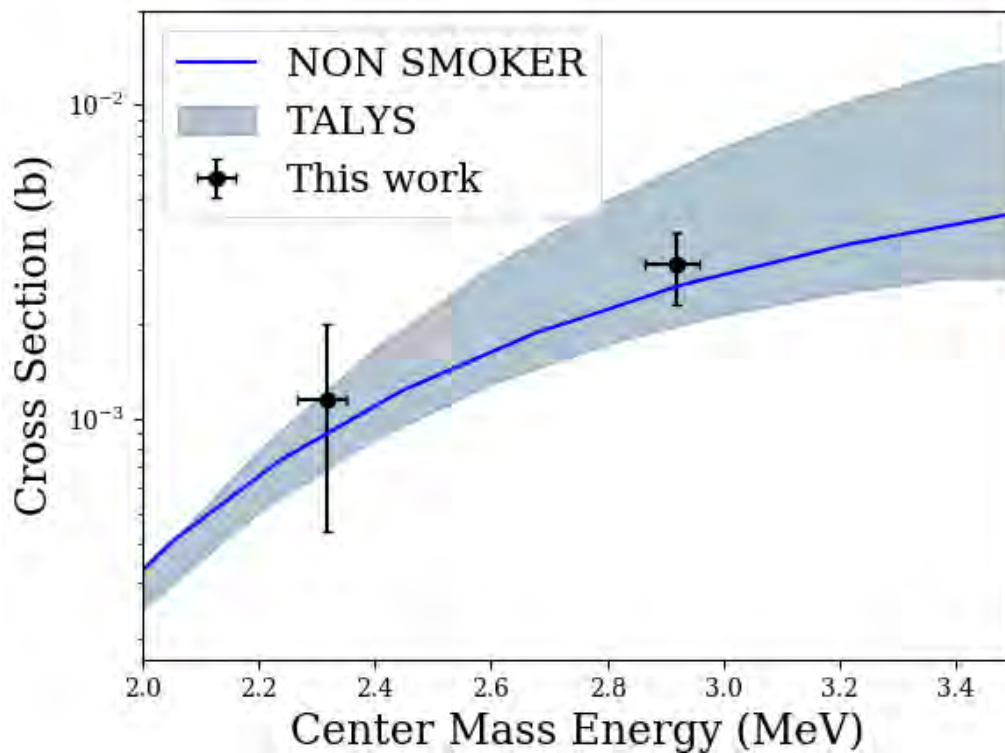


Figure 6.4 The measured cross section of the $^{73}\text{As}(p, \gamma)^{74}\text{Se}$ reaction (black dots) compared with standard NON-SMOKER theoretical calculations [174] shown in a solid line and default TALYS calculations [62] creating a band.

Table 6.2 Same as Table 6.1 for the $^{73}\text{As}(p, \gamma)^{74}\text{Se}$ reaction measurement.

Initial Beam Energy (MeV/u)	Effective Energy E_{eff} (MeV)	Total Incident Particles I_α	Total Target Particles N_t	Number of Reactions Y/ϵ	Efficiency ϵ (%)	Cross Section σ (mb)
3.7	$2.92^{+0.04}_{-0.05}$	$(2.51 \pm 0.21) \times 10^{10}$	$(7.94 \pm 0.40) \times 10^{19}$	6193 ± 1480	48.2 ± 6.5	3.11 ± 0.80
3.1	$2.32^{+0.03}_{-0.05}$	$(1.67 \pm 0.14) \times 10^9$	$(7.94 \pm 0.40) \times 10^{19}$	152^{+112}_{-95}		$1.15^{+0.86}_{-0.73}$

As discussed in the previous chapters, the challenge of running a radioactive beam experiment is apparent from the large statistical uncertainties compared to the stable beam experiment, especially in the case of the low-energy datapoint, as the measurement was limited to just 30 minutes of data acquisition (see Sec. 5.3.4). Nevertheless, this is the first experimental data provided on the $^{73}\text{As}(p, \gamma)^{74}\text{Se}$ reaction cross section, and as the measurement is performed within the Gamow window window for the astrophysical γ process, it is particularly relevant for calculating the production of ^{74}Se . The calculated cross section is in agreement with the theoretical prediction by NON-SMOKER within the experimental uncertainty, however the higher energy measurement is $\sim 18\%$ higher than the NON-SMOKER calculation.

As with the ^{82}Kr analysis, the $^{73}\text{As}(p, \gamma)^{74}\text{Se}$ cross section measured can be combined with the description of the TAS, SoS and multiplicity spectra obtained in Sec. 5.6.2, to provide a constrained TALYS band that can be used in network calculations. For this analysis, only the higher-energy data point will be utilized, as the uncertainty of the low-energy point exceeds that of TALYS.

As shown in Sec. 5.6.2 for each of the various TALYS models, the three different types of spectra (TAS, SoS and multiplicity) have been evaluated by a score described by Eq. 5.11. The calculated cross section from Fig. 6.4 is used to evaluate one last factor that contributes to the score. However, the likelihood as defined in Eq. 5.9, includes only uncertainty on the y-axis, whereas the cross section also includes uncertainty in the effective energy. The uncertainty in the effective energy reflects the energy straggling of the beam in the gas cell and hydrogen gas, and that distribution of energies has been calculated using SRIM (Fig. 5.17). This distribution can be used to weight the energies on the x-axis as shown in Fig. 6.5. The error energy range is divided into 20 bins, and the likelihood is calculated for each one of the bins weighted by its normalized probability distribution as

$$P(\sigma_{\text{exp}}|m) = \exp \left[- \sum_j^{20} w_j \frac{(\sigma_{\text{exp}} - f(E_j, m))^2}{2 \cdot \delta\sigma_{\text{exp}}^2} \right] \quad (6.2)$$

where the summation goes over the 20 energy bins with weight w_j shown in Fig. 6.5, σ_{exp} and $\delta\sigma_{\text{exp}}$ is the experimental cross section with its uncertainty from Table 6.2, and $f(E_j, m)$ is the predicted cross section from TALYS model m at the central energy E_j of each bin. Fig. 6.6(top)

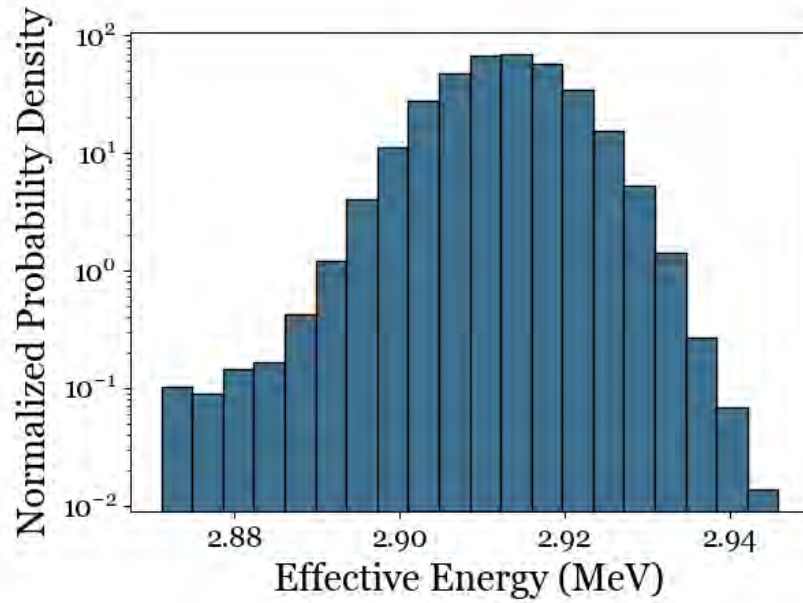


Figure 6.5 The effective energy uncertainty of the $^{73}\text{As}(p, \gamma)^{74}\text{Se}$ reaction as a function of the energy straggling distributions from Fig. 5.17.

shows the calculated cross section with the TALYS models shown in Fig 6.4, color-coded based on the likelihood calculated through Eq. 6.2. Combining this likelihood with the total score for the TAS, SoS and multiplicity spectra from Sec. 5.6.2, produces the combined score shown in Fig. 6.6(bottom). One can observe that this combination leads to a significantly narrower favored cross-section band. A complete table of the scores for all TALYS models is shown in the Appendix. This distribution is used to constrain the production of ^{74}Se in network calculations of the γ process in the following chapter. It can be seen that the favored distribution is located slightly higher than the NON-SMOKER calculation shown in red, which is the reaction adopted in astrophysical calculations, even though this deviation is within the experimental uncertainty. This is consistent with the experimental measurement being $\sim 18\%$ higher than the one calculated by NON-SMOKER.

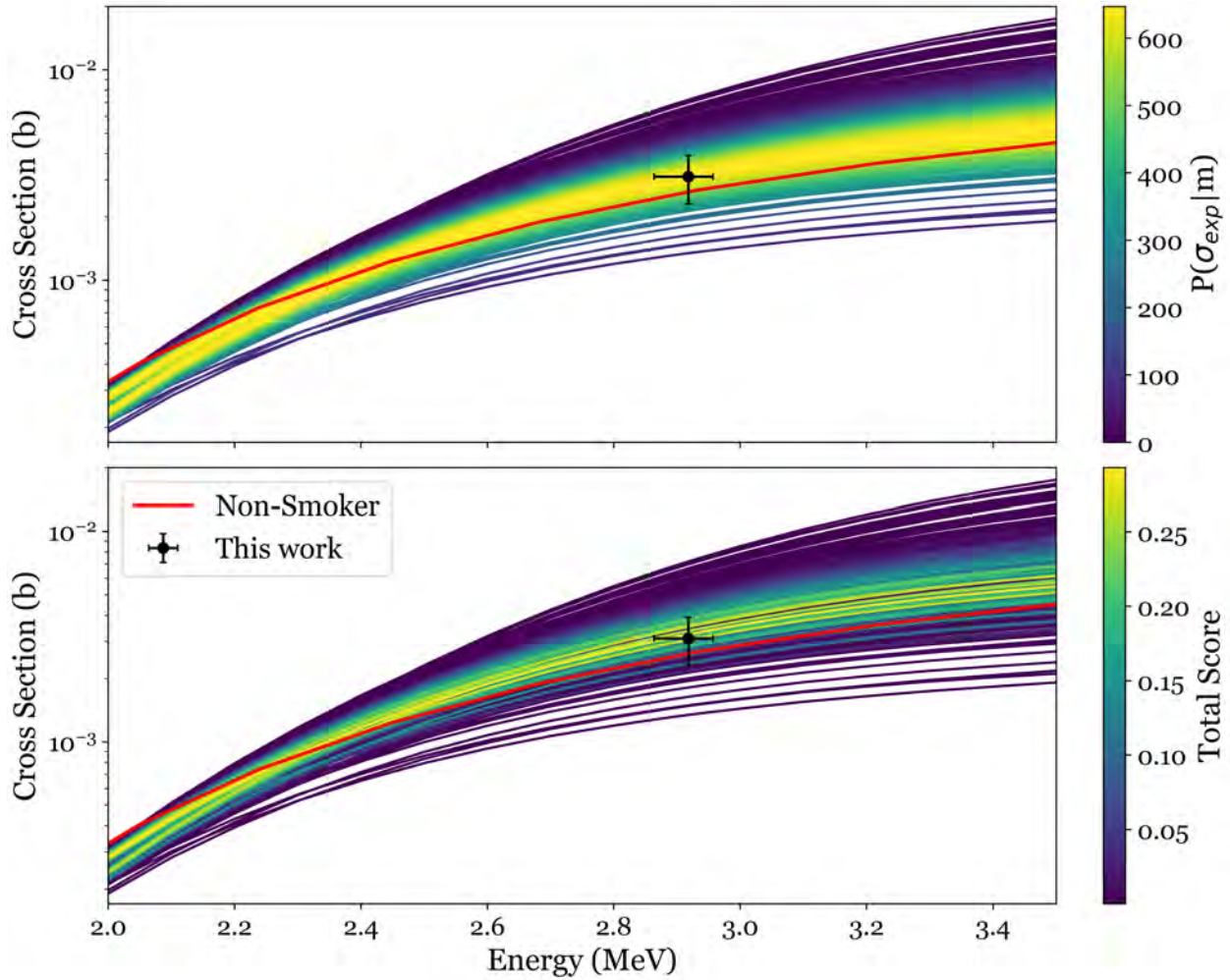


Figure 6.6 The measured cross section of the $^{73}\text{As}(p, \gamma)^{74}\text{Se}$ reaction in the 3.7 MeV/u initial beam energy compared to TALYS calculations color-coded based on (top) the likelihood calculated through Eq. 6.2 and (bottom) the combined score to reproduce all types of data (cross section, TAS, SoS and multiplicity).

CHAPTER 7

ASTROPHYSICAL IMPACT

As discussed in Sec. 3.4.1, the two main explosive environments where the γ process is thought to occur are the oxygen and neon enriched layers of a core-collapse supernovae (SNII) [133, 135, 136], and thermonuclear Type Ia supernovae (SNIa) [137, 138, 139]. The impact of the measured cross section will be examined in both cases using Monte Carlo simulations of both scenarios.

7.1 Core-Collapse Supernova - SNII

For the SNII environment, NuGrid stellar data set II models [142] were used. The most massive progenitors with solar metallicity available in these models were stars with masses of 15, 20, and 25 M_{\odot} , calculated using MESA [157]. The initial solar composition was from Grevesse and Noels [220] with isotopic ratios from Lodders [126], while the nucleosynthesis during stellar evolution and explosion was computed using the Multi-zone Post-Processing Network – Parallel (MPPNP) code [159]. The nuclear network beyond iron consisted of 74 313 reactions, for which experimental rates from the KADoNIS compilation [221] were incorporated wherever available, and any missing reaction rates were obtained from the JINA REACLIB library [222].

Among the three available mass models, the 25 M_{\odot} model ended in a failed supernova due to significant fallback, trapping all the material produced during the explosion in the remnant star. The 15 M_{\odot} model experienced a C-O shell merger event, significantly enhancing the pre-supernova production of p nuclei. Since ^{74}Se is expected to be primarily produced by the explosive component, even in the presence of a C-O shell merger [143], the 20 M_{\odot} model was chosen as a representative case, where the explosive component dominates p -nuclei production, similarly to other SNII models used in γ -process studies [136, 176, 177]. The impact of the measured cross section was expected to be similar for any SNII model reaching comparable peak temperatures during the shock wave propagation.

The produced mass fraction of ^{74}Se as the shock wave propagates through the ONe layer of the star is shown in Fig. 7.1. The maximum production of ^{74}Se occurs in the inner ONe layer, at mass

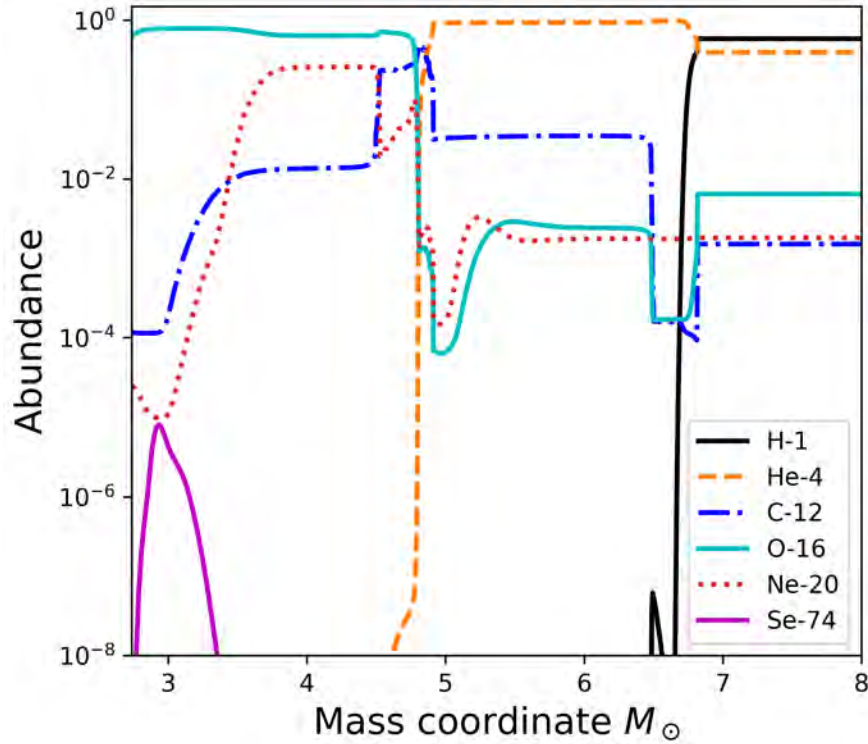


Figure 7.1 The final mass fractions of the $20 M_{\odot}$ mass model by Ritter *et al.* [142] as a function of mass coordinate. The ^{16}O , ^{20}Ne , ^{12}C , ^4He and ^1H lines indicate the different layers of the star. ^{74}Se is produced in the inner ONe layer, where the higher peak temperatures in the Gamow window for the γ process are achieved.

coordinate $M = 2.93M_{\odot}$. At this location, the temperature and density profiles are presented in Fig. 7.2, where the temperature trajectory exhibits a plateau at $T = 3.08$ GK.

To investigate the impact of the measured cross section under such conditions, the cross section predictions of the measured $^{73}\text{As}(p, \gamma)^{74}\text{Se}$ reaction from Fig. 6.6 were converted to reaction rates using TALYS. In Fig. 7.3 the reaction rate of the $^{73}\text{As}(p, \gamma)^{74}\text{Se}$ reaction is shown as a function of temperature, with models color-coded by the total score calculated in Sec. 6.2. The solid red line is the JINA-REA CLIB [222] reaction rate, while the dotted line marks the temperature of interest, $T = 3.08$ GK. A projection of the total scores along the $T = 3.08$ GK temperature is shown in Fig. 7.4, as a function of each model's total score. The various points represent the different TALYS models, and the blue bars are the normalized distribution of those rates grouped in 50 bins, between the minimum and maximum TALYS reaction rate. For Monte Carlo simulations, 10 000 rates were randomly sampled from this distribution, forming the set of rates shown by the magenta

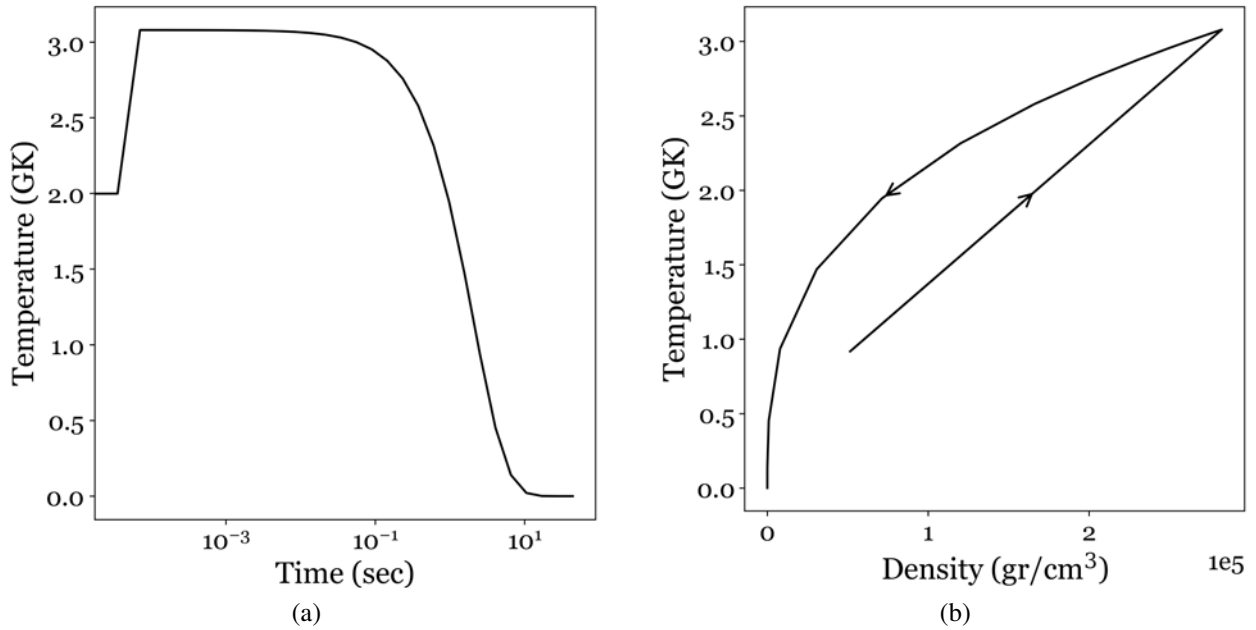


Figure 7.2 The temperature and density trajectories at mass coordinate $M = 2.93M_{\odot}$ in the $20 M_{\odot}$ mass model by Ritter *et al.* [142]. The arrows in (b) indicate the direction of time.

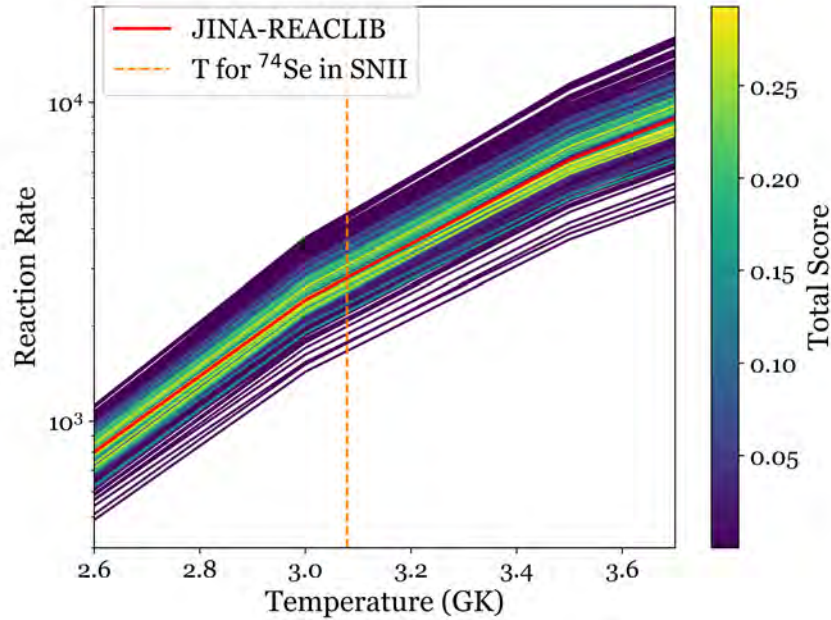


Figure 7.3 The reaction rate of the $^{73}\text{As}(p, \gamma)^{74}\text{Se}$ reaction as a function of temperature calculated using TALYS. The TALYS models are color coded based on their total score, similarly to Fig. 6.2. The red line indicates the reaction rate of the JINA-REACLIB [222] library, typically used in network calculations. The dotted line represents the peak temperature for the SNII model from Fig. 7.2a.

line.

The Monte Carlo one-zone nucleosynthesis simulations were performed using the PPN code

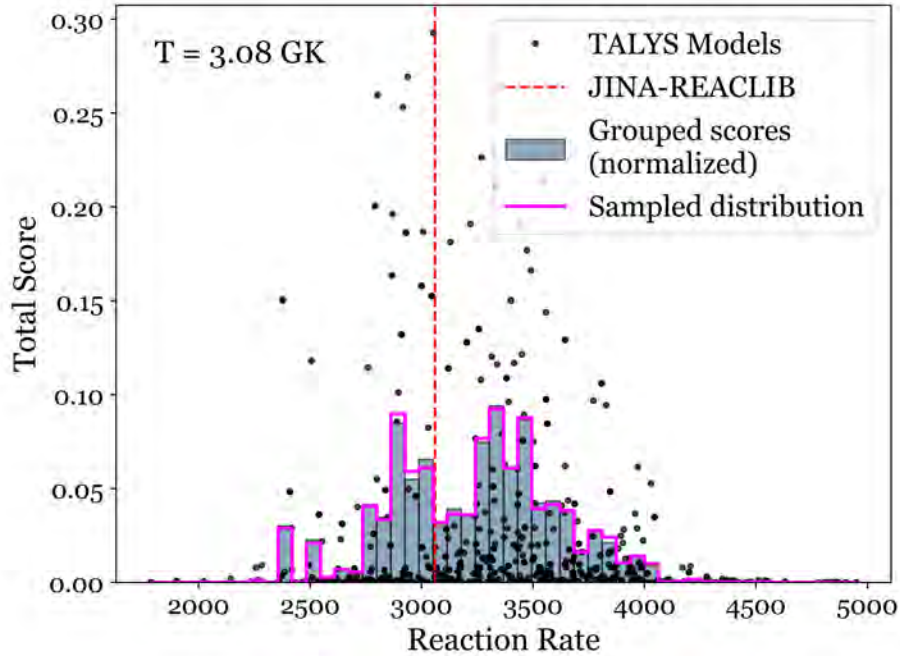


Figure 7.4 A projection of the reaction rates calculated by TALYS along the $T = 3.08$ GK temperature of interest, as a function of each model’s total score. The blue bars correspond to the TALYS models grouped in 50 bins between the minimum and maximum rate calculated by TALYS. The magenta line shows the sampled rates used in Monte Carlo simulations of the SNII scenario.

from the NuGrid framework [159]. The temperature and density profiles (Fig. 7.2), as well as the initial abundances were obtained from the $20 M_{\odot}$ mass model shown in Fig. 7.1 for the mass coordinate $M = 2.93 M_{\odot}$. The only variable varied in each of the 10 000 realizations of the code was the multiplication factor for the ${}^{73}\text{As}(p, \gamma){}^{74}\text{Se}$ reaction rate (and its inverse ${}^{74}\text{Se}(\gamma, p){}^{73}\text{As}$). This multiplication factor was calculated as the ratio of the sampled reaction rate over the JINA-REACLIB rate that is used as a default value.

The produced ${}^{74}\text{Se}$ mass fraction as a function of time is shown in Fig. 7.5. The various blue lines correspond to the 10 000 runs with varied ${}^{73}\text{As}(p, \gamma){}^{74}\text{Se}$ reaction rate, with the darker colors reflecting more lines that overlap in that region. The orange line corresponds to the mass fraction produced using the JINA-REACLIB rate, and the red dashed line are the mass fractions obtained with the minimum and maximum rate obtained from TALYS. Fig. 7.6 shows final mass fraction of ${}^{74}\text{Se}$ relative to the default JINA-REACLIB model.

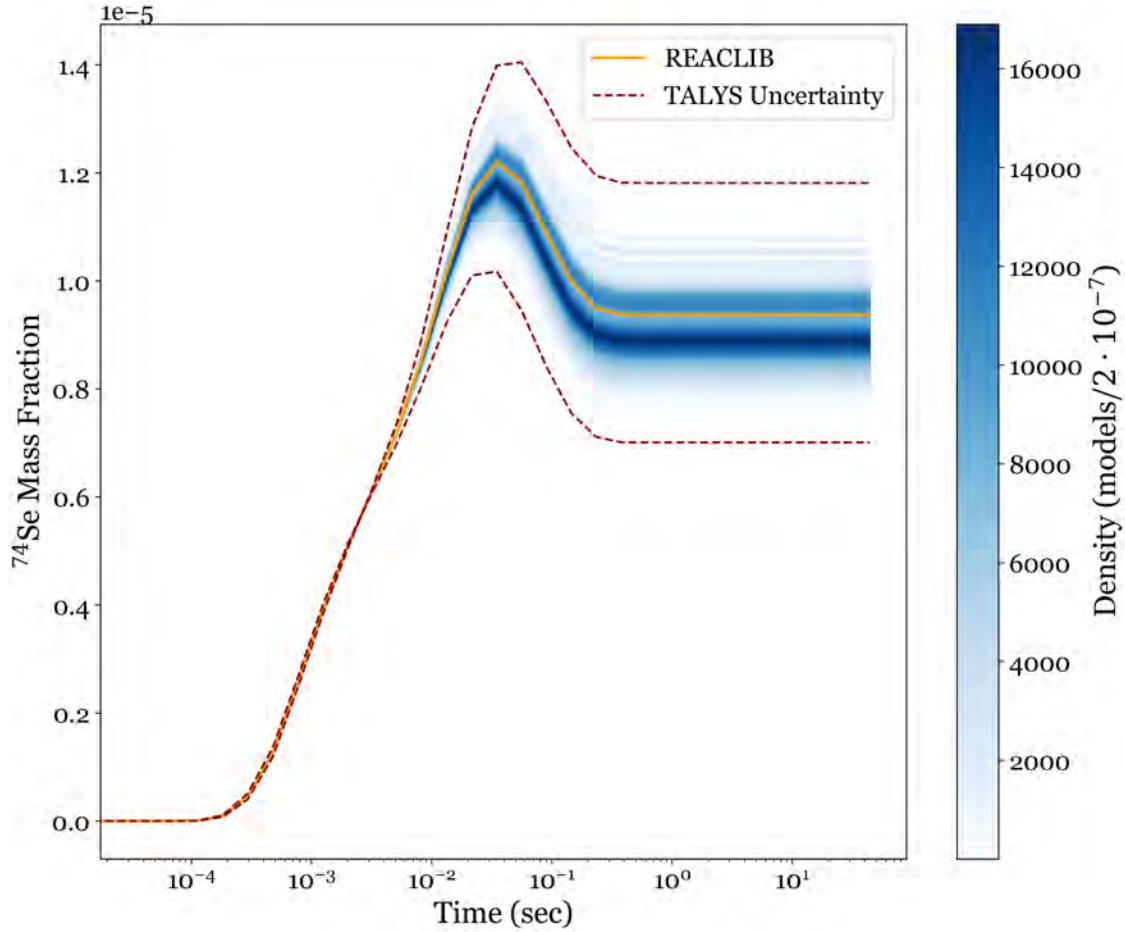


Figure 7.5 ^{74}Se mass fraction as a function of time calculated using PPN one-zone simulations. The various blue lines correspond to different $^{73}\text{As}(p, \gamma)^{74}\text{Se}$ reaction rates sampled from the distribution of Fig. 7.4, and the darker color correspond to more overlapping trajectories. The orange line corresponds to simulation using the default JINA-REACLIB reaction rate and the red dashed lines to the minimum and maximum reaction rates by TALYS.

The experimentally measured $^{73}\text{As}(p, \gamma)^{74}\text{Se}$ cross section from Sec. 6.2 is $\sim 18\%$ higher than the NON-SMOKER rate adopted in the JINA-REACLIB library but still consistent within the experimental uncertainty (Fig. 6.4). Consequently, the final ^{74}Se abundance in SNII models remains in good agreement with calculations using the JINA-REACLIB rate, though a slightly lower mean ^{74}Se production is suggested. However, this deviation is too small to indicate that the observed overproduction of ^{74}Se is driven by uncertainties in this reaction rate. Comparing the full width at half maximum of the distribution of Fig. 7.8 to the TALYS uncertainty shows that the measurement significantly reduces theoretical uncertainties in reaction rates by approximately a factor of two,

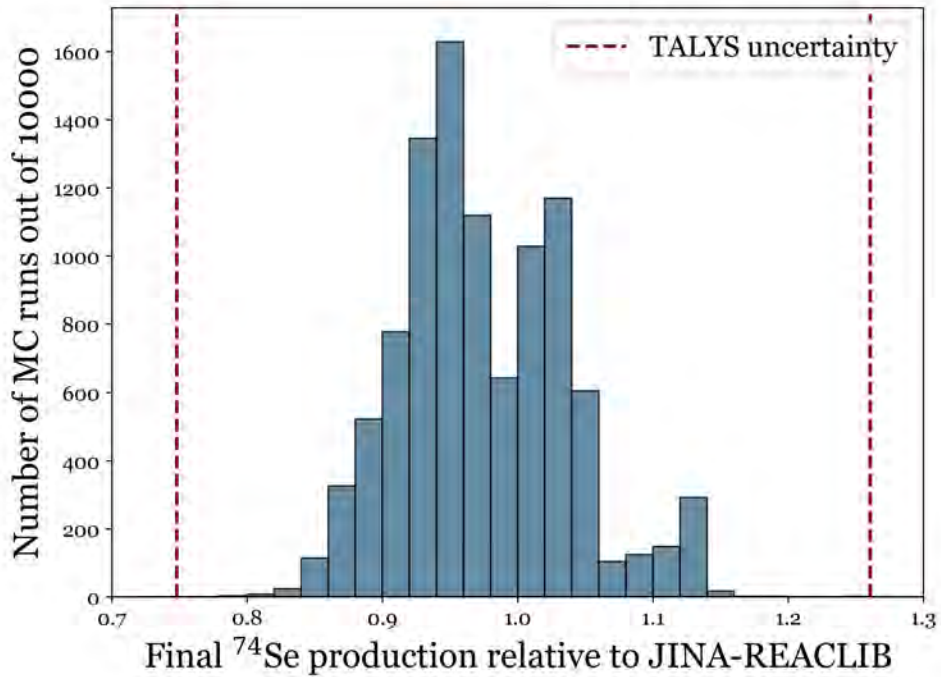


Figure 7.6 Comparison of the final ^{74}Se mass fraction distribution obtained in the Monte Carlo simulations varying the $^{73}\text{As}(p, \gamma)^{74}\text{Se}$ reaction rate relative to the default model using the JINA-REACLIB reaction rate. The dashed lines correspond to the maximum and minimum reaction rate from TALYS.

providing a more constrained and reliable input for future sensitivity studies.

7.2 Type Ia Supernova - SNIa

For the Type Ia scenario the models by Travaglio *et al.* [138] were adopted. In their work, they explored two-dimensional SNIa models of a white dwarf (WD) accreting mass from a companion star in the single degenerate (SD) scenario. The *s*-process seed distribution is assumed to be produced during the AGB phase leading to the formation of the WD, through thermal pulses that mix material from the H-rich envelope to the C-rich layers, resulting in a ^{13}C pocket (see Sec. 3.3.3.1). From the different explosion mechanisms studied by Travaglio *et al.*, the model adopted in this work is the so-called DTT-a. DTT-a is a delayed detonation model assuming the deflagration-to-detonation criterion of Kasen *et al.* [223] and a CO-WD structure by Domínguez *et al.* [224] with solar metallicity and a progenitor mass of $M = 1.5 M_{\odot}$.

The nucleosynthesis in such multidimensional simulations was calculated using the tracer parti-

cle method [225, 226] by placing 51 200 tracer particles, uniformly distributed in mass coordinate. For this work, the trajectories of three tracer particles were provided from the external layers of the model, where the peak temperatures reached allowed for γ -process nucleosynthesis. The isotopic abundances of elements heavier than Ge were also provided, while for the lighter elements solar abundances by Asplund [83] were used. The temperature and density profiles for one of the three tracers (number 2876) is shown as an example in Fig. 7.7. The other two tracer trajectories had minimal differences, and thus the tracer shown in Fig. 7.7 was chosen as a representative case.

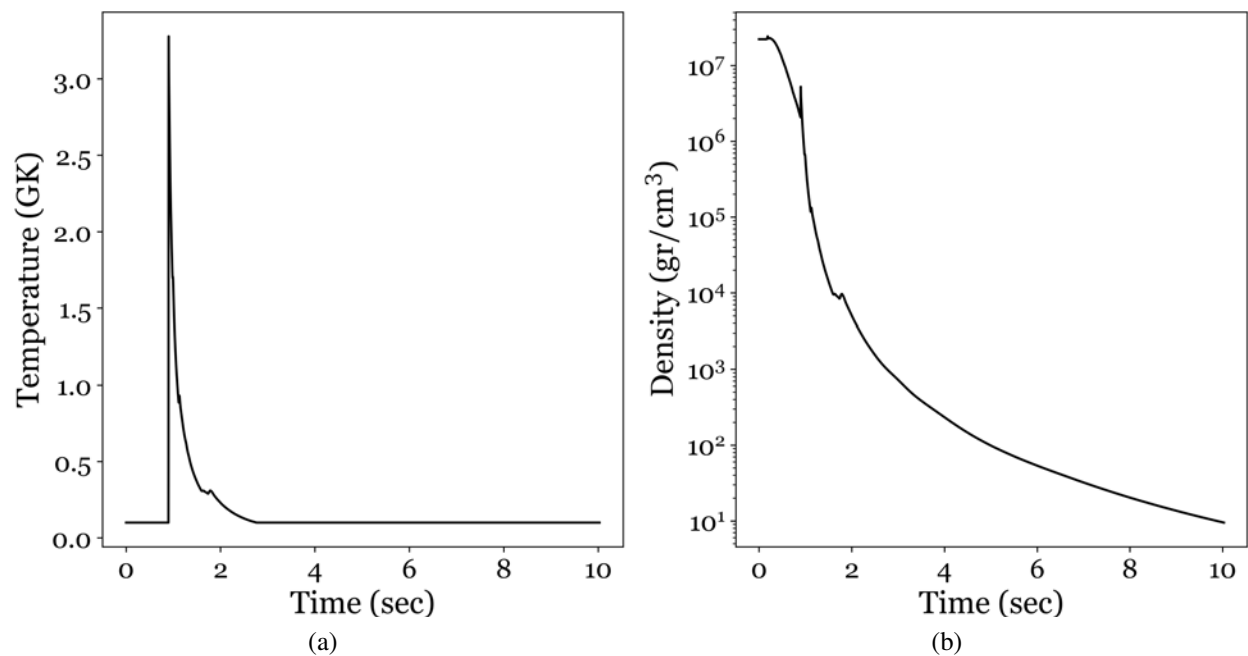


Figure 7.7 The temperature (a) and density (b) profiles of tracer 2876 of the DTT-a SNIa model by Travaglio *et al.* [138]. The tracer is located on the external layers of the SNIa model, where the peak temperatures reached allow for γ -process nucleosynthesis.

The peak temperature obtained is $T = 3.27$ GK. Similar to the SNIa scenario one-zone nucleosynthesis simulations were performed using the PPN code for the JINA-REACLIB rate, the minimum and maximum rate predicted by TALYS models at the peak temperature of interest, and a sample of the reaction rate distribution weighted by the total score. The produced ^{74}Se mass fraction as a function of time, shown in Fig. 7.8, confirms that variations in the $^{73}\text{As}(p, \gamma)^{74}\text{Se}$ reaction rate within the nuclear uncertainty predicted by TALYS do not significantly impact the final ^{74}Se

abundance. This is consistent with Ref. [162], indicating that ^{74}Se production in SNIa is affected

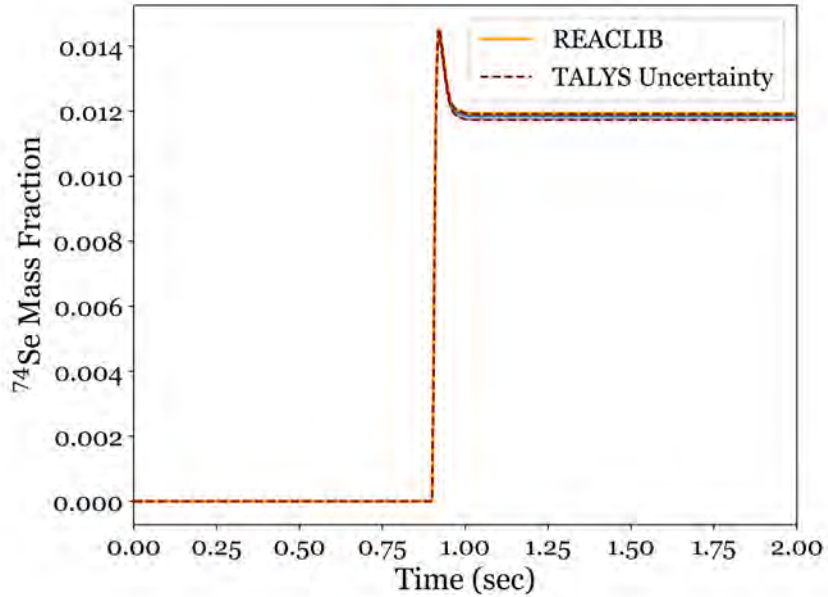


Figure 7.8 Same as Fig. 7.5 for the SNIa trajectories shown in Fig. 7.7.

by astrophysical conditions rather than nuclear uncertainties in this reaction. As the $^{73}\text{As}(p, \gamma)^{74}\text{Se}$ reaction is a destruction mechanism for ^{74}Se , it is possible that the material is not exposed to the peak temperature for a long enough time, for this destruction mechanism to become relevant. As seen in Fig. 7.7 compared to Fig. 7.2, the material is exposed to peak temperatures for fractions of a second, while in the SNII scenario the temperature exhibits a plateau that lasts for multiple seconds, allowing the $^{73}\text{As}(p, \gamma)^{74}\text{Se}$ reaction to destroy the produced ^{74}Se and impact the final abundances.

CHAPTER 8

SUMMARY & CONCLUSIONS

To summarize, the astrophysical γ process, the most established scenario for the production of the p nuclei, involves a vast network of primarily radioactive isotopes. Developing experimental techniques to directly measure photodisintegration reactions using unstable beams is essential, as reaction rates in network calculations are largely estimated through statistical model calculations, that carry significant uncertainties away from stability.

This work focused on implementing such a technique to measure reaction cross sections in inverse kinematics using a radioactive beam, the summing technique and a hydrogen gas target. The proof-of-principle application of this method was successfully demonstrated with the first measurement of the $^{82}\text{Kr}(p, \gamma)^{83}\text{Rb}$ reaction cross section. The experimental results suggest a smaller cross section than theoretically predicted, but a more consistent description of the statistical model parameters was obtained through simulations to reproduce the experiment spectra. The ability to simultaneously describe multiple observables provides stronger constraints on the model parameters than a comparison with cross-section data alone, enabling a more constrained cross section over a broader energy range than the one directly measured.

The same methodology was applied using a radioactive ^{73}As beam, leading to the first measurement of the $^{73}\text{As}(p, \gamma)^{74}\text{Se}$ reaction cross section. The measured cross section showed good agreement with the theoretical prediction from NON-SMOKER. The cross-section data, along with experimental spectra, were used to characterize various nuclear level density and γ -ray strength function models from TALYS, allowing for the extraction of an experimentally constrained cross section across the entire Gamow window of the γ process. This characterization enabled the determination of an experimentally constrained reaction rate for the $^{73}\text{As}(p, \gamma)^{74}\text{Se}$ reaction, which was then used in Monte Carlo one-zone network simulations of the γ process.

Although the production of ^{74}Se in the Type Ia supernova scenario showed no sensitivity to the constrained reaction rate, a significant impact on the final ^{74}Se abundance in Type II supernovae was observed. The uncertainty in the ^{74}Se production was reduced by a factor of two, providing a

more constrained and reliable input for future sensitivity studies.

The successful implementation of this technique opens the possibility of extending similar measurements to reactions involving heavier radioactive beams. Such studies would further constrain reaction rates relevant for the γ process, improving the accuracy of nucleosynthesis models and reducing uncertainties in astrophysical simulations.

BIBLIOGRAPHY

- [1] F. W. Aston, “Nobel Lecture,” 1922. Accessed from <https://www.nobelprize.org/prizes/chemistry/1922/aston/lecture/>.
- [2] A. S. Eddington, “The Internal Constitution of the Stars,” *The Scientific Monthly*, vol. 11, no. 4, pp. 297–303, 1920.
- [3] E. M. Burbidge, G. R. Burbidge, W. A. Fowler, and F. Hoyle, “Synthesis of the Elements in Stars,” *Rev. Mod. Phys.*, vol. 29, pp. 547–650, 1957.
- [4] IAEA, “Live Chart of Nuclides.” Accessed from <https://www-nds.iaea.org/relnsd/vcharthtml/VChartHTML.html>.
- [5] M. G. Mayer, “On Closed Shells in Nuclei,” *Phys. Rev.*, vol. 74, pp. 235–239, 1948.
- [6] C. Iliadis, *Nuclear Physics of Stars*. John Wiley & Sons, Ltd, 2007.
- [7] K. S. Krane, *Introductory Nuclear Physics*. John Wiley & Sons, Inc, 1987.
- [8] Wikimedia, “Binding Energy Curve,” 2022. This work has been released into the public domain by url https://en.m.wikipedia.org/wiki/File:Binding_energy_curve_-_common_isotopes.svg.
- [9] M. Wang, G. Audi, A. Wapstra, F. Kondev, M. MacCormick, X. Xu, and B. Pfeiffer, “The Ame2012 atomic mass evaluation,” *Chinese Physics C*, vol. 36, no. 12, p. 1603, 2012.
- [10] Ασημακόπουλος, Π. Α., Πυρηνική Φυσική, ch. 9, pp. 259–311. Ιωάννινα: Επτάλοφος, 1984.
- [11] C. A. Bertulani and A. Bonaccorso, *Direct Nuclear Reactions*, pp. 1415–1449. Singapore: Springer Nature Singapore, 2023.
- [12] W. Heisenberg, “Über den anschaulichen Inhalt der quantentheoretischen Kinematik und Mechanik,” *Zeitschrift für Physik*, vol. 43, pp. 172–198, 1927.
- [13] N. Bohr, “Neutron Capture and Nuclear Constitution,” *Nature*, vol. 137, pp. 344–348, 1936.
- [14] T. Rauscher, *Essentials of Nucleosynthesis and Theoretical Nuclear Astrophysics*. 2514-3433, IOP Publishing, 2020.
- [15] C. Rolfs and W. Rodney, *Cauldrons in the Cosmos: Nuclear Astrophysics*. Theoretical Astrophysics, University of Chicago Press, 1988.
- [16] W. Hauser and H. Feshbach, “The Inelastic Scattering of Neutrons,” *Phys. Rev.*, vol. 87, pp. 366–373, 1952.
- [17] T. Rauscher and F.-K. Thielemann, “Astrophysical Reaction Rates From Statistical Model Calculations,” *Atomic Data and Nuclear Data Tables*, vol. 75, no. 1, pp. 1–351, 2000.

- [18] C. Mahaux and H. A. Weidenmuller, “Recent Developments in Compound-Nucleus Theory,” *Annual Review of Nuclear and Particle Science*, vol. 29, no. Volume 29, 1979, pp. 1–31, 1979.
- [19] P. E. Hodgson, “The nuclear optical model,” *Reports on Progress in Physics*, vol. 34, no. 2, p. 765, 1971.
- [20] W. Dickhoff and R. Charity, “Recent developments for the optical model of nuclei,” *Progress in Particle and Nuclear Physics*, vol. 105, pp. 252–299, 2019.
- [21] A. Larsen, A. Spyrou, S. Liddick, and M. Guttormsen, “Novel techniques for constraining neutron-capture rates relevant for r-process heavy-element nucleosynthesis,” *Progress in Particle and Nuclear Physics*, vol. 107, pp. 69–108, 2019.
- [22] T. Rauscher, F.-K. Thielemann, and K.-L. Kratz, “Nuclear level density and the determination of thermonuclear rates for astrophysics,” *Phys. Rev. C*, vol. 56, pp. 1613–1625, 1997.
- [23] H. A. Bethe, “An Attempt to Calculate the Number of Energy Levels of a Heavy Nucleus,” *Phys. Rev.*, vol. 50, pp. 332–341, 1936.
- [24] J. Bardeen, L. N. Cooper, and J. R. Schrieffer, “Theory of Superconductivity,” *Phys. Rev.*, vol. 108, pp. 1175–1204, 1957.
- [25] A. Gilbert and A. G. W. Cameron, “A composite nuclear-level density formula with shell corrections,” *Canadian Journal of Physics*, vol. 43, p. 1446, 1965.
- [26] W. Dilg, W. Schantl, H. Vonach, and M. Uhl, “Level density parameters for the back-shifted fermi gas model in the mass range $40 < A < 250$,” *Nuclear Physics A*, vol. 217, no. 2, pp. 269–298, 1973.
- [27] H. Baba, “A shell-model nuclear level density,” *Nuclear Physics A*, vol. 159, no. 2, pp. 625–641, 1970.
- [28] A. V. Ignatyuk, G. N. Smirenkin, and A. S. Tishin, “Phenomenological description of energy dependence of the level density parameter,” *Yad. Fiz.*, v. 21, no. 3, pp. 485-490, 1975.
- [29] T. von Egidy and D. Bucurescu, “Statistical nuclear properties (level densities, spin distributions),” *Journal of Physics: Conference Series*, vol. 338, no. 1, p. 012028, 2012.
- [30] S. Goriely, “A new nuclear level density formula including shell and pairing correction in the light of a microscopic model calculation,” *Nuclear Physics A*, vol. 605, no. 1, pp. 28–60, 1996.
- [31] T. Ericson, “A statistical analysis of excited nuclear states,” *Nuclear Physics*, vol. 11, pp. 481–491, 1959.
- [32] A. V. Ignatyuk, K. K. Istekov, and G. N. Smirenkin, “Collective effects in level density, and the probability of fission,” *Sov. J. Nucl. Phys. (Engl. Transl.); (United States)*, vol. 30:5, 1979.

- [33] A. V. Ignatyuk, J. L. Weil, S. Raman, and S. Kahane, “Density of discrete levels in ^{116}Sn ,” *Phys. Rev. C*, vol. 47, pp. 1504–1513, 1993.
- [34] Y. Alhassid, M. Bonett-Matiz, S. Liu, and H. Nakada, “Direct microscopic calculation of nuclear level densities in the shell model Monte Carlo approach,” *Phys. Rev. C*, vol. 92, p. 024307, 2015.
- [35] P. Demetriou and S. Goriely, “Microscopic nuclear level densities for practical applications,” *Nuclear Physics A*, vol. 695, no. 1, pp. 95–108, 2001.
- [36] S. Goriely, F. Tondeur, and J. Pearson, “A Hartree–Fock Nuclear Mass Table,” *Atomic Data and Nuclear Data Tables*, vol. 77, no. 2, pp. 311–381, 2001.
- [37] S. Goriely, S. Hilaire, and A. J. Koning, “Improved microscopic nuclear level densities within the Hartree-Fock-Bogoliubov plus combinatorial method,” *Phys. Rev. C*, vol. 78, p. 064307, 2008.
- [38] S. Hilaire, M. Girod, S. Goriely, and A. J. Koning, “Temperature-dependent combinatorial level densities with the DIM Gogny force,” *Phys. Rev. C*, vol. 86, p. 064317, 2012.
- [39] G. A. Bartholomew, E. D. Earle, A. J. Ferguson, J. W. Knowles, and M. A. Lone, *Gamma-Ray Strength Functions*, pp. 229–324. Boston, MA: Springer US, 1973.
- [40] D. Brink, *Some Aspects of the Interaction of Light with Matter*. PhD thesis, Oxford University, 1955.
- [41] N. L. Iudice and F. Palumbo, “New Isovector Collective Modes in Deformed Nuclei,” *Phys. Rev. Lett.*, vol. 41, pp. 1532–1534, 1978.
- [42] K. Heyde, P. von Neumann-Cosel, and A. Richter, “Magnetic dipole excitations in nuclei: Elementary modes of nucleonic motion,” *Rev. Mod. Phys.*, vol. 82, pp. 2365–2419, 2010.
- [43] P. Axel, “Electric Dipole Ground-State Transition Width Strength Function and 7-MeV Photon Interactions,” *Phys. Rev.*, vol. 126, pp. 671–683, 1962.
- [44] J. Kopecky and R. Chrien, “Observation of the M1 giant resonance by resonance averaging in ^{106}Pd ,” *Nuclear Physics A*, vol. 468, no. 2, pp. 285–300, 1987.
- [45] J. Kopecky and M. Uhl, “Test of gamma-ray strength functions in nuclear reaction model calculations,” *Phys. Rev. C*, vol. 41, pp. 1941–1955, 1990.
- [46] S. Goriely and E. Khan, “Large-scale QRPA calculation of E1-strength and its impact on the neutron capture cross section,” *Nuclear Physics A*, vol. 706, no. 1, pp. 217–232, 2002.
- [47] M. Martini, S. Péru, S. Hilaire, S. Goriely, and F. Lechaftois, “Large-scale deformed quasi-particle random-phase approximation calculations of the γ -ray strength function using the Gogny force,” *Phys. Rev. C*, vol. 94, p. 014304, 2016.
- [48] S. Goriely, E. Khan, and M. Samyn, “Microscopic HFB + QRPA predictions of dipole strength for astrophysics applications,” *Nuclear Physics A*, vol. 739, no. 3, pp. 331–352, 2004.

- [49] S. Goriely, S. Hilaire, S. Péru, and K. Sieja, “Gogny-HFB+QRPA dipole strength function and its application to radiative nucleon capture cross section,” *Phys. Rev. C*, vol. 98, p. 014327, 2018.
- [50] D. Vretenar, N. Paar, P. Ring, and G. A. Lalazissis, “Pygmy dipole resonances in the relativistic random phase approximation,” *Phys. Rev. C*, vol. 63, p. 047301, 2001.
- [51] E. Litvinova and N. Belov, “Low-energy limit of the radiative dipole strength in nuclei,” *Phys. Rev. C*, vol. 88, p. 031302, 2013.
- [52] X. Roca-Maza, G. Pozzi, M. Brenna, K. Mizuyama, and G. Colò, “Low-lying dipole response: Isospin character and collectivity in ^{68}Ni , ^{132}Sn , and ^{208}Pb ,” *Phys. Rev. C*, vol. 85, p. 024601, 2012.
- [53] I. Daoutidis and S. Goriely, “Large-scale continuum random-phase approximation predictions of dipole strength for astrophysical applications,” *Phys. Rev. C*, vol. 86, p. 034328, 2012.
- [54] A. Voinov, E. Algin, U. Agvaanluvsan, T. Belgya, R. Chankova, M. Guttormsen, G. E. Mitchell, J. Rekstad, A. Schiller, and S. Siem, “Large Enhancement of Radiative Strength for Soft Transitions in the Quasicontinuum,” *Phys. Rev. Lett.*, vol. 93, p. 142504, 2004.
- [55] A. Simon, M. Guttormsen, A. C. Larsen, C. W. Beausang, P. Humby, J. T. Harke, R. J. Casperson, R. O. Hughes, T. J. Ross, J. M. Allmond, and *et al.*, “First observation of low-energy γ -ray enhancement in the rare-earth region,” *Phys. Rev. C*, vol. 93, p. 034303, 2016.
- [56] S. W. Jones, H. Möller, C. L. Fryer, C. J. Fontes, R. Trappitsch, W. P. Even, A. Couture, M. R. Mumpower, and S. Safi-Harb, “ ^{60}Fe in core-collapse supernovae and prospects for X-ray and gamma-ray detection in supernova remnants,” *Monthly Notices of the Royal Astronomical Society*, vol. 485, no. 3, pp. 4287–4310, 2019.
- [57] R. Schwengner, S. Frauendorf, and B. A. Brown, “Low-Energy Magnetic Dipole Radiation in Open-Shell Nuclei,” *Phys. Rev. Lett.*, vol. 118, p. 092502, 2017.
- [58] A. C. Larsen, N. Blasi, A. Bracco, F. Camera, T. K. Eriksen, A. Görge, M. Guttormsen, T. W. Hagen, S. Leoni, B. Million, and *et al.*, “Evidence for the Dipole Nature of the Low-Energy γ Enhancement in ^{56}Fe ,” *Phys. Rev. Lett.*, vol. 111, p. 242504, 2013.
- [59] A. C. Larsen and S. Goriely, “Impact of a low-energy enhancement in the γ -ray strength function on the neutron-capture cross section,” *Phys. Rev. C*, vol. 82, p. 014318, 2010.
- [60] A. Spyrou, D. Richman, A. Couture, C. E. Fields, S. N. Liddick, K. Childers, B. P. Crider, P. A. DeYoung, A. C. Dombos, P. Gastis, and *et al.*, “Enhanced production of ^{60}Fe in massive stars,” *Nature Communications*, vol. 15, 2024.
- [61] M. Guttormsen, K. O. Ay, M. Ozgur, E. Algin, A. C. Larsen, F. L. Bello Garrote, H. C. Berg, L. Crespo Campo, T. Dahl-Jacobsen, F. W. Furmyr, and *et al.*, “Evolution of the γ -ray strength function in neodymium isotopes,” *Phys. Rev. C*, vol. 106, p. 034314, 2022.

- [62] A. Koning, S. Hilaire, and S. Goriely, “TALYS: modeling of nuclear reactions,” *The European Physical Journal A*, vol. 59, p. 131, 2023.
- [63] A. Koning and J. Delaroche, “Local and global nucleon optical models from 1 keV to 200 MeV,” *Nuclear Physics A*, vol. 713, no. 3, pp. 231–310, 2003.
- [64] J. P. Jeukenne, A. Lejeune, and C. Mahaux, “Optical-model potential in nuclear matter from Reid’s hard core interaction,” *Phys. Rev. C*, vol. 10, pp. 1391–1401, 1974.
- [65] J. Jeukenne, A. Lejeune, and C. Mahaux, “Many-body theory of nuclear matter,” *Physics Reports*, vol. 25, no. 2, pp. 83–174, 1976.
- [66] J. P. Jeukenne, A. Lejeune, and C. Mahaux, “Microscopic calculation of the symmetry and Coulomb components of the complex optical-model potential,” *Phys. Rev. C*, vol. 15, pp. 10–29, 1977.
- [67] J.-P. Jeukenne, A. Lejeune, and C. Mahaux, “Optical-model potential in finite nuclei from Reid’s hard core interaction,” *Phys. Rev. C*, vol. 16, pp. 80–96, 1977.
- [68] E. Bauge, J. P. Delaroche, and M. Girod, “Semimicroscopic nucleon-nucleus spherical optical model for nuclei with $A > 40$ at energies up to 200 MeV,” *Phys. Rev. C*, vol. 58, pp. 1118–1145, 1998.
- [69] E. Bauge, J. P. Delaroche, and M. Girod, “Lane-consistent, semimicroscopic nucleon-nucleus optical model,” *Phys. Rev. C*, vol. 63, p. 024607, 2001.
- [70] D. Brink, “Individual particle and collective aspects of the nuclear photoeffect,” *Nuclear Physics*, vol. 4, pp. 215–220, 1957.
- [71] P. Axel, “Electric Dipole Ground-State Transition Width Strength Function and 7-MeV Photon Interactions,” *Phys. Rev.*, vol. 126, pp. 671–683, 1962.
- [72] S. Goriely, “Radiative neutron captures by neutron-rich nuclei and the r-process nucleosynthesis,” *Physics Letters B*, vol. 436, no. 1, pp. 10–18, 1998.
- [73] V. Plujko, O. Gorbachenko, R. Capote, and P. Dimitriou, “Giant dipole resonance parameters of ground-state photoabsorption: Experimental values with uncertainties,” *Atomic Data and Nuclear Data Tables*, vol. 123-124, pp. 1–85, 2018.
- [74] R. Capote, M. Herman, P. Obložinský, P. Young, S. Goriely, T. Belgya, A. Ignatyuk, A. Koning, S. Hilaire, V. Plujko, and *et al.*, “RIPL – Reference Input Parameter Library for Calculation of Nuclear Reactions and Nuclear Data Evaluations,” *Nuclear Data Sheets*, vol. 110, no. 12, pp. 3107–3214, 2009. Special Issue on Nuclear Reaction Data.
- [75] D. Bohle, A. Richter, W. Steffen, A. Dieperink, N. Lo Iudice, F. Palumbo, and O. Scholten, “New magnetic dipole excitation mode studied in the heavy deformed nucleus ^{156}Gd by inelastic electron scattering,” *Physics Letters B*, vol. 137, no. 1, pp. 27–31, 1984.
- [76] P. A. Moldauer, “Evaluation of the fluctuation enhancement factor,” *Phys. Rev. C*, vol. 14, pp. 764–766, 1976.

- [77] P. A. Moldauer, “Statistics and the average cross section,” *Nuclear Physics A*, vol. 344, no. 2, pp. 185–195, 1980.
- [78] J. W. Tepel, H. M. Hofmann, and H. A. Weidenmüller, “Hauser-Feshbach formulas for medium and strong absorption,” *Physics Letters B*, vol. 49, no. 1, pp. 1–4, 1974.
- [79] H. M. Hofmann, J. Richert, J. W. Tepel, and H. A. Weidenmüller, “Direct reactions and Hauser-Feshbach theory,” *Annals of Physics*, vol. 90, no. 2, pp. 403–437, 1975.
- [80] H. M. Hofmann, T. Mertelmeier, M. Herman, and J. W. Tepel, “Hauser-Feshbach calculations in the presence of weakly absorbing channels with special reference to the elastic enhancement factor and the factorization assumption,” *Zeitschrift für Physik A Atoms and Nuclei*, vol. 297, no. 2, pp. 153–160, 1980.
- [81] R. E. Atkinson and F. G. Houtermans, “Zur Frage der Aufbaumöglichkeit der Elemente in Sternen,” *Zeits. f. Physik* 54, 656, 1929.
- [82] Wikimedia, “Gamow Peak.” This work is licensed under the Creative Commons Attribution 4.0 International License. To view a copy of this license, visit <http://creativecommons.org/licenses/by/4.0/>.
- [83] M. Asplund, N. Grevesse, A. J. Sauval, and P. Scott, “The Chemical Composition of the Sun,” *Annual Review of Astronomy & Astrophysics*, vol. 47, no. 1, pp. 481–522, 2009.
- [84] J. R. Oppenheimer and G. M. Volkoff, “On Massive Neutron Cores,” *Phys. Rev.*, vol. 55, pp. 374–381, 1939.
- [85] H. J. Lamers and E. M. Levesque, *Understanding Stellar Evolution*. 2514-3433, IOP Publishing, 2017.
- [86] R. A. Alpher, H. Bethe, and G. Gamow, “The Origin of Chemical Elements,” *Phys. Rev.*, vol. 73, pp. 803–804, 1948.
- [87] E. J. Öpik, “Collision probabilities with the planets and the distribution of interplanetary matter,” *Pattern Recognition and Image Analysis*, vol. 54, pp. 165–199, 1951.
- [88] E. E. Salpeter, “Nuclear Reactions in the Stars. I. Proton-Proton Chain,” *Phys. Rev.*, vol. 88, pp. 547–553, 1952.
- [89] E. E. Salpeter, “Nuclear Reactions in Stars. Buildup from Helium,” *Phys. Rev.*, vol. 107, pp. 516–525, 1957.
- [90] F. Hoyle, D. N. F. Dunbar, R. E. Pixley, W. A. Wenzel, and W. Whaling, “The 7.68-MeV State in C^{12} ,” *Phys. Rev.*, vol. 92, pp. 649–650, 1953.
- [91] D. E. Alburger, “Gamma-Ray Decay of the 7.66-MeV Level of C^{12} ,” *Phys. Rev.*, vol. 124, pp. 193–198, 1961.
- [92] J. A. Nolen and S. M. Austin, “Measurement of the excitation energy of the 7.654 MeV state of ^{12}C and the rate of the 3α reaction,” *Phys. Rev. C*, vol. 13, pp. 1773–1779, 1976.

- [93] P. Descouvemont and I. Baraffe, “Microscopic cluster study of the 12B and 12N systems and application to a hot pp chain in zero-metal stars,” *Nuclear Physics A*, vol. 514, no. 1, pp. 66–86, 1990.
- [94] T. A. Lähde, U.-G. Meißner, and E. Epelbaum, “An update on fine-tunings in the triple-alpha process,” *The European Physical Journal A*, vol. 56, 2020.
- [95] S. Jin, S. M. Roberts, Luke F. Austin, and H. Schatz, “Enhanced triple- α reaction reduces proton-rich nucleosynthesis in supernovae,” *Nature*, vol. 588, 2020.
- [96] J. Bishop, C. E. Parker, G. V. Rogachev, S. Ahn, E. Koshchiy, K. Brandenburg, C. R. Brune, R. J. Charity, J. Derkin, N. Dronchi, and *et al.*, “Neutron-upscattering enhancement of the triple-alpha process,” *Nature Communications*, vol. 13, 2022.
- [97] F. Herwig, *Evolution of Solar and Intermediate-Mass Stars*, pp. 397–445. Dordrecht: Springer Netherlands, 2013.
- [98] R. C. Duncan, S. L. Shapiro, and I. Wasserman, “Neutrino-driven Winds from Young, Hot Neutron Stars,” *Astrophysical Journal*, vol. 309, p. 141, 1986.
- [99] J. J. Cowan and W. K. Rose, “Production of ^{14}C and neutrons in red giants.,” *The Astrophysical Journal*, vol. 212, pp. 149–158, 1977.
- [100] M. Hempel, R. J. Stancliffe, M. Lugaro, and B. S. Meyer, “The Intermediate Neutron-capture Process and Carbon-enhanced Metal-poor Stars,” *The Astrophysical Journal*, vol. 831, no. 2, p. 171, 2016.
- [101] M. Pignatari, P. Hoppe, R. Trappitsch, C. Fryer, F. Timmes, F. Herwig, and R. Hirschi, “The neutron capture process in the He shell in core-collapse supernovae: Presolar silicon carbide grains as a diagnostic tool for nuclear astrophysics,” *Geochimica et Cosmochimica Acta*, vol. 221, pp. 37–46, 2018. Astrophysical Implications of Extraterrestrial Materials: A Special issue for Ernst K. Zinner.
- [102] P. W. Merrill, “Spectroscopic Observations of Stars of Class S,” *The Astrophysical Journal*, vol. 116, p. 21, 1952.
- [103] F.-K. Thielemann, C. Fröhlich, R. Hirschi, M. Liebendörfer, I. Dillmann, D. Mocerlj, T. Rauscher, G. Martinez-Pinedo, K. Langanke, K. Farouqi, and *et al.*, “Production of intermediate-mass and heavy nuclei,” *Progress in Particle and Nuclear Physics*, vol. 59, no. 1, pp. 74–93, 2007. International Workshop on Nuclear Physics 28th Course.
- [104] M. R. Mumpower, R. Surman, D.-L. Fang, M. Beard, P. Möller, T. Kawano, and A. Aprahamian, “Impact of individual nuclear masses on r -process abundances,” *Phys. Rev. C*, vol. 92, p. 035807, 2015.
- [105] T. Marketin, L. Huther, and G. Martínez-Pinedo, “Large-scale evaluation of β -decay rates of r -process nuclei with the inclusion of first-forbidden transitions,” *Phys. Rev. C*, vol. 93, p. 025805, 2016.

- [106] J. J. Cowan, C. Sneden, J. E. Lawler, A. Aprahamian, M. Wiescher, K. Langanke, G. Martínez-Pinedo, and F.-K. Thielemann, “Origin of the heaviest elements: The rapid neutron-capture process,” *Rev. Mod. Phys.*, vol. 93, p. 015002, 2021.
- [107] K. A. Lund, J. Engel, G. C. McLaughlin, M. R. Mumpower, E. M. Ney, and R. Surman, “The Influence of β -decay Rates on r-process Observables,” *The Astrophysical Journal*, vol. 944, no. 2, p. 144, 2023.
- [108] S. E. Woosley, J. R. Wilson, G. J. Mathews, R. D. Hoffman, and B. S. Meyer, “The r-Process and Neutrino-heated Supernova Ejecta,” *The Astrophysical Journal*, vol. 433, p. 229, 1994.
- [109] K. Takahashi, J. Witt, and H. T. Janka, “Nucleosynthesis in neutrino-driven winds from protoneutron stars II. The r-process,” *Astronomy and Astrophysics*, vol. 286, pp. 857–869, 1994.
- [110] S. Wanajo, H.-T. Janka, and B. Müller, “Electron-capture Supernovae as The Origin of Elements Beyond Iron,” *The Astrophysical Journal Letters*, vol. 726, no. 2, p. L15, 2011.
- [111] C. Winteler, R. Käppeli, A. Perego, A. Arcones, N. Vassetz, N. Nishimura, M. Liebendörfer, and F.-K. Thielemann, “Magnetorotationally Driven Supernovae as the Origin of Early Galaxy r-Process Elements?,” *The Astrophysical Journal Letters*, vol. 750, no. 1, p. L22, 2012.
- [112] P. Mösta, C. D. Ott, D. Radice, L. F. Roberts, E. Schnetter, and R. Haas, “A large-scale dynamo and magnetoturbulence in rapidly rotating core-collapse supernovae,” *Nature*, vol. 528, 2015.
- [113] N. Nishimura, H. Sawai, T. Takiwaki, S. Yamada, and F.-K. Thielemann, “The Intermediate r-process in Core-collapse Supernovae Driven by the Magneto-rotational Instability,” *The Astrophysical Journal Letters*, vol. 836, no. 2, p. L21, 2017.
- [114] A. I. MacFadyen and S. E. Woosley, “Collapsars: Gamma-Ray Bursts and Explosions in “Failed Supernovae”,” *The Astrophysical Journal*, vol. 524, no. 1, pp. 262–289, 1999.
- [115] J. C. McKinney, A. Tchekhovskoy, and R. D. Blandford, “Alignment of Magnetized Accretion Disks and Relativistic Jets with Spinning Black Holes,” *Science*, vol. 339, no. 6115, pp. 49–52, 2013.
- [116] J. M. Lattimer and D. N. Schramm, “Black-Hole-Neutron-Star Collisions,” *The Astrophysical Journal*, vol. 192, p. L145, 1974.
- [117] C. Freiburghaus, S. Rosswog, and F.-K. Thielemann, “r-Process in Neutron Star Mergers,” *The Astrophysical Journal*, vol. 525, no. 2, p. L121, 1999.
- [118] B. P. Abbot *et al.* (LIGO Scientific Collaboration and Virgo Collaboration), “GW170817: Observation of Gravitational Waves from a Binary Neutron Star Inspiral,” *Phys. Rev. Lett.*, vol. 119, p. 161101, 2017.

- [119] F. K. Thielemann, M. Eichler, I. V. Panov, and B. Wehmeyer, “Neutron Star Mergers and Nucleosynthesis of Heavy Elements,” *Annual Review of Nuclear and Particle Science*, vol. 67, pp. 253–274, 2017.
- [120] L. Baiotti and L. Rezzolla, “Binary neutron star mergers: a review of Einstein’s richest laboratory,” *Reports on Progress in Physics*, vol. 80, no. 9, p. 096901, 2017.
- [121] Rosswog, S., Sollerman, J., Feindt, U., Goobar, A., Korobkin, O., Wollaeger, R., Fremling, C., and Kasliwal, M. M., “The first direct double neutron star merger detection: Implications for cosmic nucleosynthesis,” *Astronomy & Astrophysics*, vol. 615, p. A132, 2018.
- [122] B. Côté, P. Denissenkov, F. Herwig, A. J. Ruiter, C. Ritter, M. Pignatari, and K. Belczynski, “i-process Contribution of Rapidly Accreting White Dwarfs to the Solar Composition of First-peak Neutron-capture Elements,” *The Astrophysical Journal*, vol. 854, no. 2, p. 105, 2018.
- [123] Choplin, A., Siess, L., and Goriely, S., “The intermediate neutron capture process - III. The i-process in AGB stars of different masses and metallicities without overshoot,” *Astronomy & Astrophysics*, vol. 667, p. A155, 2022.
- [124] A. Spyrou, D. Mücher, P. A. Denissenkov, F. Herwig, E. C. Good, and *et al.*, “First Study of the $^{139}\text{Ba}(n, \gamma)^{140}\text{Ba}$ Reaction to Constrain the Conditions for the Astrophysical *i* Process,” *Phys. Rev. Lett.*, vol. 132, p. 202701, 2024.
- [125] V. W. Ingeberg, S. Siem, M. Wiedeking, and *et al* (The ISOLDE Collaboration), “Nuclear level density and γ -ray strength function of ^{67}Ni and the impact on the *i* process,” *Phys. Rev. C*, vol. 111, p. 015803, 2025.
- [126] K. Lodders, “Solar System Abundances and Condensation Temperatures of the Elements,” *The Astrophysical Journal*, vol. 51, 2003.
- [127] I. Dillmann, T. Rauscher, M. Heil, F. Käppeler, W. Rapp, and F.-K. Thielemann, “p-Process simulations with a modified reaction library,” *Journal of Physics G: Nuclear and Particle Physics*, vol. 35, no. 1, p. 014029, 2007.
- [128] Goriely, S., Arnould, M., Borzov, I., and Rayet, M., “The puzzle of the synthesis of the rare nuclide ^{138}La ,” *Astronomy & Astrophysics*, vol. 375, no. 2, pp. L35–L38, 2001.
- [129] S. Bisterzo, C. Travaglio, R. Gallino, M. Wiescher, and F. Käppeler, “Galactic Chemical Evolution and Solar s-Process Abundances: Dependence on the ^{13}C -Pocket Structure,” *The Astrophysical Journal*, vol. 787, no. 1, p. 10, 2014.
- [130] A. Sieverding, K. Langanke, G. Martínez-Pinedo, R. Bollig, H.-T. Janka, and A. Heger, “The ν -process with Fully Time-dependent Supernova Neutrino Emission Spectra,” *The Astrophysical Journal*, vol. 876, no. 2, p. 151, 2019.
- [131] M. Arnould and S. Goriely, “The p-process of stellar nucleosynthesis: astrophysics and nuclear physics status,” *Physics Reports*, vol. 384, no. 1, pp. 1–84, 2003.

- [132] M. Lugaro, U. Ott, and Á. Kereszturi, “Radioactive nuclei from cosmochemistry to habitability,” *Progress in Particle and Nuclear Physics*, vol. 102, pp. 1–47, 2018.
- [133] S. E. Woosley and W. M. Howard, “The p-processes in supernovae,” *The Astrophysical Journal Supplement Series*, vol. 36, pp. 285–304, 1978.
- [134] T. Rauscher, N. Dauphas, I. Dillmann, C. Fröhlich, Z. Fülöp, and G. Gyürky, “Constraining the astrophysical origin of the p-nuclei through nuclear physics and meteoritic data,” *Reports on Progress in Physics*, vol. 76, no. 6, p. 066201, 2013.
- [135] N. Prantzos, M. Hashimoto, M. Rayet, and M. Arnould, “The p-process in SN 1987A,” *Astronomy and Astrophysics*, vol. 238, pp. 455–461, 1990.
- [136] T. Rauscher, A. Heger, R. D. Hoffman, and S. E. Woosley, “Nucleosynthesis in Massive Stars with Improved Nuclear and Stellar Physics,” *The Astrophysical Journal*, vol. 576, no. 1, pp. 323–348, 2002.
- [137] W. M. Howard, B. S. Meyer, and S. E. Woosley, “A New Site for the Astrophysical Gamma-Process,” *Astrophysical Journal Letters*, vol. 373, p. L5, 1991.
- [138] C. Travaglio, F. K. Röpké, R. Gallino, and W. Hillebrandt, “Type Ia Supernovae as Sites of the p-process: Two-dimensional Models Coupled to Nucleosynthesis,” *The Astrophysical Journal*, vol. 739, no. 2, p. 93, 2011.
- [139] N. Nishimura, T. Rauscher, R. Hirschi, A. S. J. Murphy, G. Cescutti, and C. Travaglio, “Uncertainties in the production of p nuclides in thermonuclear supernovae determined by Monte Carlo variations,” *Monthly Notices of the Royal Astronomical Society*, vol. 474, no. 3, pp. 3133–3139, 2017.
- [140] Roberti, L., Pignatari, M., Fryer, C., and Lugaro, M., “The γ -process nucleosynthesis in core-collapse supernovae - II. Effect of the explosive recipe,” *Astronomy & Astrophysics*, vol. 686, p. L8, 2024.
- [141] M. Arnould, “Possibility of synthesis of proton-rich nuclei in highly evolved stars. II,” *Astronomy and Astrophysics*, vol. 46, no. 1, pp. 117–125, 1976.
- [142] C. Ritter, F. Herwig, S. Jones, M. Pignatari, C. Fryer, and R. Hirschi, “NuGrid stellar data set – II. Stellar yields from H to Bi for stellar models with $M_{ZAMS} = 1 - 25M_{\odot}$ and $Z = 0.0001-0.02$,” *Monthly Notices of the Royal Astronomical Society*, vol. 480, no. 1, pp. 538–571, 2018.
- [143] Roberti, L., Pignatari, M., Psaltis, A., Sieverding, A., Mohr, P., Fülöp, Zs., and Lugaro, M., “The γ -process nucleosynthesis in core-collapse supernovae - I. A novel analysis of γ -process yields in massive stars,” *Astronomy & Astrophysics*, vol. 677, p. A22, 2023.
- [144] M. Pignatari, R. Hirschi, M. Wiescher, R. Gallino, M. Bennett, M. Beard, C. Fryer, F. Herwig, G. Rockefeller, and F. X. Timmes, “The $^{12}\text{C} + ^{12}\text{C}$ reaction and the impact on nucleosynthesis in massive stars,” *The Astrophysical Journal*, vol. 762, no. 1, p. 31, 2012.

- [145] Choplin, A., Goriely, S., Hirschi, R., Tominaga, N., and Meynet, G., “The p-process in exploding rotating massive stars,” *Astronomy & Astrophysics*, vol. 661, p. A86, 2022.
- [146] U. Battino, M. Pignatari, C. Travaglio, C. Lederer-Woods, P. Denissenkov, F. Herwig, F. Thielemann, and T. Rauscher, “Heavy elements nucleosynthesis on accreting white dwarfs: building seeds for the p-process,” *Monthly Notices of the Royal Astronomical Society*, vol. 497, no. 4, pp. 4981–4998, 2020.
- [147] P. A. Denissenkov, F. Herwig, P. Woodward, R. Androssy, M. Pignatari, and S. Jones, “The i-process yields of rapidly accreting white dwarfs from multicycle He-shell flash stellar evolution models with mixing parametrizations from 3D hydrodynamics simulations,” *Monthly Notices of the Royal Astronomical Society*, vol. 488, no. 3, pp. 4258–4270, 2019.
- [148] Goriely, S., José, J., Hernanz, M., Rayet, M., and Arnould, M., “He-detonation in sub-Chandrasekhar CO white dwarfs: A new insight into energetics and p-process nucleosynthesis,” *Astronomy & Astrophysics*, vol. 383, no. 3, pp. L27–L30, 2002.
- [149] M. Pignatari, K. Göbel, R. Reifarth, and C. Travaglio, “The production of proton-rich isotopes beyond iron: The γ -process in stars,” *International Journal of Modern Physics E*, vol. 25, no. 04, p. 1630003, 2016.
- [150] H. Schatz, L. Bildsten, A. Cumming, and M. Wiescher, “The Rapid Proton Process Ashes from Stable Nuclear Burning on an Accreting Neutron Star,” *The Astrophysical Journal*, vol. 524, no. 2, pp. 1014–1029, 1999.
- [151] J. José, F. Moreno, A. Parikh, and C. Iliadis, “Hydrodynamic Models of Type I X-Ray Bursts: Metallicity Effects,” *The Astrophysical Journal Supplement Series*, vol. 189, no. 1, p. 204, 2010.
- [152] J. Keegans, C. L. Fryer, S. W. Jones, B. Côté, K. Belczynski, F. Herwig, M. Pignatari, A. M. Laird, and C. A. Diget, “Nucleosynthetic yields from neutron stars accreting in binary common envelopes,” *Monthly Notices of the Royal Astronomical Society*, vol. 485, no. 1, pp. 620–639, 2019.
- [153] C. Fröhlich, G. Martínez-Pinedo, M. Liebendörfer, F.-K. Thielemann, E. Bravo, W. R. Hix, K. Langanke, and N. T. Zinner, “Neutrino-Induced Nucleosynthesis of $A > 64$ Nuclei: The νp Process,” *Phys. Rev. Lett.*, vol. 96, p. 142502, 2006.
- [154] S. Wanajo, “The rp-Process in Neutrino-driven Winds,” *The Astrophysical Journal*, vol. 647, no. 2, pp. 1323–1340, 2006.
- [155] A. Psaltis, M. Jacobi, F. Montes, A. Arcones, C. J. Hansen, and H. Schatz, “Neutrino-driven Outflows and the Elemental Abundance Patterns of Very Metal-poor Stars,” *The Astrophysical Journal*, vol. 966, no. 1, p. 11, 2024.
- [156] Z. Xiong, G. Martínez-Pinedo, O. Just, and A. Sieverding, “Production of p Nuclei from r -Process Seeds: The νr Process,” *Phys. Rev. Lett.*, vol. 132, p. 192701, 2024.

- [157] B. Paxton, L. Bildsten, A. Dotter, F. Herwig, P. Lesaffre, and F. Timmes, “Modules for Experiments in Stellar Astrophysics (MESA),” *The Astrophysical Journal Supplement Series*, vol. 192, no. 1, p. 3, 2010.
- [158] F. Herwig, S. Diehl, C. L. Fryer, R. Hirschi, A. Hungerford, G. Magkotsios, M. Pignatari, G. Rockefeller, F. X. Timmes, P. Young, and M. E. Bennet, “Nucleosynthesis simulations for a wide range of nuclear production sites from NuGrid,” in *Nuclei in the Cosmos (NIC X)*, p. E23, 2008.
- [159] M. Pignatari and F. Herwig, “The NuGrid Research Platform: A Comprehensive Simulation Approach for Nuclear Astrophysics,” *Nuclear Physics News*, vol. 22, no. 4, pp. 18–23, 2012.
- [160] W. Rapp, J. Goerres, M. Wiescher, H. Schatz, and F. Kaeppeler, “Sensitivity of p-Process Nucleosynthesis to Nuclear Reaction Rates in a 25 M_⊙ Supernova Model,” *The Astrophysical Journal*, vol. 653, pp. 474 – 489, 2006.
- [161] T. Rauscher, N. Nishimura, R. Hirschi, G. Cescutti, A. S. J. Murphy, and A. Heger, “Uncertainties in the production of p nuclei in massive stars obtained from Monte Carlo variations,” *Monthly Notices of the Royal Astronomical Society*, vol. 463, no. 4, pp. 4153–4166, 2016.
- [162] N. Nishimura, T. Rauscher, R. Hirschi, A. S. J. Murphy, G. Cescutti, and C. Travaglio, “Uncertainties in the production of p nuclides in thermonuclear supernovae determined by Monte Carlo variations,” *Monthly Notices of the Royal Astronomical Society*, vol. 474, no. 3, pp. 3133–3139, 2017.
- [163] G. Gyürky, G. G. Kiss, Z. Elekes, Z. Fülöp, E. Somorjai, and T. Rauscher, “Proton capture cross-section of ^{106,108}Cd for the astrophysical p-process,” *Journal of Physics G: Nuclear and Particle Physics*, vol. 34, no. 5, p. 817, 2007.
- [164] G. Gyürky, M. Vakulenko, Z. Fülöp, Z. Halász, G. Kiss, E. Somorjai, and T. Szücs, “Cross section and reaction rate of ⁹²Mo(*p*, γ)⁹³Tc determined from thick target yield measurements,” *Nuclear Physics A*, vol. 922, pp. 112–125, 2014.
- [165] S. Harissopulos, A. Spyrou, V. Foteinou, M. Axiotis, G. Provas, and P. Demetriou, “Systematic study of proton capture reactions in medium-mass nuclei relevant to the *p* process: The case of ¹⁰³Rh and ^{113,115}In,” *Phys. Rev. C*, vol. 93, p. 025804, 2016.
- [166] J. Glorius, C. Langer, Z. Slavkovská, L. Bott, C. Brandau, B. Brückner, K. Blaum, X. Chen, S. Dababneh, T. Davinson, and et. al., “Approaching the Gamow Window with Stored Ions: Direct Measurement of ¹²⁴Xe(*p*, γ) in the ESR Storage Ring,” *Phys. Rev. Lett.*, vol. 122, p. 092701, 2019.
- [167] A. Psaltis, A. Khaliel, E.-M. Assimakopoulou, A. Kanellakopoulos, V. Lagaki, M. Lykiardopoulou, E. Malami, P. Tsavalas, A. Zyriliou, and T. J. Mertzimekis, “Cross-section measurements of radiative proton-capture reactions in ¹¹²Cd at energies of astrophysical interest,” *Phys. Rev. C*, vol. 99, p. 065807, 2019.

- [168] A. Simon, R. Kelmar, O. Olivas-Gomez, E. Churchman, P. Millican, C. S. Reingold, T. Anderson, A. M. Clark, N. Cooper, A. C. Dombos, and *et al.*, “First measurements of capture reactions for the γ -process using HECTOR,” *Journal of Physics: Conference Series*, vol. 1308, no. 1, p. 012020, 2019.
- [169] A. Banu, E. G. Meekins, J. A. Silano, H. J. Karwowski, and S. Goriely, “Photoneutron reaction cross section measurements on ^{94}Mo and ^{90}Zr relevant to the p -process nucleosynthesis,” *Phys. Rev. C*, vol. 99, p. 025802, 2019.
- [170] F. Heim, J. Mayer, M. Müller, P. Scholz, M. Weinert, and A. Zilges, “Experimental techniques to study the γ process for nuclear astrophysics at the Cologne accelerator laboratory,” *Nuclear Instruments and Methods in Physics Research Section A: Accelerators, Spectrometers, Detectors and Associated Equipment*, vol. 966, p. 163854, 2020.
- [171] H. Cheng, B.-H. Sun, L.-H. Zhu, M. Kusakabe, Y. Zheng, L.-C. He, T. Kajino, Z.-M. Niu, T.-X. Li, C.-B. Li, and *et al.*, “Measurements of $^{160}\text{Dy}(p, \gamma)$ at Energies Relevant for the Astrophysical γ Process,” *The Astrophysical Journal*, vol. 915, no. 2, p. 78, 2021.
- [172] P.-A. Söderström, A. Kuşoğlu, and D. Testov, “Prospect for measurements of (γ, n) reaction cross-sections of p -nuclei at ELI-NP,” *Frontiers in Astronomy and Space Sciences*, vol. 10, 2023.
- [173] G. Lotay, S. A. Gillespie, M. Williams, T. Rauscher, M. Alcorta, A. M. Amthor, C. A. Andreoiu, D. Baal, G. C. Ball, S. S. Bhattacharjee, and *et al.*, “First Direct Measurement of an Astrophysical p -Process Reaction Cross Section Using a Radioactive Ion Beam,” *Phys. Rev. Lett.*, vol. 127, p. 112701, 2021.
- [174] T. Rauscher and F.-K. Thielemann, “Tables of Nuclear Cross Sections and Reaction Rates: an Addendum to the Papaer “Astrophysical Reaction Rates from Statistical Model Calculations”,” *Atomic Data and Nuclear Data Tables*, vol. 79, no. 1, pp. 47–64, 2001.
- [175] Webpage hosted by the Experimental Astrophysics Group of Goethe University Frankfurt am Main at <https://exp-astro.physik.uni-frankfurt.de/fluxes/>. p -process fluxes tool. Accessed 01/19/2025.
- [176] M. Pignatari, F. Herwig, R. Hirschi, M. Bennett, G. Rockefeller, C. Fryer, F. X. Timmes, C. Ritter, A. Heger, S. Jones, U. Battino, A. Dotter, R. Trappitsch, S. Diehl, U. Frischknecht, A. Hungerford, G. Magkotsios, C. Travaglio, and P. Young, “NuGrid Stellar Data Set. I. Stellar Yields from H to Bi for Stars with Metallicities $Z = 0.02$ and $Z = 0.01$,” *The Astrophysical Journal Supplement Series*, vol. 225, no. 2, p. 24, 2016.
- [177] T. V. Lawson, M. Pignatari, R. J. Stancliffe, J. den Hartogh, S. Jones, C. L. Fryer, B. K. Gibson, and M. Lugaro, “Radioactive nuclei in the early Solar system: analysis of the 15 isotopes produced by core-collapse supernovae,” *Monthly Notices of the Royal Astronomical Society*, vol. 511, no. 1, pp. 886–902, 2021.
- [178] G. A. Krivonosov, O. L. Eklichev, B. A. Nemashkalo, V. E. Storizhko, and V. K. Chirt, “Radiative-Capture Cross Sections of Nuclides of Intermediate Atomic Weight for Low-Energy Protons,” *Bull. Russian Academy of Sciences - Physics*, vol. 41, p. 175, 1977.

- [179] G. Gyürky, Z. Fülöp, E. Somorjai, Z. Elekes, M. Kokkoris, S. Galanopoulos, P. Demetriou, S. Harissopoulos, S. Goriely, and T. Rauscher, “Se(p, γ) cross section measurements for p-process studies,” *Nuclear Physics A*, vol. 718, pp. 599–601, 2003.
- [180] Y. Skakun, S. Utenkov, V. Mishchenko, J. Farkas, Z. Fülöp, G. Gyürky, G. G. Kiss, E. Somorjai, and T. Rauscher, “Cross sections of low energy (p, γ) and (p, n)-reactions on selenium isotopes for the astrophysical γ -process,” *3rd Int. Conf. Cur. Prob. in Nucl. Phys. Atom. Ene.*, p. 207, 2010.
- [181] V. Foteinou, S. Harissopoulos, M. Axiotis, A. Lagoyannis, G. Provatas, A. Spyrou, G. Perdikakis, C. Zarkadas, and P. Demetriou, “Cross section measurements of proton capture reactions on Se isotopes relevant to the astrophysical p process,” *Phys. Rev. C*, vol. 97, p. 035806, 2018.
- [182] Z. Fülöp, A. Kiss, E. Somorjai, C. Rolfs, H. Trautvetter, T. Rauscher, and H. Oberhummer, “ $^{70}\text{Ge}(\alpha, \gamma)^{74}\text{Se}$ cross section measurements at energies of astrophysical interest,” *Zeitschrift für Physik A Hadrons and nuclei*, vol. 355, pp. 203–207, 1996.
- [183] I. Dillmann, M. Heil, F. Käppeler, T. Rauscher, and F.-K. Thielemann, “Experimental (n, γ) cross sections of the p-process nuclei ^{74}Se and ^{84}Sr ,” *Phys. Rev. C*, vol. 73, p. 015803, 2006.
- [184] A. Palmisano-Kyle, A. Spyrou, P. A. DeYoung, A. Dombos, P. Gastis, O. Olivas-Gomez, C. Harris, S. Liddick, S. M. Lyons, J. Pereira, and *et al.*, “Constraining the astrophysical p process: Cross section measurement of the $^{84}\text{Kr}(p, \gamma)^{85}\text{Rb}$ reaction in inverse kinematics,” *Phys. Rev. C*, vol. 105, p. 065804, 2022.
- [185] A. Tsantiri, A. Palmisano-Kyle, A. Spyrou, P. Mohr, H. C. Berg, P. A. DeYoung, A. C. Dombos, P. Gastis, E. C. Good, C. M. Harris, and *et al.*, “Cross-section measurement of the $^{82}\text{Kr}(p, \gamma)^{83}\text{Rb}$ reaction in inverse kinematics,” *Phys. Rev. C*, vol. 107, p. 035808, 2023.
- [186] G. B. Thomas Glasmacher, Alexandra Gade and J. Wei, “The Facility for Rare Isotope Beams: Providing New Opportunities for Science,” *Nuclear Physics News*, vol. 34, no. 3, pp. 5–12, 2024.
- [187] A. Gade and B. M. Sherrill, “NSCL and FRIB at Michigan State University: Nuclear science at the limits of stability,” *Physica Scripta*, vol. 91, no. 5, p. 053003, 2016.
- [188] C. Sumithrarachchi, Y. Liu, S. Rogers, S. Schwarz, G. Bollen, N. Gamage, A. Henriques, A. Lapierre, R. Ringle, I. Yandow, and *et al.*, “The new Batch Mode Ion Source for stand-alone operation at the Facility for Rare Isotope Beams (FRIB),” *Nuclear Instruments and Methods in Physics Research Section B: Beam Interactions with Materials and Atoms*, vol. 541, pp. 301–304, 2023.
- [189] A. C. Candia, G. Bollen, S. Campbell, A. Henriques, A. Lapierre, S. Nash, S. Schwarz, C. Sumithrarachchi, A. C. Villari, and K. A. Domnanich, “Preparation of a ^{73}As source sample for application in an offline ion source,” *Applied Radiation and Isotopes*, vol. 217, p. 111642, 2025.

- [190] A. Lapierre, G. Bollen, D. Crisp, S. W. Krause, L. E. Linhardt, K. Lund, S. Nash, R. Rencsok, R. Ringle, S. Schwarz, and *et al.*, “First two operational years of the electron-beam ion trap charge breeder at the National Superconducting Cyclotron Laboratory,” *Phys. Rev. Accel. Beams*, vol. 21, p. 053401, 2018.
- [191] S. Nash and *et al.*, “Commissioning of the FRIB/NSCL New ReA3 4-Rod Radio Frequency Quadrupole Accelerator,” in *Proc. NAPAC’19*, pp. 817–819, JACoW Publishing, Geneva, Switzerland, 2019.
- [192] A. Villari, G. Bollen, A. Henriques, A. Lapierre, S. Nash, R. Ringle, S. Schwarz, and C. Sumithrarachchi, “Gas stopping and reacceleration techniques at the Facility for Rare Isotope Beams (FRIB),” *Nuclear Instruments and Methods in Physics Research Section B: Beam Interactions with Materials and Atoms*, vol. 541, pp. 350–354, 2023.
- [193] A. Simon, S. Quinn, A. Spyrou, and *et. al.*, “SuN: Summing NaI(Tl) gamma-ray detector for capture reaction measurements,” *Nuclear Instruments and Methods in Physics Research Section A: Accelerators, Spectrometers, Detectors and Associated Equipment*, vol. 703, pp. 16–21, 2013.
- [194] S. Quinn, *Capture Cross Sections for the Astrophysical p Process*. PhD thesis, Michigan State University, 2015.
- [195] R. Hofstadter, “Alkali Halide Scintillation Counters,” *Phys. Rev.*, vol. 74, pp. 100–101, 1948.
- [196] G. Knoll, *Radiation Detection and Measurement (4th ed.)*. Hoboken, NJ: John Wiley, 2010.
- [197] C. Prokop, S. Liddick, B. Abromeit, A. Chemey, N. Larson, S. Suchyta, and J. Tompkins, “Digital data acquisition system implementation at the National Superconducting Cyclotron Laboratory,” *Nuclear Instruments and Methods in Physics Research Section A: Accelerators, Spectrometers, Detectors and Associated Equipment*, vol. 741, pp. 163–168, 2014.
- [198] A. Spyrou, H.-W. Becker, A. Lagoyannis, S. Harissopulos, and C. Rolfs, “Cross-section measurements of capture reactions relevant to the p process using a 4π γ -summing method,” *Phys. Rev. C*, vol. 76, p. 015802, Jul 2007.
- [199] E. Klopfer, J. Brett, P. A. DeYoung, A. C. Dombos, S. J. Quinn, A. Simon, and A. Spyrou, “SuNSCREEN: A cosmic-ray veto detector for capture-reaction measurements,” *Nuclear Instruments and Methods in Physics Research A*, vol. 788, pp. 5–8, 2015.
- [200] A. Spyrou, S. J. Quinn, A. Simon, T. Rauscher, and *et al.*, “Measurement of the $^{90,92}\text{Zr}(p,\gamma)^{91,93}\text{Nb}$ reactions for the nucleosynthesis of elements near $A = 90$,” *Phys. Rev. C*, vol. 88, p. 045802, 2013.
- [201] F. Naqvi, S. J. Quinn, A. Spyrou, A. Battaglia, M. Couder, P. A. DeYoung, A. C. Dombos, X. Fang, J. Görres, A. Kontos, and *et al.*, “Proton capture cross section of ^{72}Ge and astrophysical implications,” *Phys. Rev. C*, vol. 92, p. 025804, 2015.
- [202] A. Simon, M. Beard, A. Spyrou, S. J. Quinn, B. Bucher, M. Couder, P. A. DeYoung, A. C. Dombos, J. Görres, A. Kontos, and *et al.*, “Systematic study of (α, γ) reactions for stable nickel isotopes,” *Phys. Rev. C*, vol. 92, p. 025806, 2015.

- [203] R. Kelmar, A. Simon, O. Olivas-Gomez, P. Millican, C. S. Reingold, E. Churchman, A. M. Clark, S. L. Henderson, S. E. Kelly, D. Robertson, E. Stech, and W. P. Tan, “Searching for $(\gamma, \alpha)/(\gamma, n)$ branching points in the γ -process path near $A = 100$,” *Phys. Rev. C*, vol. 101, p. 015801, 2020.
- [204] J. Fallis, C. Akers, A. Laird, A. Simon, A. Spyrou, G. Christian, D. Connolly, U. Hager, D. Hutcheon, A. Lennarz, P. O’Malley, S. Quinn, J. Riley, A. Rojas, C. Ruiz, and M. Williams, “First measurement in the Gamow window of a reaction for the γ -process in inverse kinematics: $^{76}\text{Se}(\alpha, \gamma)^{80}\text{Kr}$,” *Physics Letters B*, vol. 807, p. 135575, 2020.
- [205] S. Quinn, A. Spyrou, A. Simon, A. Battaglia, M. Bowers, B. Bucher, C. Casarella, M. Couder, P. DeYoung, A. Dombos, and *et al.*, “First application of the γ -summing technique in inverse kinematics,” *Nuclear Instruments and Methods in Physics Research Section A: Accelerators, Spectrometers, Detectors and Associated Equipment*, vol. 757, pp. 62–66, 2014.
- [206] S. Quinn, A. Spyrou, A. Simon, and *et. al.*, “First application of the gamma-summing technique in inverse kinematics,” *Nuclear Instruments and Methods in Physics Research Section A Accelerators Spectrometers Detectors and Associated Equipment*, vol. 757, p. 62–66, 2014.
- [207] O. Tarasov, D. Bazin, M. Hausmann, M. Kuchera, P. Ostroumov, M. Portillo, B. Sherrill, K. Tarasova, and T. Zhang, “LISE cute++, the latest generation of the LISE ++ package, to simulate rare isotope production with fragment-separators,” *Nuclear Instruments and Methods in Physics Research Section B: Beam Interactions with Materials and Atoms*, vol. 541, pp. 4–7, 2023.
- [208] L. Kirsch and L. Bernstein, “RAINIER: A simulation tool for distributions of excited nuclear states and cascade fluctuations,” *Nuclear Instruments and Methods in Physics Research Section A: Accelerators, Spectrometers, Detectors and Associated Equipment*, vol. 892, pp. 30–40, 2018.
- [209] S. Agostinelli, J. Allison, K. Amako, J. Apostolakis, H. Araujo, P. Arce, M. Asai, D. Axen, S. Banerjee, and G. B. *et.al.*, “Geant4—a simulation toolkit,” *Nuclear Instruments and Methods in Physics Research Section A: Accelerators, Spectrometers, Detectors and Associated Equipment*, vol. 506, no. 3, pp. 250–303, 2003.
- [210] A. C. Dombos, *β -Decay Total Absorption Spectroscopy Around $A = 100$ -110 Relevant to Nuclear Structure and the Astrophysical r Process*. PhD thesis, Michigan State University, 2015.
- [211] F. James, “MINUIT Function Minimization and Error Analysis: Reference Manual Version 94.1,” tech. rep., CERN, 1994.
- [212] R. Brun and F. Rademakers, “ROOT — An object oriented data analysis framework,” *Nuclear Instruments and Methods in Physics Research Section A: Accelerators, Spectrometers, Detectors and Associated Equipment*, vol. 389, no. 1, pp. 81–86, 1997. *New Computing Techniques in Physics Research V*.
- [213] T. von Egidy and D. Bucurescu, “Experimental energy-dependent nuclear spin distributions,” *Phys. Rev. C*, vol. 80, p. 054310, 2009.

- [214] R. Hoffman, F. Dietrich, R. Bauer, K. Kelley, and M. Mustafa, “Neutron and Charged-Particle Induced Cross Sections for Radiochemistry in the Region of Bromine and Krypton,” tech. rep., Lawrence Livermore National Lab. (LLNL), Livermore, CA (United States, 2004.
- [215] M. Guttormsen, R. Chankova, U. Agvaanluvsan, and et. al., “Radiative strength functions in $^{93-98}\text{Mo}$,” *Phys. Rev. C*, vol. 71, p. 044307, 2005.
- [216] A. Gelman, J. B. Carlin, H. S. Stern, D. B. Dunson, A. Vehtari, and D. B. Rubin, *Bayesian Data Analysis*. Chapman and Hall/CRC, 3rd ed., 2013.
- [217] C. D. Pruitt, J. E. Escher, and R. Rahman, “Uncertainty-quantified phenomenological optical potentials for single-nucleon scattering,” *Phys. Rev. C*, vol. 107, p. 014602, Jan 2023.
- [218] J. F. Ziegler, M. Ziegler, and J. Biersack, “SRIM – The stopping and range of ions in matter (2010),” *Nuclear Instruments and Methods in Physics Research Section B: Beam Interactions with Materials and Atoms*, vol. 268, no. 11, pp. 1818–1823, 2010. 19th International Conference on Ion Beam Analysis.
- [219] G. Gyürky, E. Somorjai, Z. Fülöp, S. Harissopulos, P. Demetriou, and T. Rauscher, “Proton capture cross section of Sr isotopes and their importance for nucleosynthesis of proton-rich nuclides,” *Phys. Rev. C*, vol. 64, p. 065803, 2001.
- [220] N. Grevesse and A. Noels, “Atomic data and the spectrum of the solar photosphere,” in *In: Origin and Evolution of the elements*, 1993.
- [221] I. Dillmann, M. Heil, F. Käppeler, R. Plag, T. Rauscher, and F. K. Thielemann, “KADoNiS-The Karlsruhe Astrophysical Database of Nucleosynthesis in Stars,” in *Capture Gamma-Ray Spectroscopy and Related Topics* (A. Woehr and A. Aprahamian, eds.), vol. 819 of *American Institute of Physics Conference Series*, pp. 123–127, AIP, 2006.
- [222] R. H. Cyburt, A. M. Amthor, R. Ferguson, Z. Meisel, K. Smith, S. Warren, A. Heger, R. D. Hoffman, T. Rauscher, A. Sakharuk, H. Schatz, F. K. Thielemann, and M. Wiescher, “The JINA REACLIB Database: Its Recent Updates and Impact on Type-I X-Ray Bursts,” *The Astrophysical Journal Supplement Series*, vol. 189, no. 1, p. 240, 2010.
- [223] D. Kasen, F. K. Röpkke, and S. E. Woosley, “The diversity of type Ia supernovae from broken symmetries,” *Nature*, vol. 460, no. 7257, pp. 869–872, 2009.
- [224] I. Domínguez, E. Bravo, L. Piersanti, O. Straniero, and A. Tornambé, “Supernovae and Dark Energy,” in *Cosmology Across Cultures* (J. Rubiño-Martín, J. Belmonte, F. Prada, and A. Alberdi, eds.), vol. 409 of *Astronomical Society of the Pacific Conference Series*, p. 42, 2009.
- [225] Travaglio, C., Hillebrandt, W., Reinecke, M., and Thielemann, F.-K., “Nucleosynthesis in multi-dimensional sn ia explosions*,” *Astronomy & Astrophysics*, vol. 425, no. 3, pp. 1029–1040, 2004.
- [226] K. Maeda, F. Röpkke, M. Fink, W. Hillebrandt, C. Travaglio, and F.-K. Thielemann, “Nucleosynthesis in Two-Dimensional Delayed Detonation Models of Type Ia Supernova Explosions,” *The Astrophysical Journal*, vol. 712, no. 1, p. 624, 2010.

APPENDIX

TALYS SCORES FOR THE $^{73}\text{As}(p, \gamma)^{74}\text{Se}$ REACTION

Table .1 The TALYS model parameters and scores

Model #	NLD	γ^{SF} E1	γ^{SF} M1	γ^{SF} upbend	OMP	TAS Score	SoS Score	Mul Score	Cross Section Score (Eq. 6.2))	Total Score
0	1	1	1	y	JLM	0.4341	0.1215	0.1064	0.6233	3.50e-03
1	1	1	1	y	default	0.4341	0.1215	0.1064	0.4702	2.64e-03
2	1	1	1	n	JLM	0.4341	0.1215	0.1064	0.6233	3.50e-03
3	1	1	1	n	default	0.4341	0.1215	0.1064	0.4702	2.64e-03
4	1	1	2	y	JLM	0.3805	0.1132	0.0982	0.1828	7.73e-04
5	1	1	2	y	default	0.3805	0.1132	0.0982	0.1284	5.43e-04
6	1	1	2	n	JLM	0.3805	0.1132	0.0982	0.1828	7.73e-04
7	1	1	2	n	default	0.3805	0.1132	0.0982	0.1284	5.43e-04
8	1	1	3	y	JLM	0.6034	0.2326	0.3122	0.6610	2.90e-02
9	1	1	3	y	default	0.6034	0.2326	0.3122	0.4984	2.18e-02
10	1	1	3	n	JLM	0.5111	0.1921	0.1852	0.5090	9.26e-03
11	1	1	3	n	default	0.5111	0.1921	0.1852	0.3717	6.76e-03
12	1	2	1	y	JLM	0.6068	0.2244	0.2058	0.1150	3.22e-03
13	1	2	1	y	default	0.6068	0.2244	0.2058	0.3221	9.03e-03
14	1	2	1	n	JLM	0.6068	0.2244	0.2058	0.1150	3.22e-03
15	1	2	1	n	default	0.6068	0.2244	0.2058	0.3221	9.03e-03
16	1	2	2	y	JLM	0.5904	0.2119	0.1643	0.0739	1.52e-03
17	1	2	2	y	default	0.5904	0.2119	0.1643	0.2417	4.97e-03
18	1	2	2	n	JLM	0.5904	0.2119	0.1643	0.0739	1.52e-03
19	1	2	2	n	default	0.5904	0.2119	0.1643	0.2417	4.97e-03
20	1	2	3	y	JLM	0.6513	0.2892	0.3077	0.1092	6.33e-03
21	1	2	3	y	default	0.6513	0.2892	0.3077	0.3127	1.81e-02
22	1	2	3	n	JLM	0.6650	0.2708	0.2538	0.1344	6.14e-03
23	1	2	3	n	default	0.6650	0.2708	0.2538	0.3566	1.63e-02
24	1	3	1	y	JLM	0.1251	0.0336	0.0058	0.9894	2.39e-05
25	1	3	1	y	default	0.1251	0.0336	0.0058	0.9743	2.36e-05
26	1	3	1	n	JLM	0.1251	0.0336	0.0058	0.9894	2.39e-05
27	1	3	1	n	default	0.1251	0.0336	0.0058	0.9743	2.36e-05
28	1	3	2	y	JLM	0.1196	0.0306	0.0049	0.9991	1.79e-05
29	1	3	2	y	default	0.1196	0.0306	0.0049	0.9335	1.68e-05
30	1	3	2	n	JLM	0.1196	0.0306	0.0049	0.9991	1.79e-05
31	1	3	2	n	default	0.1196	0.0306	0.0049	0.9335	1.68e-05

Table .1 (cont'd)

32	1	3	3	y	JLM	0.1893	0.0519	0.0171	0.9818	1.65e-04
33	1	3	3	y	default	0.1893	0.0519	0.0171	0.9817	1.65e-04
34	1	3	3	n	JLM	0.1570	0.0410	0.0084	0.9993	5.38e-05
35	1	3	3	n	default	0.1570	0.0410	0.0084	0.9380	5.05e-05
36	1	4	1	y	JLM	0.2687	0.0755	0.0215	0.9545	4.17e-04
37	1	4	1	y	default	0.2687	0.0755	0.0215	0.8232	3.60e-04
38	1	4	1	n	JLM	0.2687	0.0755	0.0215	0.9545	4.17e-04
39	1	4	1	n	default	0.2687	0.0755	0.0215	0.8232	3.60e-04
40	1	4	2	y	JLM	0.2277	0.0663	0.0183	0.7658	2.12e-04
41	1	4	2	y	default	0.2277	0.0663	0.0183	0.5993	1.66e-04
42	1	4	2	n	JLM	0.2277	0.0663	0.0183	0.7658	2.12e-04
43	1	4	2	n	default	0.2277	0.0663	0.0183	0.5993	1.66e-04
44	1	4	3	y	JLM	0.3996	0.1296	0.0739	0.9685	3.71e-03
45	1	4	3	y	default	0.3996	0.1296	0.0739	0.8437	3.23e-03
46	1	4	3	n	JLM	0.3407	0.1024	0.0397	0.8989	1.25e-03
47	1	4	3	n	default	0.3407	0.1024	0.0397	0.7431	1.03e-03
48	1	5	1	y	JLM	0.5923	0.1996	0.1673	0.9989	1.98e-02
49	1	5	1	y	default	0.5923	0.1996	0.1673	0.9471	1.87e-02
50	1	5	1	n	JLM	0.5923	0.1996	0.1673	0.9989	1.98e-02
51	1	5	1	n	default	0.5923	0.1996	0.1673	0.9471	1.87e-02
52	1	5	2	y	JLM	0.5877	0.2218	0.2642	0.9084	3.13e-02
53	1	5	2	y	default	0.5877	0.2218	0.2642	0.7550	2.60e-02
54	1	5	2	n	JLM	0.5877	0.2218	0.2642	0.9084	3.13e-02
55	1	5	2	n	default	0.5877	0.2218	0.2642	0.7550	2.60e-02
56	1	5	3	y	JLM	0.6936	0.3048	0.4075	0.9966	8.58e-02
57	1	5	3	y	default	0.6936	0.3048	0.4075	0.9577	8.25e-02
58	1	5	3	n	JLM	0.6530	0.2735	0.3104	0.9926	5.50e-02
59	1	5	3	n	default	0.6530	0.2735	0.3104	0.8992	4.98e-02
60	1	6	1	y	JLM	0.2837	0.0897	0.0315	0.9846	7.90e-04
61	1	6	1	y	default	0.2837	0.0897	0.0315	0.8793	7.05e-04
62	1	6	1	n	JLM	0.2837	0.0897	0.0315	0.9846	7.90e-04
63	1	6	1	n	default	0.2837	0.0897	0.0315	0.8793	7.05e-04
64	1	6	2	y	JLM	0.2792	0.0873	0.0374	0.8439	7.69e-04
65	1	6	2	y	default	0.2792	0.0873	0.0374	0.6795	6.19e-04
66	1	6	2	n	JLM	0.2792	0.0873	0.0374	0.8439	7.69e-04
67	1	6	2	n	default	0.2792	0.0873	0.0374	0.6795	6.19e-04
68	1	6	3	y	JLM	0.4293	0.1508	0.1118	0.9919	7.18e-03

Table .1 (cont'd)

69	1	6	3	y	default	0.4293	0.1508	0.1118	0.8962	6.48e-03
70	1	6	3	n	JLM	0.3489	0.1266	0.0697	0.9483	2.92e-03
71	1	6	3	n	default	0.3489	0.1266	0.0697	0.8105	2.50e-03
72	1	7	1	y	JLM	0.2374	0.0712	0.0260	0.9990	4.39e-04
73	1	7	1	y	default	0.2374	0.0712	0.0260	0.9310	4.09e-04
74	1	7	1	n	JLM	0.2374	0.0712	0.0260	0.9990	4.39e-04
75	1	7	1	n	default	0.2374	0.0712	0.0260	0.9310	4.09e-04
76	1	7	2	y	JLM	0.1838	0.0661	0.0234	0.8592	2.44e-04
77	1	7	2	y	default	0.1838	0.0661	0.0234	0.6940	1.97e-04
78	1	7	2	n	JLM	0.1838	0.0661	0.0234	0.8592	2.44e-04
79	1	7	2	n	default	0.1838	0.0661	0.0234	0.6940	1.97e-04
80	1	7	3	y	JLM	0.3343	0.1170	0.0782	0.9990	3.06e-03
81	1	7	3	y	default	0.3343	0.1170	0.0782	0.9435	2.89e-03
82	1	7	3	n	JLM	0.2825	0.0976	0.0486	0.9848	1.32e-03
83	1	7	3	n	default	0.2825	0.0976	0.0486	0.8764	1.17e-03
84	1	8	1	y	JLM	0.2741	0.0703	0.0227	0.8199	3.59e-04
85	1	8	1	y	default	0.2741	0.0703	0.0227	0.9766	4.27e-04
86	1	8	1	n	JLM	0.2377	0.0656	0.0190	0.8515	2.52e-04
87	1	8	1	n	default	0.2377	0.0656	0.0190	0.9869	2.92e-04
88	1	8	2	y	JLM	0.2891	0.0690	0.0234	0.8010	3.75e-04
89	1	8	2	y	default	0.2891	0.0690	0.0234	0.9693	4.53e-04
90	1	8	2	n	JLM	0.2507	0.0662	0.0206	0.8335	2.85e-04
91	1	8	2	n	default	0.2507	0.0662	0.0206	0.9812	3.36e-04
92	1	8	3	y	JLM	0.3842	0.1075	0.0689	0.7990	2.27e-03
93	1	8	3	y	default	0.3842	0.1075	0.0689	0.9696	2.76e-03
94	1	8	3	n	JLM	0.3022	0.0826	0.0311	0.9057	7.03e-04
95	1	8	3	n	default	0.3022	0.0826	0.0311	0.9983	7.74e-04
96	1	9	1	y	JLM	0.3274	0.0837	0.0357	0.9823	9.62e-04
97	1	9	1	y	default	0.3274	0.0837	0.0357	0.8748	8.56e-04
98	1	9	1	n	JLM	0.3274	0.0837	0.0357	0.9823	9.62e-04
99	1	9	1	n	default	0.3274	0.0837	0.0357	0.8748	8.56e-04
100	1	9	2	y	JLM	0.3239	0.0785	0.0291	0.8855	6.55e-04
101	1	9	2	y	default	0.3239	0.0785	0.0291	0.7287	5.39e-04
102	1	9	2	n	JLM	0.3239	0.0785	0.0291	0.8855	6.55e-04
103	1	9	2	n	default	0.3239	0.0785	0.0291	0.7287	5.39e-04
104	1	9	3	y	JLM	0.4561	0.1359	0.0898	0.9903	5.51e-03
105	1	9	3	y	default	0.4561	0.1359	0.0898	0.8920	4.96e-03

Table .1 (cont'd)

106	1	9	3	n	JLM	0.3966	0.1131	0.0513	0.9443	2.17e-03
107	1	9	3	n	default	0.3966	0.1131	0.0513	0.8052	1.85e-03
108	2	1	1	y	JLM	0.7550	0.3980	0.4213	0.6055	7.66e-02
109	2	1	1	y	default	0.7550	0.3980	0.4213	0.8607	1.09e-01
110	2	1	1	n	JLM	0.7550	0.3980	0.4213	0.6055	7.66e-02
111	2	1	1	n	default	0.7550	0.3980	0.4213	0.8607	1.09e-01
112	2	1	2	y	JLM	0.7579	0.4332	0.6112	0.9987	2.00e-01
113	2	1	2	y	default	0.7579	0.4332	0.6112	0.9278	1.86e-01
114	2	1	2	n	JLM	0.7579	0.4332	0.6112	0.9987	2.00e-01
115	2	1	2	n	default	0.7579	0.4332	0.6112	0.9278	1.86e-01
116	2	1	3	y	JLM	0.8004	0.5198	0.7146	0.6417	1.91e-01
117	2	1	3	y	default	0.8004	0.5198	0.7146	0.8870	2.64e-01
118	2	1	3	n	JLM	0.8017	0.4793	0.6168	0.7648	1.81e-01
119	2	1	3	n	default	0.8017	0.4793	0.6168	0.9549	2.26e-01
120	2	2	1	y	JLM	0.7800	0.4271	0.3763	0.0002	3.10e-05
121	2	2	1	y	default	0.7800	0.4271	0.3763	0.0052	6.47e-04
122	2	2	1	n	JLM	0.7800	0.4271	0.3763	0.0002	3.10e-05
123	2	2	1	n	default	0.7800	0.4271	0.3763	0.0052	6.47e-04
124	2	2	2	y	JLM	0.7604	0.4153	0.3203	0.0001	1.04e-05
125	2	2	2	y	default	0.7604	0.4153	0.3203	0.0028	2.85e-04
126	2	2	2	n	JLM	0.7604	0.4153	0.3203	0.0001	1.04e-05
127	2	2	2	n	default	0.7604	0.4153	0.3203	0.0028	2.85e-04
128	2	2	3	y	JLM	0.8162	0.4802	0.4998	0.0003	5.33e-05
129	2	2	3	y	default	0.8162	0.4802	0.4998	0.0055	1.08e-03
130	2	2	3	n	JLM	0.8090	0.4547	0.4203	0.0004	5.67e-05
131	2	2	3	n	default	0.8090	0.4547	0.4203	0.0068	1.05e-03
132	2	3	1	y	JLM	0.3597	0.1108	0.0350	0.1684	2.35e-04
133	2	3	1	y	default	0.3597	0.1108	0.0350	0.4097	5.72e-04
134	2	3	1	n	JLM	0.3597	0.1108	0.0350	0.1684	2.35e-04
135	2	3	1	n	default	0.3597	0.1108	0.0350	0.4097	5.72e-04
136	2	3	2	y	JLM	0.3119	0.1065	0.0336	0.2385	2.66e-04
137	2	3	2	y	default	0.3119	0.1065	0.0336	0.5084	5.67e-04
138	2	3	2	n	JLM	0.3119	0.1065	0.0336	0.2385	2.66e-04
139	2	3	2	n	default	0.3119	0.1065	0.0336	0.5084	5.67e-04
140	2	3	3	y	JLM	0.4162	0.1681	0.1134	0.1836	1.46e-03
141	2	3	3	y	default	0.4162	0.1681	0.1134	0.4344	3.45e-03
142	2	3	3	n	JLM	0.3803	0.1359	0.0534	0.2441	6.74e-04

Table .1 (cont'd)

143	2	3	3	n	default	0.3803	0.1359	0.0534	0.5169	1.43e-03
144	2	4	1	y	JLM	0.5390	0.2134	0.0879	0.3580	3.62e-03
145	2	4	1	y	default	0.5390	0.2134	0.0879	0.6466	6.54e-03
146	2	4	1	n	JLM	0.5390	0.2134	0.0879	0.3580	3.62e-03
147	2	4	1	n	default	0.5390	0.2134	0.0879	0.6466	6.54e-03
148	2	4	2	y	JLM	0.4906	0.2055	0.0891	0.6688	6.01e-03
149	2	4	2	y	default	0.4906	0.2055	0.0891	0.9020	8.10e-03
150	2	4	2	n	JLM	0.4906	0.2055	0.0891	0.6688	6.01e-03
151	2	4	2	n	default	0.4906	0.2055	0.0891	0.9020	8.10e-03
152	2	4	3	y	JLM	0.6107	0.3340	0.3055	0.3855	2.40e-02
153	2	4	3	y	default	0.6107	0.3340	0.3055	0.6773	4.22e-02
154	2	4	3	n	JLM	0.5955	0.2653	0.1452	0.4893	1.12e-02
155	2	4	3	n	default	0.5955	0.2653	0.1452	0.7722	1.77e-02
156	2	5	1	y	JLM	0.7854	0.4463	0.4802	0.0965	1.62e-02
157	2	5	1	y	default	0.7854	0.4463	0.4802	0.2880	4.85e-02
158	2	5	1	n	JLM	0.7854	0.4463	0.4802	0.0965	1.62e-02
159	2	5	1	n	default	0.7854	0.4463	0.4802	0.2880	4.85e-02
160	2	5	2	y	JLM	0.7968	0.5018	0.6083	0.2555	6.22e-02
161	2	5	2	y	default	0.7968	0.5018	0.6083	0.5316	1.29e-01
162	2	5	2	n	JLM	0.7968	0.5018	0.6083	0.2555	6.22e-02
163	2	5	2	n	default	0.7968	0.5018	0.6083	0.5316	1.29e-01
164	2	5	3	y	JLM	0.8128	0.5518	0.6866	0.1058	3.26e-02
165	2	5	3	y	default	0.8128	0.5518	0.6866	0.3068	9.45e-02
166	2	5	3	n	JLM	0.8179	0.5174	0.6195	0.1423	3.73e-02
167	2	5	3	n	default	0.8179	0.5174	0.6195	0.3702	9.71e-02
168	2	6	1	y	JLM	0.6189	0.2926	0.1990	0.2232	8.04e-03
169	2	6	1	y	default	0.6189	0.2926	0.1990	0.4881	1.76e-02
170	2	6	1	n	JLM	0.6189	0.2926	0.1990	0.2232	8.04e-03
171	2	6	1	n	default	0.6189	0.2926	0.1990	0.4881	1.76e-02
172	2	6	2	y	JLM	0.5958	0.2853	0.2310	0.4601	1.81e-02
173	2	6	2	y	default	0.5958	0.2853	0.2310	0.7467	2.93e-02
174	2	6	2	n	JLM	0.5958	0.2853	0.2310	0.4601	1.81e-02
175	2	6	2	n	default	0.5958	0.2853	0.2310	0.7467	2.93e-02
176	2	6	3	y	JLM	0.6786	0.3997	0.4442	0.2425	2.92e-02
177	2	6	3	y	default	0.6786	0.3997	0.4442	0.5156	6.21e-02
178	2	6	3	n	JLM	0.6584	0.3403	0.2727	0.3172	1.94e-02
179	2	6	3	n	default	0.6584	0.3403	0.2727	0.6048	3.69e-02

Table .1 (cont'd)

180	2	7	1	y	JLM	0.5634	0.2482	0.1750	0.2049	5.02e-03
181	2	7	1	y	default	0.5634	0.2482	0.1750	0.4641	1.14e-02
182	2	7	1	n	JLM	0.5634	0.2482	0.1750	0.2049	5.02e-03
183	2	7	1	n	default	0.5634	0.2482	0.1750	0.4641	1.14e-02
184	2	7	2	y	JLM	0.5225	0.2405	0.1976	0.5237	1.30e-02
185	2	7	2	y	default	0.5225	0.2405	0.1976	0.8019	1.99e-02
186	2	7	2	n	JLM	0.5225	0.2405	0.1976	0.5237	1.30e-02
187	2	7	2	n	default	0.5225	0.2405	0.1976	0.8019	1.99e-02
188	2	7	3	y	JLM	0.6292	0.3374	0.4192	0.2229	1.98e-02
189	2	7	3	y	default	0.6292	0.3374	0.4192	0.4909	4.37e-02
190	2	7	3	n	JLM	0.6231	0.2853	0.2759	0.2929	1.44e-02
191	2	7	3	n	default	0.6231	0.2853	0.2759	0.5782	2.84e-02
192	2	8	1	y	JLM	0.5668	0.2143	0.1036	0.0409	5.15e-04
193	2	8	1	y	default	0.5668	0.2143	0.1036	0.1641	2.07e-03
194	2	8	1	n	JLM	0.5088	0.1901	0.0675	0.0467	3.05e-04
195	2	8	1	n	default	0.5088	0.1901	0.0675	0.1790	1.17e-03
196	2	8	2	y	JLM	0.5212	0.2127	0.1029	0.0368	4.20e-04
197	2	8	2	y	default	0.5212	0.2127	0.1029	0.1530	1.75e-03
198	2	8	2	n	JLM	0.5401	0.1860	0.0694	0.0421	2.93e-04
199	2	8	2	n	default	0.5401	0.1860	0.0694	0.1670	1.16e-03
200	2	8	3	y	JLM	0.5994	0.2829	0.2509	0.0451	1.92e-03
201	2	8	3	y	default	0.5994	0.2829	0.2509	0.1757	7.48e-03
202	2	8	3	n	JLM	0.5556	0.2240	0.1045	0.0703	9.15e-04
203	2	8	3	n	default	0.5556	0.2240	0.1045	0.2348	3.05e-03
204	2	9	1	y	JLM	0.6245	0.2380	0.1091	0.2357	3.82e-03
205	2	9	1	y	default	0.6245	0.2380	0.1091	0.5039	8.17e-03
206	2	9	1	n	JLM	0.6245	0.2380	0.1091	0.2357	3.82e-03
207	2	9	1	n	default	0.6245	0.2380	0.1091	0.5039	8.17e-03
208	2	9	2	y	JLM	0.6088	0.2378	0.1166	0.4106	6.93e-03
209	2	9	2	y	default	0.6088	0.2378	0.1166	0.6999	1.18e-02
210	2	9	2	n	JLM	0.6088	0.2378	0.1166	0.4106	6.93e-03
211	2	9	2	n	default	0.6088	0.2378	0.1166	0.6999	1.18e-02
212	2	9	3	y	JLM	0.6654	0.3563	0.3242	0.2558	1.97e-02
213	2	9	3	y	default	0.6654	0.3563	0.3242	0.5318	4.09e-02
214	2	9	3	n	JLM	0.6953	0.2917	0.1659	0.3336	1.12e-02
215	2	9	3	n	default	0.6953	0.2917	0.1659	0.6221	2.09e-02
216	3	1	1	y	JLM	0.6586	0.2592	0.2887	0.9991	4.92e-02

Table .1 (cont'd)

217	3	1	1	y	default	0.6586	0.2592	0.2887	0.9337	4.60e-02
218	3	1	1	n	JLM	0.6586	0.2592	0.2887	0.9991	4.92e-02
219	3	1	1	n	default	0.6586	0.2592	0.2887	0.9337	4.60e-02
220	3	1	2	y	JLM	0.6616	0.2761	0.3993	0.6630	4.84e-02
221	3	1	2	y	default	0.6616	0.2761	0.3993	0.4979	3.63e-02
222	3	1	2	n	JLM	0.6616	0.2761	0.3993	0.6630	4.84e-02
223	3	1	2	n	default	0.6616	0.2761	0.3993	0.4979	3.63e-02
224	3	1	3	y	JLM	0.7736	0.4157	0.6112	0.9980	1.96e-01
225	3	1	3	y	default	0.7736	0.4157	0.6112	0.9497	1.87e-01
226	3	1	3	n	JLM	0.7523	0.3517	0.4410	0.9817	1.15e-01
227	3	1	3	n	default	0.7523	0.3517	0.4410	0.8678	1.01e-01
228	3	2	1	y	JLM	0.7595	0.3203	0.2998	0.0124	9.02e-04
229	3	2	1	y	default	0.7595	0.3203	0.2998	0.0747	5.45e-03
230	3	2	1	n	JLM	0.7595	0.3203	0.2998	0.0124	9.02e-04
231	3	2	1	n	default	0.7595	0.3203	0.2998	0.0747	5.45e-03
232	3	2	2	y	JLM	0.7561	0.3050	0.2614	0.0066	3.98e-04
233	3	2	2	y	default	0.7561	0.3050	0.2614	0.0488	2.94e-03
234	3	2	2	n	JLM	0.7561	0.3050	0.2614	0.0066	3.98e-04
235	3	2	2	n	default	0.7561	0.3050	0.2614	0.0488	2.94e-03
236	3	2	3	y	JLM	0.7646	0.3777	0.4196	0.0115	1.40e-03
237	3	2	3	y	default	0.7646	0.3777	0.4196	0.0715	8.66e-03
238	3	2	3	n	JLM	0.7734	0.3516	0.3426	0.0152	1.41e-03
239	3	2	3	n	default	0.7734	0.3516	0.3426	0.0859	8.01e-03
240	3	3	1	y	JLM	0.2005	0.0523	0.0119	0.7192	9.00e-05
241	3	3	1	y	default	0.2005	0.0523	0.0119	0.9326	1.17e-04
242	3	3	1	n	JLM	0.2005	0.0523	0.0119	0.7192	9.00e-05
243	3	3	1	n	default	0.2005	0.0523	0.0119	0.9326	1.17e-04
244	3	3	2	y	JLM	0.1736	0.0496	0.0111	0.8170	7.82e-05
245	3	3	2	y	default	0.1736	0.0496	0.0111	0.9769	9.35e-05
246	3	3	2	n	JLM	0.1736	0.0496	0.0111	0.8170	7.82e-05
247	3	3	2	n	default	0.1736	0.0496	0.0111	0.9769	9.35e-05
248	3	3	3	y	JLM	0.2664	0.0819	0.0372	0.6899	5.59e-04
249	3	3	3	y	default	0.2664	0.0819	0.0372	0.9182	7.45e-04
250	3	3	3	n	JLM	0.2530	0.0680	0.0195	0.7980	2.68e-04
251	3	3	3	n	default	0.2530	0.0680	0.0195	0.9704	3.26e-04
252	3	4	1	y	JLM	0.3782	0.1190	0.0425	0.9250	1.77e-03
253	3	4	1	y	default	0.3782	0.1190	0.0425	0.9993	1.91e-03

Table .1 (cont'd)

254	3	4	1	n	JLM	0.3782	0.1190	0.0425	0.9250	1.77e-03
255	3	4	1	n	default	0.3782	0.1190	0.0425	0.9993	1.91e-03
256	3	4	2	y	JLM	0.3534	0.1071	0.0387	0.9960	1.46e-03
257	3	4	2	y	default	0.3534	0.1071	0.0387	0.9108	1.33e-03
258	3	4	2	n	JLM	0.3534	0.1071	0.0387	0.9960	1.46e-03
259	3	4	2	n	default	0.3534	0.1071	0.0387	0.9108	1.33e-03
260	3	4	3	y	JLM	0.5235	0.2008	0.1438	0.9036	1.37e-02
261	3	4	3	y	default	0.5235	0.2008	0.1438	0.9984	1.51e-02
262	3	4	3	n	JLM	0.4456	0.1513	0.0669	0.9718	4.39e-03
263	3	4	3	n	default	0.4456	0.1513	0.0669	0.9886	4.46e-03
264	3	5	1	y	JLM	0.7473	0.3399	0.3579	0.5619	5.11e-02
265	3	5	1	y	default	0.7473	0.3399	0.3579	0.8319	7.56e-02
266	3	5	1	n	JLM	0.7473	0.3399	0.3579	0.5619	5.11e-02
267	3	5	1	n	default	0.7473	0.3399	0.3579	0.8319	7.56e-02
268	3	5	2	y	JLM	0.7784	0.3781	0.4683	0.8279	1.14e-01
269	3	5	2	y	default	0.7784	0.3781	0.4683	0.9811	1.35e-01
270	3	5	2	n	JLM	0.7784	0.3781	0.4683	0.8279	1.14e-01
271	3	5	2	n	default	0.7784	0.3781	0.4683	0.9811	1.35e-01
272	3	5	3	y	JLM	0.8001	0.4469	0.6076	0.5356	1.16e-01
273	3	5	3	y	default	0.8001	0.4469	0.6076	0.8138	1.77e-01
274	3	5	3	n	JLM	0.8018	0.4171	0.5065	0.6387	1.08e-01
275	3	5	3	n	default	0.8018	0.4171	0.5065	0.8866	1.50e-01
276	3	6	1	y	JLM	0.4608	0.1674	0.1082	0.8020	6.69e-03
277	3	6	1	y	default	0.4608	0.1674	0.1082	0.9710	8.10e-03
278	3	6	1	n	JLM	0.4608	0.1674	0.1082	0.8020	6.69e-03
279	3	6	1	n	default	0.4608	0.1674	0.1082	0.9710	8.10e-03
280	3	6	2	y	JLM	0.4846	0.1600	0.1011	0.9734	7.63e-03
281	3	6	2	y	default	0.4846	0.1600	0.1011	0.9876	7.74e-03
282	3	6	2	n	JLM	0.4846	0.1600	0.1011	0.9734	7.63e-03
283	3	6	2	n	default	0.4846	0.1600	0.1011	0.9876	7.74e-03
284	3	6	3	y	JLM	0.5915	0.2519	0.2618	0.7745	3.02e-02
285	3	6	3	y	default	0.5915	0.2519	0.2618	0.9608	3.75e-02
286	3	6	3	n	JLM	0.5581	0.2189	0.1760	0.8735	1.88e-02
287	3	6	3	n	default	0.5581	0.2189	0.1760	0.9937	2.14e-02
288	3	7	1	y	JLM	0.3487	0.1293	0.0772	0.7386	2.57e-03
289	3	7	1	y	default	0.3487	0.1293	0.0772	0.9433	3.28e-03
290	3	7	1	n	JLM	0.3487	0.1293	0.0772	0.7386	2.57e-03

Table .1 (cont'd)

291	3	7	1	n	default	0.3487	0.1293	0.0772	0.9433	3.28e-03
292	3	7	2	y	JLM	0.3188	0.1213	0.0760	0.9764	2.87e-03
293	3	7	2	y	default	0.3188	0.1213	0.0760	0.9852	2.89e-03
294	3	7	2	n	JLM	0.3188	0.1213	0.0760	0.9764	2.87e-03
295	3	7	2	n	default	0.3188	0.1213	0.0760	0.9852	2.89e-03
296	3	7	3	y	JLM	0.4854	0.1975	0.2313	0.7102	1.57e-02
297	3	7	3	y	default	0.4854	0.1975	0.2313	0.9301	2.06e-02
298	3	7	3	n	JLM	0.4194	0.1675	0.1235	0.8156	7.08e-03
299	3	7	3	n	default	0.4194	0.1675	0.1235	0.9774	8.48e-03
300	3	8	1	y	JLM	0.4105	0.1086	0.0484	0.3808	8.22e-04
301	3	8	1	y	default	0.4105	0.1086	0.0484	0.6734	1.45e-03
302	3	8	1	n	JLM	0.3996	0.1008	0.0375	0.4155	6.27e-04
303	3	8	1	n	default	0.3996	0.1008	0.0375	0.7073	1.07e-03
304	3	8	2	y	JLM	0.4020	0.1122	0.0512	0.3606	8.32e-04
305	3	8	2	y	default	0.4020	0.1122	0.0512	0.6526	1.51e-03
306	3	8	2	n	JLM	0.3958	0.1015	0.0372	0.3942	5.88e-04
307	3	8	2	n	default	0.3958	0.1015	0.0372	0.6865	1.02e-03
308	3	8	3	y	JLM	0.4946	0.1639	0.1214	0.3595	3.54e-03
309	3	8	3	y	default	0.4946	0.1639	0.1214	0.6538	6.43e-03
310	3	8	3	n	JLM	0.4639	0.1251	0.0604	0.4830	1.69e-03
311	3	8	3	n	default	0.4639	0.1251	0.0604	0.7696	2.70e-03
312	3	9	1	y	JLM	0.5015	0.1410	0.0678	0.8351	4.01e-03
313	3	9	1	y	default	0.5015	0.1410	0.0678	0.9826	4.72e-03
314	3	9	1	n	JLM	0.5015	0.1410	0.0678	0.8351	4.01e-03
315	3	9	1	n	default	0.5015	0.1410	0.0678	0.9826	4.72e-03
316	3	9	2	y	JLM	0.4754	0.1318	0.0686	0.9639	4.14e-03
317	3	9	2	y	default	0.4754	0.1318	0.0686	0.9927	4.27e-03
318	3	9	2	n	JLM	0.4754	0.1318	0.0686	0.9639	4.14e-03
319	3	9	2	n	default	0.4754	0.1318	0.0686	0.9927	4.27e-03
320	3	9	3	y	JLM	0.6402	0.2289	0.1993	0.8085	2.36e-02
321	3	9	3	y	default	0.6402	0.2289	0.1993	0.9743	2.85e-02
322	3	9	3	n	JLM	0.5221	0.1771	0.1053	0.9022	8.79e-03
323	3	9	3	n	default	0.5221	0.1771	0.1053	0.9981	9.72e-03
324	4	1	1	y	JLM	0.7562	0.3451	0.5904	0.8579	1.32e-01
325	4	1	1	y	default	0.7562	0.3451	0.5904	0.9892	1.52e-01
326	4	1	1	n	JLM	0.7562	0.3451	0.5904	0.8579	1.32e-01
327	4	1	1	n	default	0.7562	0.3451	0.5904	0.9892	1.52e-01

Table .1 (cont'd)

328	4	1	2	y	JLM	0.7756	0.3670	0.6593	0.8012	1.50e-01
329	4	1	2	y	default	0.7756	0.3670	0.6593	0.6305	1.18e-01
330	4	1	2	n	JLM	0.7756	0.3670	0.6593	0.8012	1.50e-01
331	4	1	2	n	default	0.7756	0.3670	0.6593	0.6305	1.18e-01
332	4	1	3	y	JLM	0.8119	0.5291	0.6888	0.8553	2.53e-01
333	4	1	3	y	default	0.8119	0.5291	0.6888	0.9895	2.93e-01
334	4	1	3	n	JLM	0.7948	0.4647	0.7332	0.9579	2.59e-01
335	4	1	3	n	default	0.7948	0.4647	0.7332	0.9945	2.69e-01
336	4	2	1	y	JLM	0.7943	0.4419	0.5530	0.0002	3.28e-05
337	4	2	1	y	default	0.7943	0.4419	0.5530	0.0040	7.79e-04
338	4	2	1	n	JLM	0.7943	0.4419	0.5530	0.0002	3.28e-05
339	4	2	1	n	default	0.7943	0.4419	0.5530	0.0040	7.79e-04
340	4	2	2	y	JLM	0.7898	0.4155	0.5038	0.0001	1.17e-05
341	4	2	2	y	default	0.7898	0.4155	0.5038	0.0022	3.64e-04
342	4	2	2	n	JLM	0.7898	0.4155	0.5038	0.0001	1.17e-05
343	4	2	2	n	default	0.7898	0.4155	0.5038	0.0022	3.64e-04
344	4	2	3	y	JLM	0.8233	0.5187	0.7032	0.0002	5.09e-05
345	4	2	3	y	default	0.8233	0.5187	0.7032	0.0040	1.21e-03
346	4	2	3	n	JLM	0.8214	0.4829	0.6197	0.0002	5.79e-05
347	4	2	3	n	default	0.8214	0.4829	0.6197	0.0050	1.24e-03
348	4	3	1	y	JLM	0.2891	0.0773	0.0401	0.1750	1.57e-04
349	4	3	1	y	default	0.2891	0.0773	0.0401	0.4218	3.78e-04
350	4	3	1	n	JLM	0.2891	0.0773	0.0401	0.1750	1.57e-04
351	4	3	1	n	default	0.2891	0.0773	0.0401	0.4218	3.78e-04
352	4	3	2	y	JLM	0.2758	0.0740	0.0341	0.2478	1.73e-04
353	4	3	2	y	default	0.2758	0.0740	0.0341	0.5225	3.64e-04
354	4	3	2	n	JLM	0.2758	0.0740	0.0341	0.2478	1.73e-04
355	4	3	2	n	default	0.2758	0.0740	0.0341	0.5225	3.64e-04
356	4	3	3	y	JLM	0.5295	0.1570	0.2276	0.1742	3.29e-03
357	4	3	3	y	default	0.5295	0.1570	0.2276	0.4226	7.99e-03
358	4	3	3	n	JLM	0.3626	0.1036	0.0697	0.2402	6.29e-04
359	4	3	3	n	default	0.3626	0.1036	0.0697	0.5142	1.35e-03
360	4	4	1	y	JLM	0.5632	0.1828	0.1343	0.3434	4.75e-03
361	4	4	1	y	default	0.5632	0.1828	0.1343	0.6335	8.76e-03
362	4	4	1	n	JLM	0.5632	0.1828	0.1343	0.3434	4.75e-03
363	4	4	1	n	default	0.5632	0.1828	0.1343	0.6335	8.76e-03
364	4	4	2	y	JLM	0.5290	0.1685	0.1327	0.6498	7.68e-03

Table .1 (cont'd)

365	4	4	2	y	default	0.5290	0.1685	0.1327	0.8918	1.05e-02
366	4	4	2	n	JLM	0.5290	0.1685	0.1327	0.6498	7.68e-03
367	4	4	2	n	default	0.5290	0.1685	0.1327	0.8918	1.05e-02
368	4	4	3	y	JLM	0.7825	0.3546	0.5466	0.3418	5.19e-02
369	4	4	3	y	default	0.7825	0.3546	0.5466	0.6345	9.63e-02
370	4	4	3	n	JLM	0.6102	0.2481	0.2417	0.4509	1.65e-02
371	4	4	3	n	default	0.6102	0.2481	0.2417	0.7410	2.71e-02
372	4	5	1	y	JLM	0.7941	0.4369	0.6438	0.1850	4.13e-02
373	4	5	1	y	default	0.7941	0.4369	0.6438	0.4370	9.76e-02
374	4	5	1	n	JLM	0.7941	0.4369	0.6438	0.1850	4.13e-02
375	4	5	1	n	default	0.7941	0.4369	0.6438	0.4370	9.76e-02
376	4	5	2	y	JLM	0.8046	0.4883	0.7257	0.4489	1.28e-01
377	4	5	2	y	default	0.8046	0.4883	0.7257	0.7395	2.11e-01
378	4	5	2	n	JLM	0.8046	0.4883	0.7257	0.4489	1.28e-01
379	4	5	2	n	default	0.8046	0.4883	0.7257	0.7395	2.11e-01
380	4	5	3	y	JLM	0.8181	0.5647	0.7118	0.1845	6.07e-02
381	4	5	3	y	default	0.8181	0.5647	0.7118	0.4382	1.44e-01
382	4	5	3	n	JLM	0.8145	0.5357	0.7180	0.2521	7.90e-02
383	4	5	3	n	default	0.8145	0.5357	0.7180	0.5299	1.66e-01
384	4	6	1	y	JLM	0.6735	0.2304	0.2754	0.2794	1.19e-02
385	4	6	1	y	default	0.6735	0.2304	0.2754	0.5614	2.40e-02
386	4	6	1	n	JLM	0.6735	0.2304	0.2754	0.2794	1.19e-02
387	4	6	1	n	default	0.6735	0.2304	0.2754	0.5614	2.40e-02
388	4	6	2	y	JLM	0.6440	0.2495	0.3173	0.5540	2.82e-02
389	4	6	2	y	default	0.6440	0.2495	0.3173	0.8257	4.21e-02
390	4	6	2	n	JLM	0.6440	0.2495	0.3173	0.5540	2.82e-02
391	4	6	2	n	default	0.6440	0.2495	0.3173	0.8257	4.21e-02
392	4	6	3	y	JLM	0.8053	0.4060	0.6619	0.2783	6.02e-02
393	4	6	3	y	default	0.8053	0.4060	0.6619	0.5625	1.22e-01
394	4	6	3	n	JLM	0.7540	0.3112	0.4025	0.3726	3.52e-02
395	4	6	3	n	default	0.7540	0.3112	0.4025	0.6664	6.29e-02
396	4	7	1	y	JLM	0.4978	0.2143	0.2585	0.2180	6.01e-03
397	4	7	1	y	default	0.4978	0.2143	0.2585	0.4843	1.34e-02
398	4	7	1	n	JLM	0.4978	0.2143	0.2585	0.2180	6.01e-03
399	4	7	1	n	default	0.4978	0.2143	0.2585	0.4843	1.34e-02
400	4	7	2	y	JLM	0.5072	0.2039	0.2409	0.5508	1.37e-02
401	4	7	2	y	default	0.5072	0.2039	0.2409	0.8250	2.06e-02

Table .1 (cont'd)

402	4	7	2	n	JLM	0.5072	0.2039	0.2409	0.5508	1.37e-02
403	4	7	2	n	default	0.5072	0.2039	0.2409	0.8250	2.06e-02
404	4	7	3	y	JLM	0.7489	0.3448	0.5994	0.2172	3.36e-02
405	4	7	3	y	default	0.7489	0.3448	0.5994	0.4854	7.51e-02
406	4	7	3	n	JLM	0.5514	0.2550	0.3248	0.2952	1.35e-02
407	4	7	3	n	default	0.5514	0.2550	0.3248	0.5832	2.66e-02
408	4	8	1	y	JLM	0.5204	0.1786	0.1618	0.0397	5.96e-04
409	4	8	1	y	default	0.5204	0.1786	0.1618	0.1618	2.43e-03
410	4	8	1	n	JLM	0.4857	0.1550	0.1033	0.0460	3.58e-04
411	4	8	1	n	default	0.4857	0.1550	0.1033	0.1783	1.39e-03
412	4	8	2	y	JLM	0.5472	0.1742	0.1479	0.0357	5.03e-04
413	4	8	2	y	default	0.5472	0.1742	0.1479	0.1508	2.13e-03
414	4	8	2	n	JLM	0.4750	0.1525	0.0996	0.0414	2.99e-04
415	4	8	2	n	default	0.4750	0.1525	0.0996	0.1664	1.20e-03
416	4	8	3	y	JLM	0.7238	0.2818	0.4360	0.0395	3.52e-03
417	4	8	3	y	default	0.7238	0.2818	0.4360	0.1623	1.44e-02
418	4	8	3	n	JLM	0.5199	0.1905	0.1598	0.0653	1.03e-03
419	4	8	3	n	default	0.5199	0.1905	0.1598	0.2251	3.56e-03
420	4	9	1	y	JLM	0.5734	0.2016	0.1693	0.2693	5.27e-03
421	4	9	1	y	default	0.5734	0.2016	0.1693	0.5484	1.07e-02
422	4	9	1	n	JLM	0.5734	0.2016	0.1693	0.2693	5.27e-03
423	4	9	1	n	default	0.5734	0.2016	0.1693	0.5484	1.07e-02
424	4	9	2	y	JLM	0.5770	0.1886	0.1675	0.4619	8.42e-03
425	4	9	2	y	default	0.5770	0.1886	0.1675	0.7492	1.37e-02
426	4	9	2	n	JLM	0.5770	0.1886	0.1675	0.4619	8.42e-03
427	4	9	2	n	default	0.5770	0.1886	0.1675	0.7492	1.37e-02
428	4	9	3	y	JLM	0.7777	0.3632	0.5763	0.2681	4.37e-02
429	4	9	3	y	default	0.7777	0.3632	0.5763	0.5495	8.95e-02
430	4	9	3	n	JLM	0.6611	0.2617	0.2557	0.3599	1.59e-02
431	4	9	3	n	default	0.6611	0.2617	0.2557	0.6524	2.89e-02
432	5	1	1	y	JLM	0.3036	0.0750	0.0472	0.4802	5.16e-04
433	5	1	1	y	default	0.3036	0.0750	0.0472	0.3451	3.71e-04
434	5	1	1	n	JLM	0.3036	0.0750	0.0472	0.4802	5.16e-04
435	5	1	1	n	default	0.3036	0.0750	0.0472	0.3451	3.71e-04
436	5	1	2	y	JLM	0.1869	0.0707	0.0454	0.1260	7.56e-05
437	5	1	2	y	default	0.1869	0.0707	0.0454	0.0874	5.25e-05
438	5	1	2	n	JLM	0.1869	0.0707	0.0454	0.1260	7.56e-05

Table .1 (cont'd)

439	5	1	2	n	default	0.1869	0.0707	0.0454	0.0874	5.25e-05
440	5	1	3	y	JLM	0.5168	0.1586	0.1913	0.5020	7.87e-03
441	5	1	3	y	default	0.5168	0.1586	0.1913	0.3589	5.63e-03
442	5	1	3	n	JLM	0.4158	0.1247	0.1039	0.3803	2.05e-03
443	5	1	3	n	default	0.4158	0.1247	0.1039	0.2665	1.44e-03
444	5	2	1	y	JLM	0.5129	0.1558	0.1336	0.2266	2.42e-03
445	5	2	1	y	default	0.5129	0.1558	0.1336	0.4995	5.33e-03
446	5	2	1	n	JLM	0.5129	0.1558	0.1336	0.2266	2.42e-03
447	5	2	1	n	default	0.5129	0.1558	0.1336	0.4995	5.33e-03
448	5	2	2	y	JLM	0.5509	0.1469	0.1113	0.1591	1.43e-03
449	5	2	2	y	default	0.5509	0.1469	0.1113	0.4013	3.62e-03
450	5	2	2	n	JLM	0.5509	0.1469	0.1113	0.1591	1.43e-03
451	5	2	2	n	default	0.5509	0.1469	0.1113	0.4013	3.62e-03
452	5	2	3	y	JLM	0.5929	0.2068	0.2309	0.2193	6.21e-03
453	5	2	3	y	default	0.5929	0.2068	0.2309	0.4910	1.39e-02
454	5	2	3	n	JLM	0.5875	0.1936	0.1912	0.2553	5.55e-03
455	5	2	3	n	default	0.5875	0.1936	0.1912	0.5379	1.17e-02
456	5	3	1	y	JLM	0.0633	0.0205	0.0026	0.9907	3.37e-06
457	5	3	1	y	default	0.0633	0.0205	0.0026	0.8891	3.03e-06
458	5	3	1	n	JLM	0.0633	0.0205	0.0026	0.9907	3.37e-06
459	5	3	1	n	default	0.0633	0.0205	0.0026	0.8891	3.03e-06
460	5	3	2	y	JLM	0.0572	0.0193	0.0024	0.9603	2.52e-06
461	5	3	2	y	default	0.0572	0.0193	0.0024	0.8246	2.17e-06
462	5	3	2	n	JLM	0.0572	0.0193	0.0024	0.9603	2.52e-06
463	5	3	2	n	default	0.0572	0.0193	0.0024	0.8246	2.17e-06
464	5	3	3	y	JLM	0.0789	0.0344	0.0086	0.9942	2.31e-05
465	5	3	3	y	default	0.0789	0.0344	0.0086	0.8983	2.08e-05
466	5	3	3	n	JLM	0.0726	0.0262	0.0044	0.9651	7.98e-06
467	5	3	3	n	default	0.0726	0.0262	0.0044	0.8311	6.88e-06
468	5	4	1	y	JLM	0.1498	0.0464	0.0124	0.8608	7.39e-05
469	5	4	1	y	default	0.1498	0.0464	0.0124	0.6922	5.95e-05
470	5	4	1	n	JLM	0.1498	0.0464	0.0124	0.8608	7.39e-05
471	5	4	1	n	default	0.1498	0.0464	0.0124	0.6922	5.95e-05
472	5	4	2	y	JLM	0.1403	0.0422	0.0117	0.6378	4.41e-05
473	5	4	2	y	default	0.1403	0.0422	0.0117	0.4743	3.28e-05
474	5	4	2	n	JLM	0.1403	0.0422	0.0117	0.6378	4.41e-05
475	5	4	2	n	default	0.1403	0.0422	0.0117	0.4743	3.28e-05

Table .1 (cont'd)

476	5	4	3	y	JLM	0.2640	0.0871	0.0447	0.8758	9.01e-04
477	5	4	3	y	default	0.2640	0.0871	0.0447	0.7064	7.27e-04
478	5	4	3	n	JLM	0.2071	0.0709	0.0261	0.7857	3.01e-04
479	5	4	3	n	default	0.2071	0.0709	0.0261	0.6094	2.34e-04
480	5	5	1	y	JLM	0.4847	0.1357	0.1175	0.9629	7.44e-03
481	5	5	1	y	default	0.4847	0.1357	0.1175	0.8298	6.41e-03
482	5	5	1	n	JLM	0.4847	0.1357	0.1175	0.9629	7.44e-03
483	5	5	1	n	default	0.4847	0.1357	0.1175	0.8298	6.41e-03
484	5	5	2	y	JLM	0.5033	0.1501	0.1587	0.7754	9.30e-03
485	5	5	2	y	default	0.5033	0.1501	0.1587	0.6008	7.20e-03
486	5	5	2	n	JLM	0.5033	0.1501	0.1587	0.7754	9.30e-03
487	5	5	2	n	default	0.5033	0.1501	0.1587	0.6008	7.20e-03
488	5	5	3	y	JLM	0.5957	0.2289	0.3039	0.9704	4.02e-02
489	5	5	3	y	default	0.5957	0.2289	0.3039	0.8411	3.48e-02
490	5	5	3	n	JLM	0.6019	0.1969	0.2111	0.9206	2.30e-02
491	5	5	3	n	default	0.6019	0.1969	0.2111	0.7637	1.91e-02
492	5	6	1	y	JLM	0.2278	0.0558	0.0215	0.9097	2.49e-04
493	5	6	1	y	default	0.2278	0.0558	0.0215	0.7513	2.06e-04
494	5	6	1	n	JLM	0.2278	0.0558	0.0215	0.9097	2.49e-04
495	5	6	1	n	default	0.2278	0.0558	0.0215	0.7513	2.06e-04
496	5	6	2	y	JLM	0.1900	0.0566	0.0219	0.7140	1.68e-04
497	5	6	2	y	default	0.1900	0.0566	0.0219	0.5422	1.28e-04
498	5	6	2	n	JLM	0.1900	0.0566	0.0219	0.7140	1.68e-04
499	5	6	2	n	default	0.1900	0.0566	0.0219	0.5422	1.28e-04
500	5	6	3	y	JLM	0.3249	0.1036	0.0701	0.9218	2.17e-03
501	5	6	3	y	default	0.3249	0.1036	0.0701	0.7644	1.80e-03
502	5	6	3	n	JLM	0.2584	0.0821	0.0363	0.8468	6.52e-04
503	5	6	3	n	default	0.2584	0.0821	0.0363	0.6738	5.19e-04
504	5	7	1	y	JLM	0.1145	0.0435	0.0119	0.9590	5.68e-05
505	5	7	1	y	default	0.1145	0.0435	0.0119	0.8217	4.87e-05
506	5	7	1	n	JLM	0.1145	0.0435	0.0119	0.9590	5.68e-05
507	5	7	1	n	default	0.1145	0.0435	0.0119	0.8217	4.87e-05
508	5	7	2	y	JLM	0.1045	0.0416	0.0117	0.7359	3.74e-05
509	5	7	2	y	default	0.1045	0.0416	0.0117	0.5606	2.85e-05
510	5	7	2	n	JLM	0.1045	0.0416	0.0117	0.7359	3.74e-05
511	5	7	2	n	default	0.1045	0.0416	0.0117	0.5606	2.85e-05
512	5	7	3	y	JLM	0.1738	0.0770	0.0464	0.9670	6.00e-04

Table .1 (cont'd)

513	5	7	3	y	default	0.1738	0.0770	0.0464	0.8331	5.17e-04
514	5	7	3	n	JLM	0.1389	0.0593	0.0242	0.9137	1.82e-04
515	5	7	3	n	default	0.1389	0.0593	0.0242	0.7526	1.50e-04
516	5	8	1	y	JLM	0.1443	0.0449	0.0145	0.9455	8.86e-05
517	5	8	1	y	default	0.1443	0.0449	0.0145	0.9972	9.34e-05
518	5	8	1	n	JLM	0.1746	0.0410	0.0128	0.9616	8.80e-05
519	5	8	1	n	default	0.1746	0.0410	0.0128	0.9928	9.08e-05
520	5	8	2	y	JLM	0.1804	0.0441	0.0173	0.9343	1.29e-04
521	5	8	2	y	default	0.1804	0.0441	0.0173	0.9987	1.38e-04
522	5	8	2	n	JLM	0.1628	0.0403	0.0138	0.9518	8.63e-05
523	5	8	2	n	default	0.1628	0.0403	0.0138	0.9958	9.03e-05
524	5	8	3	y	JLM	0.2219	0.0691	0.0439	0.9368	6.31e-04
525	5	8	3	y	default	0.2219	0.0691	0.0439	0.9983	6.72e-04
526	5	8	3	n	JLM	0.2017	0.0517	0.0202	0.9861	2.07e-04
527	5	8	3	n	default	0.2017	0.0517	0.0202	0.9753	2.05e-04
528	5	9	1	y	JLM	0.2159	0.0514	0.0208	0.9060	2.09e-04
529	5	9	1	y	default	0.2159	0.0514	0.0208	0.7473	1.72e-04
530	5	9	1	n	JLM	0.2159	0.0514	0.0208	0.9060	2.09e-04
531	5	9	1	n	default	0.2159	0.0514	0.0208	0.7473	1.72e-04
532	5	9	2	y	JLM	0.2056	0.0489	0.0178	0.7648	1.37e-04
533	5	9	2	y	default	0.2056	0.0489	0.0178	0.5915	1.06e-04
534	5	9	2	n	JLM	0.2056	0.0489	0.0178	0.7648	1.37e-04
535	5	9	2	n	default	0.2056	0.0489	0.0178	0.5915	1.06e-04
536	5	9	3	y	JLM	0.3073	0.0948	0.0729	0.9184	1.95e-03
537	5	9	3	y	default	0.3073	0.0948	0.0729	0.7606	1.61e-03
538	5	9	3	n	JLM	0.2890	0.0722	0.0355	0.8425	6.25e-04
539	5	9	3	n	default	0.2890	0.0722	0.0355	0.6698	4.97e-04
540	6	1	1	y	JLM	0.7673	0.3867	0.4275	0.3713	4.71e-02
541	6	1	1	y	default	0.7673	0.3867	0.4275	0.6677	8.47e-02
542	6	1	1	n	JLM	0.7673	0.3867	0.4275	0.3713	4.71e-02
543	6	1	1	n	default	0.7673	0.3867	0.4275	0.6677	8.47e-02
544	6	1	2	y	JLM	0.7323	0.3952	0.5677	0.9942	1.63e-01
545	6	1	2	y	default	0.7323	0.3952	0.5677	0.9607	1.58e-01
546	6	1	2	n	JLM	0.7323	0.3952	0.5677	0.9942	1.63e-01
547	6	1	2	n	default	0.7323	0.3952	0.5677	0.9607	1.58e-01
548	6	1	3	y	JLM	0.8081	0.5319	0.7389	0.3685	1.17e-01
549	6	1	3	y	default	0.8081	0.5319	0.7389	0.6738	2.14e-01

Table .1 (cont'd)

550	6	1	3	n	JLM	0.8008	0.4783	0.6240	0.5039	1.20e-01
551	6	1	3	n	default	0.8008	0.4783	0.6240	0.7975	1.91e-01
552	6	2	1	y	JLM	0.8341	0.4911	0.4870	0.0000	1.98e-06
553	6	2	1	y	default	0.8341	0.4911	0.4870	0.0006	1.11e-04
554	6	2	1	n	JLM	0.8341	0.4911	0.4870	0.0000	1.98e-06
555	6	2	1	n	default	0.8341	0.4911	0.4870	0.0006	1.11e-04
556	6	2	2	y	JLM	0.8320	0.4784	0.4572	0.0000	6.53e-07
557	6	2	2	y	default	0.8320	0.4784	0.4572	0.0003	5.07e-05
558	6	2	2	n	JLM	0.8320	0.4784	0.4572	0.0000	6.53e-07
559	6	2	2	n	default	0.8320	0.4784	0.4572	0.0003	5.07e-05
560	6	2	3	y	JLM	0.8414	0.5451	0.6200	0.0000	2.70e-06
561	6	2	3	y	default	0.8414	0.5451	0.6200	0.0005	1.56e-04
562	6	2	3	n	JLM	0.8407	0.5200	0.5588	0.0000	3.26e-06
563	6	2	3	n	default	0.8407	0.5200	0.5588	0.0007	1.68e-04
564	6	3	1	y	JLM	0.4530	0.1323	0.0508	0.0119	3.62e-05
565	6	3	1	y	default	0.4530	0.1323	0.0508	0.0751	2.29e-04
566	6	3	1	n	JLM	0.4530	0.1323	0.0508	0.0119	3.62e-05
567	6	3	1	n	default	0.4530	0.1323	0.0508	0.0751	2.29e-04
568	6	3	2	y	JLM	0.4214	0.1312	0.0487	0.0203	5.48e-05
569	6	3	2	y	default	0.4214	0.1312	0.0487	0.1078	2.90e-04
570	6	3	2	n	JLM	0.4214	0.1312	0.0487	0.0203	5.48e-05
571	6	3	2	n	default	0.4214	0.1312	0.0487	0.1078	2.90e-04
572	6	3	3	y	JLM	0.5519	0.2078	0.1850	0.0117	2.48e-04
573	6	3	3	y	default	0.5519	0.2078	0.1850	0.0758	1.61e-03
574	6	3	3	n	JLM	0.4760	0.1645	0.0824	0.0180	1.16e-04
575	6	3	3	n	default	0.4760	0.1645	0.0824	0.1010	6.52e-04
576	6	4	1	y	JLM	0.6271	0.2633	0.1343	0.0662	1.47e-03
577	6	4	1	y	default	0.6271	0.2633	0.1343	0.2270	5.03e-03
578	6	4	1	n	JLM	0.6271	0.2633	0.1343	0.0662	1.47e-03
579	6	4	1	n	default	0.6271	0.2633	0.1343	0.2270	5.03e-03
580	6	4	2	y	JLM	0.6350	0.2416	0.1349	0.2051	4.25e-03
581	6	4	2	y	default	0.6350	0.2416	0.1349	0.4668	9.66e-03
582	6	4	2	n	JLM	0.6350	0.2416	0.1349	0.2051	4.25e-03
583	6	4	2	n	default	0.6350	0.2416	0.1349	0.4668	9.66e-03
584	6	4	3	y	JLM	0.7381	0.3871	0.4340	0.0646	8.01e-03
585	6	4	3	y	default	0.7381	0.3871	0.4340	0.2272	2.82e-02
586	6	4	3	n	JLM	0.6954	0.3223	0.2294	0.0967	4.97e-03

Table .1 (cont'd)

587	6	4	3	n	default	0.6954	0.3223	0.2294	0.2945	1.51e-02
588	6	5	1	y	JLM	0.8231	0.4822	0.5633	0.0379	8.47e-03
589	6	5	1	y	default	0.8231	0.4822	0.5633	0.1559	3.49e-02
590	6	5	1	n	JLM	0.8231	0.4822	0.5633	0.0379	8.47e-03
591	6	5	1	n	default	0.8231	0.4822	0.5633	0.1559	3.49e-02
592	6	5	2	y	JLM	0.8208	0.5158	0.6566	0.1507	4.19e-02
593	6	5	2	y	default	0.8208	0.5158	0.6566	0.3818	1.06e-01
594	6	5	2	n	JLM	0.8208	0.5158	0.6566	0.1507	4.19e-02
595	6	5	2	n	default	0.8208	0.5158	0.6566	0.3818	1.06e-01
596	6	5	3	y	JLM	0.8222	0.5742	0.7216	0.0366	1.25e-02
597	6	5	3	y	default	0.8222	0.5742	0.7216	0.1549	5.27e-02
598	6	5	3	n	JLM	0.8279	0.5517	0.6661	0.0551	1.68e-02
599	6	5	3	n	default	0.8279	0.5517	0.6661	0.2022	6.15e-02
600	6	6	1	y	JLM	0.6819	0.3159	0.2500	0.0513	2.76e-03
601	6	6	1	y	default	0.6819	0.3159	0.2500	0.1920	1.03e-02
602	6	6	1	n	JLM	0.6819	0.3159	0.2500	0.0513	2.76e-03
603	6	6	1	n	default	0.6819	0.3159	0.2500	0.1920	1.03e-02
604	6	6	2	y	JLM	0.6880	0.3103	0.2857	0.1620	9.88e-03
605	6	6	2	y	default	0.6880	0.3103	0.2857	0.4028	2.46e-02
606	6	6	2	n	JLM	0.6880	0.3103	0.2857	0.1620	9.88e-03
607	6	6	2	n	default	0.6880	0.3103	0.2857	0.4028	2.46e-02
608	6	6	3	y	JLM	0.7840	0.4414	0.5535	0.0499	9.57e-03
609	6	6	3	y	default	0.7840	0.4414	0.5535	0.1919	3.68e-02
610	6	6	3	n	JLM	0.7402	0.3730	0.3597	0.0752	7.46e-03
611	6	6	3	n	default	0.7402	0.3730	0.3597	0.2500	2.48e-02
612	6	7	1	y	JLM	0.6568	0.2637	0.2284	0.0560	2.21e-03
613	6	7	1	y	default	0.6568	0.2637	0.2284	0.2004	7.93e-03
614	6	7	1	n	JLM	0.6568	0.2637	0.2284	0.0560	2.21e-03
615	6	7	1	n	default	0.6568	0.2637	0.2284	0.2004	7.93e-03
616	6	7	2	y	JLM	0.6185	0.2533	0.2579	0.2423	9.79e-03
617	6	7	2	y	default	0.6185	0.2533	0.2579	0.5099	2.06e-02
618	6	7	2	n	JLM	0.6185	0.2533	0.2579	0.2423	9.79e-03
619	6	7	2	n	default	0.6185	0.2533	0.2579	0.5099	2.06e-02
620	6	7	3	y	JLM	0.7514	0.3744	0.5157	0.0541	7.85e-03
621	6	7	3	y	default	0.7514	0.3744	0.5157	0.1992	2.89e-02
622	6	7	3	n	JLM	0.7254	0.3146	0.3567	0.0811	6.60e-03
623	6	7	3	n	default	0.7254	0.3146	0.3567	0.2586	2.11e-02

Table .1 (cont'd)

624	6	8	1	y	JLM	0.6343	0.2487	0.1493	0.0019	4.46e-05
625	6	8	1	y	default	0.6343	0.2487	0.1493	0.0212	5.00e-04
626	6	8	1	n	JLM	0.6427	0.2310	0.1254	0.0022	4.14e-05
627	6	8	1	n	default	0.6427	0.2310	0.1254	0.0237	4.41e-04
628	6	8	2	y	JLM	0.6543	0.2480	0.1563	0.0016	4.18e-05
629	6	8	2	y	default	0.6543	0.2480	0.1563	0.0193	4.89e-04
630	6	8	2	n	JLM	0.6266	0.2282	0.1266	0.0019	3.50e-05
631	6	8	2	n	default	0.6266	0.2282	0.1266	0.0215	3.90e-04
632	6	8	3	y	JLM	0.7286	0.3404	0.3552	0.0018	1.62e-04
633	6	8	3	y	default	0.7286	0.3404	0.3552	0.0211	1.86e-03
634	6	8	3	n	JLM	0.6855	0.2694	0.1744	0.0033	1.05e-04
635	6	8	3	n	default	0.6855	0.2694	0.1744	0.0313	1.01e-03
636	6	9	1	y	JLM	0.6802	0.2770	0.1628	0.0381	1.17e-03
637	6	9	1	y	default	0.6802	0.2770	0.1628	0.1589	4.87e-03
638	6	9	1	n	JLM	0.6802	0.2770	0.1628	0.0381	1.17e-03
639	6	9	1	n	default	0.6802	0.2770	0.1628	0.1589	4.87e-03
640	6	9	2	y	JLM	0.6559	0.2671	0.1618	0.0935	2.65e-03
641	6	9	2	y	default	0.6559	0.2671	0.1618	0.2856	8.09e-03
642	6	9	2	n	JLM	0.6559	0.2671	0.1618	0.0935	2.65e-03
643	6	9	2	n	default	0.6559	0.2671	0.1618	0.2856	8.09e-03
644	6	9	3	y	JLM	0.7808	0.4074	0.4439	0.0372	5.25e-03
645	6	9	3	y	default	0.7808	0.4074	0.4439	0.1590	2.25e-02
646	6	9	3	n	JLM	0.7282	0.3324	0.2572	0.0562	3.50e-03
647	6	9	3	n	default	0.7282	0.3324	0.2572	0.2083	1.30e-02